Michał Rajek, M.Sc. Eng.

Institute of Fluid-Flow Machinery
Polish Academy of Sciences

Large Eddy Simulations of Turbulent Single-Phase and Dispersed Two-Phase Flows

Symulacje wielkowirowe przepływów turbulentnych jednofazowych oraz dwufazowych z fazą rozproszoną

A Dissertation
Submitted to the Scientific Council
of the Institute of Fluid-Flow Machinery
Polish Academy of Sciences

Doctoral advisor:
Prof. Jacek Pozorski

Gdańsk, June 2025

Contents

Streszczenie rozszerzone **i**

Extended abstract **vii**

Overview of the dissertation **xiii**

Preface **xvii**

Acknowledgments **xix**

1 Introduction **1**
1.1 Turbulent flows 1
1.2 Particle-laden turbulent flows 2

2 Direct Numerical Simulations **7**
2.1 Equations of fluid motion in physical space 7
2.2 Equations of fluid motion in Fourier space 8
2.3 Pseudo-spectral approximation 12
2.4 Aliasing errors 14
2.5 Energy balance equation 18
2.6 Initial velocity field 22
2.7 Time integration 23
2.8 Basic flow parameters 27
2.9 Time statistics and error bounds 30
2.10 Decaying turbulence 32
2.11 Forced isotropic turbulence 35
2.12 Concluding remarks 45

3 Large Eddy Simulations **49**
3.1 Equations of fluid motion in physical space 49
3.2 Problem statement 52
3.3 *A priori* Large Eddy Simulations 54
3.4 Equations of fluid motion in Fourier space 55

3.5 *A priori* spectral eddy-viscosity 60
3.6 Spectral Large Eddy Simulations 64
3.7 Adaptive parametrization 72
3.8 Concluding remarks 83

4 Lagrangian particle tracking **87**
4.1 Equations of particle motion 87
4.2 Fluid velocity at the particle location 89
4.3 B-spline interpolation 91
4.4 Time integration 97
4.5 Basic particle statistics 98
4.6 Residual fluid velocity at the particle location 105
4.7 Concluding remarks 109

5 Inertial particle dynamics **111**
5.1 Problem statement 111
5.2 DNS at low Reynolds number 114
5.3 LES at low Reynolds number 123
5.4 LES at high Reynolds number 135
5.5 Concluding remarks 144

6 Summary and future research **147**
6.1 Summary of achievements 147
6.2 Future research 150

Streszczenie rozszerzone

Ogólne wprowadzenie

Turbulentne przepływy dwufazowe z fazą rozproszoną w postaci pęcherzyków gazu, kropel cieczy lub cząstek stałych stanowią znaczącą grupę przepływów obserwowanych zarówno w środowisku naturalnym, jak i procesach przemysłowych. Należy podkreślić, że zjawisko transportu turbulentnego fazy rozproszonej stanowi wciąż duże wyzwanie tak w kontekście teoretycznym, jak i obliczeniowym. Do powodów takiego stanu rzeczy można niewątpliwie zaliczyć nieliniowość tego procesu oraz szeroki zakres skal czasowych i przestrzennych związanych nie tylko z przepływem turbulentnym, ale również z samą fazą rozproszoną. Opis przepływu dwufazowego komplikuje się jeszcze bardziej, gdy w prowadzonych rozważaniach uwzględnia się wpływ pola grawitacyjnego, reakcje chemiczne lub przemiany fazowe, ale także sprzężenie pędu fazy rozproszonej (dyskretnej) z fazą nośną (ciągłą), zderzenia i koalescencję w fazie rozproszonej oraz inne oddziaływania pomiędzy unoszonymi cząstkami. Choć w niektórych przypadkach możliwe jest wprowadzenie daleko idących uproszczeń, to w ogólności pełniejsze zrozumienie zjawisk zachodzących w przepływach dwufazowych wymaga zastosowania podejścia multidyscyplinarnego, łączącego między innymi modelowanie matematyczne, techniki eksperymentalne oraz metody obliczeniowe mechaniki płynów. Niestety pomimo znacznego rozwoju metod eksperymentalnych, ograniczenia aparatury pomiarowej oraz niekiedy inne ograniczenia techniczne często utrudniają lub nawet uniemożliwiają przeprowadzenie pomiarów zarówno w warunkach laboratoryjnych, jak i rzeczywistych. Z tego powodu, przyszłe osiągnięcia w dziedzinie modelowania przepływów dwufazowych będą prawdopodobnie uwarunkowane rozwojem nie tylko w zakresie modelowania matematycznego, ale również w dziedzinie obliczeniowej mechaniki płynów. Należy podkreślić, że znaczący postęp w zakresie możliwości obliczeniowych przyczynił się w ostatnich latach do istotnego rozwoju metod numerycznych, otwierając tym samym zupełnie nowe perspektywy eksploracji turbulentnych przepływów dwufazowych.

Tło i motywacja

Jednym z przykładów przepływu dwufazowego, gdzie niepełne zrozumienie zjawiska transportu turbulentnego fazy rozproszonej prowadzi do wciąż istotnych rozbieżności pomiędzy wynikami symulacji numerycznych a rzeczywistością, jest zjawisko formowania się tak zwanego „ciepłego" deszczu. Przy czym należy podkreślić, że określenie to dotyczy warunków, w których taki opad powstaje. Proces formowania ciepłego deszczu może zachodzić wtedy, gdy średnia temperatura chmury utrzymuje się powyżej punktu zamarzania. Opad ten stanowi około 30 % całkowitego opadu atmosferycznego na Ziemi. Krople chmurowe powstają w wyniku transportu pary wodnej w turbulentnej atmosferze oraz kondensacji tej pary na cząstkach aerozolu. Przyjmuje się, że mechanizm dyfuzyjnego wzrostu kropel chmurowych pozostaje efektywny w zakresie promieni kropel około 5–20 µm, po przekroczeniu którego dalszy wzrost następuje na skutek zderzeń prowadzących do koalescencji. Pole grawitacyjne ma dominujący wpływ na zderzenia kropel chmurowych dopiero wtedy, gdy ich promień przekroczy około 60–80 µm. Pozostawia to zatem pewną lukę w opisie mechanizmu wzrostu kropel chmurowych. Badania z ostatnich kilku dekad pozwalają stwierdzić, że w zakresie promieni kropel 20–60 µm, wzrost ten jest indukowany przez turbulencję wewnątrz chmur oraz oddziaływania aerodynamiczne pomiędzy samymi kroplami. O ile turbulencja atmosferyczna jest zjawiskiem istotnie wieloskalowym, w którym charakterystyczne skale przestrzenne mogą zmieniać się w zakresie od jednego milimetra do nawet kilkuset kilometrów, o tyle samo pogłębienie zrozumienia mechanizmu formowania ciepłego deszczu może być uzyskane również wtedy, gdy prowadzone rozważania zostaną ograniczone do modelowania procesów charakterystycznych dla mikrofizyki chmur, tj. w skalach przestrzennych zbliżonych do najmniejszych, dyssypatywnych skal przepływu turbulentnego.

Jednym z podstawowych narzędzi wykorzystywanych do badania przepływów dwufazowych są symulacje numeryczne metodą DNS (ang. *Direct Numerical Simulation*) polegającą na całkowaniu pełnych równań Naviera-Stokesa, tj. równań rządzących ruchem płynu newtonowskiego. Turbulencję atmosferyczną w mikroskali często modeluje się jako turbulencję homogeniczną i izotropową, niekiedy również statystycznie stacjonarną. Tę ostatnią cechę realizuje się zazwyczaj poprzez wprowadzenie do równania bilansu pędu dodatkowego członu wymuszającego, którego zadaniem jest kompensacja strat energii wynikających z jej dyssypacji w najmniejszych rozwiązywanych skalach przepływu turbulentnego. Należy w tym miejscu podkreślić, że o ile jest on członem sztucznym, o tyle w sensie fizycznym może być interpretowany jako zewnętrzny mechanizm zapewniający warunki sprzyjające powstawaniu turbulencji. W istocie, produkcja energii kinetycznej w rzeczywistych przepływach związana jest zazwyczaj z pewnym średnim gradientem ciśnienia lub temperatury, co implikuje anizotropię, natomiast występowanie ograniczeń geometrycznych wymusza z kolei nieho-

mogeniczność tych przepływów. Z tych powodów model turbulencji izotropowej jest częściowo niefizyczny, choć w pewnym zakresie możliwy do zrealizowania eksperymentalnie. Przykładem turbulencji izotropowej swobodnie zanikającej w czasie może być tak zwana turbulencja zasiatkowa generowana w tunelu aerodynamicznym, natomiast przykładem statystycznie stacjonarnej turbulencji izotropowej może być (w pewnym zakresie skal przestrzennych) przepływ w pobliżu osi kanału lub rury.

Metoda DNS pozwala na symulowanie zjawisk charakterystycznych dla procesów mikrofizyki chmur w zakresie skal zmieniających się od pojedynczych milimetrów do kilku metrów. Mniej więcej od początku lat 70-tych turbulencję izotropową rozwiązuje się najczęściej metodą pseudo-spektralną w obszarze obliczeniowym będącym sześcianem o określonym rozmiarze, w którym statystyczną izotropię zapewnia się poprzez wymuszenie zerowego przepływu średniego oraz zastosowanie okresowych warunków brzegowych. Statystyczną stacjonarność uzyskuje się najczęściej albo w sposób deterministyczny albo stochastyczny, przy czym należy podkreślić, że żadnego z powszechnie stosowanych członów wymuszających nie można zrealizować eksperymentalnie. Ze względu na początkowo niewielki rozmiar kropel chmurowych w odniesieniu do najmniejszych struktur wirowych w przepływie turbulentnym, są one najczęściej przybliżane za pomocą punktów materialnych, których ruch symulowany jest stosując podejście lagranżowskie, co prowadzi do tak zwanych symulacji DNS cząstek punktowych, w skrócie PP-DNS (ang. *point-particle*, PP). Pomimo wielu daleko idących uproszczeń, taki model doprowadził na przestrzeni ostatnich lat do pogłębienia zrozumienia szeregu zjawisk fizycznych charakterystycznych dla procesów mikrofizyki chmur.

W ostatnich latach odnotowano znaczący postęp zarówno w zakresie technik pomiarowych, jak i możliwości obliczeniowych. Najnowsze badania w dziedzinie przepływów dwufazowych pozwalają stwierdzić, że podejście PP-DNS bywa w obecnym sformułowaniu niewystarczające i może prowadzić do znacznych rozbieżności pomiędzy wynikami uzyskanymi na drodze symulacji numerycznych i pomiarów laboratoryjnych. Należy w tym miejscu podkreślić, że w przypadku przepływów jednofazowych, wyniki uzyskane metodą DNS pozostają w doskonałej zgodności z wynikami badań eksperymentalnych, a sama metoda uzyskała na przestrzeni ostatnich dekad status eksperymentu numerycznego. Postęp w zakresie metod obliczeniowych oraz powszechna dostępność komputerów o dużej mocy dały początek symulacjom DNS uwzględniającym skończony rozmiar cząstek, w skrócie PR-DNS (ang. *particle-resolved*, PR). W tym podejściu rozwiązuje się również ruch płynu w otoczeniu cząstek, co pozwala na dokładną reprezentację sił, z jakimi płyn oddziałuje na cząstki i odwrotnie. Niestety ze względu na ogromny koszt obliczeniowy tej metody, liczba symulowanych cząstek jest zazwyczaj niewielka. Wydaje się, że głównie ze względu na znaczący aspekt praktyczny metody PP-DNS, będzie ona w dalszym ciągu wykorzystywana do studiowania przepływów dwufazowych, jednakże przewiduje się również, że dalsze po-

głębienie zrozumienia ich dynamiki będzie następować na skutek połączenia rozważań teoretycznych, badań eksperymentalnych oraz symulacji PP-DNS, choć prawdopodobnie ulepszonych dzięki informacjom uzyskanym w metodzie PR-DNS.

Z uwagi na brak nie tylko przepływu średniego, ale również jednoznacznie określonego wymiaru charakterystycznego, turbulencję izotropową często opisuje się wykorzystując liczbę Reynoldsa opartą na mikroskali Taylora λ, która związana jest z korelacją przestrzenną pola prędkości. Należy w tym miejscu podkreślić, że tak określona skala długości może być stosunkowo prosto wyznaczona zarówno na drodze symulacji numerycznych, jak i eksperymentów. Koszt obliczeniowy metody DNS jest na tyle duży, że obecnie nie jest możliwe symulowanie turbulencji z liczbą Reynoldsa charakterystyczną dla przepływów atmosferycznych, gdzie $Re_\lambda \sim 10000$. Według najlepszego stanu wiedzy autora, obecne zasoby obliczeniowe pozwalają na symulacje DNS turbulencji izotropowej z liczbą Reynoldsa $Re_\lambda \sim 2500$ przy rozdzielczości przestrzennej $\sim 32786^3$ węzłów oraz symulacje PP-DNS z liczbą Reynoldsa $Re_\lambda \sim 600$ wymagające nie tylko $\sim 4096^3$ węzłów, ale także około $\sim 1024^3$ cząstek punktowych, w celu uzyskania stosownego udziału objętościowego fazy rozproszonej.

Jednym z osiągnięć obliczeniowej mechaniki płynów o dużym znaczeniu praktycznym jest opracowanie tak zwanej metody dużych wirów LES (ang. *Large Eddy Simulation*), w której bezpośrednio rozwiązuje się tylko duże struktury wirowe charakterystyczne dla danego przepływu turbulentnego. Turbulencja drobnoskalowa, ze względu na swoją uniwersalność (tj. niezależność od rodzaju przepływu turbulentnego i jego uwarunkowań geometrycznych), może zostać odfiltrowana, co prowadzi do znacznych oszczędności obliczeniowych. W wyniku rozpadu struktur wirowych na mniejsze, turbulencja drobnoskalowa staje się coraz bardziej izotropowa, w efekcie czego jej wpływ na dynamikę dużych wirów może zostać do pewnego stopnia sparametryzowany. Wydaje się, że metoda LES, choć coraz częściej stosowana w zagadnieniach zarówno przemysłowych, jak i środowiskowych, nie znalazła dotychczas szerokiego zastosowania w ramach badań podstawowych dotyczących dynamiki cząstek o niezerowej bezwładności. Przyczyną tego może być fakt, że o ile w przypadku przepływów jednofazowych efekt filtrowania przestrzennego może być stosunkowo prosto skompensowany, o tyle w przypadku przepływów dwufazowych nierozwiązanie turbulencji drobnoskalowej wpływa bezpośrednio na dynamikę fazy rozproszonej, co może wymagać dodatkowego, bardziej złożonego modelowania. Stosunkowo uboga literatura naukowa poświęcona jest głównie modelowaniu turbulencji drobnoskalowej, a jej głównym celem wydaje się być wyłącznie rekonstrukcja podstawowych statystyk uzyskanych w metodach DNS i PP-DNS. Literatura ta nie dostarcza natomiast informacji o tym, czy i jakie możliwości metody LES i PP-LES oferują w zakresie parametrów, dla których zostały zasadniczo opracowane.

Streszczenie

Choć jednym z ważniejszych celów tej pracy było określenie możliwości zastosowania metody dużych wirów do eksploracji przepływów dwufazowych w zakresie parametrów charakterystycznych dla zjawisk mikrofizyki chmur, to zarówno same symulacje numeryczne, jak i uzyskane w tej pracy wyniki mają charakter ogólny i mogą posłużyć do częściowego opisu różnych rodzajów przepływów turbulentnych z fazą rozproszoną, jak również zjawisk fizycznych im towarzyszących, pod warunkiem zachowania zgodności odpowiednich liczb kryterialnych. Niniejsza rozprawa została podzielona na dwie zasadnicze części dotyczące modelowania DNS i LES turbulencji odpowiednio jednofazowej i dwufazowej z przybliżeniem cząstek punktowych.

W pierwszej części opracowano nowy kod pseudo-spektralny zarówno dla turbulencji swobodnie zanikającej, jak i statystycznie stacjonarnej. Wykazano, że powszechnie raportowana w literaturze konstrukcja członu wymuszającego jest niepoprawna, co prowadzi do degradacji rozwiązania poprzez intensyfikację wpływu okresowych warunków brzegowych, w efekcie czego wyniki symulacji numerycznych istotnie różnią się od przewidywań modelu matematycznego. Wykazano również, że istnieje taka konfiguracja zasilania określonych modów Fouriera, która pozwala na uzyskanie poprawnych korelacji przestrzennych pola prędkości, w szczególności zanikających na odległościach równych połowie obszaru obliczeniowego. W zależności od liczby Stokesa, będącej w pewnym sensie miarą bezwładności cząstek, może to mieć istotnie korzystny wpływ na dynamikę fazy rozproszonej. Uzyskane wyniki pokazały, że dla zadanej rozdzielczości przestrzennej liczba Reynoldsa oparta na mikroskali Taylora jest silnie zależna od konfiguracji zasilanych modów Fouriera, co może prowadzić do nieprawdziwych wniosków dotyczących rzeczywistej zdolności rozdzielczej metody DNS. W ostatnich latach w literaturze pojawiło się co najmniej kilka prac dotyczących autonomizacji metody LES, tj. takiej parametryzacji nierozwiązanej turbulencji drobnoskalowej, która wszystkie potrzebne informacje uzyskuje na bieżąco z rozwiązywanego pola prędkości płynu. Dotyczą one zarówno klasycznego modelowania matematycznego, jak i tego opartego na sztucznych sieciach neuronowych. W ramach tej pracy zaproponowano własny model adaptacyjnie parametryzujący wpływ nierozwiązanej turbulencji drobnoskalowej na ewolucję dużych wirów poprzez wprowadzenie lepkości turbulentnej będącej funkcją charakterystycznej skali długości poszczególnych rozwiązywanych struktur wirowych. Wartość tej lepkości określa się poprzez minimalizację różnicy pomiędzy rozwiązywanym widmem energii kinetycznej a zadanym widmem referencyjnym, które może być uzyskane zarówno na drodze symulacji numerycznych lub rzeczywistych eksperymentów, jak i analitycznie, wykorzystując dobrze znane widma modelowe. Wykazano, że nowy model działa poprawnie we właściwym dla metody LES zakresie parametrów. W tej części określono również warunki niezbędne do tego, aby metoda LES mogła być rozważana w kontekście modelowania przepływów o licz-

bach Reynoldsa zbliżonych do obserwowanych zarówno w środowisku naturalnym, jak i procesach przemysłowych. W szczególności dotyczy to parametrów nowego modelu oraz wymagań dotyczących rozdzielczości przestrzennej samej metody LES.

W drugiej części, poświęconej dynamice cząstek o niezerowej bezwładności w przepływie turbulentnym, skupiono się głównie na określeniu przydatności metody LES do eksploracji niektórych zjawisk fizycznych charakterystycznych dla przepływów z fazą rozproszoną, takich jak m.in. preferencyjna koncentracja (ang. *preferential concentration*), czy preferencyjne unoszenie (ang. *preferential sweeping*). Do ilościowego opisu ruchu fazy rozproszonej wykorzystano m.in. takie statystyki jak prędkość opadania, funkcja (rozkład) gęstości prawdopodobieństwa drugiego niezmiennika tensora gradientu prędkości określonego w położeniu cząstek, widmo gęstości liczbowej cząstek oraz radialna funkcja rozkładu (ang. *radial distribution function*, RDF), czy radialna prędkość względna (ang. *radial relative velocity*, RRV). Przykładowo, dwie ostatnie statystyki stanowią główny element parametryzacji częstości zderzeń kropel chmurowych, która z kolei ma istotny wpływ na jakość mezoskalowych modeli prognozowania pogody. Wykazano, że jeżeli stosunek rozdzielczości przestrzennej DNS do LES jest rzędu 4, to statystyki cząstek o niezerowej bezwładności uzyskane w metodzie LES pozostają w doskonałej zgodności jakościowej oraz satysfakcjonującej zgodności ilościowej z metodą DNS. Wyniki najnowszych badań pokazują, że cząstki o niezerowej bezwładności wykazują tendencję do grupowania (ang. *clustering*) nie tylko na odległościach porównywalnych z rozmiarem najmniejszych rozwiązywanych wirów, ale także w skalach długości charakterystycznych dla zakresu bezwładnościowego. W pracy wykazano, że nowy model pozwala na uzyskanie statystycznego opisu tego zjawiska, który pozostaje w doskonałej zgodności jakościowej oraz bardzo dobrej zgodności ilościowej z metodą DNS. Uzyskane wyniki badań wskazują, że metoda LES wzbogacona o statystyczną parametryzację turbulencji drobnoskalowej pozwala na eksplorację przepływów dwufazowych w zakresie parametrów zbliżonym do rzeczywistych przepływów turbulentnych.

Wydaje się, że nadejście symulacji zarówno petaskalowych, jak i eksaskalowych stwarza zupełnie nowe możliwości zastosowania metody LES do eksploracji przepływów turbulentnych, w szczególności tych z fazą rozproszoną, w nieosiągalnym dotąd zakresie liczb Reynoldsa. Mimo nieuniknionych niedoskonałości samej metody, uzyskane wyniki pozwalają stwierdzić, że analizowane w tej pracy podejście stwarza potencjał do formułowania i weryfikacji nowych hipotez badawczych z zakresu dynamiki cząstek o niezerowej bezwładności w przepływie turbulentnym. Choć większość symulacji numerycznych w tej pracy została zrealizowana z wykorzystaniem komputera osobistego o przeciętnych możliwościach obliczeniowych, to wydaje się, że naturalnym jej rozszerzeniem jest rozwój nowego kodu w kierunku symulacji wielkoskalowych, z wykorzystaniem komputerów o dużej mocy obliczeniowej.

Extended abstract

General introduction

Turbulent dispersed two-phase flows with a particulate phase in the form of solid particles, droplets or bubbles represent a significant part of flows relevant to many environmental phenomena and industrial processes. It should be emphasized that the turbulent transport of the particulate phase still poses a major challenge in both theoretical and computational contexts. The reason for this can be partly attributed to the inherent non-linearity of this process and the wide range of spatial and temporal scales associated with both the underlying turbulence and the particulate phase itself. Things become even more complex if one considers not only gravitational effects, chemical reactions or phase transition, but also momentum exchange between the phases, collisions and coalescence within the dispersed phase, and other particle-particle interactions. Although in certain cases far-reaching simplifications can be introduced, a more profound understanding of the physics underlying particulate two-phase flows requires a multidisciplinary approach, combining not just theoretical predictions, mathematical modeling or laboratory and real-world experiments, but also numerical methods and high-performance computing. Despite significant developments in experimental methods, both inevitable limitations of measuring instruments and other technical constraints often make it challenging, or even unfeasible, to perform experiments relevant to turbulent dispersed two-phase flows. For this very reason, future advancements in this very matter will probably be contingent on further developments not only in mathematical and numerical modeling but also experimental methods. On the other hand, it should be emphasized that a rapid growth of computing power has contributed greatly to the development of the foregoing fields, and thus has opened up entirely new perspectives for studying the dispersed two-phase flows.

Background and motivation

The so-called "warm" rain formation is an example of a two-phase process in which an insufficient description of the turbulent transport of the particulate phase causes

significant discrepancies between model predictions and reality. Warm rain occurs when the average temperature throughout the cloud is above the freezing point. It accounts for approximately 30% of the total rainfall on Earth. It is well established that cloud droplets effectively grow by the diffusion of water vapor until they reach approximately 5–20 µm in radius, from where further growth is triggered by collision-coalescence. On the other hand, gravity-induced collisions are most pronounced for cloud droplets that have exceeded approximately 60–80 µm in radius. This essentially leaves a gap in the description of the mechanism governing the growth of cloud droplets. Based on an extensive literature on this very issue, one can conclude that the growth of droplets having approximately 20–60 µm in radius is driven by cloud turbulence and aerodynamic interactions between the them. Although the turbulent atmosphere is a truly multiscale phenomenon in which the characteristic length scales can vary from millimeters up to several hundred kilometers, a more profound understanding of the warm rain formation can be attained through modeling the microphysical processes, that is, at length scales comparable to the smallest ones in a turbulent flow.

One of the essential tools commonly used for studying particulate two-phase flows are the so-called Direct Numerical Simulations (DNS) in which the full Navier-Stokes equations governing the motion of a Newtonian fluid (possibly incompressible, as in this work) are solved without any simplifications. Turbulent atmosphere in microscale is often modeled as homogeneous and isotropic, sometimes also statistically stationary. The latter property is usually achieved by introducing a forcing term in the momentum balance equation, whose sole purpose is to compensate for the energy dissipation. At this point, it should be emphasized that while the forcing term is artificial, it attempts, from a physical perspective, to model specific mechanisms facilitating the generation of turbulence. Indeed, in real flows, kinetic energy production typically results from, e.g., the mean pressure or temperature gradients. This clearly indicates the anisotropy of the flow, whereas the inevitable presence of boundaries also implies its inhomogeneity. For these very reasons, isotropic turbulence is to some extent unphysical yet experimentally accessible mathematical model of a real turbulent flow. For instance, the so-called grid turbulence generated in a wind tunnel can be considered an example of freely decaying isotropic turbulence, whereas at certain length scales, a channel flow (assuming, e.g., a constant pressure gradient) can be considered an example of statistically stationary isotropic turbulence; however in both cases, the aforementioned approximations hold only close to the respective center lines.

The DNS allows for simulating cloud microphysical processes at length scales varying from millimeters up to several meters. Starting in the early 1970s, isotropic turbulence has most commonly been solved using the pseudo-spectral approach with a computational domain being a cube of certain size. Isotropy can be ensured by imposing both zero-mean flow and periodic boundary conditions. In addition to that,

statistical stationarity can be achieved by forcing specific Fourier modes in either deterministic or stochastic manner; however, it should be emphasized that none of the commonly used forcing terms can be implemented experimentally. Owing to the fact that cloud droplets are initially much smaller than the smallest flow scales in a turbulent flow, these entities can be safely approximated by point particles. In this case the Lagrangian particle tracking is coupled with the DNS leading to the so-called point-particle DNS (PP-DNS). Despite far-reaching simplifications, this model has contributed greatly to the understanding of various phenomena relevant not only to cloud microphysics but also other types of processes.

A significant development in both experimental and numerical methods has been observed over the past years. Recent studies focused on turbulent dispersed two-phase flows allow to conclude that the point-particle approximation may be insufficient, and thus can lead to pronounced discrepancies between numerical simulations and experiments (or even real-world observations). At this point, it should be emphasized that in the case of single-phase flows, the DNS results are usually in excellent agreement with experimental data. For this very reason, the method itself has attained the status of a numerical experiment over the past decades. It is also worth mentioning that both significant development of numerical methods and exponential growth of computing power have given rise to the so-called particle-resolved DNS (PR-DNS) in which all details of turbulence, particularly including the flow around each particle, are resolved. This allows one to determine the hydrodynamic forces exerted on a moving particle more accurately. Unfortunately, due to significant computational cost associated with this approach, the PR-DNS allows to account for a relatively small number of particles. It appears that due to invaluable practical significance, the PP-DNS will remain the method of choice for studying particulate two-phase flows. It is also anticipated that further insights into the physics underlying these flows will result from the combined developments in mathematical modeling, experimental techniques and numerical simulations using the PP-DNS, however with enhancements following from the PR-DNS.

Due to the lack of both the mean flow and a well-defined characteristic dimension, isotropic turbulence is most often characterized by means of the Reynolds number based on the Taylor microscale λ, which is associated with the spatial correlation of the velocity field. The computational cost of the DNS still prevents one from studying turbulent flows at Reynolds numbers relevant to cloud turbulence where $Re_\lambda \sim 10000$. Unfortunately, in the case of single-phase turbulence, the current state-of-the-art DNS is approximately at $Re_\lambda \sim 2500$, with the spatial resolution of $\sim 32786^3$ nodes, whereas the PP-DNS is currently at $Re_\lambda \sim 600$, with the computational grid of $\sim 4096^3$ nodes and approximately 1024^3 point particles in order to obtain the appropriate volume fraction of the dispersed phase. Considering the practical significance, it seems that one of the most important achievements in the field of computational

fluid dynamics is the development of the so-called Large Eddy Simulations (LES). In this method, only the large, energy-containing flow scales are resolved. With increasing Reynolds number, small-scale turbulence is expected to exhibit universal scaling properties regardless of the complexity of a turbulent flow, and hence can be filtered out, eventually leading to significant computational savings. The impact of the unresolved part of turbulence is usually accounted for statistically; however, different, more explicit approaches are equally often of interest. Although the LES is widely used in various industrial applications, it has not gained much attention in studying the fundamental aspects relevant to the dynamics of inertial particles suspended in a turbulent flow. It should be emphasized that in the case of single-phase turbulence, the spatial filtering can be compensated relatively easily, whereas in the case of two-phase flows, the lack of small-scale turbulence also impacts inertial particle dynamics, and thus may imply the need for more advanced modeling. The scientific literature covering this very matter remains limited and, in most cases, primarily concerned with reconstructing specific particle statistics obtained using the PP-DNS. It does not provide any insights into more practical capabilities of either the LES or the PP-LES, particularly within the range of parameters they were originally designed for.

Abstract

It should be emphasized that all simulations performed in this work are of general purpose, and thus can be potentially used to quantify different physical processes provided that relevant dimensionless numbers remain unchanged. However, mostly to provide a more physically-oriented context, this work was devoted to the application of the PP-LES in research concerning particle-laden turbulent flows, specifically within the range of parameters relevant to cloud turbulence. This dissertation is essentially composed of two parts concerning the DNS and the LES of respectively the single-phase turbulence and the particle-laden one.

In the first part, a new pseudo-spectral code for either decaying or forced isotropic turbulence was developed. In the latter case, it has been indicated that frequently reported forcing parameters can lead to artificially correlated velocity fields by amplifying the influence of periodic boundary conditions. For this very reason, the results of numerical simulations differ significantly from the model predictions. It has been shown that specific forcing parameters can be selected so that both the longitudinal and transverse velocity autocorrelation functions take correct forms, particularly vanishing at separations equal to approximately half the size of the computational box. Depending on the Stokes number, that is, a measure of particle inertia, this property can have a significantly beneficial impact on particle dynamics. In addition to the above, this research study indicates that for a given spatial resolution, the

Reynolds number based on the Taylor microscale strongly depends on the selected range of forced Fourier modes, which can lead to incorrect conclusions regarding the required spatial resolution of the DNS. Recently, many research studies have been devoted to developing the so-called autonomous LES in which all model parameters are determined from the resolved velocity field. Partly for this very reason, in this work a new approach to model the impact of the small-scale turbulence on the resolved one was developed based on a scale-dependent eddy-viscosity determined by minimizing the instantaneous difference between the resolved and reference (imposed) energy spectrum functions. It has been indicated that within the range of parameters appropriate for LES, the new approach accurately models the impact of unresolved small-scale turbulence. This part also outlines certain prerequisites (or necessary conditions) for considering the LES a tool for studying turbulent flows at high Reynolds numbers, particularly concerning the selection of model parameters and the spatial resolution of the LES itself.

The second part, concerning the motion of inertial particles suspended in a turbulent flow, was devoted to assessing the capability of the LES to capture certain particle-related phenomena, e.g., the preferential concentration and the preferential sweeping. In this part, particle dynamics was quantified by, e.g., the settling speed enhancement, the probability density function of the second invariant of the velocity gradient tensor sampled at particle locations, the spectrum of the particle number density, the radial distribution function and the radial relative velocity. For instance, the two latter statistics are of significant importance for accurate parametrization of droplet collisions, which is essential to improving the quality of mesoscale numerical weather prediction models. It has been indicated that as long as the ratio between the spatial resolution of the DNS and the LES is on the order of 4, certain particle statistics in the LES remain in exceptionally good qualitative and satisfactory quantitative agreement with the DNS. Recent studies have revealed that in addition to the clustering at length scales comparable to the smallest resolved ones in a turbulent flow, inertial particles also exhibit a tendency to cluster at length scales relevant to the inertial subrange. It has been shown that the new model allows to statistically quantify this phenomenon with outstandingly good quantitative agreement with the DNS. The results indicate that the LES enriched with the new statistical parametrization of small-scale turbulence allows for studying turbulent dispersed two-phase flows within the range of parameters relevant to turbulent atmosphere.

It appears that the advent of both petascale and exascale simulations has opened entirely new possibilities for the use of the LES for studying turbulent single-phase and dispersed two-phase flows, specifically within the range of Reynolds numbers unreachable by now. Despite inevitable deficiencies of the method itself, the results indicate that this approach creates the potential for further advancements in the understanding of the physics underlying turbulent dispersed two-phase flows. Although

all simulations considered in this work have been performed using a personal general-purpose computer, it appears that a natural extension of this research is to adapt the current pseudo-spectral code to large-scale computing.

Overview of the dissertation

Research objectives

The primary goals of this doctoral dissertation are as follows: (i) to develop a pseudo-spectral code for isotropic turbulence and to assess the agreement between the results of numerical simulations and theoretical predictions; (ii) to assess whether the LES enriched with the well-known spectral eddy-viscosity closures can capture the characteristics of the inertial subrange; (iii) to develop an alternative and computationally affordable scale-dependent eddy-viscosity closure for the fluid momentum balance equation; (iv) to investigate whether the LES allows for extending the range of Reynolds numbers currently achievable in the DNS of single-phase isotropic turbulence; (v) to assess whether the point-particle LES without any subgrid-scale modeling for the fluid velocity along particle trajectories can provide valuable insight into the physics underlying dispersed two-phase flows, specifically concerning the ability of the point-particle LES to capture certain phenomena associated with the turbulent transport of inertial particles, e.g., the preferential concentration or the preferential sweeping; (vi) to investigate whether the point-particle LES allows for extending the range of Reynolds numbers currently achievable in the DNS of particle-laden isotropic turbulence.

Based on the research objectives outlined above and taking into account the fact that all simulations in this work will be carried out within the range of parameters relevant to cloud microphysical processes, specifically concerning the process of warm rain formation, the main **dissertation statements** can be formulated as follows:

(i) *Large Eddy Simulations enriched with a scale-dependent eddy-viscosity can accurately capture the inertial range dynamics at Reynolds numbers relevant to cloud turbulence*;

(ii) *Point-Particle Large Eddy Simulations without the subgrid-scale contribution to the fluid velocity at the particle location can provide valuable insight into the turbulent transport of cloud droplets, specifically at Reynolds numbers exceeding those achievable in Direct Numerical Simulations of particle-laden isotropic turbulence.*

Chapter 1: Introduction

In this Chapter I provide a brief introduction to turbulent flows followed by a concise justification for the choice of homogeneous and isotropic turbulence as the simplest yet non-trivial example of a turbulent flow, particularly well suited for studying the fundamental aspects of its underlying physics. Thereafter, I concisely discuss some issues concerning numerical modeling of dispersed two-phase flows, with an emphasis on theoretical and computational challenges associated with the turbulent transport of the particulate phase. I briefly emphasize the need for studying these complex flows and discuss a few approaches to their modeling. I motivate the use of the LES as a means to (i) overcome the current computational limitations and (ii) to explore inertial particle statistics in turbulent flows at Reynolds numbers more relevant to environmental phenomena or industrial processes.

Chapter 2: Direct Numerical Simulations

I begin this Chapter with a concise introduction to the Navier-Stokes equations in a three-dimensional Euclidean space, followed by a more thorough derivation of their Fourier-transformed counterpart. Thereafter, I briefly introduce the pseudo-spectral method along with a short justification for the use of the fluid momentum balance equation in rotation form. I emphasize some computational difficulties inherently associated with the evaluation of the non-linear terms in the governing equations, specifically concerning the aliasing errors arising from the use of the discrete Fourier transforms. I provide the overview of several methods for removing the foregoing errors and briefly discuss more practical aspects of different dealiasing strategies. Based on the Fourier-transformed energy balance equation, I discuss some methods of forcing the incompressible isotropic turbulence along with a concise literature survey on this matter. Thereafter, I select the most common forcing term and slightly enhance it by associating its adjustable parameter with other, well-defined numerical parameters characterizing each simulation. This way, the forcing becomes to some extent self-adaptive, thus allowing to reduce the number of numerical tests preceding the final simulation. In this Chapter I also discuss the time integration of the Navier-Stokes equations and point out to some errors arising from both the improper order of computation and the inappropriate treatment of floating-point errors, which eventually cause a simulation breakdown. This is of crucial importance to ensuring long-term, stable numerical simulations. In the following sections, I briefly introduce (i) a few flow parameters to be used throughout this work to statistically quantify a turbulent flow and (ii) a method used to determine the corresponding error bounds. In this part of the dissertation, the newly developed pseudo-spectral code is validated using the reference DNS data for the three-dimensional Taylor-Green vortex at both low

and moderate Reynolds numbers. In the case of statistically stationary turbulence, I also thoroughly investigate the impact of the forcing on certain statistics used to quantify isotropic turbulence, and provide some guidelines for the proper selection of adjustable forcing parameters.

Chapter 3: Large Eddy Simulations

I begin this Chapter by introducing the spatially-filtered Navier-Stokes equations in a three-dimensional Euclidean space, followed by a few common computational difficulties arising from the filtering along with a brief literature survey on this matter. I also introduce the concept of an explicitly filtered DNS, often referred to as FDNS or *a priori* LES, whose purpose is to establish the theoretical limits of a true (*a posteriori*) LES. Thereafter, I introduce the Fourier-transformed, spatially-filtered Navier-Stokes equations and the well-established model of the so-called spectral eddy-viscosity (here referred to as the standard model), often used to close the equations governing the motion of large flow scales in a pseudo-spectral LES. I thoroughly examine the quality of the LES when compared to the reference DNS at low Reynolds number. In addition to the above, I follow a well-known approach for determining the spectral eddy-viscosity based on the reference DNS, and for the first time use such "theoretical" (here also referred to as *a priori*) spectral eddy-viscosity in a true LES. Building upon this approach, I introduce a new model, which adaptively determines the functional form of the spectral eddy-viscosity based on the imposed energy spectrum function. I thoroughly examine its performance in isotropic turbulence at high Reynolds numbers and establish some requirements that every LES should satisfy.

Chapter 4: Lagrangian particle tracking

I begin this Chapter by introducing the most general form of the particle equation of motion along with some far-reaching simplifications applicable within the range of parameters relevant to this study. I emphasize that accurate determination of the fluid velocity at particle locations, although often trivialized, is of significant importance to accurately track the motion of dispersed entities. Taking into account the latest achievements in this matter, I select the B-spline interpolation and provide a detailed description of this method (including relevant derivations), possibly filling the gaps caused by insufficient (or even confusing) explanations provided in the scientific literature. In this Chapter I also introduce some particle statistics that will be used throughout this work to statistically quantify particle motion. I specifically focus on how to determine the spectrum function of the particle number density and point out some understatements found in the scientific literature, essentially hindering

its computation. In addition to the above, I briefly discuss some deficiencies of the point-particle LES which typically result from the spatial filtering, and provide the literature survey concerning the subgrid-scale modeling for the fluid velocity along particle trajectories.

Chapter 5: Inertial particle dynamics

I begin this Chapter with a concise introduction to particle-laden flows along with a more practical motivation for studying the physics underlying some complex phenomena associated with the particulate phase suspended in the turbulent flow. It should be emphasized that all simulations considered in this work are of general purpose, and thus can be used to quantify various physical phenomena provided that relevant dimensionless numbers remain unchanged. However, to provide a more physical context, I briefly introduce the process of warm rain formation and essentially select specific parameters so that all of the simulations can be to some extent related to cloud droplets suspended in a turbulent atmosphere. I study the motion of inertial particles in the DNS of isotropic turbulence at relatively low Reynolds number and provide some insights into specific particle statistics, particularly including the radial distribution function, the radial relative velocity, the spectrum function of particle number density, the settling velocity, and the probability density function of the second invariant of the velocity gradient tensor sampled at particle locations. Thereafter, I extensively study the impact of two spectral eddy-viscosity models on the dynamics of inertial particles in the LES of isotropic turbulence at both low and high Reynolds numbers.

Chapter 6: Summary and future research

In this Chapter I provide a brief summary of what appears to be the most important achievements and contributions of this dissertation. In addition to the above, I discuss a few possible directions of further research, aimed at what can be considered a natural extension of this work.

Preface

Seeing my constantly growing frustration, my doctoral advisor once quoted the words of a Roman poet Publius Ovidius Naso—*"dripping water hollows out stone, not through force but through persistence"*. After tens of conversations we have had (not all related to this dissertation, obviously), hundreds of hours I have spent trying to figure things out, hundreds of failures, and probably just a few wins, I think I finally understand the words of an American aerospace engineer Edward A. Murphy Jr.—"*anything that can go wrong will go wrong*". Some of the readers may instantly recognize this famous epigram most commonly referred to as "Murphy's law".

At the very beginning of my doctoral studies I was involved in a Polish-Chinese research project dedicated to the fundamental aspects of numerical modeling of dispersed turbulent flows, particularly considering particle-scale interactions. I was essentially given a large and complex legacy code base with an outline of methodology for approaching this very matter. Although I considered myself as a reasonably successful mechanical engineer before joining the group, it quickly became clear that I needed not only to acquire new skills but also to further develop those I already had. To follow my conscience sincerely, I must emphasize that once I have gathered a little self-confidence and have essentially learned to stand on my own feet, I started to disagree with the approach I was initially following. My colleagues from the Department of Multiphase Flows kept encouraging me with yet another saying—*"the scientific progress is based on a constant questioning process"*. And so I did...

For the purpose of this dissertation, I (i) designed and implemented from the ground up a new code base using the modern C++ for the CPU-based architecture and (ii) developed the methodology to incorporate the LES in the process of studying the fundamental aspects of particle-laden turbulent flows, currently dominated by the DNS. These two objectives required me to synthesize a considerable body of knowledge, usually dispersed over multiple, not directly related resources. Therefore, for this very reason, I consider the foregoing accomplishments as my most important achievements in this dissertation. It is also worth mentioning that during the process, I had a chance to discuss my issues with other doctoral candidates around the world and, surprisingly enough, it turned out that in such a rapidly changing world, facing ever-growing pressure to increase productivity, students often have not enough time to develop sufficient understanding of complex research problems they attempt

to address in their work. This situation gives rise to incomplete (or even misleading) descriptions of certain methodologies, methods, algorithms and codes used to solve specific scientific issues. Further down the road, these deficiencies significantly increases the time others spend trying to incorporate the methodologies or implement the models that are reported in the scientific literature; however, in the end of the day, it usually turns out that things are much less complicated than they might seem. What is more, it also appears that the advent of large language models has initially contributed to increasing the "efficiency" of various tasks; however in the longer term, it can make one devote even less time to working on the fundamentals than at present, eventually degrading the understanding of certain concepts even more. On the one hand, it does not have to be a major issue yet, especially in large departments (or groups) which have essentially gathered an appreciable body of knowledge and experience over the years. However, on the other hand, it might be an issue that deserves closer attention.

What I have learned, partly from studying computer science (for the needs of this work), is that it actually takes quite some time to develop certain skills, or, in general, the understanding of abstract concepts often required to pursuit scientific work. Although there are almost inexhaustible resources of textbooks and research papers, I still think in certain situations the best way to learn is by taking things apart, and putting them back together. For this very reason, this doctoral dissertation has taken the form of a monograph and is intended to be more or less self-contained, so that other doctoral candidates can hopefully benefit from it in their journey of developing expertise in the mathematical modeling of turbulence and turbulent transport of dispersed entities.

Acknowledgments

This research was supported by the CI TASK, Gdańsk, Poland (grant No. PT01174) This research was partly funded by the National Science Centre, Poland (grant No. 2018/30/Q/ST8/00341, Principal investigator—Prof. Bogdan Rosa).

I would like to express my gratitude to my advisor, Prof. Jacek Pozorski, for the many late nights you spent reading this dissertation and for the discussions that helped shape and refine several parts of this work.

I am also grateful to Dr. Adam Kajzer for all the conversations we've had over the past years. Although we often disagreed, I must acknowledge that certain parts of this dissertation were only possible thanks to your philosophy of doing science—one that, whether I intended to or not, I've partly made my own.

I would like to thank Dr. Ahmad Ababaei for the many discussions we've shared over the years, for your help in resolving specific challenges I encountered during this research, and for generously sharing your insights and results whenever I asked.

I am grateful to Prof. Julian Andrzej Domaradzki for taking the time to read Chapter 3 and for the valuable comments you shared.

My sincere thanks also go to Dr. Maurizio Carbone and Dr. Josin Tom for engaging with the issues I faced in Chapter 4 and for the thoughtful discussions that followed.

I am especially thankful to Dr. Keigo Matsuda for your genuine interest in my work, for the time you spent reviewing long derivations, for your selfless support, and for sharing your insights and results, which contributed to Chapters 4 and 5.

I would like to express my heartfelt thanks to Dr. Sylwia Polesek-Karczewska, Prof. Dariusz Kardaś, Prof. Paweł Flaszyński, Prof. Piotr Lampart, and Prof. Piotr Doerffer for your encouragement, interest in my research, and the kindness I've experienced from you over the past years.

I am also grateful to Dr. Oskar Szulc and Dr. Katarzyna Majewska for taking the time to read the extensive introduction to this dissertation and for the valuable feedback that helped me improve it.

I am also grateful to Dr. Magdalena Mieloszyk and Dr. Katarzyna Majewska for your patience, willingness to help, all the conversations we've had, and all the advice that proved valuable during the past few years.

Finally, I would like to thank the most important person—without whom I would not have made it this far. Thank you, Joanna, for your selfless support and unwavering patience. Above all, thank you for everything you have sacrificed over the past few years so that I could reach this goal. I know it was a difficult time for us, but we made it through together. Let this be a reminder in the years ahead that, no matter the circumstances, we must keep moving forward side by side. I also want to thank you for the time you spent hyphenating large blocks of text that LaTeX, for some mysterious reason, refused to justify properly... Thank you as well for making sure that all references from my extensive bibliography always appeared in the correct order...

Chapter 1

Introduction

1.1 Turbulent flows

Although we all have an intuitive understanding of what a turbulent flow is, it appears to be quite demanding (if not challenging) to put forward a rigorous mathematical definition of such a flow. In general, a turbulent flow exhibits unpredictable nature in both space and time. However, the term "turbulent" often refers to flows which may differ substantially from one another with respect to certain dynamical properties. To avoid confusion (or rather a "semantic discussion" as Lesieur said [1]), it should be assumed that all turbulent flows [2]: (i) experience abrupt and irregular changes in velocity at any position in space and time; (ii) are associated with a wide range of length and time scales; (iii) show enhanced ability to mix transported quantities when compared to laminar flows.

Reynolds' classic experiment [3] turned out to be the starting point for the continuous journey of trying to capture the nature of turbulence. Reynolds was the first one to indicate that for a given fluid and pipe, the flow remains laminar for velocities below a certain critical value. He observed that beyond this point the fluid velocity rapidly changes in space and time, which essentially means the flow becomes turbulent. The transition from laminar to turbulent flow depends on the details of a particular experiment, however, Reynolds expressed a criterion for such transition in terms of a non-dimensional parameter [4] defined as

$$Re = \frac{\text{characteristic velocity} \times \text{characteristic length}}{\text{kinematic viscosity}}, \tag{1.1}$$

which in fact we call today the Reynolds number[1].

[1] In the Reynolds' pipe-flow experiment the flow remained laminar for $Re < 2300$ and became turbulent once $Re > 4000$

In general, turbulent flows are ubiquitous in the surrounding environment. Some examples include not only meteorology, oceanography, internal geophysics of Earth or even astrophysics, but also various types of engineering applications rising in aeronautical, chemical, nuclear or construction industries. With this in mind, it seems that a more profound understanding of the physics underlying turbulent flows, including the particle-laden ones, will continue to be of importance when it comes to improving (if not sustaining) the quality of people's lives. Despite our natural curiosity and eagerness to explore, the foregoing statement also explains extensive research studies focused on turbulent flows, which, following Pope [2], can be divided into three categories:

(i) performing experimental or numerical studies focused on providing more detailed information about specific flows;

(ii) developing tractable mathematical models capable of predicting the properties of turbulent flows with reasonable accuracy;

(iii) manipulating flows in order to obtain a desired change in their behavior.

The last one usually involves more practical applications, particularly concerning both active and passive flow control introduced in order to enhance the mixing of transported quantities, increase lift, reduce drag or vibrations, to name just a few. The remainder of this dissertation is primarily concerned with both (i) numerical simulations and (ii) the mathematical modeling of turbulent flows, with a particular emphasis on the dispersed two-phase ones.

When studying the physics of turbulence one should rather concentrate on the simplest yet non-trivial examples of turbulent flows, possibly confined to relatively simple geometries, such as flows through pipes or plane channels, free jets and wakes, flows past a sphere or a flat plate. It is well established that homogeneous and isotropic turbulence is the most fundamental example of a turbulent flow [1, 5], which, at least to some extent, can be realized experimentally [6]. Since this dissertation is focused on the fundamental aspects of turbulent dispersed two-phase flows, all considerations regarding the continuous carrier phase will be confined to isotropic turbulence, which is often referred to as the flow "within a box", albeit in some sense unbounded.

1.2 Particle-laden turbulent flows

A more profound understanding of turbulent transport, spatial distribution, collisions and possibly coalescence of dispersed entities in the form of small inertial particles,

droplets or bubbles is of significant importance to many industrial and environmental applications. These include not only fuel atomization and mixing, spray combustion, cyclone separation, pneumatic transport, bubble column reactors, but also volcanic ash dispersion, sediment transport, warm rain formation or even the motion of dust particles in protoplanetary disks.

Due to a wide range of spatial and temporal scales, studying the physics underlying particle-laden turbulent flows requires the use of various numerical methods, see, e.g., Kuerten [7] and Elghobashi [8] for a comprehensive state-of-the-art reviews. To reduce the overall complexity of a particle-laden turbulent flow, this dissertation focuses on dilute suspensions of particles smaller than the smallest (dissipative) flow scales existing in a turbulent flow. In this case, dispersed entities can be safely approximated as point particles, whose trajectories can be determined using the the approach called the Lagrangian Particle Tracking. This method can be coupled with either Direct Numerical Simulation (DNS) or Large Eddy Simulation (LES), essentially applied to solve the equations governing the evolution of the underlying turbulence. Due to the fact that particle-laden turbulent flows are inherently unsteady, Reynolds-Averaged-Navier-Stokes (RANS) simulations are usually not taken into account, except for industrial applications, when studying the motion of inertial particles suspended in a turbulent flow.

It should be emphasized that many environmental phenomena and industrial processes occur at high Reynolds numbers, say on the order of millions, and thus the DNS, which essentially accounts for all length and time scales of fluid motion, will not be feasible for many years to come. This is one of the reasons why the LES has emerged as a promising tool for studying turbulent flows over approximately the last 30 years. Presumably the single most attractive feature of the LES is the (appreciably) reduced computational cost when compared to the DNS. This results from the assumption that with increasing Reynolds number, the smallest, dissipative flow scales exhibit universal scaling properties regardless of the complexity of a turbulent flow. Therefore, such flow scales can be filtered out while their impact on the remaining ones has to be taken into account by means of the so-called subgrid-scale model. In the case of single-phase flows, it is usually sufficient to statistically quantify the impact of the unresolved (filtered out) flow scales. Unfortunately, the motion of inertial particles may depend (and usually does) on the details of all scales of fluid motion, and thus additional subgrid-scale model in the particle equation of motion may be required in order to improve the prediction of certain particle statistics.

In the point-particle approximation, the fluid velocity field in the vicinity of dispersed entities is not resolved. Hence, the forces exerted on a moving particle are typi-

cally approximated by the Stokes drag, possibly enhanced with the Schiller-Naumann correction; however, depending on the phenomenon being studied or the required level of detail, additional forces may be included, e.g., the buoyancy, lift or Basset history forces. This will be thoroughly discussed in Section 4.1. The approach which only considers the Stokes drag has been widely used over the years and essentially provided a significant contribution to the understanding of the dynamics of inertial particles suspended in turbulent flows, see, e.g., [9, 10, 11, 12, 13, 14, 15, 16, 17, 18]. It is widely accepted that the motion of inertial particles can significantly differ from that of inertia-free ones (fluid particles). Depending on the Stokes number, that is, the particle-to-fluid characteristic time scales ratio, some particles may be particularly susceptible to the instantaneous changes in the fluid velocity field, eventually giving rise to complex phenomena such as the preferential concentration or the preferential sweeping. On the other hand, if the Stokes number is sufficiently large, then particles become insensitive to abrupt changes in the flow behavior. Moreover, if the particle mass loading (particulate phase-to-fluid mass ratio) is sufficiently large, then inertial particles can exhibit the ability to modulate (attenuate or augment, or even both simultaneously) the underlying turbulence regardless of the Stokes number; however, there is a good amount of evidence that in the point-particle approximation such modulation is underpredicted when compared to experiments. One can refer to, e.g., [10, 19, 20, 21, 22], but also, e.g., [23, 24] for comprehensive reviews on this matter along with the current state-of-the-art. In general, the description of dispersed two-phase flows is further complicated if the physics become more complex, e.g., by including the gravitational effects, chemical reactions, collisions or coalescence of dispersed entities, and also other types of particle-particle interactions. As indicated by Eaton [22] and Balachandar & Eaton [23], within a certain range of parameters, the point-particle approximation (in the current formulation) is not appropriate for accurate particle tracking, and therefore further efforts are necessary not only to improve and validate this approach, but also to establish its scope of application. Despite significant advances in measurement techniques, experimental research studies focused on particle-laden turbulent flows are, however, still limited. For this reason (and partly due to significant advances in both computer technology and numerical methods), the so-called particle-resolved DNS has emerged as a promising tool for enhancing the understanding of the physics underlying particle-laden turbulent flows. This approach has received a significant interest in the past decade and has contributed to developing (or extending) various numerical methods. This includes among others body-fitted methods [25], front-tracking methods [26], immersed boundary methods [27, 28], and sharp interface methods [29, 30, 31]. Owing to the fact that

the flow around dispersed entities of finite size is fully resolved, the hydrodynamic forces exerted on a particle can be accurately determined by integrating the fluid stress on its surface. However, it should be emphasized that some level of uncertainty is inevitable, mostly due to the lack of sufficient (if any) spatial resolution between two colliding particles[2]. Nevertheless, it is anticipated that particle-resolved simulations, once thoroughly validated, will provide valuable input for lower-order models such as point-particle approximation [24].

This dissertation attempts to provide some insights into both the physics and the modeling of turbulent particulate two-phase flows, specifically within the range of parameters relevant to cloud turbulence. This particular choice stems solely from the research project preceding this work; however, a more general justification is as follows:

(i) an atmospheric turbulent flow (especially in cumulus clouds) can be considered, to a good approximation, homogeneous and isotropic on a representative range of length scales [32];

(ii) not only the turbulent transport of cloud droplets but also droplet-turbulence and droplet-droplet interactions are some of the many phenomena relevant to cloud microphysics which are still regarded as not well understood; in general, insufficient description of cloud microphysical processes is considered a significant source of uncertainty in numerical weather forecasting, particularly concerning the process of warm rain formation [33];

(iii) under the conditions relevant to this study, e.g., the specific values of droplet sizes, droplet-to-fluid density ratio or the volume fraction of droplets, numerical simulations can be greatly simplified.

Concerning the process of warm rain formation, quite a few mechanisms have been put forward to explain the growth of cloud droplets [32, 34]. It is well-established that the growth of droplets with size smaller than approximately 5–20 µm in radius results from the turbulent transport of water vapor and its subsequent condensation on small atmospheric aerosols, also referred to as the cloud condensation nuclei. Once the droplets exceed approximately 60–80 µm in radius, gravitational effects become significant, essentially causing the droplets to further grow by the gravity-induced collision-coalescence. None of the foregoing mechanisms is efficient in the intermediate range of droplet sizes, that is within 20–60 µm, often referred to as the "size-gap". The actual mechanism triggering the growth of these droplets remains unclear. It is also

[2]Lubrication force can be used to compensate for the lack of the spatial resolution, see, e.g., [28]

considered to be one of the reasons of significant discrepancies between theoretical predictions and experimental observations [35]. Based on extensive research focused on this issue, it can be concluded that the growth of these medium-sized droplets is most likely driven by cloud turbulence and particle-particle interactions [33]; however, the range of flow scales influencing this process remains undetermined.

It should be emphasized that in the turbulent atmosphere, the characteristic length scales can extend from millimeters up to several hundreds of meters, essentially resulting in the so-called Taylor microscale Reynolds number on the order of $Re_\lambda \sim 10000$ [34]. To the best of the author's knowledge, the current state-of-the-art DNS reaches at most $Re_\lambda \sim 2500$ in the case of single-phase flows, and approximately $Re_\lambda \sim 600$ for particle-laden ones. This simply indicates that the DNS of particulate two-phase flows at environmentally- and industrially-relevant Reynolds numbers will remain unfeasible for (presumably) many years to come.

For this very reason, it seems necessary to somehow reduce the computational cost of such simulations, and perhaps to reconsider the LES as one of possible choices when exploring the physics underlying turbulent dispersed two-phase flows, specifically at high Reynolds numbers. Due to the lack of universal (or "good-enough", so to speak) subgrid-scale models, particularly for the residual fluid velocity along particle trajectories [36], this approach has been systematically ignored in the context of atmospheric turbulent flows. To the best of the author's knowledge, there have been relatively few attempts to use the LES for studying the motion of inertial particles suspended in isotropic turbulence, specifically within the range of parameters relevant to cloud microphysical processes, see, e.g., [37, 38, 39, 40, 41]. In addition to that, it should be emphasized that in these works: (i) the LES was applied to solve isotropic turbulence at relatively low Reynolds numbers, say $Re_\lambda < 300$, and therefore without a well-defined inertial subrange; (ii) the emphasis was put almost exclusively on the modeling of the subgrid-scale fluid velocity along particle trajectories, and its impact on the capability of the LES to restore specific particle-related statistics obtained using the DNS; (iii) no attempts have been made to provide new insights into the physics underlying particulate two-phase flows. The latter observation raises questions concerning the actual reason for using an inherently deficient method for studying turbulent (dispersed) flows, specifically at Reynolds numbers for which the well-established one is readily available and, most importantly, computationally affordable.

Chapter 2

Direct numerical simulations of isotropic turbulence

2.1 Equations of fluid motion in physical space

Considering the motion of an incompressible fluid[1], the continuity equation, simply expressing the principle of conservation of mass, is given as

$$\frac{\partial \rho(\boldsymbol{x},t)}{\partial t} + \frac{\partial \rho(\boldsymbol{x},t) U_\alpha(\boldsymbol{x},t)}{\partial x_\alpha} = 0 \tag{2.1}$$

where $\rho(\boldsymbol{x},t)$ and $U_\alpha(\boldsymbol{x},t)$ are respectively the fluid density and velocity at position $\boldsymbol{x}$ and time t; it is important to note that the Cartesian coordinate system will be used throughout this work. Assuming the density of the fluid remains constant, the above equation reduces to

$$\frac{\partial U_\alpha(\boldsymbol{x},t)}{\partial x_\alpha} = 0. \tag{2.2}$$

It should also be emphasized that in this work the Einstein summation convention is assumed, and therefore, except where indicated, repeated indices are implicitly summed over. According to Newton's second law of motion, the rate of change of fluid momentum can be expressed as

$$\frac{\mathrm{D}U_\alpha(\boldsymbol{x},t)}{\mathrm{D}t} = F_\alpha(\boldsymbol{x},t) + \frac{1}{\rho}\frac{\partial}{\partial x_\beta}\sigma_{\alpha\beta}(\boldsymbol{x},t), \tag{2.3}$$

[1]Seeking a more detailed description of the conditions under which this assumption remains valid, one can refer to [42]

where $F_\alpha(\boldsymbol{x},t)$ is an external body force acting on the fluid, $\sigma_{\alpha\beta}(\boldsymbol{x},t)$ is the stress tensor, which for a Newtonian fluid can be expressed as

$$\sigma_{\alpha\beta}(\boldsymbol{x},t) = -P(\boldsymbol{x},t)\delta_{\alpha\beta} + 2\mu\left[S_{\alpha\beta}(\boldsymbol{x},t) - \frac{1}{3}\delta_{\alpha\beta}\frac{\partial U_\gamma}{\partial x_\gamma}\right], \tag{2.4}$$

where μ is the dynamic viscosity of the fluid, $P(\boldsymbol{x},t)$ is the pressure field, $\delta_{\alpha\beta}$ is the Kronecker delta, and $S_{\alpha\beta}(\boldsymbol{x},t)$ denotes the rate-of-strain tensor is given as

$$S_{\alpha\beta}(\boldsymbol{x},t) = \frac{1}{2}\left[\frac{\partial}{\partial x_\beta}U_\alpha(\boldsymbol{x},t) + \frac{\partial}{\partial x_\alpha}U_\beta(\boldsymbol{x},t)\right]. \tag{2.5}$$

With the substitution of Eq. (2.5) into Eq. (2.4) and taking advantage of Eq. (2.2), the momentum balance for an incompressible Newtonian fluid can be expressed as

$$\frac{\partial U_\alpha}{\partial t} + U_\beta\frac{\partial U_\alpha}{\partial x_\beta} = -\frac{1}{\rho}\frac{\partial P}{\partial x_\alpha} + \nu\frac{\partial^2 U_\alpha}{\partial x_\beta \partial x_\beta} + F_\alpha, \tag{2.6}$$

where, in addition to the density of the fluid, its viscosity was also assumed constant. Hereinafter, the explicit dependence on position and time will be omitted in order to simplify the notation.

Despite a relatively "simple-looking" form, the Navier-Stokes equations provide the most detailed description of the motion of a Newtonian fluid, and thus are the starting point for studying the physics underlying turbulent flows.

2.2 Equations of fluid motion in Fourier space

An arbitrary velocity field U_α can be decomposed into the ensemble mean and a fluctuation about that mean [4] to give

$$U_\alpha = \langle U_\alpha \rangle + u_\alpha, \tag{2.7}$$

where $\langle\cdot\rangle$ denotes the ensemble average, which satisfies the following property

$$\langle U_\alpha \rangle = \langle \langle U_\alpha \rangle \rangle + \langle u_\alpha \rangle = \langle U_\alpha \rangle + \langle u_\alpha \rangle. \tag{2.8}$$

It is therefore readily apparent that such an approach, which in fact we call today the Reynolds decomposition, implies that $\langle u_\alpha \rangle = 0$. Therefore, the intensity of velocity fluctuations u_α should rather be measured by the variance $\langle u_\alpha^2 \rangle$. The velocity field can only be isotropic in the absence of preferential directions, which, in turn, implies

that

$$\langle U_\alpha \rangle = 0. \tag{2.9}$$

Therefore, with the substitution of U_α from Eq. (2.7) and the use of Eq. (2.9), the momentum balance equation, given by Eq. (2.6), can be rewritten so as to describe the evolution of the zero-mean velocity field

$$\frac{\partial u_\alpha}{\partial t} + u_\beta \frac{\partial u_\alpha}{\partial x_\beta} = -\frac{1}{\rho}\frac{\partial p}{\partial x_\alpha} + \nu \frac{\partial u_\alpha}{\partial x_\beta \partial x_\beta} + f_\alpha, \tag{2.10}$$

where f_α will henceforth be referred to as the forcing; however, its definition is deferred until it becomes relevant.

At this point, it seems convenient to introduce an idealized turbulent flow confined to a cubic box of size L_B. The size of the box should be selected so that the features of flow scales smaller than L_B closely reflect the features of a turbulent flow one aims to study [1]. Apart from being statistically uniform in space (homogeneity) and having no preferred directions (isotropy), isotropic turbulence must also be remote from boundaries, or, in other words, be infinite in extent [5]. The latter property is ensured by imposing periodic (cyclic) boundary conditions on the computational box. It should be emphasized that at a particular moment in the analysis, the box will be allowed to become infinitely large. The periodic velocity field can be expanded as an infinite series to give

$$u_\alpha(\boldsymbol{x}, t) = \left(\frac{2\pi}{L_B}\right)^3 \sum_{\boldsymbol{k}} \hat{u}_\alpha(\boldsymbol{k}, t) e^{i\boldsymbol{k}\cdot\boldsymbol{x}}, \tag{2.11}$$

where the wavevector $\boldsymbol{k}$ is defined as

$$\boldsymbol{k} = k_0 \boldsymbol{n} = k_0(n_1 \boldsymbol{e_1} + n_2 \boldsymbol{e_2} + n_3 \boldsymbol{e_3}), \tag{2.12}$$

with n_α being positive or negative integer values; $k_0 = 2\pi L_B^{-1}$ is the lowest non-zero wavenumber and $(\hat{})$ is used to differentiate between the Fourier and physical space representations. In the limit of $L_B \to \infty$, Eq. (2.11) takes an integral form given as

$$u_\alpha(\boldsymbol{x}, t) = \int \hat{u}_\alpha(\boldsymbol{k}, t) e^{i\boldsymbol{k}\cdot\boldsymbol{x}} \mathrm{d}\boldsymbol{k}. \tag{2.13}$$

Consequently, its inverse becomes

$$\hat{u}_\alpha(\boldsymbol{k}, t) = \left(\frac{1}{2\pi}\right)^3 \int u_\alpha(\boldsymbol{x}, t) e^{-i\boldsymbol{k}\cdot\boldsymbol{x}} \mathrm{d}\boldsymbol{x}, \tag{2.14}$$

where $\mathrm{d}\boldsymbol{x} = \mathrm{d}x_1\mathrm{d}x_2\mathrm{d}x_3$.

One of the most useful (if not rewarding) properties of the Fourier transform is that the differential operator $\partial/\partial x_\alpha$ is reduced to a simple complex multiplier ik_α, which appreciably simplifies the equations. Taking advantage of this property, the continuity equation given by Eq. (2.2) becomes

$$ik_\alpha \hat{u}_\alpha = 0, \tag{2.15}$$

essentially indicating that $\boldsymbol{k}$ and $\hat{\boldsymbol{u}}$ are mutually orthogonal vectors[2]. Applying Eq. (2.14) to the Navier-Stokes equations given by Eq. (2.10), and taking into account the fact that in the case of an incompressible fluid, the non-linear term can be expressed as

$$\frac{\partial u_\alpha u_\beta}{\partial x_\beta} = u_\beta \frac{\partial u_\alpha}{\partial x_\beta} + u_\alpha \frac{\partial u_\beta}{\partial x_\beta} = u_\beta \frac{\partial u_\alpha}{\partial x_\beta}, \tag{2.16}$$

one obtains

$$\frac{\partial \hat{u}_\alpha}{\partial t} + ik_\beta \mathcal{F}\left(u_\alpha u_\beta\right) = -ik_\alpha \frac{\hat{p}}{\rho} - \nu k^2 \hat{u}_\alpha + \hat{f}_\alpha, \tag{2.17}$$

where $k^2 = k_\alpha k_\alpha = |\boldsymbol{k}|^2$. Taking the divergence of the above equation, that is multiplying both sides by ik_α, and renaming dummy indices appropriately[3], one can express the pressure field as

$$\hat{p} = -\rho \frac{k_\beta k_\gamma}{k^2} \mathcal{F}\left(u_\beta u_\gamma\right). \tag{2.18}$$

This term can be substituted back into Eq. (2.17) to give

$$\frac{\partial \hat{u}_\alpha}{\partial t} + ik_\beta \mathcal{F}\left(u_\alpha u_\beta\right) = -ik_\alpha \frac{k_\beta k_\gamma}{k^2} \mathcal{F}\left(u_\beta u_\gamma\right) - \nu k^2 \hat{u}_\alpha + \hat{f}_\alpha. \tag{2.19}$$

With some rearrangement, and introducing the so-called projection tensor given as

$$P_{\alpha\beta}(\boldsymbol{k}) = \delta_{\alpha\beta} - \frac{k_\alpha k_\beta}{k^2}, \tag{2.20}$$

one obtains

$$\left(\frac{\partial}{\partial t} + \nu k^2\right) \hat{u}_\alpha = -ik_\gamma P_{\alpha\beta} \mathcal{F}\left(u_\beta u_\gamma\right) + \hat{f}_\alpha. \tag{2.21}$$

The non-linear term on the right-hand side of the above equation introduces additional mathematical and computational difficulties, and therefore requires special attention.

[2] $k_1\hat{u}_1 + k_2\hat{u}_2 + k_3\hat{u}_3 = \boldsymbol{k} \cdot \hat{\boldsymbol{u}} = 0$

[3] $\alpha \to \beta$ and $\beta \to \gamma$

Applying the Fourier transform gives

$$\mathcal{F}(u_\beta u_\gamma) = \frac{1}{(2\pi)^3}\int u_\beta u_\gamma e^{-i\boldsymbol{k}\cdot\boldsymbol{x}}\mathrm{d}\boldsymbol{x}, \tag{2.22}$$

from where with the substitution of Eq. (2.11), and some minor rearrangement, one obtains

$$\begin{aligned}\mathcal{F}(u_\beta u_\gamma) &= \frac{(2\pi)^3}{L_B^6}\int \sum_{\boldsymbol{p}}\sum_{\boldsymbol{q}} \hat{u}_\beta(\boldsymbol{p})\hat{u}_\gamma(\boldsymbol{q}) e^{-i(\boldsymbol{k}-\boldsymbol{p}-\boldsymbol{q})\cdot\boldsymbol{x}}\mathrm{d}\boldsymbol{x} \\ &= \left(\frac{2\pi}{L_B}\right)^3 \sum_{\boldsymbol{p}}\sum_{\boldsymbol{q}} \hat{u}_\beta(\boldsymbol{p})\hat{u}_\gamma(\boldsymbol{q}) \frac{1}{L_B^3}\int e^{-i(\boldsymbol{k}-\boldsymbol{p}-\boldsymbol{q})\cdot\boldsymbol{x}}\mathrm{d}\boldsymbol{x}.\end{aligned} \tag{2.23}$$

The exponential term on the right-hand-side evaluates to

$$\frac{1}{L_B^3}\int e^{-i(\boldsymbol{k}-\boldsymbol{p}-\boldsymbol{q})\cdot\boldsymbol{x}}\mathrm{d}\boldsymbol{x} = \begin{cases} 1, & \text{if } \boldsymbol{p}+\boldsymbol{q}=\boldsymbol{k}, \\ 0, & \text{otherwise,}\end{cases} \tag{2.24}$$

and therefore Eq. (2.23) can be rewritten as

$$\mathcal{F}(u_\beta u_\gamma) = \left(\frac{2\pi}{L_B}\right)^3 \sum_{\boldsymbol{p}+\boldsymbol{q}=\boldsymbol{k}} \hat{u}_\beta(\boldsymbol{p})\hat{u}_\gamma(\boldsymbol{q}). \tag{2.25}$$

The Navier-Stokes equations govern the non-linear interactions between the two Fourier modes $\boldsymbol{p}$ and $\boldsymbol{q}$, causing the energy to be either injected into or drained from mode $\boldsymbol{k}$, on condition that the three wavevectors form a triangle given as $\boldsymbol{p}+\boldsymbol{q}=\boldsymbol{k}$ [5]. The above equation essentially expresses the convolution theorem, which indicates that any product in physical space becomes a convolution in Fourier space. With the substitution of Eq. (2.25) into Eq. (2.21), one obtains the Fourier-transformed Navier-Stokes equations in the solenoidal form given as

$$\left(\frac{\partial}{\partial t}+\nu k^2\right)\hat{u}_\alpha = -ik_\gamma P_{\alpha\beta}\left(\frac{2\pi}{L_B}\right)^3 \sum_{\boldsymbol{p}+\boldsymbol{q}=\boldsymbol{k}} \hat{u}_\beta(\boldsymbol{p})\hat{u}_\gamma(\boldsymbol{q}) + \hat{f}_\alpha. \tag{2.26}$$

For completeness, and to some extent for consistency with the scientific literature relevant to the current subject, one can introduce an additional operator given as

$$M_{\alpha\beta\gamma} = (2i)^{-1}(k_\beta P_{\alpha\gamma} + k_\gamma P_{\alpha\beta}), \tag{2.27}$$

which essentially remains symmetric under the interchange of the indices β and γ. With the substitution of Eq. (2.27) into Eq. (2.21), one obtains the Fourier-

transformed solenoidal Navier-Stokes equations in the symmetrized from given as

$$\left(\frac{\partial}{\partial t}+\nu k^2\right)\hat{u}_\alpha = M_{\alpha\beta\gamma}\left(\frac{2\pi}{L_B}\right)^3 \sum_{\boldsymbol{p}+\boldsymbol{q}=\boldsymbol{k}} \hat{u}_\beta(\boldsymbol{p})\hat{u}_\gamma(\boldsymbol{q}) + \hat{f}_\alpha. \tag{2.28}$$

2.3 Pseudo-spectral approximation

Consider once again the homogeneous and isotropic turbulence confined to a cubic box with an edge length of $L_B = 2\pi$. As indicated in Section 2.2, the fluid velocity field U_α must satisfy both the "zero-mean" condition given as $\langle U_\alpha \rangle = \langle u_\alpha \rangle = 0$ and the periodic boundary conditions expressed as

$$U_\alpha(x_1 + 2\pi n_1, x_2 + 2\pi n_2, x_3 + 2\pi n_3) = U_\alpha(x_1, x_2, x_3, t). \tag{2.29}$$

In practice, the fluid velocity field is expanded as a finite series to give

$$u_\alpha = \sum_{\boldsymbol{k}} \hat{u}_\alpha(\boldsymbol{k}, t) e^{i\boldsymbol{k}\cdot\boldsymbol{x}} = \sum_{\boldsymbol{k}} \hat{u}_\alpha e^{i\boldsymbol{k}\cdot\boldsymbol{x}}, \tag{2.30}$$

where the wavevector $\boldsymbol{k}$ is defined similar to Eq. (2.12), however, with n_α selected as consecutive integer values between $-\frac{1}{2}N + 1$ and $\frac{1}{2}N$; $x_\alpha = (2\pi/N)j$, where $j = 0, 1, 2 \ldots, N-1$ for $\alpha = 1, 2, 3$; N is the number of nodes, usually selected as a power of 2. For completeness, the largest resolved wavenumber in each direction is given as

$$k_{\max} = \frac{1}{2}Nk_0 = \frac{1}{2}\frac{2\pi N}{L_B} = \frac{N}{2}. \tag{2.31}$$

In general, additional restrictions are typically imposed on the maximum resolved wavenumber. However, further discussion is deferred until it becomes relevant. One can observe that in each spatial direction a specific wavevector component, i.e., $k_\alpha = N/2$, appears unsymmetrically. If the corresponding Fourier mode has a non-zero imaginary part, then $u_\alpha(\boldsymbol{x}, t)$ ceases to be a real-valued function. For this very reason, these modes are usually set equal to zero [43].

As already indicated in Section 2.2, the non-linear terms on the right-hand side of the Navier-Stokes equations, Eq. (2.28), introduces significant computational difficulties following from the fact that its evaluation in spectral space requires $\mathcal{O}(N^3)$ operations. This renders the direct summation inappropriate for practical applications (if any) [43]. However, taking advantage of the convolution theorem, Eq. (2.25), Orszag [44, 45] introduced the so-called pseudo-spectral approximation in which the product on the left-hand side of Eq. (2.25) is first evaluated in physical space, and

then transformed back to Fourier space by means of the fast Fourier transform (FFT) algorithm developed in [46]. This approach allows to evaluate the non-linear terms in (only) $\mathcal{O}(N^3 \log_2 N)$ operations. However, Orszag [44] indicated that if the pseudo-spectral approximation is applied to the Navier-Stokes equations in the form given by Eqs. (2.2) and (2.6), then, due to the so-called aliasing errors, the resulting equations are subject to unconditional instability. However, this issue can be mitigated if the pseudo-spectral approximation is applied to the Navier-Stokes equations expressed in the rotation form instead. In this case, one obtains

$$\frac{\partial u_\alpha}{\partial t} = N_\alpha - \frac{\partial \tilde{p}}{\partial x_\alpha} + \nu \frac{\partial^2 u_\alpha}{\partial x_\beta \partial x_\beta} + f_\alpha, \tag{2.32}$$

where $N_\alpha = u_\beta \partial_\alpha u_\beta - u_\beta \partial_\beta u_\alpha$ and $\tilde{p} = \left(\frac{p}{\rho} + \frac{1}{2}u^2\right)$ is the modified pressure field. As indicated by Orszag [44], this approach semiconserves the energy (in the inviscid limit), and hence makes the resulting equations less prone to convective instabilities [47]. With this in mind, one can apply the Fourier transform to the above equation to get

$$\frac{\partial \hat{u}_\alpha}{\partial t} + \nu k^2 \hat{u}_\alpha = \hat{N}_\alpha - i k_\alpha \hat{\tilde{p}} + \hat{f}_\alpha. \tag{2.33}$$

At this point, the pressure term can be eliminated by multiplying the above equation by ik_α and using Eq. (2.15) to give

$$\hat{\tilde{p}} = \frac{-i k_\beta \hat{N}_\beta}{k^2}. \tag{2.34}$$

With the substitution of $\hat{\tilde{p}}$ from Eq. (2.34), and the use of Eq. (2.20), Eq. (2.33) can be rewritten as

$$\frac{\partial \hat{u}_\alpha}{\partial t} + \nu k^2 \hat{u}_\alpha = \delta_{\alpha\beta} \hat{N}_\beta - \frac{i k_\alpha k_\beta \hat{N}_\beta}{k^2} + \hat{f}_\alpha = P_{\alpha\beta} \hat{N}_\beta + \hat{f}_\alpha, \tag{2.35}$$

which refers to as the solenoidal, rotation form of the Navier-Stokes equations in Fourier space. At this point, it should be emphasized that $\hat{f}_\alpha$ is assumed to be not only homogeneous and isotropic but also solenoidal, i.e., $k_\alpha \hat{f}_\alpha = 0$. To get acquainted with the errors introduced by applying the pseudo-spectral approximation to Eq. (2.35), one can refer to [45] (Section 7), and the references therein.

For completeness, it is worth mentioning that since the somewhat pioneering work of Orszag [44], the pseudo-spectral approximation to the rotation form of the Navier-Stokes equations has become one of the essential methods for simulating homogeneous and isotropic turbulence.

2.4 Aliasing errors

As indicated in Section 2.3, if the pseudo-spectral approximation is applied to the Navier-Stokes equations, then the convective terms are evaluated through the combined use of the discrete convolution theorem and a high-performance FFT algorithm. Such an approach, although impressively efficient, introduces the aliasing errors, which should be at least partly removed in order to obtain reliable and long-term stable numerical simulations of turbulent flows.

To better understand the source of aliasing errors, it is convenient to first consider a one-dimensional product formed in physical space to give

$$w(x) = u(x)v(x), \tag{2.36}$$

where $u(x)$ and $v(x)$ are arbitrary functions defined on a discrete grid given as $x = nL_B/N$ for $n = 0, 1, ..., N-1$. It is assumed that the discrete Fourier transform pair, relating $u(x)$ and $v(x)$ to their respective Fourier components $\hat{u}(k)$ and $\hat{v}(k)$, and vice versa, takes the usual form given as

$$\begin{aligned} u(x) &= \sum_{p \le N/2} \hat{u}(p) e^{ipx}, & v(x) &= \sum_{q \le N/2} \hat{v}(q) e^{iqx}, \\ \hat{u}(p) &= \frac{1}{N} \sum_{x} u(x) e^{-ipx}, & \hat{v}(q) &= \frac{1}{N} \sum_{x} v(x) e^{-iqx}. \end{aligned} \tag{2.37}$$

With the substitution of Eqs. (2.37), the product in physical space becomes

$$w(x) = \sum_{p,q \le N/2} \hat{u}(p)\hat{v}(q) e^{i(p+q)x}. \tag{2.38}$$

Hence, with some rearrangement, its inverse discrete Fourier transform is given as

$$\hat{w}(k) = \sum_{\substack{p+q=k \\ p,q \le N/2}} u(p)v(q) \frac{1}{N} \sum_{n=0}^{N-1} e^{-i(k-p-q)x_n}. \tag{2.39}$$

Following from the roots of unity [45], the exponential term on the right-hand side evaluates to

$$\frac{1}{N} \sum_{n=0}^{N-1} e^{-i(k-p-q)x_n} = \begin{cases} 1, & \text{if } p+q = k \ (\text{mod } N), \\ 0, & \text{otherwise.} \end{cases} \tag{2.40}$$

Thereafter, with the substitution of Eq. (2.40) into Eq. (2.39), the convolution sum

becomes

$$\hat{w}(k) = \sum_{\substack{p+q=k \\ p,q\leq N/2}} u(p)v(q) + \sum_{\substack{p+q=k+N \\ p,q\leq N/2}} u(p)v(q) + \sum_{\substack{p+q=k-N \\ p,q\leq N/2}} u(p)v(q), \tag{2.41}$$

where the last two terms on the right-hand side, of which at most one can be non-zero [45], stem from the fact that $e^{i(k\pm N)x_n} = e^{ikx_n}$ for all integer n, k. In other words, the discrete Fourier transform essentially "does not distinguish" between the wavenumber k and its aliases, i.e., $k \pm jN$ for any integer j, as simply depicted in Fig. 2.1. Many different methods for removing the aliasing errors have been put forward over the years. Some of them are relatively efficient, whereas others introduce significant computational overhead. For a comprehensive discussion, inquisitive readers can refer to [43, 45, 48] and the references therein.

One of the most commonly used methods for removing the aliasing errors requires additional padding (and truncation) and is often referred to as the 3/2 rule, or, interchangeably, the 2/3 rule [43]. The discrete Fourier transform is evaluated on M rather than N points to give

$$u(x) = \sum_{p=-M/2+1}^{M/2} \hat{\tilde{u}}(p)e^{ipx_n} \quad \text{for } n = 0, 1, ..., M-1, \tag{2.42}$$

where $M \geq 3N/2$; $\hat{\tilde{u}}(p)$ is given as

$$\hat{\tilde{u}}(p) = \begin{cases} \hat{u}(p), & p \leq N/2, \\ 0, & \text{otherwise.} \end{cases} \tag{2.43}$$

Thereafter, the one-dimensional convolution sum given by Eq. (2.41) becomes

$$\hat{w}(k) = \sum_{\substack{p+q=k \\ p,q\leq N/2}} u(p)v(q) + \sum_{\substack{p+q=k\pm M \\ p,q\leq N/2}} u(p)v(q), \tag{2.44}$$

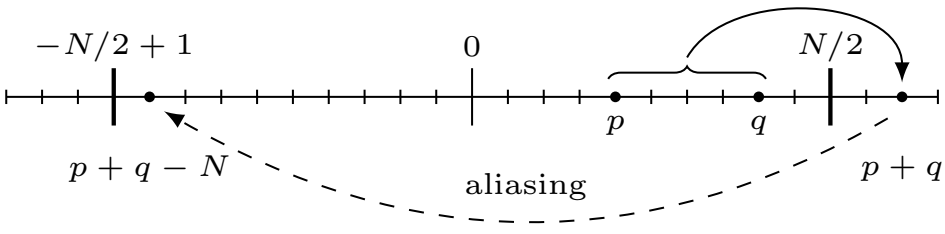

Figure 2.1: Aliasing errors due to the use of the discrete Fourier transform.

where the second term on the right-hand side vanishes for $k \leq N/2$. At this point, it should be emphasized that if the FFT library supports the powers of 2 only, then M should rather be set equal to $2N$. Evaluating the convolution sum using the foregoing approach introduces approximately 50% larger computational overhead when compared to its aliased counterpart given by Eq. (2.41) [43]. However, it must be emphasized that the 3/2 dealiasing technique is most widely used in pseudo-spectral codes due to its straightforward (if not effortless) implementation. In addition to that, it should also be noted that the extension of 3/2 dealiasing method to higher dimensions is straightforward.

Another dealiasing method introduces the so-called phase shifts where $u(x)$ and $v(x)$ in Eq. (2.37) are replaced with

$$\begin{aligned} u'(x+\Delta) &= \sum_{p=-N/2+1}^{N/2} \hat{u}(p) e^{ip(x_n+\Delta)} \\ v'(x+\Delta) &= \sum_{q=-N/2+1}^{N/2} \hat{v}(q) e^{iq(x_n+\Delta)} \quad \text{for } n = 0, 1, ..., N-1, \end{aligned} \tag{2.45}$$

simply denoting the discrete Fourier transforms evaluated on a grid shifted by Δ in physical space. If the "shifted" product $w'(x+\Delta) = u'(x+\Delta)q'(x+\Delta)$ is Fourier-transformed to give

$$\hat{w}'(k) = \sum_{\substack{p+q=k \\ p,q \leq N/2}} \hat{u}(p)\hat{v}(q) \frac{1}{N} \sum_{n=0}^{N-1} e^{-i(k-p-q)(x_n+\Delta)}, \tag{2.46}$$

then the "shifted" convolution sum becomes

$$\hat{w}'(k) = \sum_{\substack{p+q=k \\ p,q \leq N/2}} u(p)v(q) + e^{\pm iN\Delta} \sum_{\substack{p+q=k\pm N \\ p,q \leq N/2}} u(p)v(q), \tag{2.47}$$

where the effect of shifting is readily apparent when compared to Eq. (2.41). Patterson & Orszag [48] indicated that if $w(x)$ and $w'(x+\Delta)$ are evaluated on grids shifted by $\Delta = \pi/N$, or, more generally, $\Delta = L_B/(2N)$, then the aliased terms vanish. Therefore, the fully-dealiased discrete Fourier transform of the one-dimensional product given by Eq. (2.36) is obtained at the cost of two evaluations of the convolution sum, and thus

$$\hat{W}(k) = \frac{1}{2}\Big[\hat{w}(k) + \hat{w}'(k)\Big]. \tag{2.48}$$

It should be emphasized that extending Eq. (2.41) to three dimensions is not straightforward. Therefore, to focus on the primary objective, such derivation is omitted. For more details, one can refer to the extensive literature providing relevant derivations, see, e.g., [48, 49]. As already discussed, if an arbitrary vector field $u_\alpha(\boldsymbol{x})$ for $\alpha = 1, 2, 3$ is defined on points of the discrete grid $\boldsymbol{x}$ given as $x_\alpha = nL_B/N$ for $n = 0, 1, ..., N-1$, and whose Fourier modes $\hat{u}_\alpha(\boldsymbol{k})$ are defined on $\boldsymbol{k}$ restricted to $-N/2+1 \leq k_\alpha \leq N/2$, then the non-linear term given in physical space as $\boldsymbol{u} \cdot \nabla \boldsymbol{u}$, becomes a convolution in Fourier space, see Eq. (2.25). The corresponding triple convolution sum therefore becomes

$$\begin{aligned}\hat{w}_{\beta\gamma} = (1/N^3)\Big[&\sum_{\substack{\boldsymbol{p}+\boldsymbol{q}=\boldsymbol{k} \\ |\boldsymbol{p}|,|\boldsymbol{q}|\leq N/2}} \hat{u}_\beta \hat{u}_\gamma \quad + \sum_{\substack{\boldsymbol{p}+\boldsymbol{q}=\boldsymbol{k}\pm N\boldsymbol{e}_1 \\ |\boldsymbol{p}|,|\boldsymbol{q}|\leq N/2}} \hat{u}_\beta \hat{u}_\gamma \quad + \sum_{\substack{\boldsymbol{p}+\boldsymbol{q}=\boldsymbol{k}\pm N\boldsymbol{e}_2 \\ |\boldsymbol{p}|,|\boldsymbol{q}|\leq N/2}} \hat{u}_\beta \hat{u}_\gamma \quad + \\ &\sum_{\substack{\boldsymbol{p}+\boldsymbol{q}=\boldsymbol{k}\pm N\boldsymbol{e}_3 \\ |\boldsymbol{p}|,|\boldsymbol{q}|\leq N/2}} \hat{u}_\beta \hat{u}_\gamma \quad + \sum_{\substack{\boldsymbol{p}+\boldsymbol{q}=\boldsymbol{k}\pm N\boldsymbol{e}_1\pm N\boldsymbol{e}_2 \\ |\boldsymbol{p}|,|\boldsymbol{q}|\leq N/2}} \hat{u}_\beta \hat{u}_\gamma \quad + \sum_{\substack{\boldsymbol{p}+\boldsymbol{q}=\boldsymbol{k}\pm N\boldsymbol{e}_1\pm N\boldsymbol{e}_3 \\ |\boldsymbol{p}|,|\boldsymbol{q}|\leq N/2}} \hat{u}_\beta \hat{u}_\gamma \quad + \\ &\sum_{\substack{\boldsymbol{p}+\boldsymbol{q}=\boldsymbol{k}\pm N\boldsymbol{e}_2\pm N\boldsymbol{e}_3 \\ |\boldsymbol{p}|,|\boldsymbol{q}|\leq N/2}} \hat{u}_\beta \hat{u}_\gamma \quad + \sum_{\substack{\boldsymbol{p}+\boldsymbol{q}=\boldsymbol{k}\pm N\boldsymbol{e}_1\pm N\boldsymbol{e}_2\pm N\boldsymbol{e}_3 \\ |\boldsymbol{p}|,|\boldsymbol{q}|\leq N/2}} \hat{u}_\beta \hat{u}_\gamma \Big],\end{aligned} \tag{2.49}$$

where the explicit dependence on $\boldsymbol{k}$, $\boldsymbol{p}$, and $\boldsymbol{q}$ is dropped in order to simplify the notation. The second, third, and fourth term on the right-hand side are referred to as the singly-aliased terms, the fifth, sixth, and seventh are the so-called doubly-aliased terms, and the last one denotes the triply-aliased contribution. Thereafter, with the use of the grid-shifting approach, the fully-dealiased non-linear terms in the Navier-Stokes equations can be determined at the cost of eight evaluations of the convolution sum. The computational overhead becomes prohibitively large, and therefore such an approach is not appropriate for practical applications (if any).

Fortunately, Patterson & Orszag [48] pointed out that singly-aliased terms can be effectively removed if the convolution sum expressed as

$$\hat{w}_{\beta\gamma}(\boldsymbol{k}) = (1/N^3) \sum_{\substack{\boldsymbol{p}+\boldsymbol{q}=\boldsymbol{k} \\ |\boldsymbol{p}|,|\boldsymbol{q}|\leq N/2}} \hat{u}_\beta(\boldsymbol{p}) \hat{u}_\gamma(\boldsymbol{q}), \tag{2.50}$$

is evaluated at two grids shifted by half a grid cell in each spatial direction, and subsequently averaged to give

$$\hat{W}_{\beta\gamma}(\boldsymbol{k}) = \frac{1}{2}\left[\hat{w}_{\beta\gamma}(\boldsymbol{k}) + \hat{w}'_{\beta\gamma}(\boldsymbol{k})\right], \tag{2.51}$$

where $\hat{w}'_{\beta\gamma}(\boldsymbol{k})$ is evaluated with the use of $\boldsymbol{x}' = \boldsymbol{x} + (L_B/2N, L_B/2N, L_B/2N)$, whereas the primary grid $\boldsymbol{x}$ is used to determine $\hat{w}_{\beta\gamma}(\boldsymbol{k})$. The very same authors also indicated

that if $\boldsymbol{k}$ additionally satisfies

$$|\boldsymbol{k}| \leq \frac{\sqrt{2}}{3}N, \tag{2.52}$$

then both doubly- and triply-aliased terms vanish. The foregoing condition will henceforth be referred to as the spherical truncation. With this in mind, one can note that the non-linear terms in the Navier-Stokes equations can be devoid of aliasing errors with the combined use of the grid-shifting approach given by Eq. (2.51) and the spherical truncation defined as in Eq. (2.52). It should be emphasized that in practice, the latter condition is usually expressed as $k_{\max} = \lfloor \sqrt{2}N/3 + 0.5 \rfloor$ where $\lfloor \cdot \rfloor$ denotes the largest integer smaller than or equal to a given number.

For completeness, and to some extent for consistency with the scientific literature related to this very matter, it is worth mentioning that Rogallo [50] developed the so-called random grid-shifting method in which the convolution sum is evaluated on two randomly shifted grids, with additional constraint imposed on their offset. This method: (i) can be implemented with no additional computational overhead; (ii) reduces the aliasing errors to $\mathcal{O}(\Delta t^2)$ times the ordinary pseudo-spectral aliasing errors [43] rather than fully removing them; (iii) was primarily developed for the second-order Runge-Kutta methods, which are not the subject of interest in this work. Those seeking a detailed derivation or more practical guidelines can refer to, e.g., [43, 49, 50, 51].

In general, the only possible way to determine whether the aliasing errors affect the stability and/or accuracy of the simulation is through numerical tests. For certain forms of the Navier-Stokes equations, as for example the rotation one given by Eq. (2.35), the need for fully-dealiased convective terms may often be ignored [52]. Additionally, in the case of strongly-dissipative flows, rather small differences are observed between the results obtained with partially- and fully-dealiased simulations [53]. In this work, due to limited computational resources, all simulations will be partially-dealiased using the spherical truncation given by Eq. (2.52).

2.5 Energy balance equation and forced isotropic turbulence

Assuming the velocity field is real-valued, thus implying that its Fourier transform satisfies the Hermitian symmetry given as $\hat{u}_\alpha(-\boldsymbol{k}) = \hat{u}^\star_\alpha(\boldsymbol{k})$, one can rewrite Eq. (2.35) to give

$$\frac{\partial \hat{u}^\star_\alpha}{\partial t} + \nu k^2 \hat{u}^\star_\alpha = P^\star_{\alpha\beta}\hat{N}^\star_\beta + \hat{f}^\star_\alpha, \tag{2.53}$$

where $(^\star)$ denotes the complex conjugate. Hence, multiplying equations Eqs. (2.35) and (2.53) respectively by $\hat{u}_\alpha^\star$ and $\hat{u}_\alpha$, and subsequently taking the average, one obtains

$$\langle \hat{u}_\alpha^\star \frac{\partial \hat{u}_\alpha}{\partial t} + \nu k^2 \hat{u}_\alpha \hat{u}_\alpha^\star \rangle = \langle \hat{u}_\alpha^\star P_{\alpha\beta} \hat{N}_\beta \rangle + \langle \hat{u}_\alpha^\star \hat{f}_\alpha \rangle, \tag{2.54}$$

and

$$\langle \hat{u}_\alpha \frac{\partial \hat{u}_\alpha^\star}{\partial t} + \nu k^2 \hat{u}_\alpha \hat{u}_\alpha^\star \rangle = \langle \hat{u}_\alpha P_{\alpha\beta}^\star \hat{N}_\beta^\star \rangle + \langle \hat{u}_\alpha \hat{f}_\alpha^\star \rangle. \tag{2.55}$$

Adding the above equations together, and multiplying the result by $2\pi k^2$ gives

$$\left(\frac{\partial}{\partial t} + 2\nu k^2 \right) 2\pi k^2 \langle \hat{u}_\alpha \hat{u}_\alpha^\star \rangle = \mathrm{Re}[4\pi k^2 \langle \hat{u}_\alpha^\star P_{\alpha\beta} \hat{N}_\beta \rangle] + \mathrm{Re}[4\pi k^2 \langle \hat{u}_\alpha^\star \hat{f}_\alpha \rangle], \tag{2.56}$$

or, more concisely,

$$\frac{\partial}{\partial t} E(k) + D(k) = T(k) + W(k), \tag{2.57}$$

where $E(k) = 2\pi k^2 \langle \hat{u}_\alpha \hat{u}_\alpha^\star \rangle$, $D(k) = 2\nu k^2 E(k)$, $T(k) = \mathrm{Re}[4\pi k^2 \langle \hat{u}_\alpha^\star P_{\alpha\beta} \hat{N}_\beta \rangle]$ and $W(k) = \mathrm{Re}[4\pi k^2 \langle \hat{u}_\alpha^\star \hat{f}_\alpha \rangle]$ are respectively the energy, dissipation, transfer, and work spectrum functions. It should be noted that the left-hand side of Eq. (2.56) is purely real since $\hat{u}_\alpha$ is multiplied by its complex conjugate. For this very reason, only the real parts (denoted as $\mathrm{Re}[\cdot]$) of both terms on the right-hand side of Eq. (2.56) are taken into account.

Integrating Eq. (2.57) with respect to k, and taking advantage of the fact that $\int T(k)\mathrm{d}k = 0$ (one can note that the sole purpose of $T(k)$ is to transfer the energy between flow scales), one obtains

$$\frac{\partial}{\partial t} E_K(t) = \epsilon_f - \epsilon, \tag{2.58}$$

where E_K is the total kinetic energy of the flow, $\epsilon_f = \int W(k,t)\mathrm{d}k$ is the rate at which the energy is injected into the system (the subscript f refers to forcing) and $\epsilon = \int 2\nu k^2 E(k,t)\mathrm{d}k$ is the energy dissipation rate, i.e., the rate at which energy is drained from the system. At this point, it seems evident that if the energy injection rate is (reasonably) constant, then the turbulent flow will adjust itself (at least statistically) until $\partial_t E_K(t) = 0$, which implies that $\epsilon_f = \epsilon$. It should be emphasized that in the case of freely decaying turbulent flows, i.e., $\epsilon_f = 0$, the change of kinetic energy is caused by viscous dissipation only. Taking the foregoing reasoning into account, it appears evident that in order to compensate for kinetic energy losses, and consequently to obtain a statistically stationary isotropic turbulence, an artificial forcing must be introduced. It is generally accepted that in isotropic turbulence at high Reynolds

number, small flow scales depend weakly on the details of the large, energy-containing ones [2]. For this reason, one usually expects the time-averaged small-scale quantities to be relatively undisturbed by the large-scale forcing. The reader can refer to [54] where a detailed justification for the use of forcing is provided.

Energy injection schemes referred to as deterministic typically use a forcing term in the form given as

$$\hat{f}_\alpha(\boldsymbol{k}, t) = C_f \hat{u}_\alpha(\boldsymbol{k}, t). \tag{2.59}$$

The forcing is usually confined to Fourier modes for which $k_{f,\min} \leq |\boldsymbol{k}| \leq k_{f,\max}$; however the origin, i.e., $|\boldsymbol{k}| = 0$, is excluded in order to ensure the zero-mean flow condition; $C_f = C_f(\boldsymbol{k}, t)$ can be adjusted to obtain specific features of the forcing.

For instance, Grossmann and Lohse [55] expressed C_f as

$$C_f(\boldsymbol{k}, t) = \frac{\epsilon_f}{2E_f(t)}, \tag{2.60}$$

where E_f is the is the total kinetic energy of the forced Fourier modes. Defined this way, the forcing allows to control the energy dissipation of the flow, and therefore also the smallest resolved length scales. This type of forcing was used among many others in [56, 57, 58, 59]. Witkowska et al. [60] replaced ϵ_f in Eq.(2.60) with $\epsilon(t)$ so as to precisely compensate for the energy drained from the system through the viscous dissipation. Such modification was also used in [16, 18, 61].

Some authors kept the energy of the lowest wavenumber shells constant (usually for $k_{f,\max} \leq \sqrt{6}$) by "freezing" the amplitudes of the Fourier modes [62, 63]. Wang et al. [64] sustained the energy of the first two wavenumber shells at a fixed level, and additionally enforced the energy ratio between them to be consistent with the $k^{-5/3}$ scaling. This method was extensively used by other authors in both single-phase flows [65, 66] and two-phase ones [40, 67]; however, it must be emphasized that such a forcing can lead to artificially constrained energy spectra in the two-way momentum coupling regime [68], and gives little to no control over the spatial resolution of the simulation. The latter issue implies the need for a large number of numerical tests in order to select the appropriate forcing parameters.

Eswaran & Pope [54] developed a stochastic energy injection scheme in which the forcing term is defined as

$$\hat{f}_\alpha(\boldsymbol{k}, t) = P_{\alpha\beta} b_\beta(\boldsymbol{k}, t), \tag{2.61}$$

where $b_\beta(\boldsymbol{k}, t)$ is a complex vector-valued stochastic process composed of 6 independent Uhlenbeck-Ornstein random processes, each with a prescribed variance σ^2 and a time-scale T_L. This scheme has been extensively used over the years for both single-

phase flows [69] as well as two-phase ones [12, 14]; however, it turns out that the simulated turbulence depends strongly on the selected forcing parameters.

Due to relatively straightforward implementation and the lack of artificial randomness introduced into the large flow scales, in this work, the forcing term is expressed as in [55] to give

$$\hat{f}_\alpha(\boldsymbol{k}) = \begin{cases} (\epsilon_f/2E_f)\hat{u}_\alpha(\boldsymbol{k}), & k_{f,\min} \leq |\boldsymbol{k}| \leq k_{f,\max}, \\ 0, & \text{otherwise}, \end{cases} \tag{2.62}$$

where ϵ_f, in addition to the energy injection rate, can be referred to as the expected dissipation rate. To ensure accurate resolution of the smallest, dissipative flow scales, in this work the energy injection rate is expressed as

$$\epsilon_f = \nu^3 \left(\frac{k_{\max}\eta}{k_{\max}} \right)^{-4}, \tag{2.63}$$

where $k_{\max}\eta$ is a well-established parameter describing the small-scale resolution. In the case of single-phase flows, it is usually sufficient to keep this parameter larger than unity; however, more stringent restrictions may be required. The total amount of energy injected into the system per unit time can be determined by integrating the work spectrum function with respect to k to give

$$\int_{k_{f,\min}}^{k_{f,\max}} W(k)\mathrm{d}k = \frac{\epsilon_f}{E_f} \int_{k_{f,\min}}^{k_{f,\max}} 2\pi k^2 \langle \hat{u}_\alpha \hat{u}_\alpha^\star \rangle \mathrm{d}k \equiv \epsilon_f, \tag{2.64}$$

which simply indicates that the flow is forced at a constant rate. Thereafter, taking the advantage of Eq. (2.58), one can expect the system to reach statistical stationarity within a finite time; usually it takes at most several large-eddy turnovers, i.e., the characteristic time scale of the large, energy-containing flow scales. It can be noticed that the proposed forcing is also self-adaptive in the sense that, using Eq. (2.63), sufficient resolution (measured by $k_{\max}\eta$) is ensured regardless of the grid size. In fact, it may be convenient to rewrite Eq. (2.63) as

$$\nu = \left[\epsilon_f \left(\frac{k_{\max}\eta}{k_{\max}} \right)^4 \right]^{1/3}, \tag{2.65}$$

since it is arguably more intuitive to control the turbulence intensity through the energy injection rate rather than the kinematic viscosity of the fluid. This way, one can achieve the desired small-scale resolution with minimum effort. Based on the available literature, it seems that such explicit binding of parameters as given by Eqs. (2.63)

or (2.65), constitutes a minor yet original enhancement of the well-established forcing term given by Eq. (2.62). It can be readily noticed that in order to fully define the forcing, one has to determine the range of forced Fourier modes by appropriately selecting both $k_{f,\min}$ and $k_{f,\max}$. However, to the best of the author's knowledge, the available scientific literature provides no universal (if any) guidelines on this very issue. To make things worse, the most commonly reported configurations lead to inappropriate large-scale resolution, eventually resulting in unphysical spatial correlation of the velocity field. Further discussion is deferred until it becomes relevant, see Section 2.11.

2.6 Initial velocity field

In the pseudo-spectral method the velocity field can be initialized in either physical or Fourier space. However one chooses to proceed with initialization, the velocity field should be solenoidal, statistically isotropic, and, ideally, its energy spectrum function should take a reasonable form [44].

In this research study, the initial velocity field was generated by selecting the Fourier modes independently from a Gaussian distribution, each with zero mean and a unit variance, i.e., $\hat{\widetilde{u}}_\alpha(\boldsymbol{k}, t=0) \in \mathcal{N}(0,1)$ for $\alpha = 1,2,3$. In addition to that, the Hermitian symmetry $\hat{\widetilde{u}}_\alpha(-\boldsymbol{k},t) = \hat{\widetilde{u}}^\star_\alpha(\boldsymbol{k},t)$ was manually imposed where appropriate. Once accomplished, the projection tensor given by Eq. (2.20) was applied to give

$$\hat{u}_\alpha(\boldsymbol{k},0) = \left(\delta_{\alpha\beta} - \frac{k_\alpha k_\beta}{k^2}\right)\hat{\widetilde{u}}_\beta(\boldsymbol{k},0), \tag{2.66}$$

which simply ensures the initial velocity field is divergence-free. In addition to that, selected Fourier modes were rescaled so that the initial energy spectrum function took the form given as in [70], that is,

$$E_0(k) = \frac{16}{\sqrt{\pi/2}}\frac{u_0^2 k^4}{k_p^5} e^{-2k^2/k_p^2}, \tag{2.67}$$

where $u_0^2 = 1$ is the initial r.m.s. fluid velocity, and $k_p = 3$ points to the (initially) most energetic wavenumber shell. This way, at $t = 0$ the energy is distributed over a relatively narrow range of wavenumbers and $E(t=0) = 3/2$.

2.7 Time integration of the Navier-Stokes equations

Long-term stable time integration of the Navier-Stokes equations requires both the spatial and the temporal discretization errors to be kept reasonably low. In most of the turbulence-related research, particularly focusing on homogeneous and isotropic turbulence, this is achieved with the use of infinite-order accurate Galerkin spectral or pseudo-spectral methods, compulsorily supplemented with a high-order temporal integrator [45].

According to the best of the author's knowledge, in the majority of research relevant to this study, the viscous terms in the Navier-Stokes equations were solved implicitly using the integrating factor, whereas the explicit second-order (less often third- and fourth-order) Runge-Kutta [49, 51, 54, 64, 65] or second-order Adams-Bashforth [52] methods were employed to advance the convective terms in time. Some authors also reported the combination of both the implicit Crank-Nicolson and the second-order Adams-Bashforth methods for viscous and convective terms, respectively, see, e.g., [12].

It is important to note that in the case of single-phase flows for which the pseudo-spectral solvers are used, the computational cost is mostly associated with the repetitive application of discrete Fourier transforms. The standard pseudo-spectral algorithm needs at least three 3D DFTs to calculate the non-linear terms. It should be emphasized that the required number of discrete Fourier transforms is multiplied by the total number of stages in a specific time-stepping scheme (for instance, the second-order Runge-Kutta method requires six 3D DFTs). In addition to that, it should be emphasized that if the grid-shifting approach is considered for dealiasing purposes, then (except for the random grid-shifting [50]) the number of DFTs increases even more. In the case of two-phase flows, the computational overhead of the particulate phase is non-negligible, and thus the use of any multistage time-stepping scheme can quickly become inefficient, but definitely not unfeasible, see, e.g., [69, 71, 72].

To integrate the viscous terms exactly, it is convenient to introduce the integrating factor $e^{\nu k^2 t}$ and multiply Eq. (2.35) both sides to give[4]

$$\frac{\partial}{\partial t}\left(\hat{u}_\alpha e^{\nu k^2 t}\right) = \left(P_{\alpha\beta}\hat{N}_\beta + \hat{f}_\alpha\right) e^{\nu k^2 t}. \tag{2.68}$$

Hence, integrating with respect to time, one eventually obtains

$$\hat{u}_\alpha^{t_{n+1}} = \hat{u}_\alpha^{t_n} e^{-\nu k^2 \Delta t} + e^{-\nu k^2 t_{n+1}} \int_{t_n}^{t_{n+1}} \left(P_{\alpha\beta}\hat{N}_\beta + \hat{f}_\alpha\right) e^{\nu k^2 t'} \mathrm{d}t'. \tag{2.69}$$

[4]Note that $(\partial_t \hat{u}_\alpha)e^{\nu k^2 t} + \hat{u}_\alpha \nu k^2 e^{\nu k^2 t} = \partial_t(\hat{u}_\alpha e^{\nu k^2 t})$

Thereafter, introducing a time step Δt such that $t_n = n\Delta t$, the remaining integral can be approximated using, e.g., the explicit fourth-order Adams-Bashforth method to give

$$\hat{u}_\alpha^{n+1} = \hat{u}_\alpha^n e^{-\nu k^2 \Delta t} + \frac{\Delta t}{24}\Bigg[55\Pi_\alpha^n e^{-\nu k^2 \Delta t} - 59\Pi_\alpha^{n-1} e^{-2\nu k^2 \Delta t} + 37\Pi_\alpha^{n-2} e^{-3\nu k^2 \Delta t} - 9\Pi_\alpha^{n-3} e^{-4\nu k^2 \Delta t}\Bigg], \tag{2.70}$$

where

$$\Pi_\alpha^n = P_{\alpha\beta}\hat{N}_\beta^n + \hat{f}_\alpha^n \tag{2.71}$$

is introduced temporarily in order to simplify the notation.

At this point, it should be emphasized that exclusively due to the floating-point arithmetic, the above equation is ill-defined leading to a time-stepping scheme that is susceptible to numerical instabilities originating from the round-off errors. To clarify, it should be emphasized that adding together two solenoidal vector fields does not necessarily guarantee that the result will remain divergence-free over time. Although this form was often used, see, e.g., [16, 49, 51], the issue has not been reported except for [73]. It also remains unclear whether any preventive measures were included in the relevant codes. The aforementioned computational deficiency gradually degrades the velocity field that eventually ceases to satisfy the continuity equation, Eq. (2.15). This phenomenon can be monitored by, e.g., the r.m.s. velocity divergence D' (not shown here). In all test cases $D' = \mathcal{O}(1)$ was reached within $t = \mathcal{O}(100T_e)$, resulting in a simulation breakdown. Although this significantly exceeds a typical simulation time reported for single-phase flows, even longer times may be required if the motion of a particulate phase is considered.

Wang & Rosa [73] reported a somewhat bizarre time evolution of the velocity field while using the same time-stepping scheme as given in Eq. (2.70), except that the convective terms were advanced in time with the use of the second-order Adams-Bashforth method. The authors indicated that the primary cause of the reported issue was that the velocity field became no longer solenoidal due to the round-off errors amplified by the forcing. The authors developed a theory predicting the spurious evolution of their turbulent flow and proposed two "remedies", so to speak, in which: (i) additional projection operator is applied at the end of every n time-steps; (ii) fractional-step method is employed so that zero-divergence is enforced at the end of each time step. The outcome of this work is actually quite surprising in the sense that: (i) the issue appears to follow exclusively from the round-off errors, therefore its

root-cause is solely the improper order of computation; and (ii) the provided remedies are no different from the algorithm that Vincent & Meneguzzi [52] had suggested almost 20 years earlier.

It should be emphasized that the forcing term $\hat{f}_\alpha$ is assumed, or, rather "designed", to be solenoidal and statistically isotropic. Therefore, it seems that any deviation from this state should result from some sort of computational imperfections, e.g., the floating-point arithmetic or implementation errors. The forcing can be effectively added to the non-linear terms before the projection operator is applied, and thus

$$\Pi_\alpha^n = P_{\alpha\beta}\left(\hat{N}_\beta^n + \hat{f}_\beta^n\right). \tag{2.72}$$

Numerical experiments (not shown here) confirmed that the time-stepping scheme given by Eqs. (2.70) and (2.72) ensures that the continuity equation, Eq. (2.15), is satisfied with machine precision, however, with D' still exhibiting large oscillations.

As indicated by Vincent & Meneguzzi [52], the divergence-free projection can be effectively applied at the end of each time step. To get a better understanding of this approach, one can first consider the Navier-Stokes equations given by Eq. (2.33), where the viscous terms are solved implicitly using the integrating factor to give

$$\frac{\partial}{\partial t}\left(\hat{u}_\alpha e^{\nu k^2 t}\right) = \left(\hat{N}_\alpha + \hat{f}_\alpha\right) e^{\nu k^2 t} - ik_\alpha \hat{\tilde{p}} e^{\nu k^2 t}. \tag{2.73}$$

Integrating both sides with respect to time, and with some rearrangement, one obtains

$$\hat{u}_\alpha^{n+1} = \hat{u}_\alpha^n e^{-\nu k^2 \Delta t} + e^{-\nu k^2 t_{n+1}} \int_{t_n}^{t_{n+1}} \left(\hat{N}_\alpha + \hat{f}_\alpha\right) e^{\nu k^2 t'} \mathrm{d}t' - ik_\alpha \hat{P}^{n+1}, \tag{2.74}$$

where $\hat{P}^{n+1} = e^{-\nu k^2 t_{n+1}} \int \hat{\tilde{p}} e^{\nu k^2 t} \mathrm{d}t'$ is introduced temporarily in order to simplify the notation. The velocity field at the intermediate stage denoted as $\hat{u}_\alpha^{n,*}$ can be determined from

$$\begin{aligned} \hat{u}_\alpha^{n,*} = \hat{u}_\alpha^n e^{-\nu k^2 \Delta t} + \frac{\Delta t}{24}\Bigg[& 55\Pi_\alpha^n e^{-\nu k^2 \Delta t} - 59\Pi_\alpha^{n-1} e^{-2\nu k^2 \Delta t} + \\ & 37\Pi_\alpha^{n-2} e^{-3\nu k^2 \Delta t} - 9\Pi_\alpha^{n-3} e^{-4\nu k^2 \Delta t}\Bigg], \end{aligned} \tag{2.75}$$

where Π^n is defined as in Eq. (2.72). With the use of (2.75), one can advance the velocity field according to

$$\hat{u}_\alpha^{n+1} = \hat{u}_\alpha^{n,*} - ik_\alpha \hat{P}^{n+1}. \tag{2.76}$$

At this point, the pressure term can be eliminated by multiplying the above equation

by ik_α, and taking advantage of Eq. (2.15) to give

$$\hat{P}^{n+1} = \frac{-ik_\beta \hat{u}_\beta^{n,*}}{k^2}. \tag{2.77}$$

Finally, with the substitution of Eq. (2.77) into Eq. (2.76), and the use of Eq. (2.20), one obtains the velocity field at the next time step given as

$$\hat{u}_\alpha^{n+1} = P_{\alpha\beta}\hat{u}_\beta^{n,*}. \tag{2.78}$$

To avoid convective instabilities, in this work Δt was limited in order to satisfy the Courant-Friedrichs-Lewy criterion given as

$$\frac{\sqrt{3}u_{\max}}{\Delta x/\Delta t} \leq C_{\max} = 0.2, \tag{2.79}$$

where $u_{\max}$ is the maximum magnitude of the fluid velocity within the box.

Interestingly, the time-stepping scheme defined by either Eqs. (2.70) and (2.72) or Eqs. (2.75) and (2.78) can still exhibit long-term instabilities causing a spurious evolution of a turbulent flow rather than a rapid simulation breakdown. After a series of numerical tests and careful examination of the current code, it has been concluded that due to the floating-point arithmetic, certain Fourier modes eventually cease to satisfy the Hermitian symmetry causing the energy to spuriously accumulate in the lowest resolved wavenumbers. This essentially leads to a "tornado-like" velocity field, similar to [73].

To clarify, consider a wavevector $\boldsymbol{k}$ with components confined to $-N/2+1 \leq k_\alpha \leq N/2$ for $\alpha = 1, 2, 3$. Due to the Hermitian symmetry, approximately half of the wavenumber space is redundant, and thus one obtains, e.g., $-N/2+1 \leq k_{1,2} \leq N/2$ and $0 \leq k_3 \leq N/2$, where in such configuration, $k_3 = 0$ essentially becomes the symmetry plane[5]. In a 3D DFT, the Hermitian symmetry is ensured by the FFT library, however usually only outside the symmetry plane, e.g., $k_3 > 0$. It turns out that certain Fourier modes associated with the symmetry plane are prone to the aforementioned round-off errors. In fact, Wang & Rosa [73] suggested that the forcing somehow amplifies the spurious evolution of turbulence, however, did not properly recognize the root cause of this, possibly due to the specific forcing used in their work, which kept the energy for $|\boldsymbol{k}| < \sqrt{6}$ frozen. For this very reason, any deviation from the Hermitian symmetry (essentially causing spurious accumulation of kinetic energy) was implicitly (and probably unintentionally) compensated at the end

[5]Note that the selection of specific direction is arbitrary

of each time step. After a series of numerical tests performed during this research, it has been concluded that (i) ensuring the proper order of computation in the time-stepping scheme and (ii) enforcing the Hermitian symmetry of specific Fourier modes each time these are modified in some way, are the necessary (and sufficient) steps to completely eliminate all of the aforementioned issues, thus allowing for long-term stable simulations.

2.8 Basic flow parameters

This section introduces a few basic flow parameters used throughout this work to statistically quantify different turbulent flows.

In a pseudo-spectral solver, the turbulent kinetic energy E_K can be determined in either physical or Fourier space as follows

$$E_K = \frac{3}{2}u'^2 = \frac{1}{2}\langle u_i u_i \rangle = \int_0^{k_{\max}} E(k)\mathrm{d}k = \sum_{\boldsymbol{k}} \widetilde{E_K}(\boldsymbol{k}), \tag{2.80}$$

where $\langle\cdot\rangle$ denotes the volume-averaging, u' is the r.m.s. fluid velocity or the turbulence intensity, $E(k)$ is the three-dimensional energy spectrum function, and $\widetilde{E_K}(\boldsymbol{k}) = \hat{u}_i\hat{u}_i^\star/2$ is simply the contribution to E_K from mode $\boldsymbol{k}$. Following Eswaran and Pope [54], the shell-averaged energy spectrum function can be expressed as

$$E(k) = \frac{4\pi k^2}{N_k} \sum_{\boldsymbol{k}} \widetilde{E_K}(\boldsymbol{k}), \tag{2.81}$$

for all Fourier modes $\boldsymbol{k}$ confined to $k - \Delta k/2 < |\boldsymbol{k}| \leq k + \Delta k/2$, where $\Delta k = 1$; N_k is the number of modes within a wavenumber band centered at integer k. As the authors suggested, such a "smoothing is necessary because of the uneven distribution of nodes in the spherical shells [...]". It is however unclear whether such a smoothing should be introduced solely for postprocessing purposes, see, e.g., [49] for a more thorough discussion about the consequences of the aforementioned smoothing. In this work, the shell-averaged energy spectrum function is given as

$$E(k) = \frac{1}{\Delta k} \sum_{\boldsymbol{k}} \widetilde{E_K}(\boldsymbol{k}), \tag{2.82}$$

which essentially implies that the energy of the k-th wavenumber shell is determined by summing the contributions from its constituent modes, as one would intuitively expect.

The dissipation spectrum function $D(k)$, already introduced in Section 2.5, integrates to the volume-averaged dissipation rate ϵ given as

$$\epsilon = 2\nu \int_0^{k_{\max}} k^2 E(k) \mathrm{d}k = 2\nu \sum_{\boldsymbol{k}} |\boldsymbol{k}|^2 \widetilde{E_K}(\boldsymbol{k}). \tag{2.83}$$

With the use of E_K and ϵ, the turbulence time and length scales can be expressed as $\tau_t = E_K/\epsilon$ and $L_t = E_K^{3/2}/\epsilon$, respectively. The latter quantity can be further used to determine the turbulence Reynolds number $Re_t = u' L_t/\nu$. The Kolmogorov length, time and velocity scales are determined using their usual forms given as $\eta = (\nu^3/\epsilon)^{1/4}$, $\tau_\eta = (\nu/\epsilon)^{1/2}$ and $u_\eta = (\nu\epsilon)^{1/4}$, respectively.

Longitudinal (L_1) and transverse (L_2) integral length scales can be determined using the two-point velocity correlation tensor $R_{\alpha\alpha,\beta}(r) = \langle u_\alpha(\boldsymbol{x}) u_\alpha(\boldsymbol{x} + r\boldsymbol{e}_\beta)\rangle$ as in [69] to give

$$L_{\alpha\alpha,\beta} = \frac{1}{\langle u_\alpha^2 \rangle} \int_0^{L_B/2} R_{\alpha\alpha,\beta} \mathrm{d}r, \tag{2.84}$$

where the Einstein summation convention does not apply; $\boldsymbol{e}_\beta$ denotes a unit vector in a given direction. It should be emphasized that the above integral can be evaluated using, e.g., Simpson's 1/3 rule. In addition to that, averages can be taken over statistically identical components, e.g., $L_1 = (L_{11,1} + L_{22,2} + L_{33,3})/3$. The longitudinal and transverse velocity autocorrelation functions can be determined in the very same manner, e.g., $R_1(r) = (R_{11,1}/\langle u_1^2\rangle + R_{22,2}/\langle u_2^2\rangle + R_{33,3}/\langle u_3^2\rangle)/3$. In isotropic turbulence, the longitudinal integral length scale can also be evaluated from

$$L_1 = L = \frac{\pi}{2u'^2} \int_0^{k_{\max}} k^{-1} E(k) \mathrm{d}k = \frac{\pi}{2u'^2} \sum_{\boldsymbol{k}} |\boldsymbol{k}|^{-1} \widetilde{E_K}(\boldsymbol{k}), \tag{2.85}$$

which is subsequently most often used to determine both the integral-scale Reynolds number $Re_L = u' L/\nu$ and the large-eddy turnover time $T_e = L/u'$. Additionally, the Taylor microscale takes the usual form given as $\lambda = (15\nu u'^2/\epsilon)^{1/2}$, and can further be used to determine the Taylor-scale Reynolds number $Re_\lambda = u'\lambda/\nu$.

Small-scale resolution is typically measured using the non-dimensional parameter $k_{\max}\eta$ that, according to well-established guidelines [54, 69], should be kept larger than unity for single-phase flows. At this point, however, it should be emphasized that more stringent requirements may be imposed on the spatial resolution when two-phase flows are considered. In this work the small-scale resolution was kept constant and equal to $k_{\max}\eta = 1.5$.

To settle whether the resolved velocity field is indeed isotropic, one can use the

so-called "isotropy" coefficient given as

$$I^2 = \Psi_1/\Psi_2, \tag{2.86}$$

first proposed by Curry et al. [74], in which

$$\Psi_1 = \langle |\boldsymbol{e}_1(\boldsymbol{k}) \cdot \hat{\boldsymbol{u}}(\boldsymbol{k})|^2 \rangle \qquad \Psi_2 = \langle |\boldsymbol{e}_2(\boldsymbol{k}) \cdot \hat{\boldsymbol{u}}(\boldsymbol{k})|^2 \rangle, \tag{2.87}$$

where $\langle \cdot \rangle$ denotes the shell-averaging; $\boldsymbol{e}_1$ and $\boldsymbol{e}_2$ are two mutually orthogonal unit vectors given as

$$\boldsymbol{e}_1(\boldsymbol{k}) = \frac{\boldsymbol{k} \times \hat{\boldsymbol{z}}}{|\boldsymbol{k} \times \hat{\boldsymbol{z}}|} \quad \text{and} \quad \boldsymbol{e}_2(\boldsymbol{k}) = \frac{\boldsymbol{k} \times \boldsymbol{e}_1(\boldsymbol{k})}{|\boldsymbol{k} \times \boldsymbol{e}_1(\boldsymbol{k})|}, \tag{2.88}$$

where $\hat{\boldsymbol{z}}$ is a randomly oriented unit vector[6] such that $|\hat{\boldsymbol{z}} \cdot (\boldsymbol{k}/|\boldsymbol{k}|)| \neq 1$. In isotropic turbulence one expects that $I = 1$, which implies that $\Psi_1 = \Psi_2$, simply indicating the equipartition of energy along $\boldsymbol{e}_1$ and $\boldsymbol{e}_2$. In addition to that, it should be emphasized that if the summation in Eq. (2.87) is restricted to the Fourier modes confined to the spherical shell centered at k, then another spectrum function can be defined as $I(k)^2 = \Psi_1(k)/\Psi_2(k)$ [49, 51, 75]. It arguably gives some sort of insight into the isotropy of specific flow scales.

The second invariant of the velocity gradient tensor Q provides more insight into the local flow structure and allows to distinguish between the rotational and strain-dominated regions in a turbulent flow. This quantity is given as

$$Q = \frac{1}{2}\left(\|\boldsymbol{\Omega}\|^2 - \|\boldsymbol{S}\|^2\right) = -\frac{1}{2}\frac{\partial u_\alpha}{\partial x_\beta}\frac{\partial u_\beta}{\partial x_\alpha}, \tag{2.89}$$

where $\boldsymbol{S}$ and $\boldsymbol{\Omega}$ are respectively the strain-rate and vorticity tensors. In addition to the above, this parameter will also be meaningful in the context of particle dynamics since, as will be seen shortly, both of the aforementioned regions have a non-trivial impact on particle motion.

For completeness, one can introduce additional measures of turbulence dynamics, i.e., the skewness S and flatness F of the longitudinal velocity derivative given as

$$S = \frac{\langle (\partial u_\alpha/\partial x_\alpha)^3 \rangle}{\langle (\partial u_\alpha/\partial x_\alpha)^2 \rangle^{3/2}}, \qquad F = \frac{\langle (\partial u_\alpha/\partial x_\alpha)^4 \rangle}{\langle (\partial u_\alpha/\partial x_\alpha)^2 \rangle^2}, \tag{2.90}$$

where in addition to the above definitions, averages can be taken over statistically identical components of the velocity gradient.

[6] $(\hat{})$ denotes vector normalization, i.e., $\hat{\boldsymbol{z}} = \boldsymbol{z}/|\boldsymbol{z}|$, rather than Fourier space representation

2.9 Time statistics and error bounds

Once the energy dissipation balances the energy injection rate, i.e., when a turbulent flow becomes statistically stationary, the ensemble average of an arbitrary quantity $P(t)$ and its corresponding error bounds can be estimated from a set of statistically independent measurements. This can be achieved on condition that the sampling interval T_s is on the order of $\sim T_e$. Following other authors, see, e.g., [54], a more rigorous estimation of the sampling interval can be based on the autocorrelation function of each quantity of interest expressed as in [76] to give

$$r(l) = \frac{\sum_{m=1}^{n-l} \Big(P_m - \langle P \rangle\Big)\Big(P_{m+l} - \langle P \rangle\Big)}{\sum_{m=1}^{n-l} \Big(P_m - \langle P \rangle\Big)^2} \qquad l = 0, 1, 2, ..., l_{\max}, \tag{2.91}$$

where n is the total number of measurements separated by a time interval $\Delta t' \ll T_s$; l is the number of such $(\Delta t')$ intervals often referred to as the lag[7]. In this work, $\Delta t'$ was selected so as to obtain approximately 50 measurements over the large-eddy turnover time. The sampling interval can be estimated as the time within which the sample autocorrelation function falls from 1 to approximately $1/e$. To provide some insight into this process, Fig. 2.2 shows a time history of the total kinetic energy (left panel) and its autocorrelation function plotted against the lag (right panel). For each

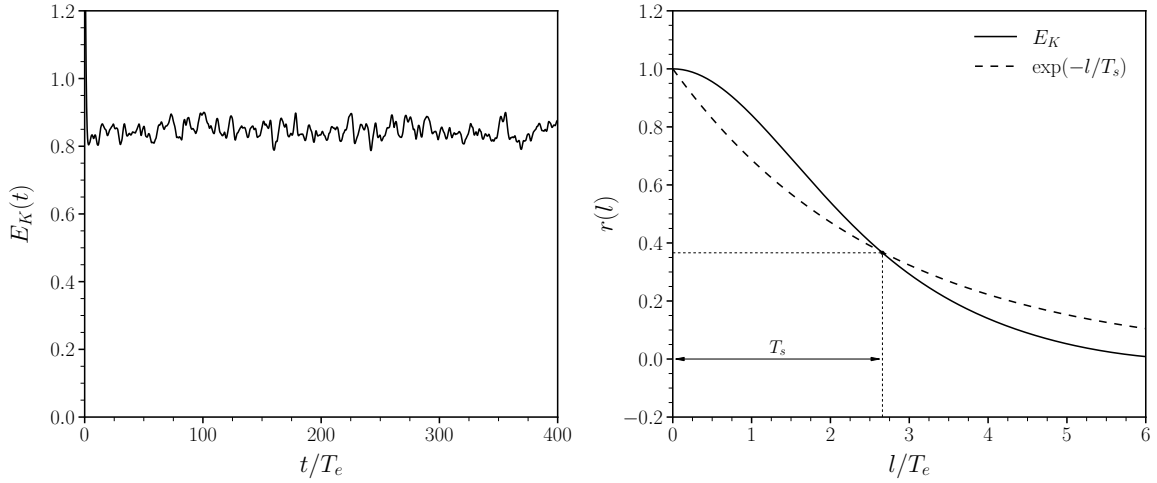

Figure 2.2: Time history (left panel) and the autocorrelation function (right panel) of the total kinetic energy in forced isotropic turbulence at $Re_\lambda \sim 32$; T_s denotes the sampling interval.

[7]Although the literature suggests that $l_{\max} = n/4$ [76], in practice, $l_{\max}$ should be orders of magnitude smaller than the number of samples n

and every flow parameter introduced in Section 2.8, different values of the sampling interval were obtained, however, all of these values fell within the range given as

$$1 < \frac{T_s}{\langle T_e \rangle} < 3. \tag{2.92}$$

This is in fact is consistent with the observations reported in [75]. Certain flow statistics, e.g., the longitudinal or transverse integral length scales defined in Eq. (2.84), require particularly long averaging times[8]. Hence, in order to reduce the overall computational cost of the simulation, the sampling interval must be decreased, while maintaining a reasonable uncertainty of the results. In this work, the upper limit of the foregoing range essentially denotes the time within which the autocorrelation of the total kinetic energy falls below $1/e$. It should be emphasized that this time scale strongly depends on the evolution of large, energy-containing flow scales (particularly including the forced ones) [69]. In general, according to the Kolmogorov theory of turbulence, small flow scales are expected to evolve in much shorter time scales than the large ones, thus making the relevant statistics decorrelate faster. Unfortunately, due to computational limitations, in this work, all flow statistics were sampled every $T_s \approx 0.5T_e$.

With this in mind, the sample mean of a given quantity $P(t)$ over a set of n measurements takes the usual form given as

$$\langle P \rangle = \frac{1}{n} \sum_{i=1}^{n} P(t_i) \tag{2.93}$$

and essentially represents an estimate of the population mean μ, in which case $n \to \infty$. The corresponding standard deviation is expressed as

$$\sigma = \left[\frac{1}{n-1} \sum_{i=1}^{n} \Big(P(t_i) - \langle P \rangle \Big)^2 \right]^{1/2} \tag{2.94}$$

and, in turn, represents the dispersion of measurements about the sample mean. In addition to a single measurement uncertainty, one can also introduce the standard deviation of the sample mean itself[9], often referred to as the standard error given as

$$\sigma_m \cong \left[\frac{1}{n(n-1)} \sum_{i=1}^{n} \Big(P(t_i) - \langle P \rangle \Big)^2 \right]^{1/2} = \frac{\sigma}{\sqrt{n}}, \tag{2.95}$$

[8] In addition to that, some of the particle statistics need to be averaged over at least $\sim 100T_e$

[9] In the sense that one has access to a large set of n measurements, each of which provides its own mean

which approximately measures the dispersion of the sample mean about the population mean. Based on Chebyshev's inequality [77], it is accepted that a random variable is unlikely to differ from its expected value μ more than a few standard deviations σ_m. With this in mind, it can be readily noticed that with increasing number of samples, σ_m decreases, and therefore the sample mean $\langle P \rangle$ becomes an increasingly better estimate of the population mean.

2.10 Decaying turbulence

This section is primarily focused on a three-dimensional vortex field that was first considered by Taylor & Green [78] in order to better understand the enhancement of vorticity by vortex-line stretching, eventually causing the generation of small-scale turbulence [79]. This vortex field is a relatively simple example of decaying turbulence, which essentially develops from a single-mode initial condition [80] given as

$$\begin{aligned} u_1(\boldsymbol{x}, t=0) &= \quad \sin(x_1)\cos(x_2)\cos(x_3) \\ u_2(\boldsymbol{x}, t=0) &= -\cos(x_1)\sin(x_2)\cos(x_3) \\ u_3(\boldsymbol{x}, t=0) &= 0. \end{aligned} \tag{2.96}$$

Despite providing a more profound understanding of fundamental mechanisms underlying turbulent flows, the Taylor-Green vortex flow has also been extensively used as a benchmark for debugging, testing and validating numerical simulation codes.

Although the current code was designed and implemented almost entirely from the ground up, it employs algorithms, libraries, and numerical methods that have already been extensively verified over the years in terms of accuracy and efficiency. For this very reason, the remainder of this section focuses solely on verifying the implementation rather than validating the method (or the algorithm) itself.

Some results were compared against the reference data reported by Orszag [81] for a three-dimensional, incompressible Taylor-Green vortex at a relatively low Reynolds number, that is $Re = 1/\nu = 200$. In that work, the turbulence was confined to a cubic box of side $L_B = \pi$, with the spatial resolution of 32^3 nodes, essentially resulting in $k_{\max} = 16$. Explicit second-order Adams-Bashforth and implicit Crank-Nicolson schemes were used for convective and viscous terms, respectively.

Time histories of both the volume-averaged enstrophy $\Omega(t) = \langle |\boldsymbol{\omega}(\boldsymbol{x}, t)|^2 \rangle$ and the energy dissipation rate are compared in Fig. 2.3. Some minor discrepancies presumably result from inaccurate digitization of the reference plots. However, the overall agreement is satisfactory, and thus it can be concluded that the newly developed code

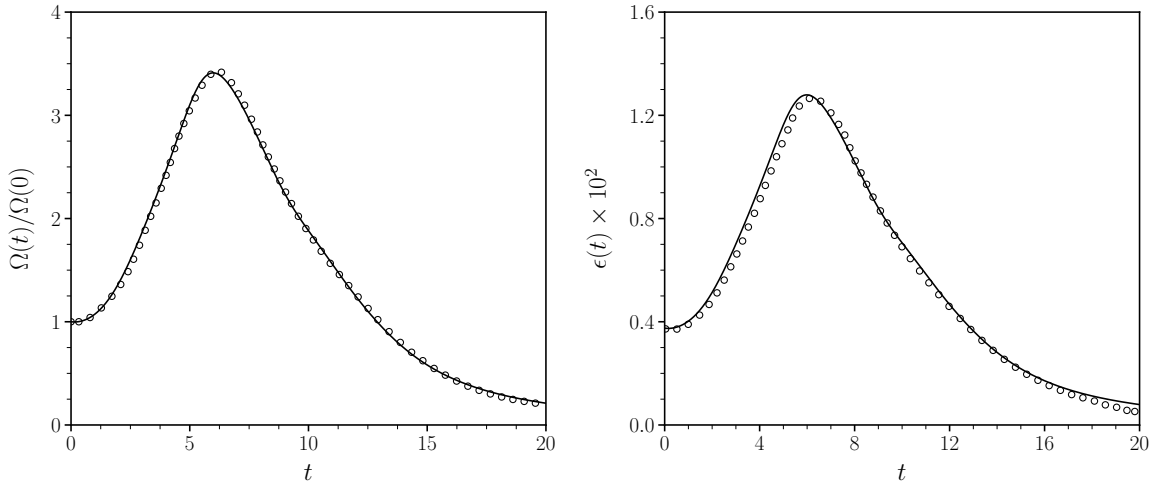

Figure 2.3: Time histories of the volume-averaged enstrophy (left panel) and the energy dissipation rate (right panel) at $Re = 200$; solid line denotes the current code; circles represent the reference data digitized and replotted from [81].

accurately captures the rapid generation of small-scale turbulence.

Following Orszag [81], the anisotropy of both the kinetic energy and its dissipation rate can be conveniently measured using respectively

$$E_3/E_1 = \sum_{\boldsymbol{k}} |\hat{u}_3|^2 \Big/ \sum_{\boldsymbol{k}} |\hat{u}_1|^2 \tag{2.97}$$

and

$$D_3/D_1 = \sum_{\boldsymbol{k}} k^2 |\hat{u}_3|^2 \Big/ \sum_{\boldsymbol{k}} k^2 |\hat{u}_1|^2. \tag{2.98}$$

These statistics are compared in Fig. 2.4, from which it is readily apparent that the kinetic energy (left panel) remains far from isotropy, whereas the energy dissipation (right panel) becomes approximately isotropic for $t \in [5, 15]$. In general, this is consistent with a theory of turbulence as put forward by Kolmogorov, which essentially states that small flow scales (triggering the energy dissipation) approach isotropy much faster than the characteristic decay time of turbulence. On the other hand, large flow scales (dominating the kinetic energy) evolve with a time scale comparable to the decay time, and hence pronounced anisotropy is observed instead [81]. Visible discrepancies between the reference data and the current results can be partly attributed to both the use of different time-stepping scheme and the round-off errors, where the latter can in turn result from, e.g., different standards or implementations of the floating-point arithmetic. The comparison between modern CPU's can be reassuring in this matter, see, e.g., Fig. 2.5. The current solution has been confirmed to be grid- and time-step-independent (not shown here).

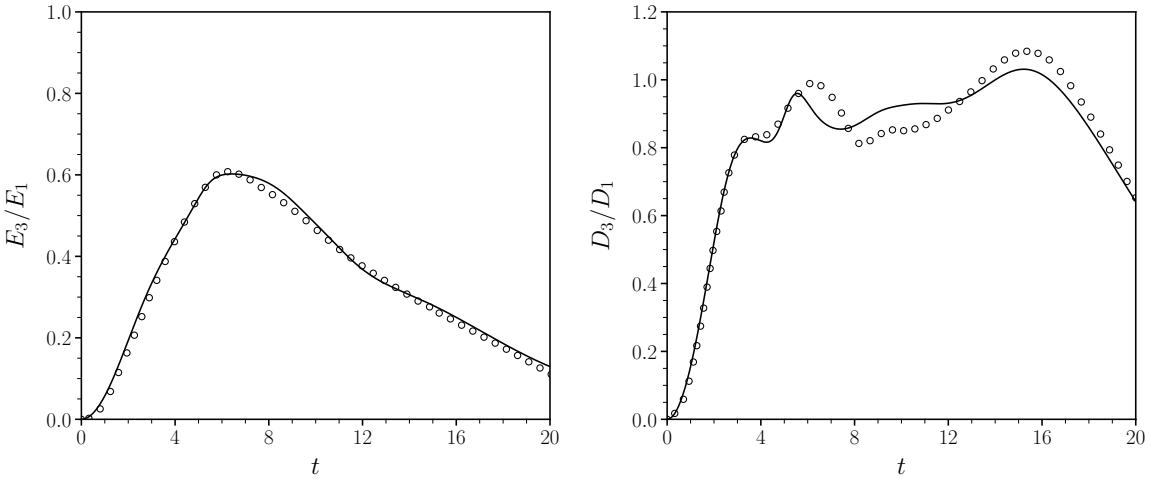

Figure 2.4: Anisotropy of the total kinetic energy (left panel) and its dissipation rate (right panel) at $Re = 200$; solid line denotes the current code; circles represent the reference data digitized and replotted from [81].

For completeness, some results were compared against the data reported by Dairay et al. [80] for a moderate Reynolds number, that is $Re = 1600$. In that work, the solenoidal Navier-Stokes equations were solved with the use of the 6^{th}-order compact finite difference on a uniform grid with the spatial resolution of 512^3 nodes. Time histories of both the turbulent kinetic energy and its dissipation rate are depicted in Fig. 2.5. Despite using a coarser grid ($N = 256$), an excellent quantitative agreement is readily observed. For this case additional tests were performed in order to quantify the impact of certain dealiasing approaches (spherical truncation, 2/3 rule, and phase-

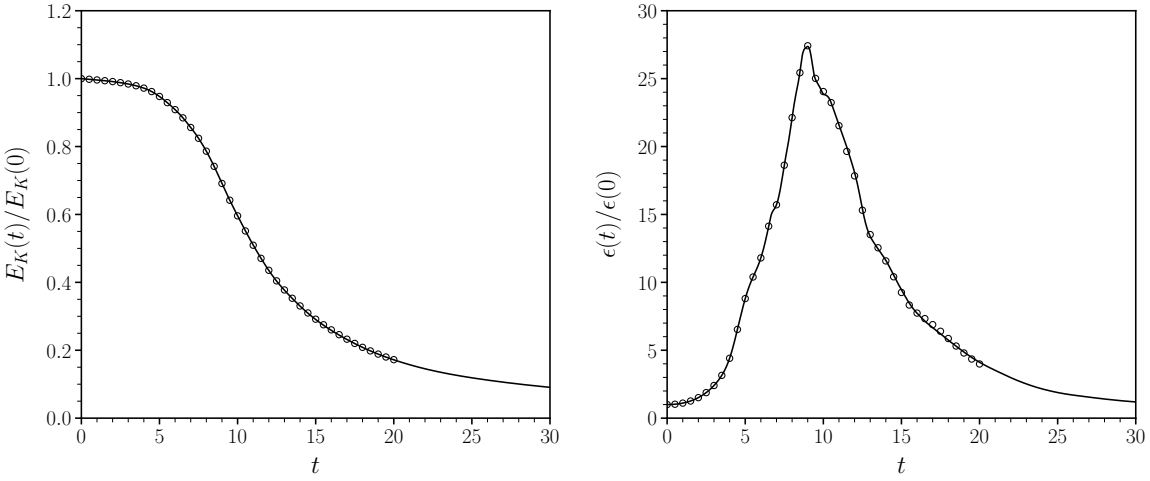

Figure 2.5: Time histories of the total kinetic energy (left panel) and its dissipation rate (right panel) at $Re = 1600$; solid line denotes the current code; circles represents the reference data replotted from [80].

shifting), however no significant differences were observed, say less than 5% (now shown here).

2.11 Forced isotropic turbulence

As indicated in Section 2.5, the forcing given by Eqs. (2.62) and (2.63) ensures appropriate small-scale resolution on condition that a reasonable value of $k_{\max}\eta$ is imposed. On the other hand, it appears to be of equal importance that the size of the computational box L_B is sufficient to accurately resolve all the energy-containing flow scales. Isotropic turbulence typically requires $L_B = 8L$ [2]. To the best of the author's knowledge, usually at most $L_B \approx 5L$ is reported, however without a thorough (if any) assessment of how it influences the simulated turbulence. According to Eq. (2.85), the integral length scale L can be adjusted by modifying the energy distribution among resolved flow scales. One way to achieve this is by applying the forcing to appropriately selected range of Fourier modes. Yeung & Pope [69] studied the Lagrangian statistics of various quantities in a statistically stationary isotropic turbulence. In that work, the forcing was restricted by either $k_{f,\max} = \sqrt{2}k_0$ or $k_{f,\max} = 2\sqrt{2}k_0$, and thus the energy was injected into respectively 18 and 92 Fourier modes. In other research studies, the forcing has equally often been restricted to the lowest two wavenumber shells for which $0.5 \leq |\boldsymbol{k}| < 1.5$ and $1.5 \leq |\boldsymbol{k}| < 2.5$, and therefore, when compared to Yeung & Pope, the total number of forced modes was reduced to 80, since $k_{f,\max} = \sqrt{6}k_0$.

To verify the large-scale resolution, one can consider different forcing configurations given in Table 2.1. Each turbulent flow was allowed to evolve in time for approximately $120T_e$, with flow parameters sampled every $T_s \approx 0.5T_e$. Basic flow statistics from selected simulations are given in Table 2.2. The reasons for particular selections are as follows: (i) cases 1 and 2 represent the forcing confined to the lowest resolved wavenumber shell, and thus are expected to provide the largest Reynolds number, or, in other words, the largest flow scale separation; (ii) case 6 corresponds

$k_{f,\min}$ \ $k_{f,\max}$	$\sqrt{1}$	$\sqrt{2}$	$\sqrt{3}$	$\sqrt{4}$	$\sqrt{5}$	$\sqrt{6}$	$\sqrt{8}$	$\sqrt{9}$	$\sqrt{10}$	$\sqrt{11}$	$\sqrt{12}$
$\sqrt{1}$	1	2	3	4	5	6	7	8	9	10	11
$\sqrt{2}$	-	12	13	14	15	16	17	18	19	20	21
$\sqrt{3}$	-	-	22	23	24	25	26	27	28	29	30
$\sqrt{4}$	-	-	-	31	32	33	34	35	36	37	38

Table 2.1: Test case IDs for different forced wavenumber bands confined to $k \in [k_{f,\min}, k_{f,\max}]$; other forcing parameters are $\epsilon_f = 0.3$, $k_{\max} = 30$, $k_{\max}\eta = 1.5$.

-	case 1	case 2	case 6	case 12	case 28
Re_λ	65	56	44	48	31
Re_L	133	110	83	87	50
Re_t	981	631	310	403	109
u'/u_η	4.97	4.63	4.11	4.30	3.46
T_e/τ_η	6.57	6.26	5.94	5.72	5.09
τ_t/τ_η	20.83	17.97	14.14	15.45	9.97
L/L_B	0.26	0.23	0.19	0.20	0.14
L/η	32.64	28.93	24.43	24.58	17.60
L_t/L_B	1.01	0.81	0.57	0.65	0.34
L_t/η	127.05	101.92	71.31	81.39	42.24
λ/L_B	0.13	0.12	0.10	0.11	0.09
λ/η	15.89	14.77	13.11	13.70	11.01
L_1/L_B	0.31	0.27	0.21	0.16	0.14
L_2/L_B	0.14	0.11	0.10	0.11	0.07
L_1/L_2	2.31	2.38	2.14	1.41	1.96
I	1.02	1.02	1.02	0.99	1.00
S	-0.39	-0.43	-0.48	-0.54	-0.50
F	4.46	4.33	4.23	4.27	3.98

Table 2.2: Basic flow statistics for different forced wavenumber bands; other forcing parameters are $\epsilon_f = 0.3$, $k_{\max}\eta = 1.5$, $k_{\max} = 30$.

to the frequently reported configuration in which the forcing is limited to the first two wavenumber shells, see, e.g., [67, 68, 82, 83, 84, 85, 86]; (iii) case 12 appears to be the recently favored configuration, see, e.g., [16, 18, 59, 87, 88] and the follow-up articles; (iv) case 28 represents the configuration which seems to provide the appropriate large-scale resolution. As initially expected, for a given spatial resolution, the highest Re_λ is obtained on condition that the forcing is confined to the lowest resolved wavenumber, that is k_0. This is consistent with the findings reported in [69].

As already indicated in Section 2.9, an artificial forcing applied to the largest resolved flow scales can lead to significant spatial correlations of the velocity field at large separations. It is therefore of great importance to ensure that both the longitudinal and transverse velocity autocorrelation functions vanish at distances comparable to $L_B/2$, or, in other words, to ensure that the turbulence (and thus also the dispersed phase) is not considerably affected by the unphysical periodic boundary conditions. From Fig. 2.6, it is readily apparent that the highest Re_λ is obtained at the expense of a significantly correlated velocity field. This issue can be mitigated by either extending the range of wavenumbers where the forcing is applied or shifting the energy injection toward higher wavenumbers; however, both approaches lower the achievable Reynolds number. While significantly better results can be obtained for the frequently

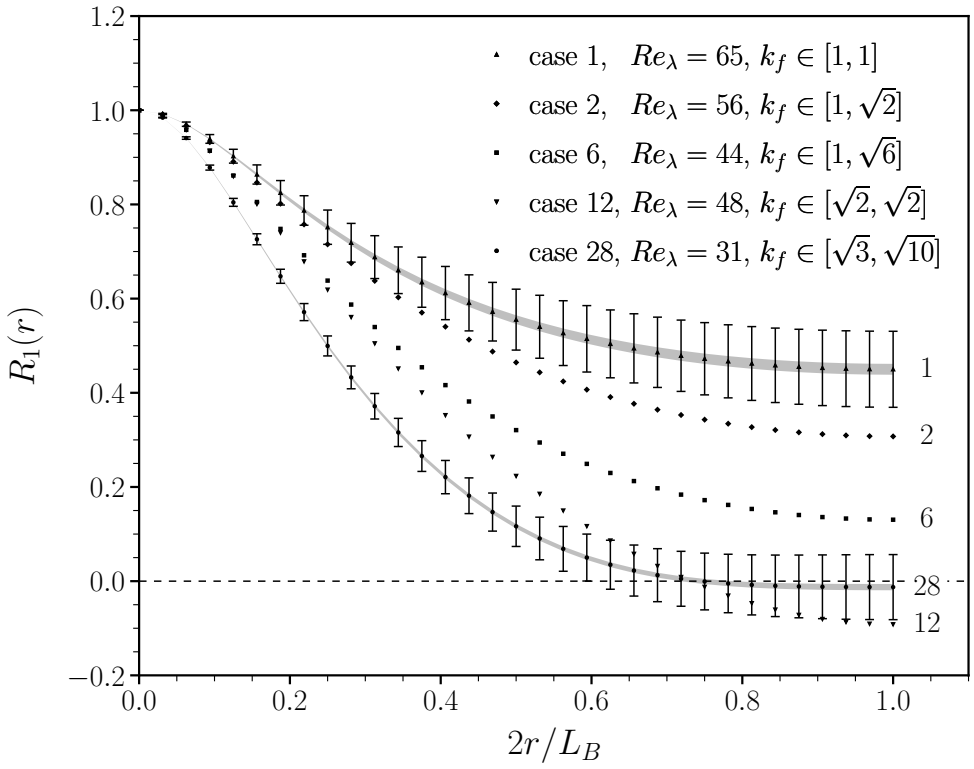

Figure 2.6: The impact of forcing on the longitudinal velocity autocorrelation function.

reported range of the forced Fourier modes, as given by case 6, the velocity field remains noticeably correlated at the maximum separation, thus leading to inaccurate estimation of the integral length scales given by Eq. (2.84). This can be considered less important insofar as the main objective is to statistically quantify the smallest resolved flow scales [69]. On the other hand, if particulate two-phase flows are considered, then an artificially correlated velocity field can have a non-negligible impact on particle trajectories. In fact, inertial particles exhibit a tendency to preferentially interact with specific range of flow scales that can be approximately identified based on the ratio of the particle-to-turbulence characteristic time scales. A more thorough discussion of this phenomenon is deferred until it becomes relevant. It is therefore somewhat surprising that in other similar research studies related to particulate two-phase flows, the authors do not thoroughly address the physical correctness of their results, while pushing numerical simulation codes to the limits of achievable Reynolds numbers, see, e.g., [67, 68, 83].

In a fully developed turbulence, the largest flow scales are not necessarily the most energetic ones. Therefore, shifting the forced wavenumber band toward smaller length scales is, to some extent, justified. Taking advantage of this fact, the forcing was limited to Fourier modes for which $\sqrt{3} \leq |\boldsymbol{k}| \leq \sqrt{10}$, see case 28 in Table 2.2.

This way, the integral length scale of turbulence can be significantly reduced, thus improving the large-scale resolution, see Fig. 2.6. It turns out that if appropriate spatial resolution is ensured on both ends of the resolved range of flow scales, then the longitudinal and transverse velocity autocorrelation functions take forms which are in excellent qualitative agreement with theoretical predictions based on the theory of homogeneous and isotropic turbulence [2], see Fig. 2.7.

In this work, despite ensuring a reasonable value of the integral length scale, i.e., $L/L_B \approx 0.2$ (one can recall that this value is often reported in the scientific literature), the ratio of integral length scales L_1/L_2 significantly deviates from its theoretical "isotropic" value, i.e., $L_1/L_2 = 2$ [89], with discrepancies significantly exceeding statistical uncertainties, compare cases 6 and 12 in either Fig. 2.6 or Table 2.2. These differences are usually attributed to either periodicity and statistical errors [69], or the anisotropy of the forcing [89]; however, in the author's view, the aforementioned explanations appear unsatisfactory and provide no insight into the issue. Although the instantaneous values of L_1 and L_2 can vary significantly, say up to 10%, both the respective mean values and the mean value of their ratio L_1/L_2 are determined with low uncertainties, that is less than approximately 2%. For this very reason, the

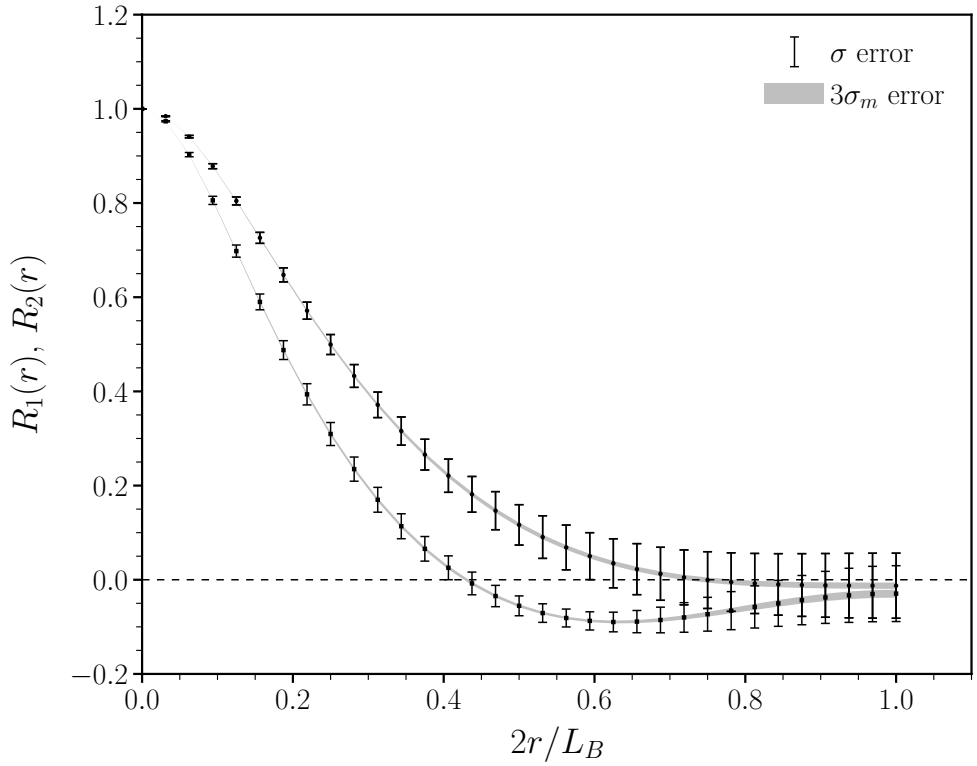

Figure 2.7: Longitudinal and transverse velocity autocorrelation functions at $Re_\lambda \sim 32$, case 28.

aforementioned discrepancies should not be attributed to statistical uncertainty (at least not exclusively). It should be noted that with improving large-scale resolution (reducing the integral length scale, while maintaining the spatial resolution constant), the ratio of L_1/L_2 converges to its theoretical value, with statistical uncertainty not exceeding 2%. To some extent, this confirms the stringent large-scale resolution requirement for isotropic turbulence given as $L_B = 8L$ [2].

Although in principle the deterministic forcing proposed in this work does not impose any preferred direction, some degree of anisotropy appears inevitable, particularly in the low-wavenumber range [69, 89]. From Fig. 2.8, it is readily apparent that the most pronounced deviation from isotropy can be observed for a relatively narrow range of wavenumbers, say $|\boldsymbol{k}|/k_{\max} \leq 0.15$. In general, it can be concluded that the impact of the artificial forcing vanishes relatively quickly with increasing wavenumber. Therefore, in this particular case, approximately 85% of the resolved flow scales exhibit a high degree of isotropy, essentially measured with the volume- and time-averaged isotropy coefficient given by Eq. (2.86). Interestingly, according to the results given in Table 2.2, the aforementioned measure of isotropy seems to be unaffected by the forcing, and thus possibly also by the large-scale resolution. This conclusion is actually quite confusing. To address this issue, one can note that for all

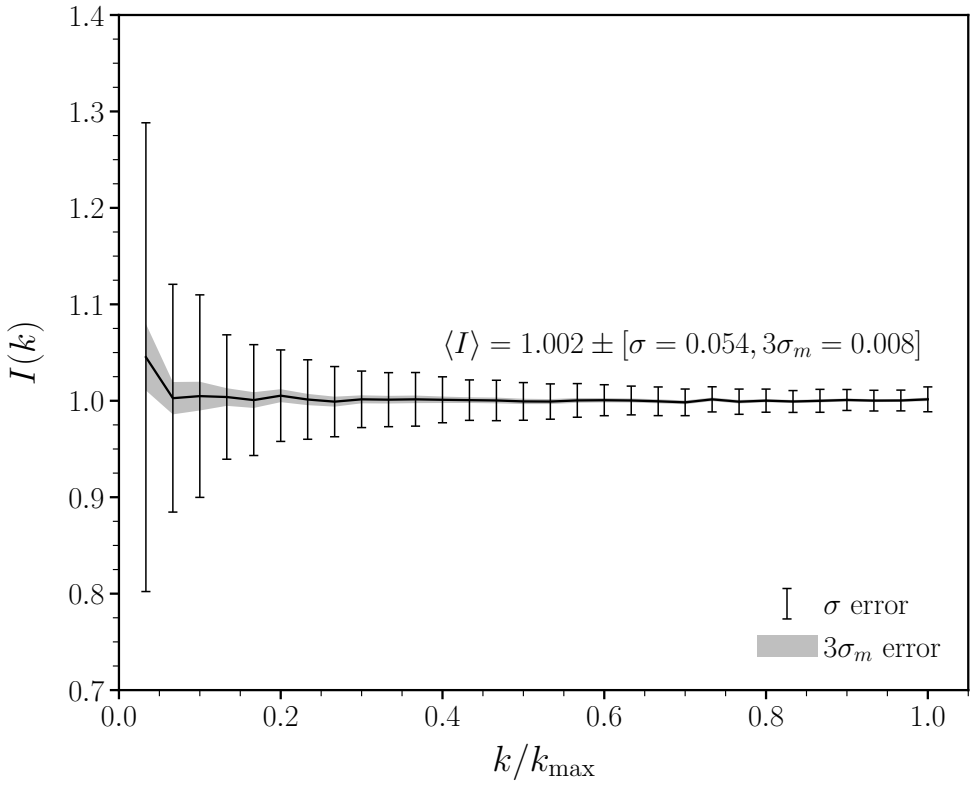

Figure 2.8: Isotropy spectrum function at $Re_\lambda \sim 32$, case 28.

considered simulations, the isotropy coefficient is, to a good approximation, $I = 1$, clearly indicating the equipartition of kinetic energy, and thus possibly also the absence of preferred directions; however, in most simulations, the ratio of L_1/L_2 differs from the theoretical prediction, with discrepancies reaching approximately 30%, see, e.g., case 12. Thus, somewhat contrary to the previous statement, the results may suggest considerable anisotropy. At this point, perhaps the most general conclusion is that in order to reliably assess the isotropy of simulated turbulence, one has to take into account multiple measures.

Consider the normalized energy spectrum function depicted in Fig. 2.9. It seems that the energy distribution among the approximately isotropic range of flow scales, that is $k\eta \geq 0.2$ or $k/k_{\max} \geq 0.15$ as in Fig. 2.8, remains unchanged regardless of the specific range of Fourier modes selected for the energy injection. Thus, it also seems that for a given spatial resolution, even a significant decrease in Re_λ (compare cases 1 and 28) is expected to have a minor impact on inertial particle statistics since, as is readily apparent, the range of the resolved flow scales essentially remains unchanged. The foregoing statement applies for those particles which are expected to preferentially interact with the specific range of flow scales, say these for which

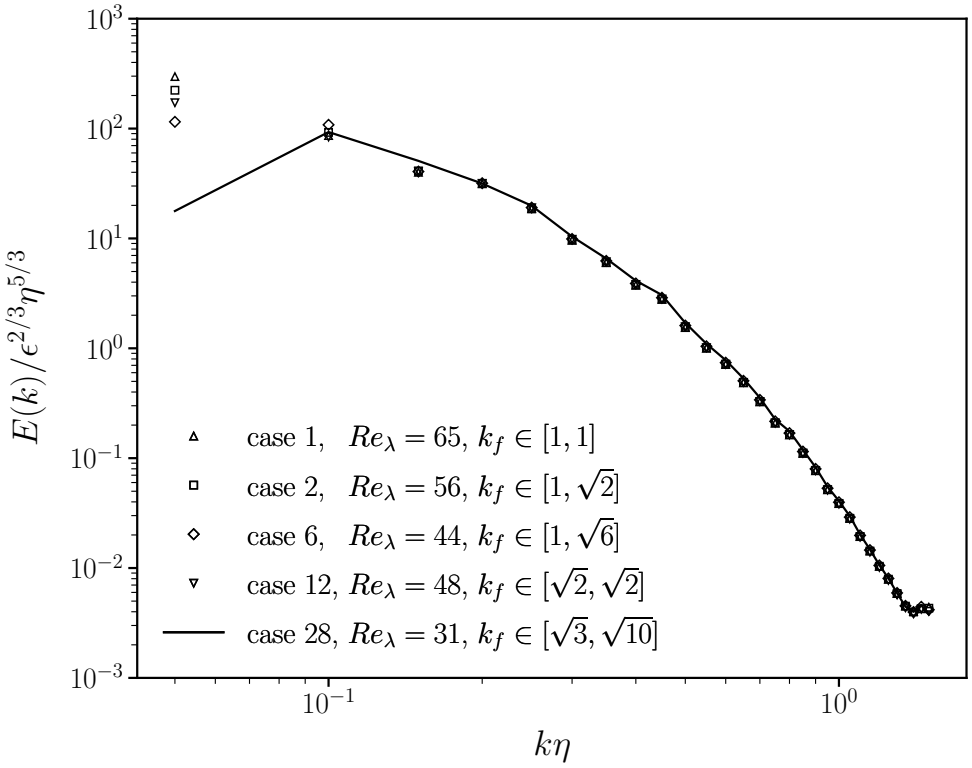

Figure 2.9: The impact of forcing on the energy distribution and the Taylor microscale Reynolds number.

$k\eta \geq 0.2$. To the best of the author's knowledge, in most research studies concerning the motion of inertial particles suspended in forced isotropic turbulence, the impact of the artificially forced Fourier modes on particle dynamics is neither removed nor even reduced. Based on the above reasoning, it seems that increasing the value of Re_λ at the expense of the quality of simulated turbulence is unjustified. In other words, it appears evident that for a given spatial resolution, pushing numerical simulations codes to the limits of achievable Reynolds numbers inevitably leads to artificially correlated velocity fields, which, in turn, can significantly distort particle statistics.

Once the appropriate range of Fourier modes intended for the energy injection had been successfully identified, and thus the forcing term had been fully defined, the final set of simulations was performed according to Table 2.3. By adjusting the energy injection rate ϵ_f, these simulations were parametrized to have the same turbulence intensity u' and small-scale resolution given as $k_{\max}\eta = 1.5$. It can be readily noticed that in this work, the highest achievable Taylor microscale Reynolds number is on

N	64	128	256	256†
Re_λ	32	56	94	112
Re_L	51	117	278	384
Re_t	127	411	1126	1610
ϵ_f	0.367	0.315	0.289	0.220
u'	0.75	0.76	0.75	0.75
u'/u_η	2.85	3.81	4.92	5.38
T_e/τ_η	6.25	8.04	11.49	13.24
τ_t/τ_η	12.21	21.81	36.36	43.54
$\tau_\eta/\Delta t$	51.54	73.97	108.04	118.45
L/L_B	0.142	0.122	0.112	0.141
L/η	17.84	30.66	56.56	71.27
L_t/L_B	0.34	0.41	0.43	0.57
L_t/η	42.67	101.85	219.22	287.25
λ/L_B	0.088	0.059	0.038	0.041
λ/η	11.05	14.77	19.06	20.86
L_1/L_B	0.146	0.119	0.110	0.139
L_2/L_B	0.070	0.059	0.055	0.069
L_1/L_2	2.090	2.029	2.004	2.033
I	1.002	1.016	1.001	0.986
S	-0.49	-0.50	-0.52	-0.52
F	4.01	4.57	5.29	5.49

† The forcing is restricted to Fourier modes for which $\sqrt{2} \leq |\boldsymbol{k}| \leq \sqrt{6}$

Table 2.3: Final set of simulations (DNS); other forcing parameters are $k_{\max}\eta = 1.5$, $k_{\max} = \lfloor\sqrt{2}N/3 + 0.5\rfloor$; $\nu = (\eta^4\epsilon_f)^{1/3}$; $\eta = k_{\max}\eta/k_{\max}$; all parameters were averaged over $\sim 100T_e$.

the order of $Re_\lambda \sim 100$. Due to the selected range of forced Fourier modes, i.e., those for which $\sqrt{3} \leq |\boldsymbol{k}| \leq \sqrt{10}$, the integral length scale approximately satisfies $L_B = 8L$ regardless of the spatial resolution N. One can also note that in all simulations both velocity autocorrelation functions take qualitatively correct forms, see Fig. 2.10, and thus the ratio of the corresponding integral length scales reaches its theoretical value for isotropic turbulence, that is $L_1/L_2 = 2$, with statistical uncertainty smaller than approximately 2%.

From Fig. 2.11 (left panel), it is apparent that for $Re_\lambda \sim 94$, the energy spectrum function approximately follows the Kolmogorov $k^{-5/3}$ scaling over $0.025 < k\eta < 0.1$, with the forcing imposed on $0.025 < k\eta < 0.04$. The referenced model spectrum function is given as

$$E_m(k) = C_K f_L(kL) f_\eta(k\eta) \epsilon^{2/3} k^{-5/3}, \tag{2.99}$$

where $C_K = 1.62$ is the Kolmogorov constant; $f_L(kL)$ and $f_\eta(k\eta)$ are non-dimensional functions, which determine the shape of both the energy-containing range and the dissipation one, respectively. Following Pope [2], f_L can be expressed as

$$f_L(kL) = \left\{ \frac{kL}{\left[(kL)^2 + c_L\right]^{1/2}} \right\}^{5/3+p_0}, \tag{2.100}$$

where $p_0 = 4$ and $c_L = 6.78$. The other function is given as

$$f_\eta(k\eta) = \exp\left\{ -\beta \left\{ \left[(k\eta)^4 + c_\eta^4\right]^{1/4} - c_\eta \right\} \right\}, \tag{2.101}$$

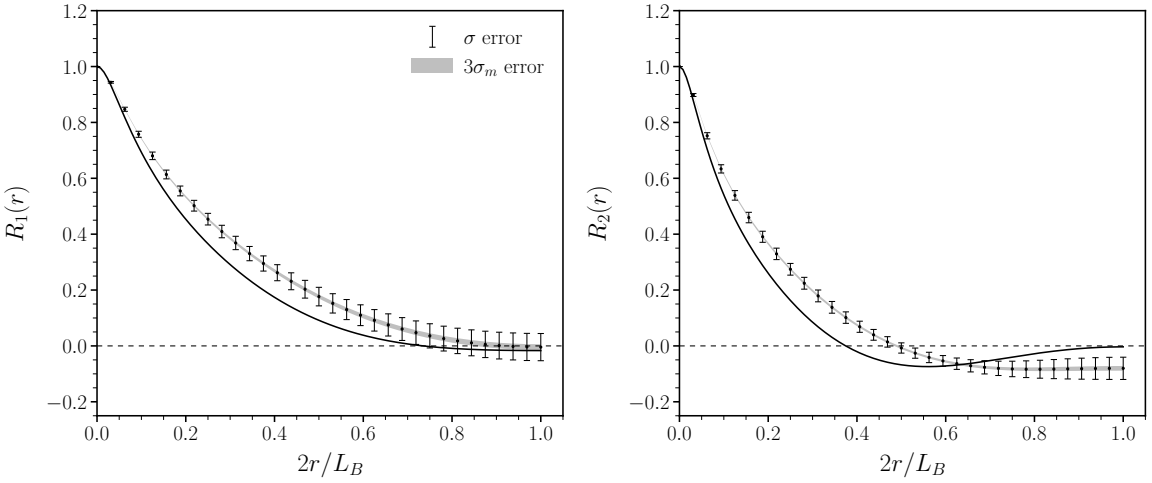

Figure 2.10: Velocity autocorrelation functions: longitudinal (left panel) and transverse (right panel); solid line – $Re_\lambda \sim 94$ with forcing restricted to $\sqrt{3} \leq |\boldsymbol{k}| \leq \sqrt{10}$; (•) – $Re_\lambda \sim 112$ with forcing restricted to $\sqrt{2} \leq |\boldsymbol{k}| \leq \sqrt{6}$.

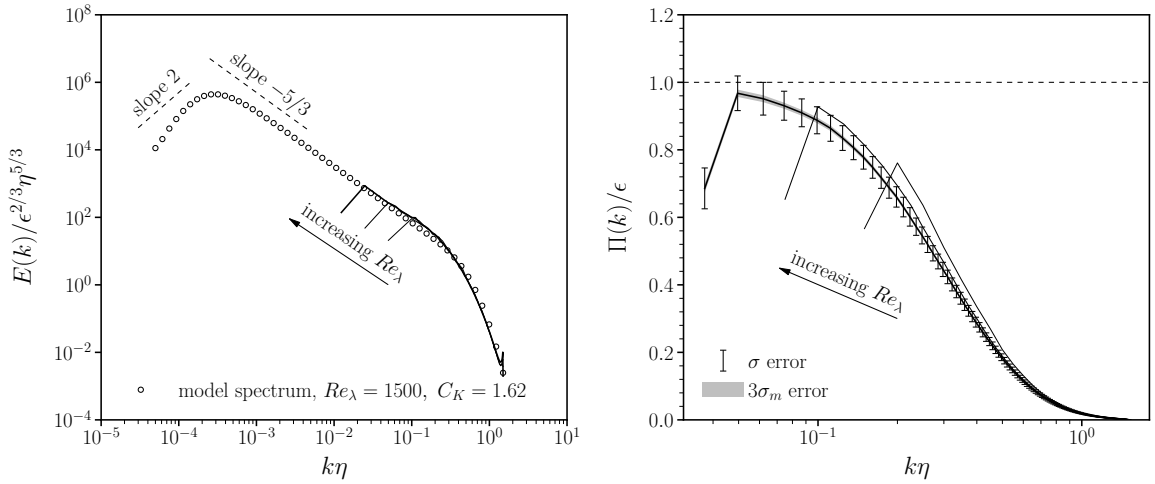

Figure 2.11: Energy (left panel) and energy flux (right panel) spectrum functions; thin line – $Re_\lambda \sim 32$, medium line – $Re_\lambda \sim 56$, and thick line – $Re_\lambda \sim 94$.

where $\beta = 5.2$ and $c_\eta = 0.4$. It should be emphasized that both constants c_L and c_η are determined so that the model spectrum $E_m(k)$ and the corresponding dissipation spectrum $D_m(k)$ integrate to E_K and ϵ, respectively. Based on a considerable body of numerical evidence, it can be concluded that the model spectrum correlates exceptionally well with experimental data, see, e.g., [90].

The width of the inertial subrange can be approximately estimated using the spectrum of the energy flux given as

$$\Pi(k_m) = \int_{k_m}^{\infty} T(k)\mathrm{d}k = -\int_{0}^{k_m} T(k)\mathrm{d}k, \tag{2.102}$$

which can be considered as the total rate of energy transfer per unit mass to all wavenumbers beyond a certain wavenumber k_m; $T(k)$ is the energy transfer function already introduced in Section 2.5. Within the inertial subrange, the energy is transferred independently of viscosity [91], and thus the scale-dependent energy flux $\Pi(k)$ becomes

$$\Pi(k) = \epsilon. \tag{2.103}$$

From Fig. 2.11 (right panel), it readily apparent that the Reynolds number, or, to be more specific, the separation of the resolved flow scales, is essentially too small for the inertial range to be fully developed. In fact, it becomes evident that the above condition, Eq. (2.103), is not satisfied within the range of Reynolds numbers achievable in this work. It should be once again emphasized that in the majority of either environmental or industrial turbulent flows, the Reynolds number based on the Taylor microscale is large, say on the order of $Re_\lambda \sim 10000$ rather than $Re_\lambda \sim 100$.

Therefore (unfortunately), it can be concluded that in this work, the DNS, with the maximum achievable spatial resolution of 256^3 nodes, can only capture the dissipation subrange of such turbulent flows, and, presumably, the onset of the inertial one.

From Table 2.3, it is readily apparent that the integral length scale L decreases by approximately 20% when the spatial resolution increases from $N = 64$ to $N = 256$. This presumably results from the fact that the energy distribution among the Fourier modes selected for the energy injection is not constrained, so to speak. To the best of the author's knowledge, in most research studies relevant to this work, forced isotropic turbulence is obtained using the top-bottom approach. This means that the energy distribution among the forced wavenumber band is either manually fixed or saturates solely due to both constant energy injection rate and the restriction of forcing to the largest resolved flow scales. On the other hand, due to the specific form of the forcing proposed in this work, recall Eqs. (2.62) and (2.65), the smallest resolved flow scales are constrained by imposing the specific value of $k_{\max}\eta$, while the large, energy-containing ones adjust accordingly (bottom-top approach). Therefore, with increasing Reynolds number the energy is distributed over a wider range of flow scales, causing the energy of the smallest resolved wavenumber shells to decrease. One can recall that the largest flow scales contribute most to estimating the integral length scale L, and thus the overall scale separation L/η becomes smaller than the expected. This essentially makes the DNS slightly less effective than it could be. On the other hand, by simply selecting different range of wavenumbers, the simulations can be parametrized so that the integral length scale remains approximately constant, compare cases $N = 64$ and $N = 256^{\dagger}$ in Table 2.3. Although the ratio of L_1/L_2 is almost unchanged, both velocity autocorrelation functions change qualitatively and quantitatively, with differences significantly exceeding statistical uncertainty, see Fig. 2.10 (both panels). Therefore, to avoid confusion and to achieve high-fidelity results, the aforementioned reduced efficiency of the DNS will be ignored, and hence all forcing parameters will remain constant throughout the remaining parts of this work.

For completeness, from Fig. 2.12, it can be readily observed that, even at low Reynolds numbers, the PDF of the second invariant of the velocity gradient tensor Q retains the non-Gaussian nature previously observed in other DNS studies. This clearly indicates the presence of intermittent regions of high vorticity and strain. With increasing Reynolds numbers, the intermittent regions become more intense, which usually results in broader tails of the PDF, so to speak. As will be discussed in Section 4.5, those intermittent regions of high vorticity and strain drive the non-trivial turbulence-particle interaction, and thus can have a significant impact on particle dynamics and the relevant statistics.

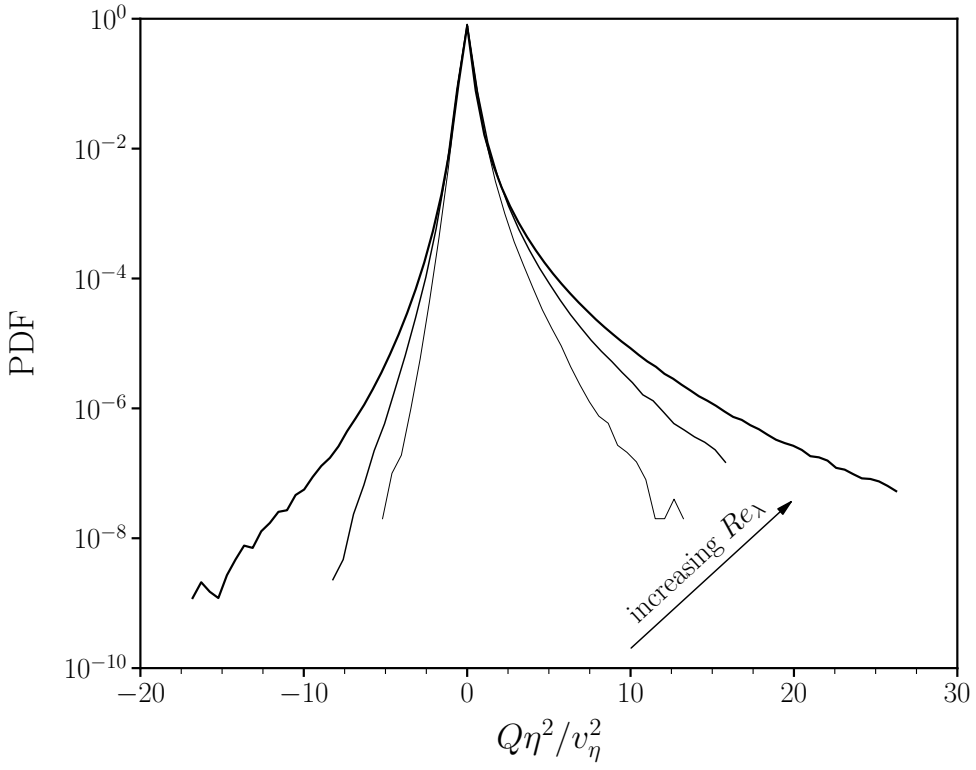

Figure 2.12: The probability density function of the second invariant of the velocity gradient tensor Q; thin line – $Re_\lambda \sim 32$; medium line – $Re_\lambda \sim 56$; thick line – $Re_\lambda \sim 94$.

2.12 Concluding remarks

This Chapter outlined the most important steps in developing an accurate pseudo-spectral DNS solver for isotropic turbulence. The purpose of this was as follows: (i) to provide a self-contained guideline and (ii) to revisit, emphasize and reassert good practices concerning the DNS; (iii) to develop an accurate tool for the research concerning the DNS of particle-laden isotropic turbulence; (iv) to gather the reference data for the research concerning both the single-phase LES and the particle-laden one. A summary of what appear to be the most important achievements and contributions of this part of the research is provided in the following paragraphs.

First, this Chapter provided a self-contained, detailed, organized and focused, hence, possibly also beginner-friendly, walk-through of the most important steps of the pseudo-spectral approximation to the solenoidal Navier-Stokes equations, particularly including relevant derivations and best practices concerning the DNS of isotropic turbulence. In the author's view, the descriptions of certain methodologies encountered in the scientific literature are often insufficiently detailed, or even superficial, thus making it challenging for the newcomers to catch up with the current state-of-

the-art in the matters of interest. This Chapter hopefully fills some of these gaps, and therefore also serves as an encouragement for others to learn by developing their own set of tools for the numerical modeling of turbulent flows.

Second, this Chapter elaborates on the well-known deterministic forcing first proposed in [55] and given by Eq. (2.62), where following a simple dimensional analysis, the required energy injection rate was expressed as $\epsilon_f = \nu^3\eta^{-4}$. However, to ensure the appropriate small-scale resolution, typically assessed using the well-established parameter $k_{\max}\eta > 1$, it has been proposed to express the kinematic viscosity of the fluid as $\nu = (\eta^4\epsilon_f)^{1/3}$, where the smallest resolved length scale can be estimated as $\eta = k_{\max}\eta/k_{\max}$. It has been pointed out that ϵ_f basically controls the turbulence intensity u', and therefore it has been argued that its adjustment is more intuitive than that of the kinematic viscosity. In all pseudo-spectral simulations $k_{\max}$ is usually constrained by the selected dealiasing strategy. Therefore, assuming the spherical truncation given by Eq. (2.52), in this work, the maximum resolved wavenumber was constrained by $k_{\max} = \lfloor\sqrt{2}N/3+0.5\rfloor$, where N is the number of nodes in each spatial direction and $\lfloor\cdot\rfloor$ denotes the largest integer smaller than or equal to a given number. The proposed parametrization ensures that for a given grid size N, the flow will adjust itself to maintain a proper resolution of the smallest, dissipative flow scales, however, on condition that a reasonable value of $k_{\max}\eta$ is imposed (Section 2.5, p. 21). It should be emphasized that well-established guidelines concerning the selection of the resolution parameter are readily available in the scientific literature. To the best of the author's knowledge, the proposed parametrization has not been reported by now, even though it appears to be straightforward and obvious. Probably the most important contribution from this part of the research involves a thorough assessment of the impact of the selected range of forced wavenumbers $k \in [k_{f,\min}, k_{f,\max}]$ on the simulated turbulence. It has been concluded that frequently reported configurations (i) artificially increase the Taylor microscale Reynolds number, leading to false conclusions regarding the actual resolving capacity of the pseudo-spectral DNS (Section 2.11, p. 40), and (ii) cause a pronounced mismatch between the largest flow scales and the size of the computational box, leading to artificially correlated velocity fields. Presumably due to historical reasons, and perhaps also the willingness to achieve the highest possible Reynolds numbers, the forcing is usually confined to either $|\boldsymbol{k}| < \sqrt{6}k_0$ or $|\boldsymbol{k}| < 2\sqrt{2}k_0$, and recently also $|\boldsymbol{k}| = \sqrt{2}k_0$. This causes both the longitudinal and transverse velocity autocorrelation functions to take incorrect forms, specifically not vanishing at length scales comparable to half of the computational box. In addition to that, in such cases, the ratio of the corresponding integral length scales L_1/L_2 significantly deviates from 2, i.e., a well-known value in isotropic turbulence (Section 2.11,

p. 37). This issue has not been rigorously studied by now; however, a limited scientific literature attributes this discrepancy to periodicity, statistical uncertainty, and, to some extent, the anisotropy of the forcing. It has been shown that: (i) the periodicity seems to be the only reason of the foregoing deficiencies; (ii) what appears to be the universal configuration, i.e., $\sqrt{3} \leq |\boldsymbol{k}| \leq \sqrt{10}$, ensures, to a good approximation, that both longitudinal and transverse velocity autocorrelation functions vanish at the maximum separation. In addition to that, the ratio of the corresponding integral length scales reaches the value of $L_1/L_2 = 2$, with statistical uncertainty not exceeding 2%. It has been concluded that: (i) the aforementioned parametrization of adjustable forcing parameters ensures the time-averaged energy dissipation rate $\langle\epsilon\rangle$ matches the imposed energy injection rate ϵ_f, with statistical uncertainty below 2%; (ii) the results are in excellent agreement with theoretical predictions based on a simple dimensional analysis following from the Kolmogorov theory of turbulence. For this very reason, not only the relevant forcing parameters but also certain parameters statistically quantifying the simulated turbulence can be estimated *a priori*, essentially removing the need for any prior time-consuming numerical testing and adjustments.

Third, it has been pointed out that exclusively due to floating-point arithmetic, it is not guaranteed that the sum of two solenoidal vector fields remains divergence-free over a long period of time. Therefore, it seems that solely due to improper order of computation in the time-stepping algorithm, the velocity field eventually ceases to satisfy the continuity equation. Although the time-stepping algorithm essentially circumventing this issue had been proposed in [52], in this dissertation, it has been shown that the floating-point arithmetic can still cause an unphysical evolution of the velocity field, even if the continuity equation is satisfied with machine precision (Section 2.7, p. 24). It has been concluded that due to uncontrolled round-off errors in a three-dimensional DFT, specific Fourier modes cease to satisfy the Hermitian symmetry. It has been shown that this issue can be fully fixed once that property is enforced each time Fourier modes are modified in some way, e.g., through addition, subtraction or multiplication (Section 2.7, p. 26). One (and possibly the most efficient) way to accomplish this is by averaging the real and imaginary parts of specific Fourier modes constituting the Hermitian symmetry pairs.

Fourth, upon successful validation, it has been concluded that the newly developed pseudo-spectral solver provides accurate and, most importantly, physically correct results, thus providing a reliable reference for the research concerning the LES modeling. It is worth mentioning that the majority of pseudo-spectral solvers for the solenoidal Navier-Stokes equations employ the algorithms, libraries and numerical methods that have already been extensively tested over the years in terms of their accuracy and

efficiency. Therefore, the aforementioned validation was focused rather on verifying the actual implementation of the relevant algorithms.

Chapter 3

Large Eddy Simulations of isotropic turbulence

3.1 Equations of fluid motion in physical space

It is well established that a time-dependent, three-dimensional solution of the Navier-Stokes equations explicitly accounts for all scales of fluid motion, which in general range from the large, energy-containing ones[1] to the smallest, which eventually vanish due to viscous dissipation. In a turbulent flow at high Reynolds number, the range of resolved flow scales can be estimated as

$$\frac{L_t}{\eta} \sim \frac{L_t}{(\nu^3/\epsilon)^{1/4}} = Re_t^{3/4}, \tag{3.1}$$

where L_t and Re_t are the turbulence length scale and the corresponding Reynolds number, respectively, see also Section 2.8. This essentially means that the total number of spatial degrees of freedom in a three-dimensional turbulent flow is on the order of $\mathcal{O}(Re_t^{9/4})$ [92]. Despite significant developments in both computer technology and numerical methods, the resolution of all scales of fluid motion at Reynolds numbers relevant to various environmental phenomena and industrial processes has yet to be attained; however, at this point in time, it appears unfeasible in the near (or perhaps even distant) future.

Fortunately, it is the large flow scales that usually provide a useful prediction of turbulent transport of either momentum or heat [1]. It should be emphasized that the motion of large flow scales strongly depends on specific physical conditions and/or geometrical constraints associated with a given turbulent flow. For this reason, such flow scales should always be resolved explicitly to the extent possible. On the other

[1]Usually constrained by either the boundaries or periodic boundary conditions as in this work

hand, it should be emphasized that with increasing scale separation, and consequently the Reynolds number, see Eq. (3.1), the smallest (dissipative) flow scales are expected to display universal scaling properties regardless of the complexity of a turbulent flow [93]. For this reason, the velocity field can be spatially filtered, thus reducing the computational cost of the simulation. As will be seen shortly, the overall impact of unresolved (filtered out) flow scales on the resolved ones has to be accounted for, at least statistically.

Leonard [94] introduced the filtering operation given as

$$\overline{u}_\alpha(\boldsymbol{x},t) = \int G_\alpha(\boldsymbol{x}-\boldsymbol{x}')u_\alpha(\boldsymbol{x}')\mathrm{d}\boldsymbol{x}', \tag{3.2}$$

where the overline denotes the filtered quantity; G is a compactly supported filter of width Δ, which additionally satisfies the normalization condition expressed as

$$\int G_\alpha(\boldsymbol{x}-\boldsymbol{x}')\mathrm{d}\boldsymbol{x}' = 1. \tag{3.3}$$

Applying the above filtering to the Navier-Stokes equations in the form given by Eq. (2.10), and taking advantage of Eq. (2.16), one obtains

$$\overline{\frac{\partial u_\alpha}{\partial t}} + \overline{\frac{\partial u_\alpha u_\beta}{\partial x_\beta}} = -\frac{1}{\rho}\frac{\partial \overline{p}}{\partial x_\alpha} + \nu\overline{\frac{\partial^2 u_\alpha}{\partial x_\beta \partial x_\beta}}, \tag{3.4}$$

where without loss of generality $f_\alpha = 0$ for $\alpha = 1,2,3$ is assumed. The filtering can be simultaneously applied to the continuity equation, Eq. (2.2), to give

$$\overline{\frac{\partial u_\alpha}{\partial x_\alpha}} = 0. \tag{3.5}$$

Insofar as the filter width remains constant throughout the entire computational domain, the filtering operator commutes with both temporal and spatial derivatives to give

$$\frac{\partial \overline{u}_\alpha}{\partial t} + \frac{\partial \overline{u_\alpha u_\beta}}{\partial x_\beta} = -\frac{1}{\rho}\frac{\partial \overline{p}}{\partial x_\alpha} + \nu\frac{\partial^2 \overline{u}_\alpha}{\partial x_\beta \partial x_\beta}, \tag{3.6}$$

and

$$\frac{\partial \overline{u}_\alpha}{\partial x_\alpha} = 0, \tag{3.7}$$

where the non-linear term in the momentum balance equation requires further attention.

In general, the filtering decomposes the velocity field according to

$$u_\alpha(\boldsymbol{x},t) = \overline{u}_\alpha(\boldsymbol{x},t) + u'_\alpha(\boldsymbol{x},t), \tag{3.8}$$

where the second term on the right-hand side is referred to as the residual velocity field. With the use of Eq. (3.8), the filtered product $\overline{u_\alpha u_\beta}$ can be rewritten as

$$\overline{u_\alpha u_\beta} = \overline{\overline{u}_\alpha \overline{u}_\beta} + \overline{\overline{u}_\alpha u'_\beta} + \overline{u'_\alpha \overline{u}_\beta} + \overline{u'_\alpha u'_\beta} \approx \overline{u}_\alpha \overline{u}_\beta + \overline{u'_\alpha u'_\beta}. \tag{3.9}$$

Thereafter, introducing the so-called residual stress tensor $\tau_{\alpha\beta} = \overline{u_\alpha u_\beta} - \overline{u}_\alpha \overline{u}_\beta$, the filtered momentum balance equation given by Eq. (3.6) can be rewritten so as to describe the evolution of large flow scales

$$\frac{\partial \overline{u}_\alpha}{\partial t} + \frac{\partial \overline{u}_\alpha \overline{u}_\beta}{\partial x_\beta} = -\frac{1}{\rho}\frac{\partial \overline{p}}{\partial x_\alpha} + \nu \nabla^2 \overline{u}_\alpha - \frac{\partial \tau_{\alpha\beta}}{\partial x_\beta}, \tag{3.10}$$

where $\tau_{\alpha\beta}$ has to be expressed in terms of the resolved velocity field components. It is worth noting that other decompositions exist. For instance, Leonard [94] proposed to express the residual stress tensor as a sum of three components stresses given as

$$\tau_{\alpha\beta} = L_{\alpha\beta} + C_{\alpha\beta} + R_{\alpha\beta}, \tag{3.11}$$

where $L_{\alpha\beta} = \overline{\overline{u}_\alpha \overline{u}_\beta} - \overline{u}_\alpha \overline{u}_\beta$, $C_{\alpha\beta} = \overline{\overline{u}_\alpha u'_\beta} + \overline{u'_\alpha \overline{u}_\beta}$, and $R_{\alpha\beta} = \overline{u'_\alpha u'_\beta}$ are called respectively the Leonard, cross, and "subgrid-scale" Reynolds stresses [2]. As indicated by Speziale [95], the Leonard and cross terms are not Galilean-invariant, and thus usually a different decomposition is preferred. To get a more thorough insight into the issue, one can refer to [96].

For completeness, it is worth mentioning the somewhat pioneering work of Smagorinsky [97] who was the first one to close the equations for the filtered velocity field given by Eq. (3.10). Following the general eddy-viscosity concept, the traceless part of the residual stress tensor can be assumed proportional to the resolved strain rate to give

$$\tau_{\alpha\beta} - \frac{1}{3}\delta_{\alpha\beta}\tau_{\gamma\gamma} = -2\nu_e \overline{S}_{\alpha\beta}, \tag{3.12}$$

where $\overline{S}_{\alpha\beta}$ is defined as in Eq. (2.5), except that u_α is replaced with its filtered counterpart; ν_e is an eddy-viscosity, which, following Smagorinsky, can be expressed as

$$\nu_e = (C_s \Delta)^2 \sqrt{2\overline{S}_{\alpha\beta}\overline{S}_{\alpha\beta}}, \tag{3.13}$$

where C_s is a model constant, which in the case of homogeneous and isotropic tur-

bulence takes the value of 0.18 [98]. However, some adjustments may be required depending on the type of the flow [99]. Finally, it should be emphasized that despite its simplicity, the model of Smagorinsky turned out to be the starting point for the development of more advanced residual closures [2, 100].

3.2 Problem statement

As already indicated, the equations governing the motion of large flow scales given by Eqs. (3.7) and (3.10), can be obtained by applying the spatial filtering to the Navier-Stokes equations. The width of the filter is usually selected so as to resolve all the relevant physical features; however, in some cases, it can be almost exclusively constrained by the available computational resources. To get acquainted with different forms of filter functions (of which the box, Gaussian and spectral filters are the most popular ones), one can refer to [2], Section 13.2.2. However, in practice, the spatial filtering is usually applied implicitly by coarsening (with respect to the corresponding DNS) the grid on which the governing equations are solved. In this case, the filter width Δ becomes comparable to the grid spacing. Although the spatial filtering significantly reduces the computational cost of the simulation, additional terms are introduced, which, in practice, require modeling in order to close the equations governing the motion of large flow scales. Different residual (or "subgrid-scale") models can be roughly divided into functional and structural ones [101].

The first group of subgrid-scale models associates all eddy-viscosity-based closures and essentially aims at providing (at least statistically) the transfer of energy from the resolved flow scales to the residual ones at approximately correct rate. The model of Smagorinsky, although being extensively used over the years, see, e.g., [102, 103, 104], is strictly dissipative and yields $\nu_e > 0$ even in laminar flows. Hence, it is not appropriate for, e.g., modeling the laminar-turbulent transition in a boundary-layer, and essentially requires additional adjustments near the wall [1]. To account for the aforementioned deficiencies, Germano et al. [105] proposed a dynamic evaluation of the model parameter C_s, see Eq. (3.13), by introducing an additional filtering of the resolved velocity field. The primary advantages of this approach are that: (i) the model does not contain any adjustable parameters; (ii) C_s becomes dependent on space and time. In addition to that, its value is reduced near the walls and, most importantly, vanishes for well resolved laminar flows. However, C_s exhibits large oscillations, and therefore has to be averaged over homogeneous directions [106]. The model was further generalized for compressible turbulence and scalar transport by Moin et al. [107]. Subsequently, Lilly [108] proposed the evaluation of C_s using the

least-squares method[2]. For completeness, it should be indicated that Ghosal et al. [56] further extended the model to account for inhomogeneous flows.

The second group concerns the models which primarily aim at generating the residual velocity field based on the filtered one. Such a semi-synthetic field is most often used to determine the residual stress tensor, essential for closing the equations governing the large-scale velocity field, see Eq. 3.10. Bardina et al. [109] proposed a scale-similarity model in which the residual stress tensor is approximated assuming equality between the smallest resolved and the largest residual flow scales. This assumption eventually leads to $\tau_{\alpha\beta} \approx \overline{\overline{u}_\alpha \overline{u}_\beta} - \overline{\overline{u}}_\alpha \overline{\overline{u}}_\beta$. The model accounts for the backscatter (backward energy transfer from small to large flow scales); however, the subgrid-scale dissipation turns out to be underestimated. For this reason, the scale-similarity model is usually combined with the model of Smagorinsky. Stolz & Adams [110] introduced the so-called approximate deconvolution method in which a truncated series expansion of the inverse filter operator is used to obtain an approximation of the residual velocity field. The method does not explicitly account for the residual flow scales, and hence only those of size comparable to the filter width are enhanced. Domaradzki proposed the so-called velocity estimation procedure developed in both Fourier [111] and physical spaces [112]. In this approach, the residual stress tensor is estimated with the use of the filtered velocity field enriched with the subgrid-scale components approximated at length scales two times smaller than the filter width. Scotti & Meneveau [113] determined the residual stress tensor with the use of a synthetic residual velocity field obtained through the so-called fractal interpolation. In their approach the resolved velocity field is iteratively mapped to scales much smaller than the filter width. It should be noted that the model turns out to be sufficiently dissipative as well as yields good correlations between the actual (determined from the spectrally-filtered DNS) and modeled subgrid-scale quantities. Yet another, recently favored class of models concerns the so-called spectral enrichment based on either dynamically adjusted differential filters [114, 115] or Gabor modes [116, 117]. Although being partly successful in predicting specific flow statistics, and sometimes referred to as "simple", these models not only appear to pose a significant entry barrier due to their complexity, but also introduce a non-negligible computational overhead, which, to some extent, may hinder their implementation, and thus possibly also discourages one from their further development. Recently, Hausmann et al. [118] developed a model based on the linearized momentum balance equations governing the subgrid-scale velocity field. These equations are essentially solved within statistically homogeneous subdomains; however, this approach implies the need for additional interpolation between

[2]In fact, these days the model is often called the Germano-Lilly dynamic subgrid-scale model

the subdomains to ensure continuous and solenoidal small-scale turbulence. When compared to the reference DNS, the spectrally-enriched LES predicts exceptionally well the PDF of (i) the second invariant of the velocity gradient tensor and (ii) the longitudinal and transverse velocity gradients. As pointed out by the authors, a few adjustable model parameters turn out to be of limited importance and the computational cost of the simulation increases at most by a factor of 2 when compared to pure LES. To eliminate the need for additional interpolation, Hausmann et al. [119] proposed to use the wavelet vector basis with coefficients determined using the local least squares so that a continuous and solenoidal subgrid-scale velocity field is obtained. The modified approach increases the computational cost of the simulation by a factor of 4 when compared to pure LES. The new model accurately predicts not only specific flow statistics in homogeneous and isotropic turbulence but also the spatial velocity correlations in a turbulent shear flow.

3.3 *A priori* Large Eddy Simulations

The effect of filtering (or filter width, to be more specific) can be conveniently quantified using explicitly filtered Navier-Stokes equations. This approach is most often referred to as either filtered DNS (FDNS) or *a priori* LES. In Fourier space, the filtering usually takes the form of a sharp spectral filter given as

$$\hat{\overline{u}}_\alpha(\boldsymbol{k},t) = \begin{cases} \hat{u}_\alpha(\boldsymbol{k},t), & k \leq k_c, \\ 0, & \text{otherwise}, \end{cases} \tag{3.14}$$

where k_c is a hypothetical (virtual) cutoff wavenumber, which essentially implies that $\Delta \sim k_c^{-1}$. It should be emphasized that in this approach, the numerical solution of the governing equations explicitly accounts for all scales of fluid motion. The only feature that distinguishes the FDNS from the DNS is that instead of the full velocity field (as it is the latter case), the filtered one, i.e., $k \leq k_c$, is used to statistically quantify the simulated turbulence. In the case of particulate two-phase flows, the filtered fluid velocity is used to solve the particle equation of motion. Therefore, the FDNS can be considered, in some sense, the LES devoid of (subgrid-scale) modeling errors.

3.4 Equations of fluid motion in Fourier space

Before introducing the filtered Navier-Stokes equations in Fourier space, one can consider the energy balance equation given as

$$\left[\frac{\partial}{\partial t} + 2\nu k^2\right] E(k) = T(k), \qquad k \leq k_{\max}, \tag{3.15}$$

where $W(k) = 0$ is assumed without the loss of generality, see also Eq. (2.57). Using the hypothetical spectral cutoff $k_c \in [k_0, k_{\max}]$, the energy balance equation can be rewritten as

$$\left[\frac{\partial}{\partial t} + 2\nu k^2\right] E(k) = T_{<k_c}(k) + T_{>k_c}(k), \qquad k \leq k_{\max}, \tag{3.16}$$

where $T_{<k_c}(k)$ denotes the total contribution to $T(k)$ from triads $(\boldsymbol{k}, \boldsymbol{p}, \boldsymbol{q})$ such that $|\boldsymbol{k}|, |\boldsymbol{p}|, |\boldsymbol{q}| < k_c$, or, in other words, the energy transfer among the resolved flow scales; $T_{>k_c}(k)$ is thence the kinetic energy transfer across k_c, i.e., associated with triads $(\boldsymbol{k}, \boldsymbol{p}, \boldsymbol{q})$ for which $|\boldsymbol{k}| < k_c$, and either $|\boldsymbol{p}|$ or $|\boldsymbol{q}| > k_c$ [1]. Kraichnan [91] proposed to express the second term on the right-hand side of Eq. (3.16) as

$$T_{>k_c}(k) = -2\nu_e(k; k_c) k^2 E(k), \tag{3.17}$$

where $\nu_e(k; k_c)$ denotes the spectral eddy-viscosity acting on the resolved flow scales due to the non-linear interactions with the residual ones; therefore, it is equally often referred to as effective eddy-viscosity. With the substitution of Eq. (3.17) into Eq. (3.16), one obtains the filtered energy balance equation given as

$$\left(\frac{\partial}{\partial t} + 2\Big[\nu + \nu_e(k; k_c)\Big] k^2\right) E(k) = T_{<k_c}(k), \qquad k \leq k_c, \tag{3.18}$$

where the functional form of $\nu_e(k; k_c)$ has to be determined.

Chollet & Lesieur [120] proposed to use the spectral eddy-viscosity in the filtered Fourier-transformed Navier-Stokes equations to give[3]

$$\left(\frac{\partial}{\partial t} + \Big[\nu + \nu_e(k; k_c)\Big] k^2\right) \hat{\overline{u}}_\alpha = P_{\alpha\beta} \hat{\overline{N}}_\beta + \hat{f}_\alpha, \tag{3.19}$$

[3]One can note the effortless implementation of the time-stepping scheme for the filtered velocity field when compared to the DNS, see Section 2.7

with the spectral eddy-viscosity expressed as

$$\nu_e(k;k_c,t) = \nu_e^+(k;k_c)\left[\frac{E(k_c,t)}{k_c}\right]^{1/2}, \tag{3.20}$$

where $E(k_c)$ is the energy spectrum evaluated at the cutoff. Assuming that k_c lies deep in the inertial subrange and using the Eddy-Damped-Quasi-Normal Markovian approximation (see also [121]) to compute the subgrid-scale energy transfers, the authors estimated the functional form of $\nu_e^+(k;k_c)$ and indicated that it reaches a positive plateau for $k \lessapprox 0.3k_c$ with $\nu_e^+(0) = 0.267$ [120]; however, due to incomplete triad interactions as first pointed out by Kraichnan [91], $\nu_e^+(k;k_c)$ exhibits a strong cusp in the vicinity of the spectral cutoff. As indicated in [122], "the constants and the form of $\nu_e^+(k;k_c)$ need to be determined by E.D.Q.N.M. or some other theory". This presumably allows for a certain degree of flexibility in determining the non-dimensional eddy-viscosity. In this work, it is essentially expressed as in [123] to give

$$\nu_{e,s}^+(k;k_c) = C_K^{-3/2}(0.441 + 15.2e^{-3.03k_c/k}), \tag{3.21}$$

where C_K is the Kolmogorov constant set equal to 1.4 in order to approximately match the spectral eddy-viscosity reported in [124]

$$\nu_{e,s}(k;k_c,t) = \left(0.267 + 9.21e^{-3.03k_c/k}\right)\left[\frac{E(k_c,t)}{k_c}\right]^{1/2}, \tag{3.22}$$

hereinafter referred to as the standard eddy-viscosity or, simply, as the standard model. For completeness, it should be emphasized that the functional form given by Eq. (3.21) appears somewhat unfortunate, in the sense that it may suggest that C_K can take arbitrary values. In fact, many authors use it solely as a means of reducing the discrepancies between the DNS and the LES, which inevitably leads to bizarre values of the Kolmogorov constant, see, e.g. [37, 40, 66, 82]. A more detailed discussion of this issue is given in Section 5.3.

In general, as indicated by Lesieur & Métais [122], the model "gives reasonably good results for isotropic turbulence". In particular, the kinetic energy is drained from the filtered flow scales at approximately correct rate [120, 124]. In addition to that, Chollet [125] justified the use of the model on condition that the cutoff wavenumber k_c is sufficiently separated from both the large, energy-containing flow scales and the smallest resolved ones. On the other hand, this naturally raises questions regarding the legitimacy of using the spectral eddy-viscosity proposed by Chollet & Lesieur in isotropic turbulence at low Reynolds numbers.

To the best of the author's knowledge, despite significant developments in high-performance computing, the highest reported to date Taylor microscale Reynolds number in DNS of single-phase isotropic turbulence is on the order of $Re_\lambda \sim 1200$, while maintaining a reasonable small-scale resolution, that is $k_{\max}\eta \geq 1.5$, see, e.g., [126, 127, 128, 129]. It is also worth mentioning that Ishihara et al. [130] reported $Re_\lambda \sim 2300$, however with arguably insufficient small-scale resolution, i.e., $k_{\max}\eta \sim 1$. Recently, Yeung et al. [131] reported initial attempts to simulate isotropic turbulence at $Re_\lambda \sim 2500$. Due to limited computational resources, the highest achievable Reynolds number in this work is typically on the order of $Re_\lambda \sim 100$. As already indicated, in this case the inertial subrange is barely developed (if at all). Interestingly, the pseudo-spectral LES was mostly used to simulate isotropic turbulence at similar Reynolds numbers [37, 82] or higher, yet typically not exceeding $Re_\lambda \sim 200$ [40, 66], see also Fig. 3.1 for a visual comparison. Although in such cases the spectral cutoff may be sufficiently separated from the largest forced wavenumber, it is relatively close to the

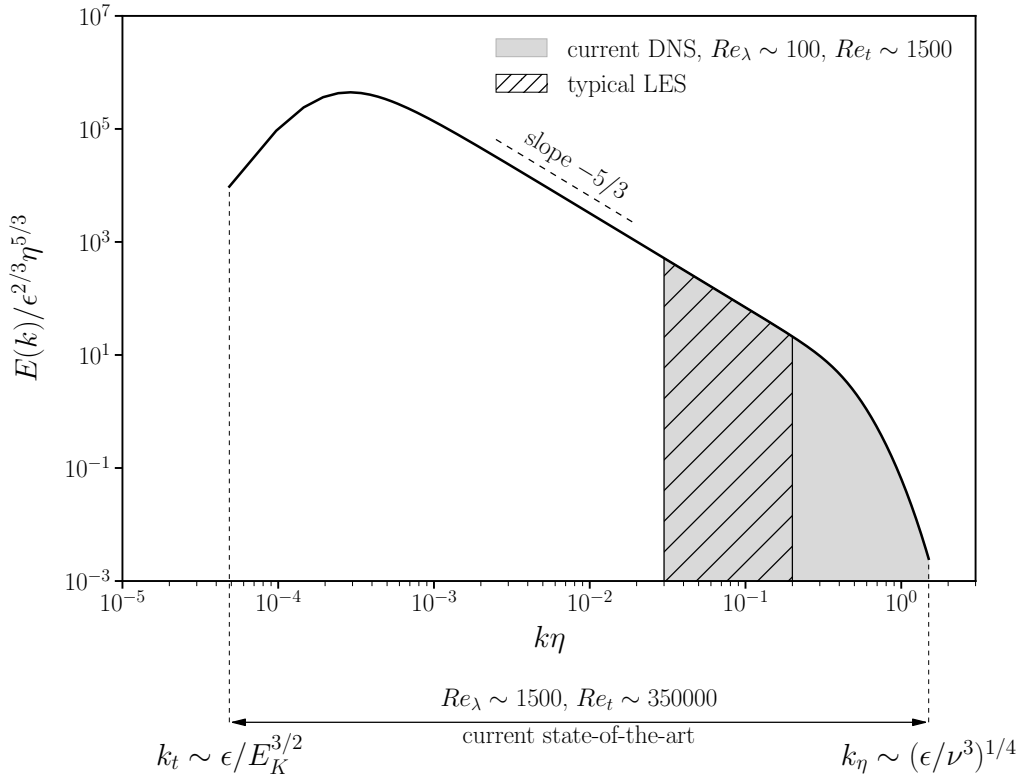

Figure 3.1: Model energy spectrum function at $Re_\lambda \sim 1500$; solid line reflects the state-of-the-art DNS of isotropic turbulence; shaded region denotes the current code; hatched area reflects the most often reported pseudo-spectral LES.

dissipation subrange, clearly violating the recommendations given by Chollet [125]. Using the standard spectral eddy-viscosity outside its intended scope of application does not appear inherently wrong, however, it raises more questions regarding the legitimacy and/or usefulness of such simulations, especially for cases where the DNS is computationally affordable.

To partially answer these questions, one can compare an example LES ($N = 64$) enriched with the spectral eddy-viscosity given by Eq. (3.22) against the DNS at $Re_\lambda \sim 94$ ($N = 256$), see also Table 2.3. From Fig. 3.2, it is readily apparent that the energy is transferred as well as drained from the system at approximately correct rate, which confirms previous findings reported in [120, 124]. For the first few wavenumber shells, say $k\eta < 0.1$, the energy distribution is mostly overestimated when compared to the reference DNS, with differences reaching at most 15%. For the remaining part of the resolved wavenumber space, the energy is mostly underestimated with differences reaching up to 50%. On average, the current LES accounts for roughly 96% of the total kinetic energy. It should be emphasized that for the given spatial resolution of $N = 64$, which results in $k_{\max} = 30$, the *a priori* LES accounts for roughly 98% of the energy. If the spectral eddy-viscosity is set to $\nu_e(k; k_c) = 0$, in which case the

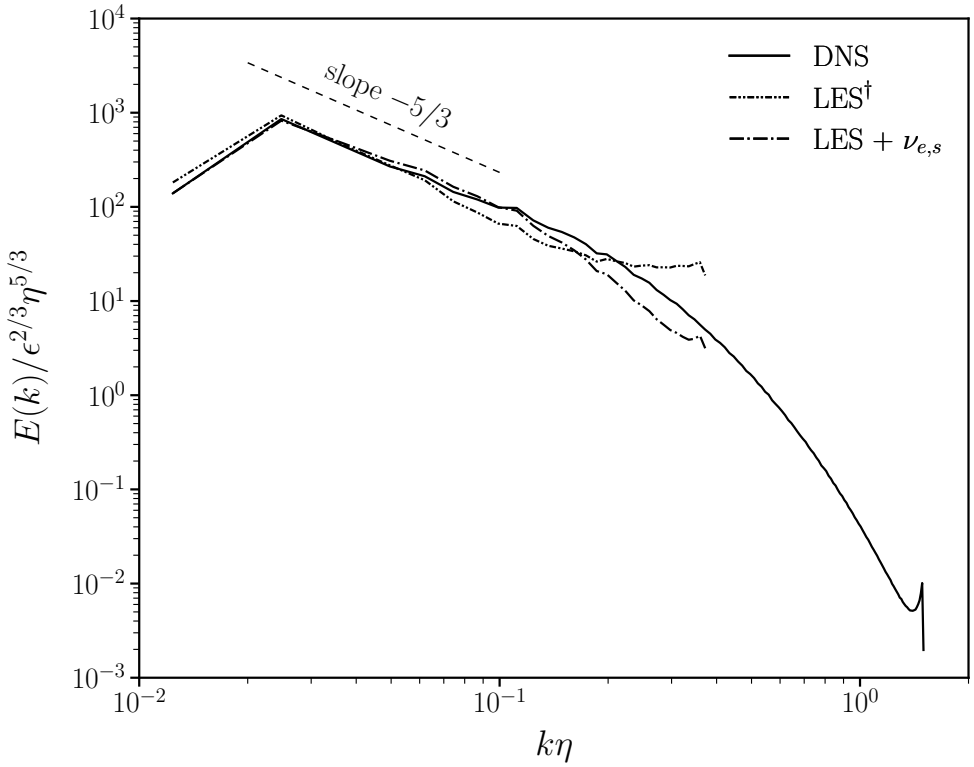

Figure 3.2: Energy spectrum function in LES at $Re_\lambda \sim 100$; LES† denotes an "under-resolved DNS" for which $\nu_e(k; k_c) = 0$.

LES simply becomes an "underresolved DNS", the energy spectrum function takes an unphysical form. Interestingly, this is exactly the case in [82], which may indicate a potentially improper use of the subgrid-scale model. The overall isotropy is rather satisfactory, see Fig. 3.3, with approximately 85% of the resolved flow scales having $I(k) \sim 1$, similar to the DNS, recall Fig. 2.8 for comparison. Although the energy distribution in LES is mostly correct (which is usually the case for the eddy-viscosity models), the flow structure is significantly affected by the spatial filtering. From Fig. 3.4, it is readily apparent that in the LES enriched with the standard model, the probability density function (PDF) of the second invariant of the velocity gradient tensor Q retains the non-Gaussian form, however, with significantly shortened tails. This clearly indicates that the LES weakens the simulated turbulence by filtering out the (majority of) intermittent regions of high vorticity and strain. It should be emphasized that this is expected to have a non-negligible impact on particle dynamics. This phenomenon will be thoroughly discussed in Section 5.3.

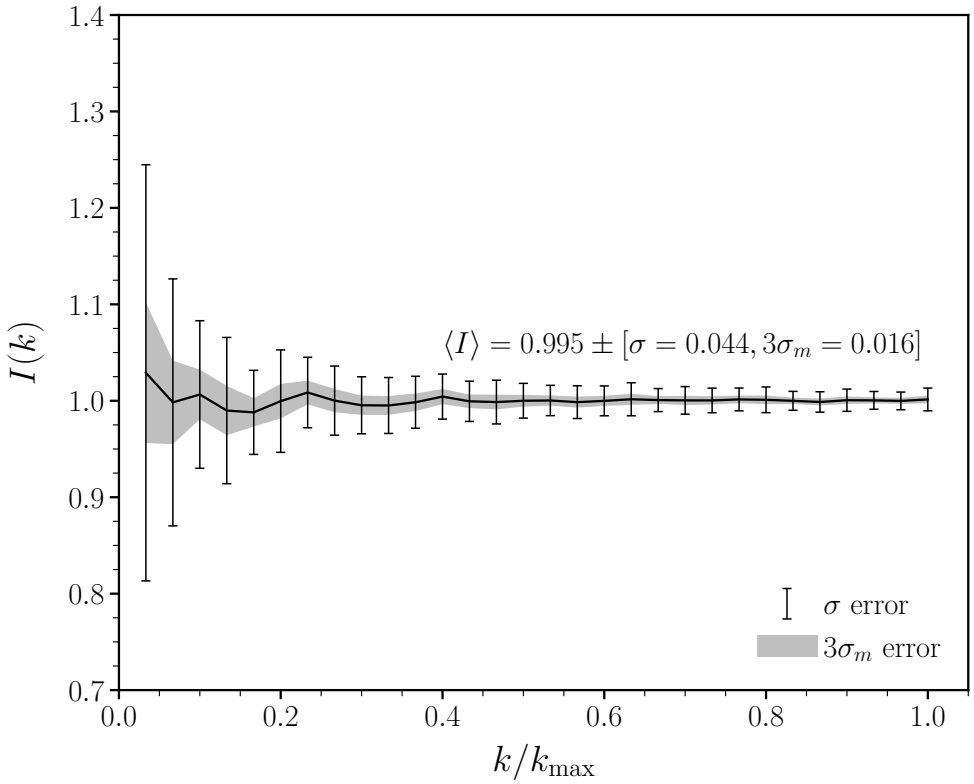

Figure 3.3: Isotropy spectrum in LES at $Re_\lambda \sim 100$.

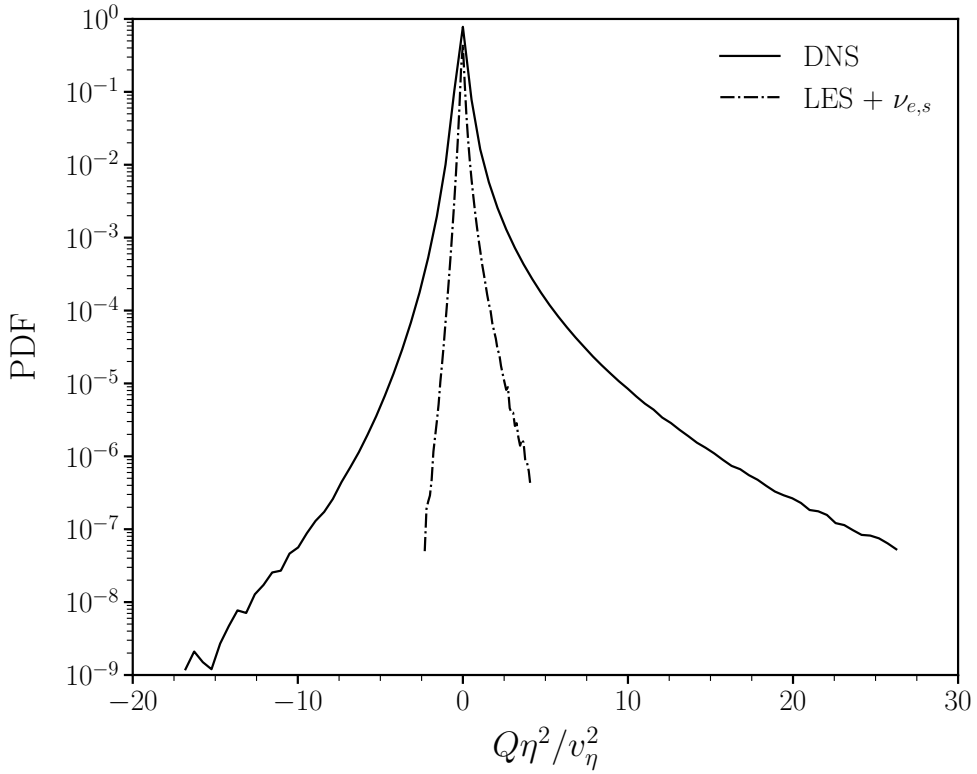

Figure 3.4: The impact of spatial filtering and subgrid-scale modeling on the PDF of Q at $Re_\lambda \sim 100$.

3.5 *A priori* spectral eddy-viscosity

It turns out that the FDNS can also serve as an alternative approach to modeling the spectral eddy-viscosity, particularly valid in the limit of low- to moderate-Reynolds numbers. Recall that Chollet & Lesieur [120] elaborated on the pioneering work of Kraichnan [91], assuming an infinite inertial subrange, thus implying that $Re_t \to \infty$. To overcome this restriction, one can note that the energy transfer across a certain wavenumber k_c, given by Eq. (3.17), can be rearranged so as to obtain

$$T(k) - T_{<k_c}(k;k_c) = -2\nu_{e,th}(k;k_c)k^2E(k), \qquad k \leq k_c, \tag{3.23}$$

where $\nu_{e,th}(k;k_c)$ will hereinafter be referred to as the theoretical or *a priori* spectral eddy-viscosity. One can recall that $T(k)$ is the total energy transfer given as

$$T(k) = \mathrm{Re}\left[\langle \hat{u}_\alpha^\star(\boldsymbol{k}) P_{\alpha\beta} \hat{N}_\beta(\boldsymbol{k})\rangle\right] \qquad k \leq k_{\max}, \tag{3.24}$$

and that the second term on the left-hand side of Eq. (3.23) denotes the energy transfer between mode $\boldsymbol{k}$ and two others, both of which lie within the range of resolved

wavenumbers. It can be readily noticed that using a sharp spectral filter given by Eq. (3.14), the filtered non-linear transfer $T_{<k_c}(k;k_c)$ can be obtained from Eq. (3.24), thus allowing to determine the functional form of $\nu_{e,th}(k;k_c)$ from Eq. (3.23). Domaradzki et al. [132] were the first to use this approach in order to determine the scale-dependent eddy-viscosity based on the DNS of decaying isotropic turbulence at $Re_\lambda \sim 100$. In line with the expectations, essentially based on Kraichnan's prediction which assumed the existence of an infinite inertial subrange [91], the "theoretical" eddy-viscosity exhibits a strong cusp in the vicinity of the spectral cutoff. Interestingly, instead of a positive asymptotic value in the low-wavenumber range, say $k \leq 0.4k_c$, as previously suggested in [91, 120], the authors reported small negative eddy-viscosities, possibly mimicking the backward energy transfer. This is clearly in contradiction with the general eddy-viscosity concept. While the molecular viscosity is a physical property of the fluid, the eddy-viscosity can be considered as a property of the flow. In some sense, it is a model viscosity which increases the energy dissipation, and thus essentially imitates the energy transfer from large to small flow scales. Lesieur [1] addressed the observations reported in [132] and, based on the E.D.Q.N.M. theory, concluded that if the energy spectrum k^{-m} is assumed for $k > k_c$, then the eddy-viscosity becomes negative on condition that $m > 5$.

Consider a non-dimensional spectral eddy-viscosity determined from the FDNS at $Re_\lambda \sim 94$ using different values of the spectral cutoff, selected so that $k_c\eta \in [0.15, 1.1]$. In line with the expectations, the *a priori* eddy-viscosity increases rapidly near the spectral cutoff, see Fig. 3.5 (left panel). In addition to that, its value at the cutoff, given as $\nu^+_{e,th}(k = k_c; k_c)$, increases almost exponentially until $k_c\eta = 1$, and drops

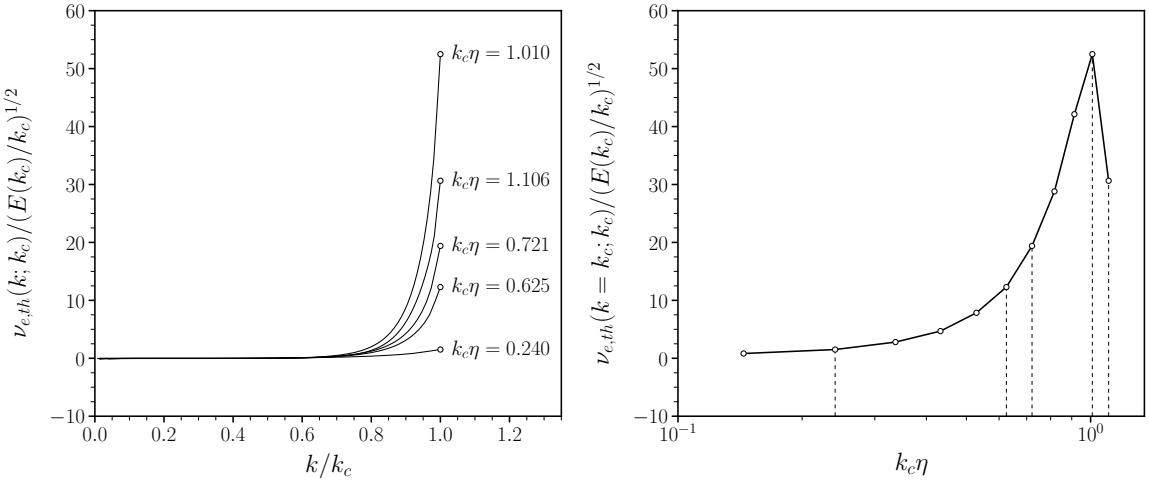

Figure 3.5: The impact of the spectral cutoff on the *a priori* eddy-viscosity in FDNS at $Re_\lambda \sim 100$ (left panel); theoretical eddy-viscosity at the cutoff (right panel).

rapidly when this is exceeded, see Fig. 3.5 (right panel). With increasing spatial resolution of LES, i.e., $k_c \to \eta^{-1}$, the energy spectrum at the cutoff $E(k_c)$ decreases, and so does the scaling factor $[E(k_c)/k_c]^{1/2}$. This seems to explain the aforementioned increase observed for $k_c\eta \leq 1$. On the other hand, if the spatial resolution increases further, i.e., $k_c \to k_{\max} > \eta^{-1}$, then the LES essentially converges to the DNS, and therefore $\nu^+_{e,th}(k;k_c) \to 0$ is expected for all resolved wavenumber shells.

To assess the impact of the spectral eddy-viscosity on the large-scale turbulence, its form was determined using the FDNS at $Re_\lambda \sim 94$, however, assuming the spectral cutoff at $k_c = 30$, which, in this work, essentially corresponds to the LES with the spatial resolution of 64^3 nodes. From Fig. 3.6 (right panel), it is readily apparent that in the low-wavenumber range, say $k < 0.4k_c$, the eddy-viscosity becomes negative, with absolute values close to the molecular viscosity. On the other hand, considering the range of wavenumbers corresponding to the smallest resolved flow scales, specifically those of size comparable to the filter width, it can be observed that $\nu^+_{e,th}(k;k_c)$ increases by approximately an order of magnitude as k changes from $0.7k_c$ to k_c. This agrees well with the results reported in [132]. Unsurprisingly, the alternative form of the spectral eddy-viscosity significantly improves the energy spectrum function, see Fig. 3.6 (left panel). In fact, the *a priori* eddy-viscosity allows to restore the DNS energy spectrum within almost the entire range of the resolved flow scales; one can note minor discrepancies in the vicinity of the spectral cutoff, say $k\eta > 0.2$. The spectrally-vanishing nature of the *a priori* eddy-viscosity suggests that as long as sufficient spatial resolution is ensured, the filtered Navier-Stokes equations accurately model the motion of large flow scales, even without artificially increased viscosity.

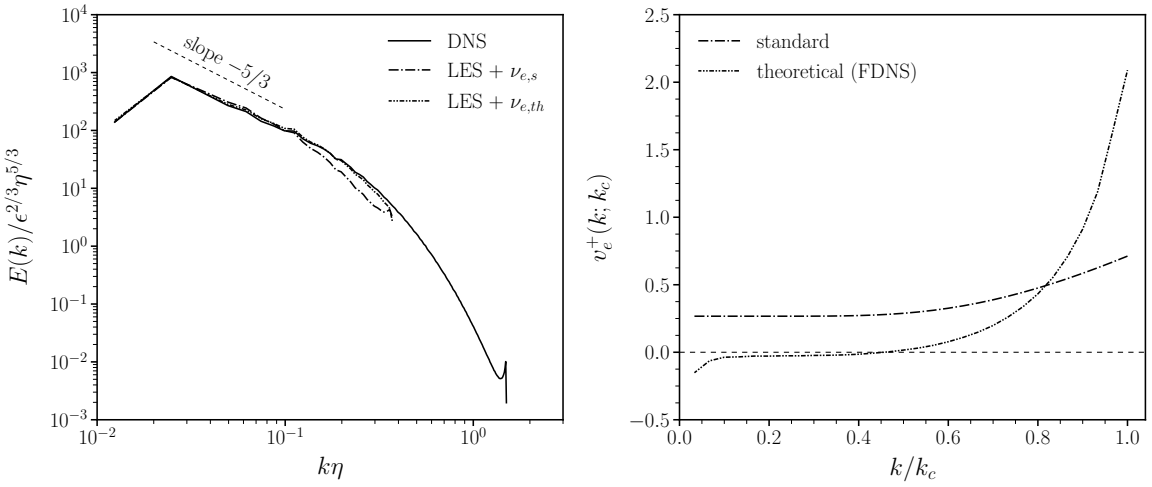

Figure 3.6: The impact of subgrid-scale modeling on the energy spectrum function in LES at $Re_\lambda \sim 100$ (left panel); different forms of the spectral eddy-viscosity (right panel).

This statement will be thoroughly discussed in Section 3.7.

At this point, it should be emphasized that although the energy transfer among the resolved flow scales is significantly enhanced, the *a priori* eddy-viscosity cannot restore small-scale turbulence, and therefore the overall flow structure remains nearly unchanged when compared to the standard model, see Fig. 3.7. However, with increasingly more accurate reconstruction of the energy spectrum function, the LES seems to approach the FDNS. At this point, one can recall that the FDNS represents the direct (isolated) impact of spatial filtering on the simulated turbulence, and thus, in some sense, also establishes the potential of LES, which, on the other hand, can be further increased by means of more advanced subgrid-scale modeling.

Based on the foregoing reasoning, it seems that the *a priori* spectral eddy-viscosity, as given by Eq. (3.23), can be regarded as a perfectly valid approach to modeling the impact of the unresolved flow scales in LES of single-phase isotropic turbulence. However, it should also be emphasized that due to the need for specific DNS data, the model has no real predictive value at Reynolds numbers exceeding those achievable in the DNS. On the other hand, due to the improvement of the energy distribution in the vicinity of the spectral cutoff, the model possibly also improves the evolution of the

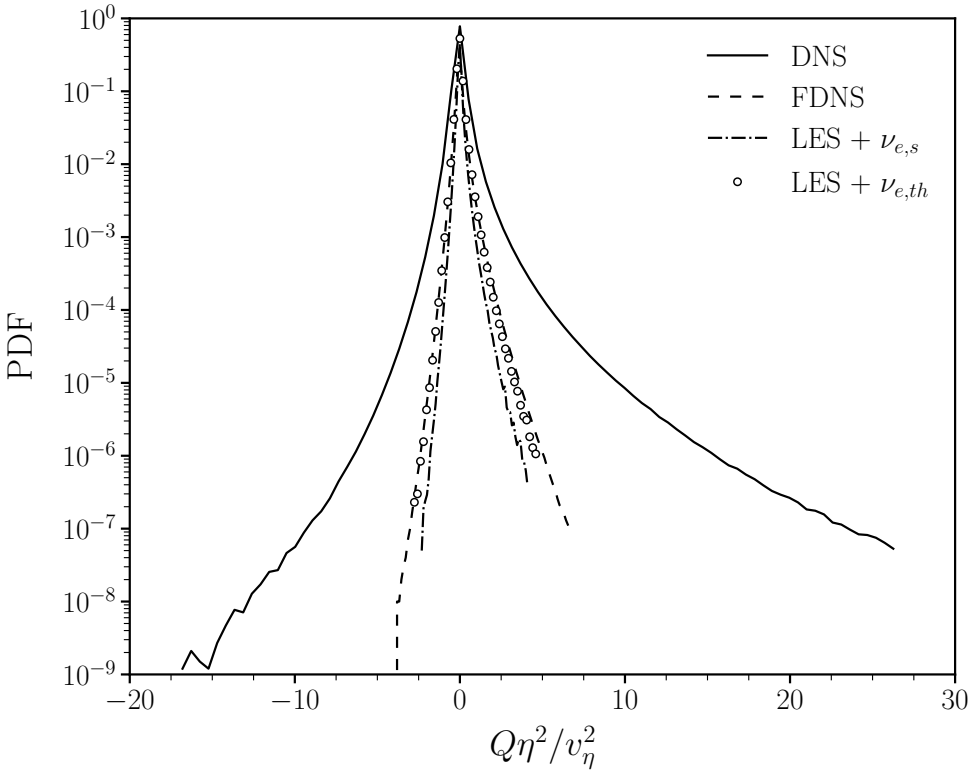

Figure 3.7: The impact of filtering and subgrid-scale modeling on the PDF of Q at $Re_\lambda \sim 100$.

corresponding flow scales. Therefore, in the case of particle-laden isotropic turbulence, it seems justified to expect an appreciable improvement of certain particle statistics when compared to the LES enriched with the standard eddy-viscosity. One can also note that due to the lack of small-scale turbulence, the two models are not expected to significantly influence the motion of inertial particles preferentially interacting with the unresolved range of flow scales. This phenomenon will be thoroughly addressed in Section 5.3.

3.6 Spectral Large Eddy Simulations

It is often argued that an LES can be considered well-resolved on condition that the filtered velocity field accounts for the bulk of the kinetic energy [36, 133], say more than 80% [2, 134]. Considering an example turbulent flow at $Re_\lambda \sim 94$, see Fig. 2.11, approximately 80% of the energy is contained in the first few wavenumber shells, say $k\eta \leq 0.15$. Assuming the spherical truncation, Eq. (2.52), the given range of wavenumbers can be fully resolved in the pseudo-spectral LES with the spatial resolution of at most 32^3 nodes. In fact, it turns out to be sufficient for capturing the bulk of the kinetic energy even at high Reynolds numbers [134]. On the other hand, as already indicated, such a coarse grid is expected to filter out a significant part of the intermittent regions of high vorticity and strain, see Fig. 3.7. Hence, for certain applications, particularly including particle-laden turbulent flows, higher spatial resolution is most likely to be required. Interestingly, based exclusively on raw and compensated energy spectra, Domaradzki [123] suggested that a single-phase LES with the spatial resolution of 64^3 nodes, enriched with a spectral eddy-viscosity similar to the standard one used in this work, should capture the characteristics of the inertial subrange. Due to this very statement, the following Section is primarily focused on assessing the performance of the LES supplemented with a scale-dependent eddy-viscosity in isotropic turbulence at high Reynolds numbers, with a particular emphasis on its ability to capture the inertial range dynamics. One can recall that in such conditions, the inertial subrange is expected to be sufficiently large to justify the use of the standard model given by Eq. (3.22).

Individual length scales characteristic to cumulus clouds can extend from millimeters up to tens of meters, resulting in the turbulence Reynolds numbers on the order of $Re_t \sim 10^6 - 10^7$ [135]. This inevitably implies a strong (reaching up to several orders of magnitude) intermittency of specific physical quantities, e.g., the kinetic energy dissipation rate [136]. Exclusively due to computational limitations, in this work, a single set of relevant physical quantities was assumed, that is $\epsilon = 6 \times 10^{-2}$ m^2/s^3

and $\nu = 1.5 \times 10^{-5}$ m^2/s. This results in the length, velocity, and time scales on the order of $\eta \sim 0.5 \times 10^{-3}$ m, $v_\eta \sim 0.3 \times 10^{-2}$ m/s and $\tau_\eta \sim 1.5 \times 10^{-2}$ s, respectively. In this case, the Reynolds number based on the Taylor microscale is on the order of $Re_\lambda \sim 10000$, and thus as indicated by Domaradzki [123], inertial range theories should apply. The current state-of-the-art for the DNS is approximately an order of magnitude smaller, as already indicated in Section 3.4, see also Fig. 3.1. It should be emphasized that only recently, the LES has been applied to study turbulent flows in such conditions [99, 123, 137]. Based on these research studies, it has been concluded that LES recovers the inertial range energy spectrum with the Kolmogorov constant within $1.4 < C_K < 2.1$. At this point, it should be once again emphasized that the $k^{-5/3}$ scaling in the energy spectrum function is a necessary yet not sufficient criterion for identifying or estimating the extent of the inertial subrange.

Consider a turbulent flow confined to a cubic box with an edge length of $L_B = 2\pi$, for which the turbulence length scale is $L_t \equiv E_K^{3/2}/\epsilon$ and $Re_\lambda = 2E_K\,[5/(3\nu\epsilon)]^{1/2}$. A few basic flow statistics, predicted based on a simple dimensional analysis as given by the Kolmogorov theory of turbulence, are listed in Table 3.1. At this point, it should be clarified that in all simulations the actual spatial resolution was fixed at $N = 256$. The ratio $N_{\rm DNS}/N_{\rm LES}$ simply refers to the corresponding "hypothetical" DNS. In other words, the required kinematic viscosity of the fluid was determined as in Section 2.5, i.e., using $\nu = (\eta^4\epsilon_f)^{1/3}$ where $\epsilon_f = 0.3$, $\eta = k_{\rm max}\eta/k_{\rm max}$, $k_{\rm max}\eta = 1.5$, and $k_{\rm max} = \lfloor\sqrt{2}N_{\rm DNS}/3+0.5\rfloor$. Based on the model spectrum, Pope [2] (Section 6.5.7, p. 244) indicated that at high Reynolds numbers the ratio of L_t/L_1 asymptotically approaches the value of 0.43. Therefore, assuming $L_B/L_1 = 8$, the proper large-scale resolution is arguably ensured on condition that $L_t/L_B = 1/(8\times0.43) \approx 0.3$; however,

case	$N_{\rm DNS}/N_{\rm LES}$	Re_t	Re_λ	u'	L_t	L_B [m]	u' [m/s]
0 (DNS)	-	1411	97	0.775	2.855	0.25	0.15
1	2	3511	153	0.775	2.839	0.49	0.19
2	4	8,930	244	0.774	2.853	0.99	0.24
3	8	22,465	387	0.775	2.852	1.97	0.31
4	16	56,549	614	0.775	2.849	3.94	0.39
5	32	142,594	975	0.775	2.850	7.88	0.49
6	64	359,446	1,548	0.775	2.581	15.75	0.62
7	128	906,265	2,458	0.775	2.852	31.51	0.78
8	256	2,281,500	3,900	0.775	2.850	63.02	0.98
9	512	5,747,415	6,190	0.775	2.850	126.04	1.23
10	1024	14,479,594	9,825	0.775	2.849	252.09	1.55

Table 3.1: Flow statistics in LES predicted based on dimensional analysis; relevant physical quantities are $\epsilon = 6 \times 10^{-2}$ m^2/s^3 and $\nu = 1.5 \times 10^{-5}$ m^2/s; $N_{\rm LES} = 256$.

taking into account the results summarized in Table 2.3, it seems that a higher value can be safely imposed, that is, $L_t/L_B \approx 0.45$.

The actual results of numerical simulations are listed in Table 3.2. It can be readily noticed that the results from the DNS (case 0) agree well with the prediction given in Table 3.1. Henceforth, it can be concluded that the results from the current numerical simulations align well with the Kolmogorov theory of turbulence, thus the aforementioned dimensional analysis is expected to provide an accurate estimation of length scales relevant to the current LES and, consequently, the order of specific Reynolds numbers based on those length scales. It can be observed in Fig. 3.8 (left panel) that as the Reynolds number increases, the range of flow scales where the energy spectrum function approximately follows the Kolmogorov $k^{-5/3}$ scaling expands. At this point, it should be clarified that the energy spectra are plotted in the same order as given in Table 3.1; however, the results start to overlap from approximately $Re_\lambda \sim 1000$, and therefore become statistically indistinguishable. To get a clearer view of this, one can refer to Fig. 3.8 (right panel), from which it is evident that $E(k_c)$ reaches a saturation point at approximately $N_{\text{DNS}}/N_{\text{LES}} \approx 32$. In this work, this essentially corresponds to the "hypothetical" DNS at $Re_\lambda \sim 1000$ as given in Table 3.1. It can be concluded that beyond this point (assuming a fixed spatial resolution), the simulated turbulence in LES is not significantly enriched, if at all. At high Reynolds numbers, say $Re_\lambda \sim 10000$, the inertial subrange developed in LES should theoretically span almost the entire resolved range of flow scales outside the forced wavenumber band, with the Kolmogorov constant C_K taking the value between 1.4 and 2.1 [138], as one would intuitively expect based on Fig. 3.8 (left panel). At this point, one can note that for a given turbulent flow, the actual value of C_K can

case	Re_λ	Re_L	Re_t	$\epsilon^\dagger$	u'	τ_t	T_e	$k_c\lambda$
0 (DNS)	94	278	1126	0.289	0.753	2.95	0.931	28.60
1	152	690	3,109	0.299	0.772	2.99	0.89	18.30
2	244	1,716	8,062	0.300	0.775	3.01	0.87	11.56
3	396	4,451	21,698	0.300	0.784	3.07	0.87	7.36
4	626	10,992	54,113	0.300	0.782	3.07	0.86	4.63
5	993	27,661	135,836	0.300	0.782	3.06	0.86	2.91
6	1,589	71,119	350,458	0.300	0.785	3.09	0.87	1.84
7	2,503	175,635	862,192	0.300	0.782	3.06	0.86	1.16
8	4,025	454,552	2,260,263	0.300	0.787	3.10	0.87	0.73
9	6,357	1,134,569	5,611,475	0.300	0.785	3.09	0.87	0.46
10	10,067	2,829,103	14,040,931	0.300	0.784	3.08	0.86	0.29

Continued on next page

case	L/L_B	L_t/L_B	L_1/L_B	L_2/L_B	L_1/L_2	I	S	F
0 (DNS)	0.112	0.433	0.110	0.055	2.004	1.001	-0.52	5.29
1	0.109	0.449	0.113	0.055	2.065	0.996	-0.47	5.26
2	0.107	0.455	0.106	0.054	1.982	1.008	-0.40	4.86
3	0.109	0.470	0.104	0.054	1.941	1.008	-0.35	4.64
4	0.107	0.468	0.108	0.054	2.025	1.013	-0.33	4.52
5	0.107	0.466	0.106	0.053	2.022	0.991	-0.32	4.50
6	0.109	0.472	0.109	0.054	2.046	0.996	-0.32	4.48
7	0.107	0.467	0.103	0.052	2.018	1.001	-0.32	4.48
8	0.109	0.476	0.106	0.055	1.925	0.988	-0.32	4.46
9	0.108	0.472	0.108	0.055	1.991	1.003	-0.32	4.48
10	0.107	0.471	0.102	0.055	1.881	1.000	-0.32	4.47

† $\epsilon = 2\int_0^{k_{\max}}[\nu + \nu_e(k;k_{\max})]k^2E(k)\mathrm{d}k$; DNS implies that $\nu_e(k;k_{\max}) = 0$

Table 3.2: Final set of simulations (LES); all parameters were averaged over $\sim 100T_e$; in all cases the grid size is $N = 256$ and $\Delta t/T_e \approx 7.5 \times 10^{-4}$.

be estimated from the compensated energy spectrum given as

$$C_K(k) = E(k)k^{-5/3}/\epsilon^{2/3}. \tag{3.25}$$

From Fig. 3.9, it can be observed that as the Reynolds number increases, $C_K(k)$ asymptotically approaches a constant value[4]; however instead of reaching a plateau, an unexpected positive trend for $k/k_c > 0.1$ begins to develop at approximately

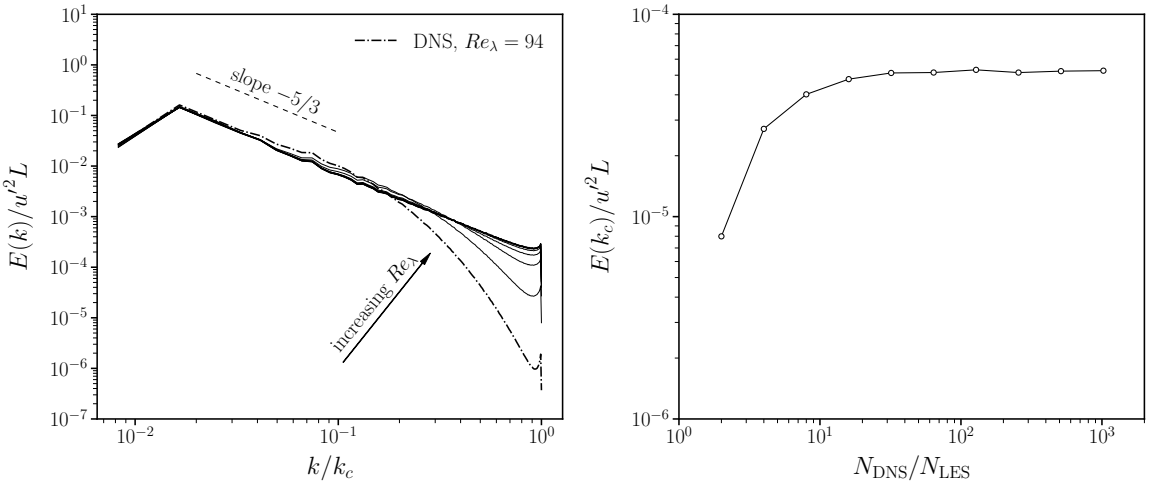

Figure 3.8: Normalized energy spectrum function (left panel) and its value at the cutoff (right panel); $N_{\mathrm{DNS}}/N_{\mathrm{LES}} = 2^i$ for $i = 1, 2, \ldots, 10$.

[4]In the sense that $C_K(k)$ approaches a constant value for all wavenumber shells k

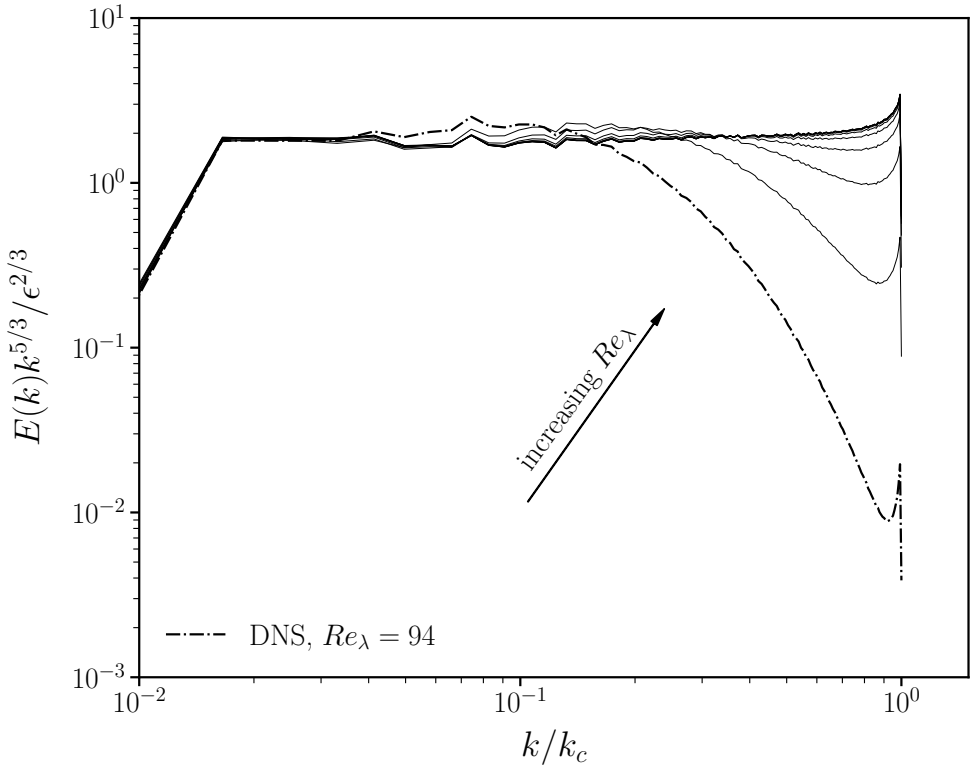

Figure 3.9: The impact of the Taylor microscale Reynolds number on the compensated energy spectrum function in LES with a spatial resolution of 256^3 nodes (solid lines); $Re_\lambda \in (150, 10000)$.

$Re_\lambda \sim 1000$, see also Fig. 3.10 (left panel). This trend, however, is not observed at $Re_\lambda \sim 600$. Nevertheless, based on Fig. 3.10 (left panel), it can be concluded that in general, $C_K(k)$ falls within the expected range of values for approximately 75% of the

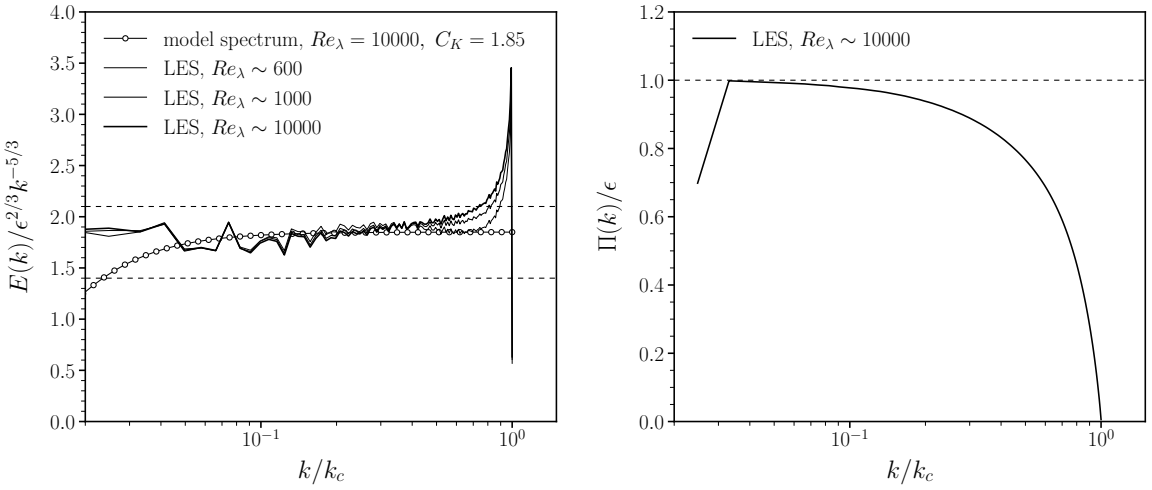

Figure 3.10: Compensated energy spectrum function (left panel) and the normalized energy flux (right panel) in LES.

resolved wavenumber space. Notable discrepancies occur near the spectral cutoff with differences reaching up to 65%. On the other hand, it seems that $C_K(k)$ begins to increase at approximately $k/k_c = 0.4$. This behavior is rather consistent with that of $\nu^+_{e,s}(k)$, see Fig. 3.6 (right panel), and can indicate an incorrect functional form of the spectral eddy-viscosity, or, in other words, an insufficient dissipation at length scales comparable to the filter width. Indeed, in the limit of low- to moderate-Reynolds numbers, the *a priori* eddy-viscosity was found to have a much steeper cusp near the spectral cutoff, see also Fig. 3.6 (right panel). Based on the above reasoning, it can be concluded that similar behavior may also be desirable at high Reynolds numbers.

As already indicated, the compensated energy spectrum function should asymptotically approach a constant value within the inertial subrange, see the model spectrum depicted in Fig. 3.10 (left panel), where the plateau is exactly at the prescribed value of $C_K = 1.85$. Based on the preceding discussion, it seems that the inertial subrange developed in the current LES extends over a range of flow scales that is somewhat smaller than one would expect. In fact, this can be confirmed by the the normalized scale-dependent energy flux given in Fig. 3.10 (right panel), where the subrange for which $\Pi(k) \approx \epsilon$ is confined to the first few wavenumber shells even at $Re_\lambda \sim 10000$. In contrast to the previous paragraph, this may suggest excessive dissipation in the intermediate range of resolved flow scales.

At this point, one can recall that Chollet [125] suggested that the use of the spectral eddy-viscosity given by Eq. (3.22) is sufficiently justified on condition that the cutoff wavenumber is located deep in the inertial subrange. On the other hand, assuming that the Taylor microscale determines the range of flow scales relevant to the inertial subrange, and hence also the LES itself, an additional condition can be imposed on the "small-scale" resolution, e.g., $k_c\lambda$. It this work, it is postulated, essentially by drawing an analogy from the DNS, that a reasonable criterion would appear to be $k_c\lambda > 1$; however, taking into account the above results, it seems that more stringent requirements may need to be satisfied, see also Table 3.2. It can be concluded that in order to accurately capture the motion of large flow scales in the LES enriched with the standard spectral eddy-viscosity, the maximum Reynolds number achievable in this work can be at most on the order of $Re_\lambda \sim 1000$, which is rather unsatisfactory when compared to the current state-of-the-art in the DNS of isotropic turbulence. In addition to that, it should be emphasized that the actual scale separation in LES is significantly smaller than the one that would be obtained in the DNS at the very same Reynolds number.

Similar to the DNS, the anisotropy introduced by the forcing vanishes relatively quickly, and thus the entire range of the resolved flow scales outside the forced

wavenumber band display a high degree of isotropy, see Fig. 3.11.

In addition to that, both longitudinal and transverse velocity autocorrelation functions take correct forms and vanish, to a good approximation, at length scales comparable to $r = L_B/2$, see Fig. 3.12, thus providing a relatively good estimate of the corresponding integral length scales. A minor deviation of L_1/L_2 from its theoretical prediction presumably results from both the spatial filtering and the statistical uncertainty.

From Table 3.2, particularly concerning the skewness S and the flatness F, it is readily apparent that as the Reynolds number increases (and consequently the range of the unresolved flow scales expands), the turbulence becomes progressively attenuated. Similar to the previous findings, both parameters saturate at approximately $Re_\lambda \sim 1000$, which essentially corresponds to $N_{\mathrm{DNS}}/N_{\mathrm{LES}} = 32$, see case 5. To get more insight into the issue, one can also consider the PDF of Q depicted in Fig. 3.13. It can be readily observed that the PDF retains its non-Gaussian characteristics even if the spatial filtering is significant, e.g., at $Re_\lambda \sim 10000$ and $k_c\lambda \approx 0.29$. The PDF reaches the saturation point relatively quickly, and thus only a minor turbulence enrichment is observed when the Taylor microscale Reynolds number increases by an order of magnitude. One can recall that in a fully-resolved turbulent flow (DNS),

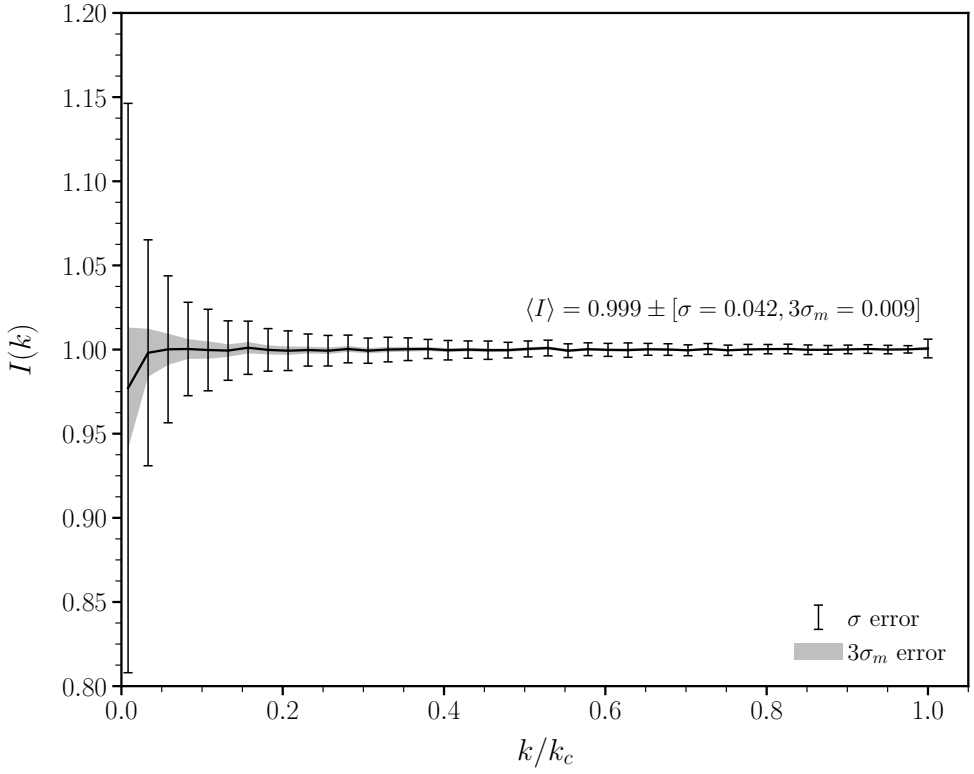

Figure 3.11: Isotropy spectrum function in LES at $Re_\lambda \sim 10000$.

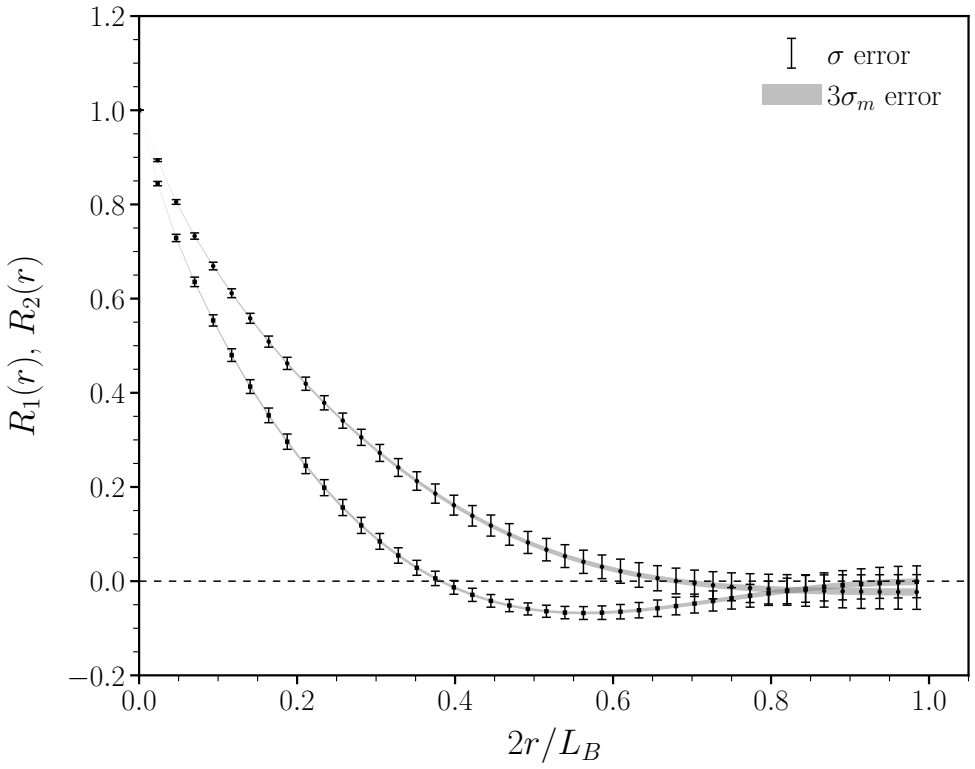

Figure 3.12: Longitudinal and transverse velocity autocorrelation functions in LES at $Re_\lambda \sim 10000$.

increasing the Reynolds number results in broader tails of the PDF, see, e.g., Fig. 2.12, thus indicating a higher probability of encountering the regions of high vorticity and strain.

In general, it appears that most physical quantities predicted using the LES enriched with the standard eddy-viscosity remain in good agreement with the Kolmogorov theory of turbulence. It is also worth noting that (i) the bulk of flow scales larger than the artificially forced ones exhibit high degree of isotropy, and (ii) both longitudinal and transverse velocity correlation functions take correct forms, particularly vanishing at length scales comparable to half of the computational box. On the other hand, it seems that due to an suboptimal functional form of the standard model, particularly considering its positive plateau in the low-wavenumber range, the large flow scales are numerically suppressed due to excessive dissipation. For this very reason, the LES cannot capture the inertial range dynamics even at very high Reynolds numbers. At this point, it should also be emphasized that with increasing spatial resolution, the scaling factor given as $[E(k_c)/k_c]^{1/2}$ is expected to progressively decrease, see Eq. (3.22), and so is the spectral eddy-viscosity, thus reducing the adverse impact on the evolution of large flow scales. However, due to computational limitations, this statement cannot be supported in this work.

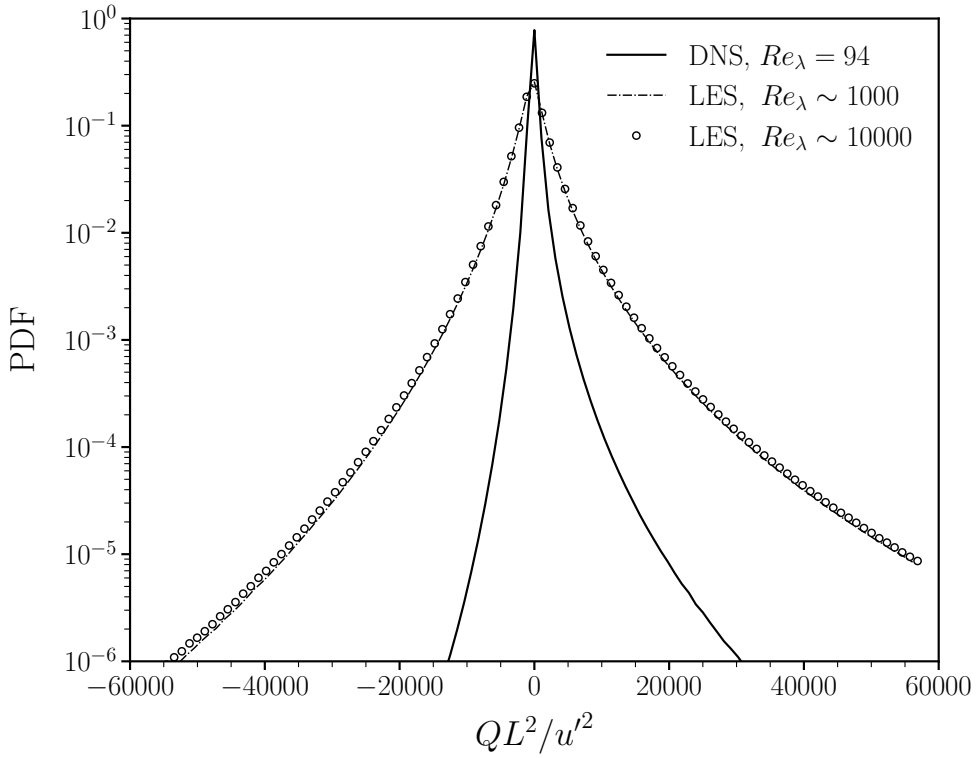

Figure 3.13: The impact of the Taylor microscale Reynolds number on the PDF of Q in LES with the spatial resolution of 256^3 nodes.

Nevertheless, taking into account to some extent satisfactory physical correctness of the resolved velocity field, one may reasonably expect that the foregoing deficiencies of the LES enriched with the standard model will impact particle statistics at most quantitatively, whereas certain phenomena related to the turbulent transport of inertial particles should be captured with qualitative accuracy. This hypothesis will be thoroughly addressed in Section 5.3.

3.7 Adaptive parametrization of small flow scales in isotropic turbulence

In view of the above results, it seems that the LES enriched with either the standard spectral eddy-viscosity given by Eq. (3.22), first proposed by Chollet & Lesieur [120], or, arguably, any other non-vanishing (in the limit of $k \to k_0$) eddy-viscosity [99, 123, 137] may be inappropriate for studying the physics underlying turbulent flows. To clarify, although the energy is drained from the system at approximately correct rate, the development of the inertial subrange is numerically suppressed due to excessive dissipation in the low-wavenumber range.

In Section 3.5, it has been shown that the spectral eddy-viscosity can be predicted reasonably well using the DNS data along with the methodology first proposed by Domaradzki et al. [132]. It turned out that such a theoretical eddy-viscosity significantly improves the energy distribution near the spectral cutoff, effectively restoring the reference DNS energy spectrum, see Fig. 3.6. In addition to that, possibly due to improved resolution of flow scales comparable to $\Delta \sim k_c^{-1}$, the PDF of Q in LES is approximately aligned with the reference FDNS, see Fig. 3.7.

Taking into account the above reasoning, in this section an alternative approach to modeling the scale-dependent eddy-viscosity is developed based on a differential regulator, designed to ensure an imposed energy spectrum function is restored.

Bearing in mind an extensive body of numerical research, see, e.g., [91, 99, 120, 123, 124, 125, 132, 137], it is assumed that a scale-dependent eddy-viscosity (i) reaches a positive asymptotic value of $\mathcal{P}$ in the low-wavenumber range, say for $k \leq 0.5k_c$, and (ii) exhibits a strong cusp in the vicinity of the spectral cutoff k_c. In practice, it is unfeasible to satisfy the conditions for which the use of the standard spectral eddy-viscosity given by Eq. (3.22) is justified [120, 125]. For this reason, the primary focus of this Section is to account for the finite spatial resolution of LES. The proposed general form of the scale-dependent eddy-viscosity is depicted in Fig. 3.14, and can

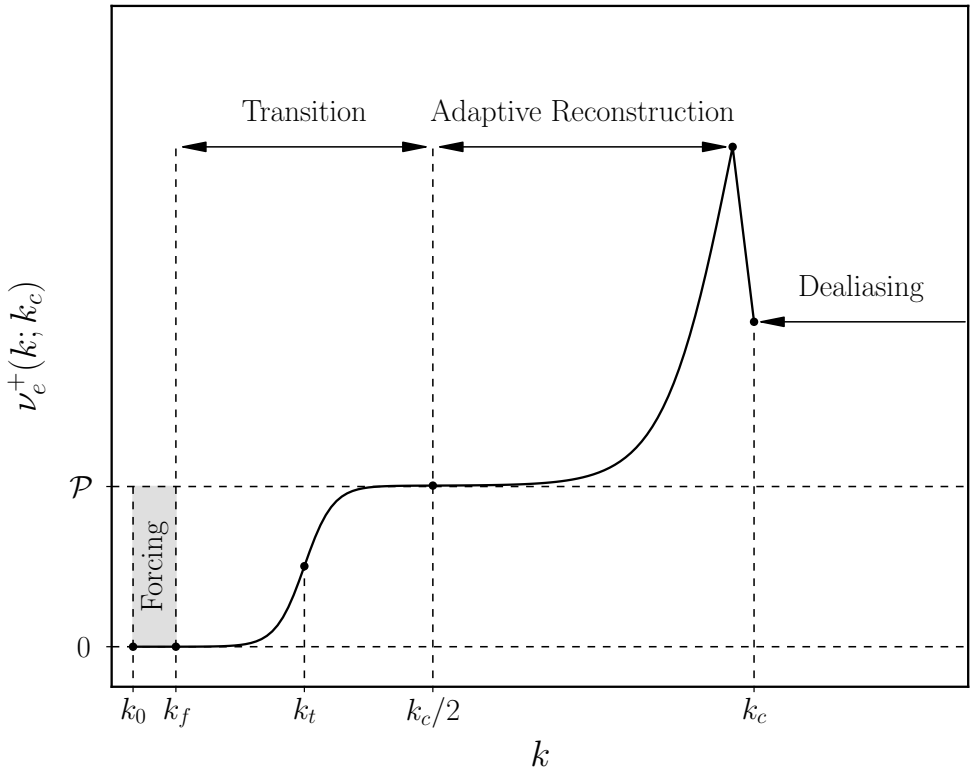

Figure 3.14: A proposed general form of the spectral eddy-viscosity.

be divided into four distinctive regions, that is (i) forcing; (ii) transition, (iii) adaptive reconstruction, and (iv) dealiasing. The purpose of each region is discussed below.

To avoid an undesirable damping of the forced Fourier modes, it seems reasonable to set the normalized eddy-viscosity to $\nu_e^+(k) = 0$ for $k \leq k_{f,\max}$. One can recall that the proper configuration of the forcing has already been comprehensively discussed in Section 2.11. In addition to that, is should be once again emphasized that in the pseudo-spectral simulation of isotropic turbulence, possibly confined to a cubic box of size L_B, the largest resolved length scales remain reasonably constant regardless of the Reynolds number. For instance, in this work, the turbulence length scale is approximately equal to $L_t \sim 0.45L_B$, whereas the integral one is $L \sim 0.125L_B$. Therefore, it seems justified to assume that the proper evolution of those flow scales does not require an artificially increased viscosity.

Introducing the Heaviside function given as

$$H(k) = \begin{cases} 1, & \text{for } k \geq 0 \\ 0, & \text{for } k < 0, \end{cases} \tag{3.26}$$

the transition from $\nu_e^+(k) = 0$ to $\nu_e^+(k) = \mathcal{P}$ can be achieved with ease using a smooth approximation to $H(k)$ given as

$$B(k; k_t) \approx \frac{1}{2} + \frac{1}{2} \tanh\Big[\alpha(k - k_t)\Big], \tag{3.27}$$

where α controls the steepness of the transition at $k = k_t$. Based on numerical tests (not shown here), it turned out that α has no impact on the final outcomes, and thus, in this work, it was set arbitrarily to 0.75. Prior to determining the point at which the transition occurs, one can recall the reasoning given in Section 3.6, indicating that shifting k_t toward k_f, and thus expanding the positive plateau in the spectral eddy-viscosity, essentially results in decreasing the resolved part of the inertial subrange, for which the energy is expected to be transferred independently of viscosity, see, e.g., Fig. 3.10 (right panel). According to Kraichnan [91], approximately 75% of the subgrid-scale energy transfer comes from the smallest resolved flow scales for which $k_c/2 \leq |\boldsymbol{k}| \leq k_c$, possibly implying that

$$k_f < k_t \leq k_c/2, \tag{3.28}$$

where a more precise condition is yet to be determined.

Although the energy spectrum function obtained using the LES enriched with the standard eddy-viscosity remains in satisfactory agreement with the model spectrum

given by Eq. (2.99) with $C_K = 1.85$, see Fig. 3.15, there is still some potential for improvement, particularly in the vicinity of the spectral cutoff, where the eddy-viscosity is clearly insufficient. It is worth mentioning that the improvement of the energy distribution over this particular range of flow scales was essentially the primary reason (motivation) for the development of the approximate deconvolution for LES [7, 110].

Based on the above reasoning, in this work, it is postulated that a better agreement between the resolved and imposed energy spectrum functions can be achieved using a simple differential regulator given as

$$\frac{\mathrm{d}\nu_{e,a}^{+}(k,t)}{\mathrm{d}t} = \frac{F(k,t)}{\tau(k)} = \frac{F[E(k,t);E_m(k)]}{\tau(k)}, \tag{3.29}$$

where $\tau(k)$ represents a time scale that governs its responsiveness; $E_m(k)$ is a predefined energy spectrum function; to clarify the subscript a denotes either adaptive or adaptively-determined eddy-viscosity, F represents a control function, which form is yet to be determined. It should be emphasized once again that the need for a reference energy spectrum is by no means a stringent requirement, in the sense that it does not

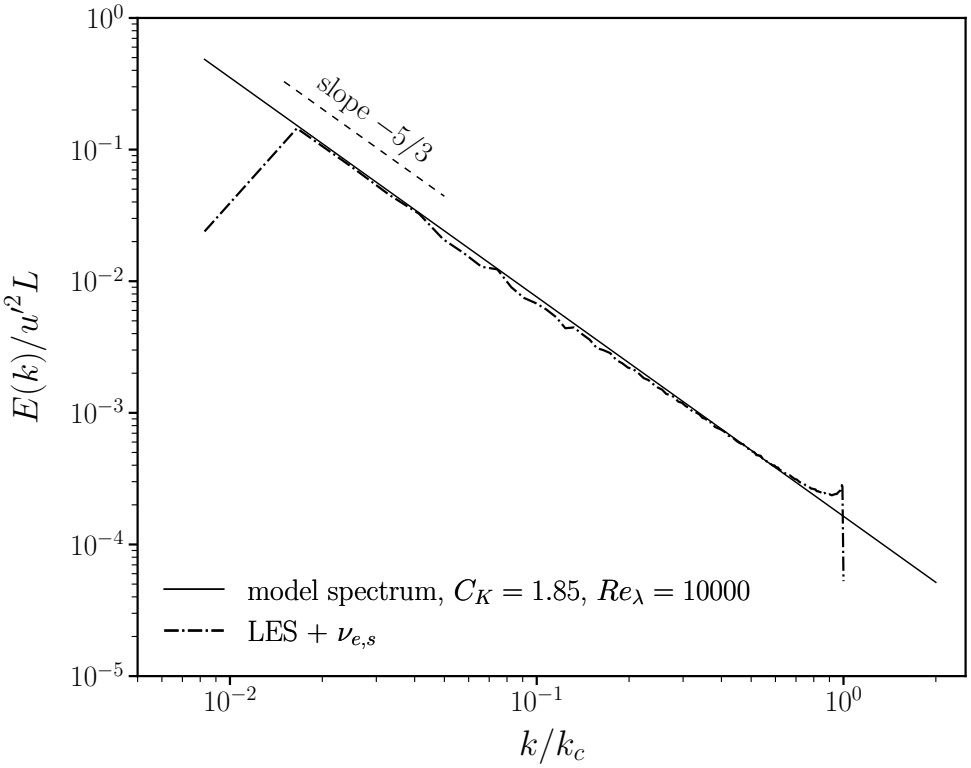

Figure 3.15: Normalized energy spectrum function in LES enriched with the standard spectral eddy-viscosity at $Re_\lambda \sim 10000$.

affect the predictive value of the model, as it was in the case of the *a priori* spectral eddy-viscosity. The reason for this is that the reference energy spectrum can be obtained from either experimental measurements or well-established model spectra, which, as already indicated, are in excellent agreement with numerical simulations.

Given that the regulator is expected to respond to abrupt changes in the energy distribution, in this work, it is proposed to set its time scale $\tau(k)$ proportional to the scale-dependent eddy turnover time to give

$$\tau(k) = c_1 \left[k^3 E_m(k)\right]^{-1/2}, \tag{3.30}$$

where the constant of proportionality was set equal to $c_1 = 1$; however, different values of c_1, or even alternative forms of $\tau(k)$ can be used to either expedite or slow down the changes in $\nu^+_{e,a}(k; k_c)$.

Overholt & Pope [90] introduced a deterministic forcing where a similar k-dependent regulator was used to amplify the low-wavenumber modes. Building on their reasoning, in this work, $F(k,t)$ takes a general form given as

$$F(k,t) = S(k,t) - D_1(k,t) + D_2(k,t). \tag{3.31}$$

The exact form of the control function is essentially arbitrary since its sole purpose is to drive the energy distribution toward a predefined state. In this work, the source term $S(k,t)$ is given as

$$S(k,t) = c_2 \ln\Big[R(k,t)\Big], \tag{3.32}$$

where $R(k,t) = E(k,t)/E_m(k)$; an adjustable parameter c_2 basically controls how quickly the regulator responds to changes in the energy spectrum. In this work it was set equal to $c_2 = 0.25$; however, no significant impact on the final outcomes was observed. The two damping terms can be expressed as

$$D_1(k,t) = c_3 H\Big[R(k,t) - 1\Big]\nu^+_{e,a}(k,t), \tag{3.33}$$

and

$$D_2(k,t) = c_4 H\Big[1 - R(k,t)\Big]\nu^+_{e,a}(k,t). \tag{3.34}$$

These terms were initially proposed to prevent from or control unexpected increases and decreases of the eddy-viscosity. Both parameters c_3 and c_4 serve a similar purpose as c_2 in Eq. (3.32); however, based on numerical tests, it turned out that $c_3 = c_4 = 0$ can be safely imposed.

To control the behavior of the regulator, one can use a simple operator P expressed

as in [90] to give

$$P[F(k,t)] = \begin{cases} B(k;k_t)F(k,t), & \text{for } \nu^+_{e,a}(k,t) > 0, \\ B(k;k_t)F(k,t), & \text{for } \nu^+_{e,a} = 0 \text{ and } F(k,t) > 0, \\ 0, & \text{for } \nu^+_{e,a} = 0 \text{ and } F(k,t) < 0, \end{cases} \tag{3.35}$$

which essentially ensures that the energy is drained from the system but not added through a "negative damping", so to speak. Using the Heaviside function, Eq. (3.31) can be rewritten in a more concise form to give

$$\begin{aligned} \frac{\mathrm{d}\nu^+_{e,a}}{\mathrm{d}t} &= \frac{P[F(k,t)]}{\tau(k)} \\ &= \left\{ H(\nu^+_{e,a}) + [1 - H(\nu^+_{e,a})]H(F) \right\} \frac{BF}{\tau}, \end{aligned} \tag{3.36}$$

where the explicit dependence on (k,t) is dropped to simplify the notation. For the sake of clarity, the operator P is applied at the end of each time step. Taking into account that the evaluation of $R(k,t)$ is computationally expensive, an explicit, single-stage time-stepping scheme (e.g., the second-order Adams-Bashforth method) is recommended to solve the above equation.

From Fig. 3.16 (left panel), it is readily apparent that, when compared to the standard model, the adaptively-determined eddy-viscosity significantly improves the resolution of certain flow scales in the vicinity of the spectral cutoff k_c, effectively restoring the reference DNS energy spectrum function. The impact of the new model

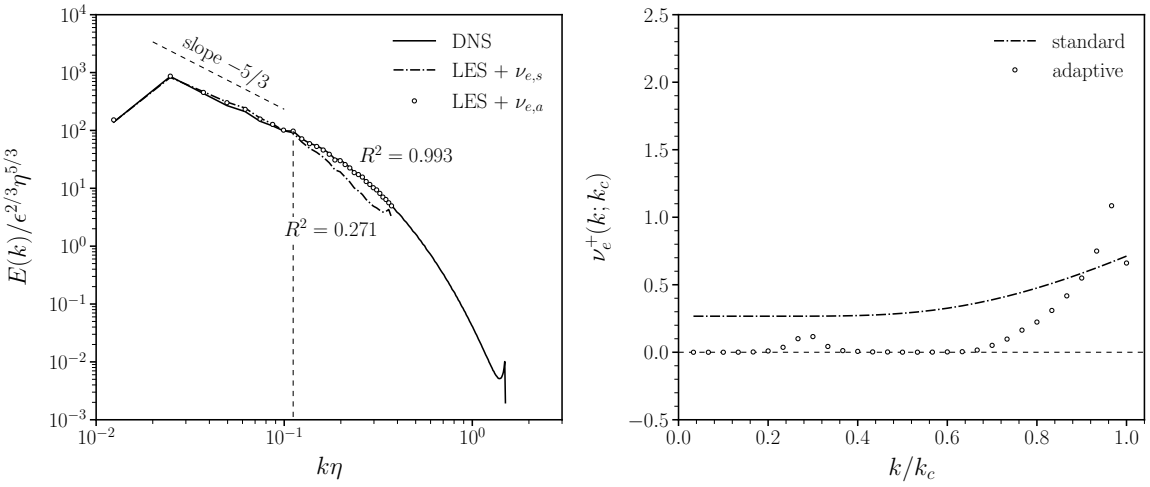

Figure 3.16: The impact of subgrid-scale modeling on the energy spectrum function in LES at $Re_\lambda \sim 100$ (left panel), vertical dashed line points to the step-like artifact; different forms of the spectral eddy-viscosity (right panel).

is quantified using the coefficient of determination R^2 evaluated at the relevant range of flow scales, i.e., $k_c/2 \leq |\boldsymbol{k}| < k_c$. In line with the expectations, the form of the adaptive eddy-viscosity differs both quantitatively and qualitatively not only from the standard formulation but also from the *a priori* one, see Fig. 3.6 (right panel) for comparison[5]. One can also note that the value of $\nu^+_{e,a}(k)$ rapidly drops at $k = k_c$. This results solely from the applied dealiasing method. The spherical truncation already removes a significant part of the energy contained in the smallest resolved wavenumber shell, thus reducing the need for substantial eddy-viscosity.

The bump in $\nu^+_{e,a}(k)$ which starts from $k/k_c \approx 0.2$, see Fig. 3.16 (right panel) or, equivalently, $k\eta \approx 0.1$, essentially corresponds to the minor step-like artifact in the energy spectrum function, see Fig. 3.16 (left panel, vertical dashed line), whose origin remains unclear; however, such artifacts can to some extent result from the lack of smoothing often applied to account for the uneven distribution of modes in wavenumber shells [54], see also Eq. (2.82). From Eq. (3.36), it appears evident that the regulator governs the evolution of $\nu^+_{e,a}(k)$ independently of k, thus, as already indicated, making the adaptively-determined eddy-viscosity particularly susceptible to the local changes in the energy spectrum. However, instead of introducing an additional diffusion-like term in Eq. (3.31), one can consider a model eddy-viscosity given as

$$\nu^+_{e,m}(k,t) = \nu^+_{e,m}(k;k_c;A) = a_0 + a_1\left\{1 - \tanh\left[\left(\frac{k_c - k}{a_2 k_c}\right)^{a_3}\right]\right\}, \tag{3.37}$$

$$A = \arg\min_{A} \sum_{k_t \leq k < k_c} \left[\langle \nu^+_{e,a}(k,t)\rangle - \nu^+_{e,m}(k,t)\right]^2, \tag{3.38}$$

where the set $A = \{a_0, a_1, a_2, a_3\}$ essentially depends on time since the model eddy-viscosity can vary between consecutive fitting intervals; $\langle\cdot\rangle$ here denotes the average over the fitting interval T_f confined to

$$k_c^{-3/2} E_m(k_c)^{-1/2} < T_f < T_e. \tag{3.39}$$

In all simulations, the model eddy-viscosity was determined every $T_f = 0.5T_e$, with $\nu^+_{e,a}(k;k_c)$ being sampled in such a way that at least 10 samples were obtained over the given interval.

In this work, it is also proposed to determine the spatially-smoothed adaptive

[5]In this case quantitative differences are expected for $|\boldsymbol{k}| < k_c/2$ since the adaptive eddy-viscosity is not allowed to take negative values

eddy-viscosity given as

$$\widetilde{\nu}^{+}_{e,a}(k,t) = \gamma\nu^{+}_{e,a}(k,t) + (1-\gamma)\nu^{+}_{e,m}(k,t)B(k;k_t)D(k), \tag{3.40}$$

where $\gamma = 0.75$ for $t = T_f$ and $\gamma = 1$ otherwise. This under-relaxation-like procedure is introduced in order to reduce the disruption of Eq. (3.36) resulting from the spatial smoothing imposed by Eqs. (3.37) and (3.38); $D(k)$ is a simple correction given as

$$D(k) = \begin{cases} \left(\frac{4\pi k^2}{N_k} - 1\right)^{3/2}, & \text{for } k = k_c \\ 1, & \text{otherwise,} \end{cases} \tag{3.41}$$

which is designed to account for the selected dealiasing method, Eq. (2.52); N_k is the number of modes contained in the wavenumber shell centered at k.

In general, the computational overhead of both the regulator and the least-squares fitting given respectively by Eq. (3.36) and Eqs. (3.37) and (3.38), can be completely removed by introducing the concept of an adaptively-reconstructed eddy-viscosity given as

$$\nu^{+}_{e,ar}(k;k_c) = \nu^{+}_{e,m}(k;k_c,A')B(k;k_t)D(k), \tag{3.42}$$

where $\nu^{+}_{e,m}(k;k_c,A')$ is given by Eq. (3.37), however, with the set of unknown coefficients A' determined from

$$A' = \arg\min_{A'} \sum_{k_t \le k < k_c} \left[\langle\widetilde{\nu}^{+}_{e,a}(k,t)\rangle - \nu^{+}_{e,m}(k;k_c;A')\right]^2. \tag{3.43}$$

The angular brackets $\langle\cdot\rangle$ here denote the average over the interval $t \in (5T_e, nT_e]$, where the initial transient period $t \le 5T_e$ is recommended to be dropped; n has to be adjusted based on how quickly the flow reaches statistical stationarity[6]. To clarify, in this approach, the spectral eddy-viscosity is first adaptively determined using Eqs. (3.36) and (3.40) over the time interval $t \in (5T_e, nT_e]$, and subsequently its time-averaged form is transformed into the model eddy-viscosity given by Eq. (3.37), with the set of unknown coefficients given by Eq. (3.43).

From Fig. 3.17 (right panel), it is readily apparent that the spatial smoothing removes the artificial bump previously observed in $\nu^{+}_{e,a}(k;k_c)$ at $k/k_c \approx 0.2$, and that the adaptively-reconstructed eddy-viscosity ensures the reference DNS energy spectrum function is restored with $R^2 = 0.994$ as depicted in Fig. 3.17 (left panel).

From Fig. 3.18, it can be observed that the adaptively-reconstructed eddy-viscosity

[6]Depending on the selected forcing scheme, this time typically varies from 5 up to 15 large eddy turnovers

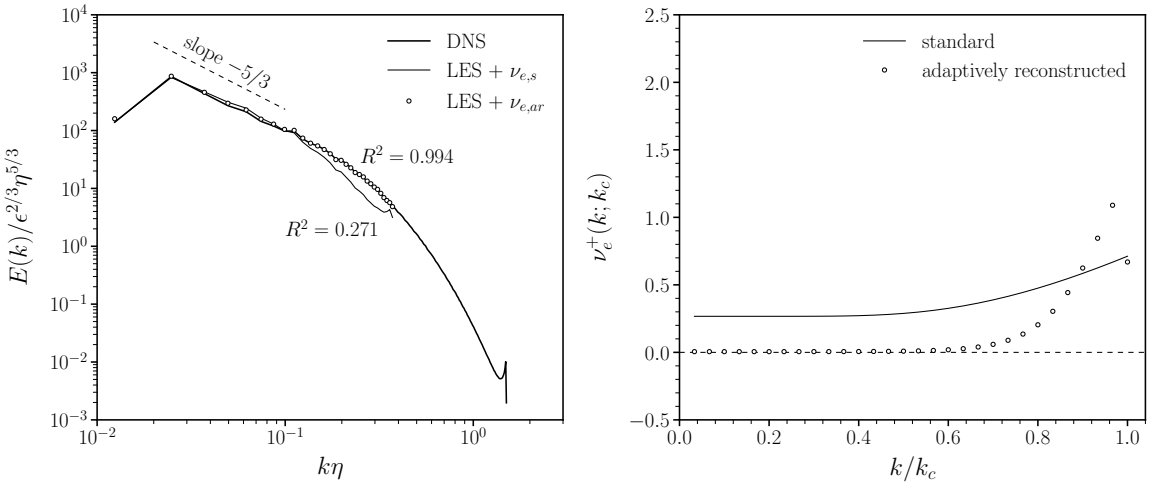

Figure 3.17: The impact of subgrid-scale modeling on the energy spectrum function in LES at $Re_\lambda \sim 100$ (left panel); different forms of the spectral eddy-viscosity (right panel).

slightly enhances the PDF of Q when compared to the LES enriched with the standard model, however, it does not appear to further enrich the resolved flow scales when compared to the LES supplemented with the *a priori* eddy-viscosity, see also Fig. 3.7.

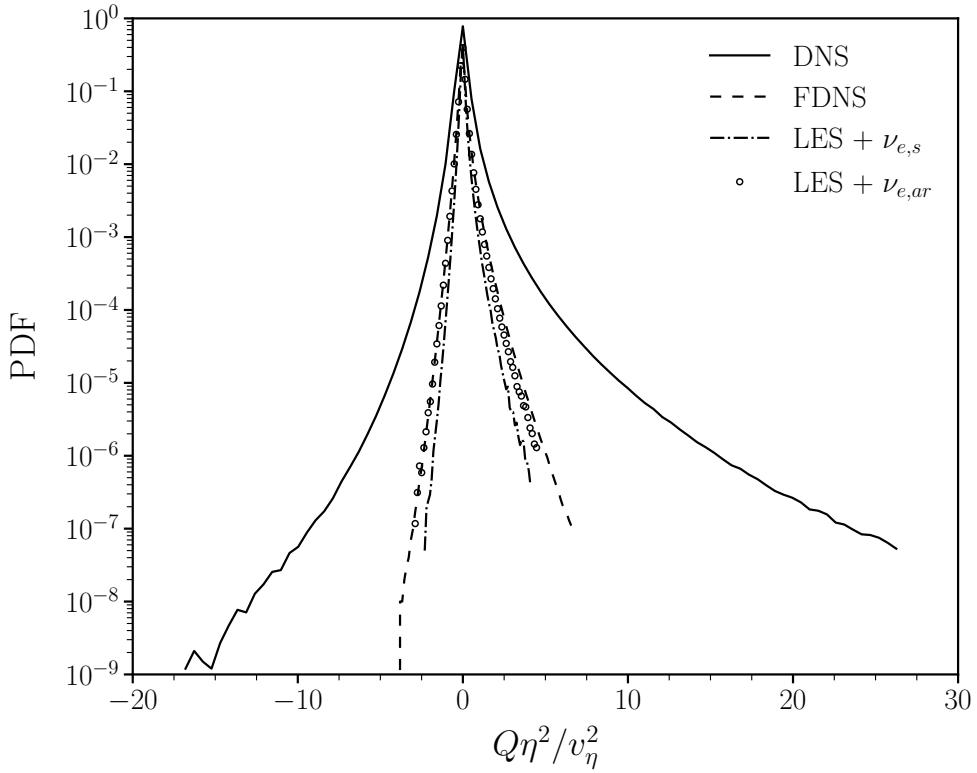

Figure 3.18: The impact of the model spectral eddy-viscosity on the PDF of Q at $Re_\lambda \sim 100$.

In the case of the standard eddy-viscosity, the scaling factor was set to $[E(k_c)/k_c]^{1/2}$, see Eq. (3.20). However, as indicated by the original model proponents [120, 125], although being established based on dimensional analysis, the sole purpose of its functional form is to postpone the drain of energy until it reaches k_c, so that the large flow scales are not suppressed during the initial stage of the simulation. Based on numerical tests, in this work, instead of a single scaling factor based on $E(k_c)/k_c$, a scale-dependent one is proposed to give

$$\nu_e(k;k_c,t) = \nu_e^+(k;k_c)\left[\frac{E(k,t)}{k}\right]^{1/2}. \tag{3.44}$$

It should be noted that the above form has at least a few advantages over the original one given as in Eq. (3.20). That is: (i) it makes the regulator more responsive to the changes in the energy distribution, thus reducing the artifacts (bumps) in the adaptively-determined eddy-viscosity; (ii) taking into account the previous reason, it also improves the fitting in Eqs. (3.38) and (3.43); (iii) it mitigates the impact of the floating-point errors on either $\nu_{e,a}^+(k;k_c)$ or $\nu_{e,ar}^+(k;k_c)$. To clarify the latter reason, one can note that with increasing spatial resolution, the ratio of $E(k_c)/k_c$ tends to 0.

For completeness, one has to address the proper selection of the transition point in Eq. (3.28), see also Fig. 3.14. Consider the energy spectrum function in isotropic turbulence at $Re_\lambda \sim 10000$ with the transition point fixed at $k_t = 0.4k_c$. From Fig. 3.19 (left panel), it appears evident that regardless of the spatial resolution, the adaptively-reconstructed eddy-viscosity ensures the energy is drained from the system

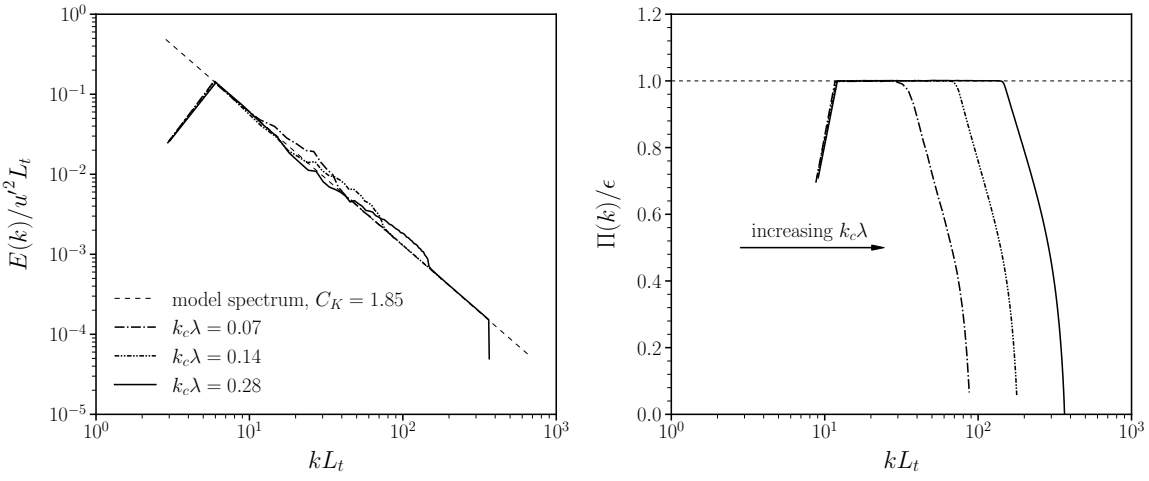

Figure 3.19: The impact of spatial resolution on the energy (left panel) and the energy flux (right panel) spectrum functions in LES at $Re_\lambda \sim 10000$ with the transition point fixed at $k_t = 0.4k_c$.

at approximately correct rate for $k \geq k_c/2$, or, equivalently, $kL_t \gtrapprox 175$. Although in this range the energy spectrum function strictly follows the $k^{-5/3}$ scaling, the energy is not transferred independently of viscosity, which leads to $\Pi(k) \neq \epsilon$. This essentially means that the inertial subrange is to some extent numerically suppressed, see Fig. 3.19 (right panel), due to excessive eddy-viscosity, which, in turn, follows from insufficient spatial resolution. For the fixed transition point and Reynolds number, increasing k_c effectively increases the range of flow scales for which $\Pi(k) = \epsilon$; however, possibly due to the insufficient range of flow scales where $\nu_e(k) > 0$, the energy accumulates in wavenumbers preceding $k_c/2$.

From Fig. 3.20 (left panel), it is readily apparent that for the fixed spatial resolution and Reynolds number, decreasing k_t significantly improves the energy distribution over the range of wavenumbers preceding $k_c/2$, or, equivalently, $kL_t \lessapprox 175$. It is worth noting that for $k_t = 0.1k_c$, the energy spectrum function shows a relatively good agreement with the reference one; however, in this case at most 15% of the resolved flow scales exhibit the characteristics of the inertial subrange, i.e., $\Pi(k) = \epsilon$, see also Fig. 3.20 (right panel).

In this work, it is postulated that a certain range of flow scales in the LES enriched with the scale-dependent eddy-viscosity can be considered well-resolved on condition that the corresponding eddy-viscosity is approximately 0, or, in other words, their evolution is not constrained (suppressed) by an artificially increased viscosity. Moreover, it appears that the onset of the inertial subrange can only be captured quantitatively on condition that a sufficiently large separation between k_t and k_c is ensured. Based

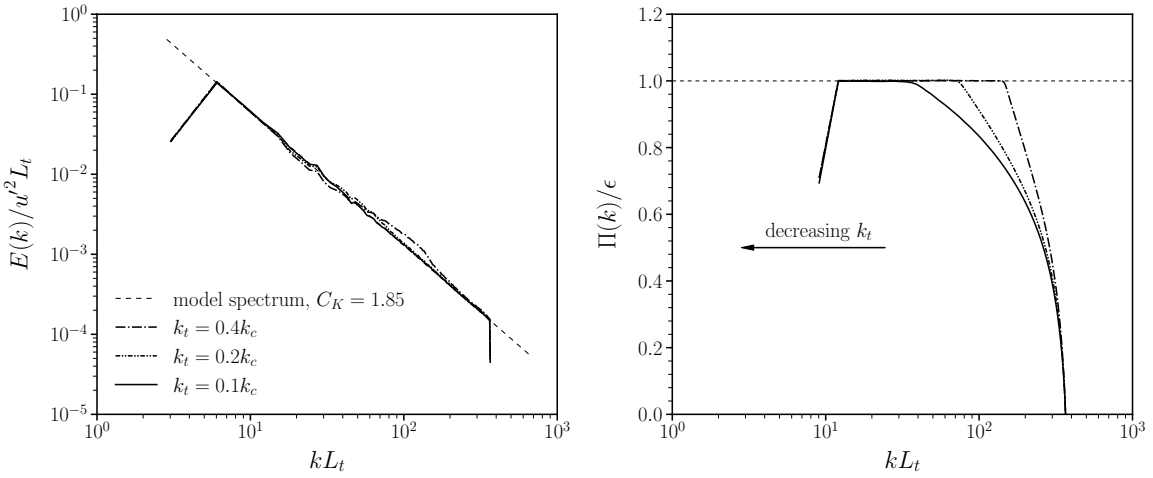

Figure 3.20: The impact of the transition point on the energy (left panel) and the energy flux (right panel) spectrum functions in LES at $Re_\lambda \sim 10000$ with the spatial resolution fixed at $k_c\lambda = 0.28$.

on the above reasoning, the following condition can be proposed

$$k_f < k_t \lesssim 0.1 k_c, \tag{3.45}$$

see also Eq. (3.28) for comparison. On the other hand, assuming that the Taylor microscale λ defines the conceptual lower limit of the inertial subrange, it appears that the LES of isotropic turbulence can be considered well-resolved on condition that the relevant range of flow scales display the characteristics of the inertial subrange. This implies $k_t \sim 1/\lambda$, and thus, using Eq. (3.45), $k_c\lambda \sim 10$. Interestingly, for a typical cloud conditions, say at $Re_\lambda \sim 10000$, it means that resolving almost the entire inertial subrange without the need for an artificially increased viscosity would require between $\sim 8192^3$ and $\sim 16384^3$ nodes; one can compare this to the required spatial resolution of approximately $\sim 262144^3$ nodes in the corresponding hypothetical DNS, see also Table 3.1. It should be emphasized that such large-scale simulations have recently become possible with the use of modern high-performance computing clusters, see, e.g., [129, 130, 131, 139].

3.8 Concluding remarks

This Chapter outlined the most important steps in developing an accurate pseudo-spectral LES solver for isotropic turbulence. Due to relatively limited resources relevant to this very matter, this part of the research was intended to: (i) establish a reliable methodology and good practices concerning the pseudo-spectral LES of isotropic turbulence, specifically at high Reynolds numbers; (ii) assess the overall ability of LES to capture the inertial range dynamics; (iii) assess the performance and the scope of application of the well-known, scale-dependent eddy-viscosity closures for the filtered Navier-Stokes equations in Fourier space; (iv) develop a computationally affordable spectral eddy-viscosity closure and assess its impact on the evolution of large flow scales at high Reynolds numbers; (v) gather reliable reference data for the research concerning particle-laden flows. A summary of what appear to be the most important achievements and contributions of this part of the research is provided in the following paragraphs.

First, this chapter provided a concise, organized and focused introduction to the pseudo-spectral LES of isotropic turbulence, particularly concerning the issues associated with the spatial filtering of the governing Navier-Stokes equations. It has been pointed out that: (i) there are relatively few subgrid-scale models developed in Fourier space, and that (ii) most of the research conducted to date was confined to rather

small Reynolds numbers, say $Re_\lambda < 200$, for which the DNS can be performed with ease. To extend the latter conclusion, it has been pointed out that the outcomes of those research studies provided neither (iii) new insights into the dynamics of large flow scales, particularly those relevant to the inertial subrange, nor (iv) any guidance regarding the possible use of LES to study the physics underlying turbulent flows at high Reynolds numbers.

Second, the LES enriched with the standard spectral eddy-viscosity, as proposed by Chollet & Lesieur [120], was compared against the reference DNS at low Reynolds number. In line with other studies, it has been confirmed that spatial filtering significantly attenuates turbulence, even though the LES at $Re_\lambda \sim 100$ accounts for approximately 96% of the total kinetic energy (Section 3.4, p. 58); however, it has been concluded that the overall quality of the simulated turbulence is satisfactory. Using the method proposed in [132], the *a priori* spectral eddy-viscosity was determined by means of the *a priori* LES (FDNS) and, to the best of the author's knowledge, applied for the first time as a subgrid-scale model in the *a posteriori* LES (Section 3.5, p. 61). It has been shown that: (i) the functional form of the *a priori* spectral eddy-viscosity significantly differs (qualitatively and quantitatively) from the standard one; (ii) both the reference (DNS) energy spectrum function within the resolved range of flow scales and the reference (FDNS) PDF of Q can be well recovered; (iii) while the *a priori* spectral eddy-viscosity is a reliable subgrid-scale model, which allows to enhance the energy distribution near the spectral cutoff with ease, it has no real predictive value at Reynolds numbers exceeding those achievable in the DNS. On the other hand, to extend the latter conclusion, it has to be emphasized that: (i) the LES enriched with the *a priori* spectral eddy-viscosity can provide insights into the physics of large flow scales comparable to those provided by the corresponding DNS, but at significantly lower computational cost; (ii) usually multiple particle-laden simulations are performed based on the same statistically stationary solution, and thus such LES has the potential to provide new insights into the dynamics of inertial particles suspended in a turbulent flow.

Third, the performance of the LES enriched with the standard spectral eddy-viscosity has been assessed in isotropic turbulence at high Reynolds numbers, with a particular emphasis on its ability to capture the inertial range dynamics. This was motivated by a recent comment made in [123], suggesting that the LES with a scale-dependent eddy-viscosity and the spatial resolution of 64^3 can recover the characteristic features of the inertial subrange in isotropic turbulence at $Re_\lambda \sim 10000$. From the current research it has been concluded that: (i) most results are in satisfactory agreement with the Kolmogorov theory of turbulence (Section 3.6, p. 65); (ii) the over-

all quality of the large-scale velocity field is generally good, particularly concerning its isotropy, the longitudinal and transverse velocity autocorrelation functions, and also the non-Gaussian nature of the PDF of Q; (iii) although the LES develops the energy spectrum function which approximately follows the $k^{-5/3}$ scaling, the energy is not transferred independently of viscosity, $\Pi(k) \neq \epsilon$, and thus the development of the inertial subrange is essentially suppressed even at $Re_\lambda \sim 10000$ (with the spatial resolution of 256^3 nodes (Section 3.6, p. 68); (iv) the functional form of the standard eddy-viscosity appears to be suboptimal regardless of the Reynolds number. Presumably, one of the most important conclusions to be drawn from this Chapter is that capturing the inertial range dynamics in LES of isotropic turbulence (at high Reynolds number) heavily depends on both the spatial resolution and the functional form of the spectral eddy-viscosity. In particular, it has been pointed out that an excessive dissipation, essentially suppressing the development of the correct large-scale dynamics, follows from the positive plateau in the spectral eddy-viscosity, whose existence was suggested in [91, 99, 120, 125]; however, somewhat contrary to those research studies, in this dissertation it is postulated that (i) the positive plateau is highly undesirable and (ii) its existence is a strong indication of an insufficient spatial resolution.

Fourth, an alternative approach to modeling the spectral eddy-viscosity in LES of isotropic turbulence has been proposed. The new model: (i) is based on a simple differential regulator, which governs the evolution of the scale-dependent eddy-viscosity (Section 3.7, p. 77); (ii) introduces a small number of adjustable parameters, which, in general, have a negligible impact on the final outcomes; (iii) requires a predefined reference energy spectrum, which, however, can be obtained from experimental measurements, numerical simulations or the well-established model spectra; (iv) has a negligible computational overhead when compared to both the pure LES and the LES enriched with either the standard model or the recently developed spectral eddy-viscosity models [99, 137], which rely on computationally intensive evaluations of the non-linear energy transfers. In addition to the above, the adaptively-determined spectral eddy-viscosity: (i) differs both qualitatively and quantitatively from the standard one (Section 3.7, p. 62); (ii) shows good qualitative agreement with the *a priori* eddy-viscosity, particularly concerning the prediction of both the "cusp" behavior near k_c [91] and the spectrally-vanishing nature for approximately $k < k_c/2$ [80], without relying on any specific assumptions; (iii) allows to recover the predefined energy spectrum with the coefficient of determination $R^2 > 0.99$ for $k_c/2 < k < k_c$, thus significantly enhancing the energy distribution near the spectral cutoff when compared to both the pure LES and the one enriched with the standard model (Section 3.7, p. 62); (iv) allows to recover the reference (FDNS) PDF of Q at $Re_\lambda \sim 100$. Con-

trary to [91, 99, 120], however in line with [80, 140, 141, 142], the current research strongly suggests that accurate modeling of large flow scales in isotropic turbulence does not imply the need for artificially increased viscosity. Based on this reasoning, a new functional form of the spectral eddy-viscosity was proposed, whose unknown coefficients can be determined with ease using the least-squares fitting (Section 3.7, p. 78). The performance of the newly developed model has been assessed at high Reynolds numbers. Presumably, the most important conclusions from this study are that: (i) the spectral LES of isotropic turbulence can capture the inertial range dynamics on condition that sufficient spatial resolution is ensured, say on the order of $k_c\lambda \sim 10$; (ii) the spatial resolution of at most $\sim 16384^3$ nodes is arguably sufficient to resolve almost the entire inertial subrange at $Re_\lambda \sim 10000$ (Section 3.7, p. 83). To extend the latter conclusion, it should be emphasized that although such resolution remains computationally demanding, the LES enriched with a scale-dependent eddy-viscosity can provide reliable insight into the physics of large flow scales, specifically within the range of Reynolds numbers relevant to many environmental phenomena or industrial processes.

When compared to the DNS, the current LES requires only one additional input parameter, i.e., the value of the Kolmogorov constant C_K. It should be once again emphasized that this parameter can be determined experimentally. On the other hand, it is also worth noting that the value of C_K can be determined on-the-fly from the compensated energy spectrum, simply making the LES standalone, or fully-autonomous, so to speak; however, in the case of the pseudo-spectral solution of the statistically stationary isotropic turbulence confined to a cubic box of size L_B, there is virtually no need for such an over-engineered approach.

The resolution of all scales of fluid motion at Reynolds numbers relevant to many environmental phenomena or industrial processes is likely to be beyond hope. Therefore, it seems that the computational tractability of LES along with its subgrid-scale closure should be as important as its physical correctness, so to speak. Although this Chapter was focused on the functional modeling, which often introduces some empiricism, such models appear to accurately mimic certain physical phenomena, e.g., the energy transfer from large to small flow scales. After all, as noted by Pope [134], "perhaps the holy grail of turbulence is *the statistical resolution of all scales* [...]".

Chapter 4

Lagrangian particle tracking

4.1 Equations of particle motion

Consider a small, non-deformable sphere of radius a and mass m_p centered at $\boldsymbol{x}_p(t)$, that is moving with velocity $\boldsymbol{V}[\boldsymbol{x}_p(t), t]$ in an undisturbed flow whose velocity field $\boldsymbol{u}(\boldsymbol{x}, t)$ satisfies the solenoidal Navier-Stokes equations[1]. Building upon the somewhat pioneering work of Tchen [143], Corrsin & Lumley [144] proposed the following equation of particle motion

$$\begin{aligned} m_p \frac{\mathrm{d}V_\alpha}{\mathrm{d}t} &= m_f \left(\frac{\mathrm{D}u_\alpha}{\mathrm{D}t} - \nu \nabla^2 u_\alpha \right)_{\boldsymbol{x}_p(t)} \\ &\quad - \frac{1}{2} m_f \frac{\mathrm{d}}{\mathrm{d}t} \left\{ V_\alpha(t) - u_\alpha[\boldsymbol{x}_p(t), t] \right\} \\ &\quad - 6\pi a \mu \left\{ V_\alpha(t) - u_\alpha[\boldsymbol{x}_p(t), t] \right\} \\ &\quad - 6\pi a^2 \mu \int_{-\infty}^{t} \frac{\mathrm{d}/\mathrm{d}\tau \left\{ V_\alpha(\tau) - u_\alpha[\boldsymbol{x}_p(\tau), \tau] \right\}}{\sqrt{\pi \nu (t - \tau)}} \mathrm{d}\tau \\ &\quad + (m_p - m_f) g_\alpha, \end{aligned} \tag{4.1}$$

where m_f is the mass of fluid displaced by the sphere and μ is the dynamic viscosity of the fluid; $u_\alpha[\boldsymbol{x}_p(t), t]$ are the Cartesian components of the local fluid velocity at the particle location. At this point, it is important to distinguish between the time derivative $\mathrm{d}/\mathrm{d}t$ following the moving sphere and the time derivative following a fluid element $\mathrm{D}/\mathrm{D}t$. Hence,

$$\frac{\mathrm{d}}{\mathrm{d}t} u_\alpha \left[\boldsymbol{x}_p(t), t \right] = \left(\frac{\partial u_\alpha}{\partial t} + V_\beta \frac{\partial u_\alpha}{\partial x_\beta} \right)_{\boldsymbol{x}_p(t)} \tag{4.2}$$

[1] Particle size is considered small when compared to the smallest length scales of a turbulent flow, i.e., $a \ll \eta$

denotes the time derivative of the fluid velocity, and

$$\frac{\mathrm{D}u_\alpha}{\mathrm{D}t} = \left(\frac{\partial u_\alpha}{\partial t} + u_\beta \frac{\partial u_\alpha}{\partial x_\beta}\right)_{\boldsymbol{x}_p(t)} \tag{4.3}$$

is the fluid acceleration evaluated at the center of the sphere. The terms on the right-hand side of Eq. (4.1) correspond to the effects of pressure gradient of the undisturbed flow, added mass, viscous Stokes drag, the history of particle acceleration, gravity and buoyancy, respectively. As pointed out by Riley [145], for a sphere smaller than the length scale of the disturbance flow induced by its motion, the effects of viscous shear stress may be comparable to those of pressure gradient of the undisturbed flow. Under the assumption that the net effect must be equal to the product of fluid mass and its local acceleration, the author suggested that the first term on the right-hand side of Eq. (4.1) should rather be replaced with

$$m_f \left.\frac{\mathrm{D}u_\alpha}{\mathrm{D}t}\right|_{\boldsymbol{x}_p(t)}. \tag{4.4}$$

Assuming that particles are isolated (in the sense that both particle-particle and particle-boundary interactions are excluded), and that the Reynolds number of the disturbance flow induced by the particle motion is sufficiently low[2], Maxey & Riley [146] put forward the following equation of particle motion

$$\begin{aligned} m_p \frac{\mathrm{d}V_\alpha}{\mathrm{d}t} = {} & m_f \left.\frac{\mathrm{D}u_\alpha}{\mathrm{D}t}\right|_{\boldsymbol{x}_p(t)} \\ & - \frac{1}{2} m_f \frac{\mathrm{d}}{\mathrm{d}t}\left\{V_\alpha(t) - u_\alpha[\boldsymbol{x}_p(t),t] - \frac{1}{10}a^2\nabla^2 u_\alpha\Big|_{\boldsymbol{x}_p(t)}\right\} \\ & - 6\pi a\mu\left\{V_\alpha(t) - u_\alpha[\boldsymbol{x}_p(t),t] - \frac{1}{6}a^2\nabla^2 u_\alpha\Big|_{\boldsymbol{x}_p(t)}\right\} \\ & - 6\pi a^2\mu\int_0^t \frac{\mathrm{d}/\mathrm{d}\tau\left\{V_\alpha(t) - u_\alpha[\boldsymbol{x}_p(t),t] - \frac{1}{6}a^2\nabla^2 u_\alpha\Big|_{\boldsymbol{x}_p(t)}\right\}}{\sqrt{\pi\nu(t-\tau)}}\mathrm{d}\tau \\ & + (m_p - m_f)g_\alpha, \end{aligned} \tag{4.5}$$

where the Faxen corrections [147] were included to account for the finite size of the particle, and thus also the spatial variability of the velocity field at this very length scale. Auton et al. [148] indicated that in certain situations the added mass term

[2]So that the fluid forces exerted on the particle surface can be determined from the results of unsteady Stokes flow

given as in Eq. (4.5) is incorrect and should be replaced with

$$\frac{1}{2}m_f\left(\frac{\mathrm{d}V_\alpha}{\mathrm{d}t}-\left.\frac{\mathrm{D}u_\alpha}{\mathrm{D}t}\right|_{\boldsymbol{x}_p(t)}\right). \tag{4.6}$$

As pointed out by Maxey & Riley, however, there is no distinction between the two in the low Reynolds number approximation.

In addition to the foregoing reasoning, if the particle density ρ_p is much larger than that of the fluid, $\rho_p/\rho \gg 1$, then the Maxey-Riley equation of motion takes the simplified form given as

$$\begin{aligned}\frac{\mathrm{d}V_\alpha}{\mathrm{d}t} &= -f_D\frac{V_\alpha - u_\alpha[\boldsymbol{x}_p(t),t]}{\tau_p}+g_\alpha\\ \frac{\mathrm{d}x_{p,\alpha}}{\mathrm{d}t} &= V_\alpha,\end{aligned} \tag{4.7}$$

where $\tau_p = 2\rho_p a^2/9\mu$ is the particle response time [11] and f_D is a non-dimensional coefficient which accounts for the deviations from Stokes' law.

Consider a non-dimensional parameter

$$Re_p = \frac{|\boldsymbol{w}|d}{\nu}, \tag{4.8}$$

where $\boldsymbol{w} = \boldsymbol{V} - \boldsymbol{u}[\boldsymbol{x}_p(t),t]$ is the particle-fluid relative velocity. This parameter is often referred to as particle Reynolds number and can be used to identify different flow regimes in the vicinity of each particle [149]. It is well known that for $Re_p > 0.1$, the drag coefficient of a spherical particle deviates from the one determined in the Stokes regime. To account for those discrepancies, Schiller & Naumann [150] put forward an empirical correction given as

$$f_D = 1 + 0.15Re_p^{0.687} \qquad Re_p < 1000. \tag{4.9}$$

Moreover, it is worth mentioning that other empirical corrections can be found for different flow regimes or particles.

4.2 Fluid velocity at the particle location

As already mentioned, to solve the equation of motion given by Eq. (4.7), the fluid velocity at the particle location must be determined beforehand. If the fluid velocity is expanded in the Fourier series given by Eq. (2.11), as it is in the case of both the pseudo-spectral DNS and LES, then the local fluid velocity at the particle location

can be determined simply by summing the series. Although this approach provides the highest possible accuracy, its computational overhead grows with increasing number of modes, thus making the method unsuitable for the majority of applications. However, in the case of the pseudo-spectral approximation, the fluid velocity is readily available in physical space, and therefore interpolation to the particle location should be relatively straightforward. Riley & Patterson [151] used a linear interpolation to determine single-particle statistics of both fluid and small-inertia particles in decaying isotropic turbulence. Part of this work was further extended by Yeung & Pope [71] who carefully quantified the interpolation errors and concluded that the accuracy of a simple linear interpolation is insufficient if Lagrangian statistics of fluid particles are considered, e.g., velocity autocorrelation or structure functions. Assuming sufficient spatial resolution of the velocity field, the authors indicated that these statistics can be accurately predicted on condition that particle velocities are determined using either cubic splines or the 13-point, third-order Taylor series interpolation. This issue was also thoroughly examined by Balachandar & Maxey [152] who studied the impact of various interpolation schemes on two-particle statistics, with a particular emphasis on turbulent dispersion where accurate determination of particle relative velocities is essential. From a wide range of existing approaches, the authors compared the 6^{th} order Lagrange and Hermite [153] interpolation methods and concluded that the latter approach gives more accurate results in terms of both particle displacement and relative velocities. It is worth noting that the Lagrange interpolation has been extensively used in many research studies concerning the motion of discrete particles suspended in a turbulent flow. This includes not only the turbulent diffusion of fluid particles [66] but also collision-related statistics of inertial particles for which particle-particle aerodynamic interactions were either considered [85, 86] or neglected [40]. Recently, this interpolation method was used to study particle collisions considering not only the two-way momentum coupling [68, 83] but also particle-scale interactions [67], and even non-continuum molecular effects [84]. Regrettably, although accurate determination of both particle displacements and particle relative velocities is of key importance in predicting two-particle statistics, none of the aforementioned research studies provided a rigorous (if any) evaluation of the interpolation errors incurred in the process. Ireland [16] extensively studied the impact of various interpolation methods on particle velocity in forced isotropic turbulence, particularly concerning the linear, Hermite, Lagrange and B-spline [154] interpolation. For the latter two methods, 4, 6, 8, and 10 neighboring points were used. The author compared interpolated velocities against the spectral summation and concluded that the 8-point B-spline interpolation provides the best trade-off between accuracy and computational efficiency.

It is also important to note that if the two-way momentum coupling is considered, then the interpolation must be "reversible", so to speak. To clarify, one can distinguish between "forward" and "backward" interpolation. The former one is used to determine the fluid velocity at the particle location, whereas the latter type is used to approximate the contribution to the fluid momentum source term from the particulate phase. Hence, both methods must be symmetric [155] in order to ensure the conservation of energy. Carbone [59] studied the B-spline interpolation with a particular emphasis on the two-way momentum coupling and concluded that this interpolation method provides significantly better results when compared to other, lower-order but most commonly used ones.

4.3 B-spline interpolation

As indicated by Yeung & Pope [69, 71] and Balachandar & Maxey [152], high-order interpolation is essential if the Lagrangian particle tracking is considered. For the sake of simplicity, this section is primarily focused on one-dimensional interpolation; however, it should be emphasized that its generalization to higher dimensions can be usually accomplished in a straightforward manner. The interpolation method is typically selected so as to achieve a reasonable balance between the order of convergence, order of continuity, and the computational cost.

High order of convergence can be obtained using for example the well-established Lagrange interpolation in which the highest possible degree of the polynomial function is $m = M - 1$; M is basically the number of points between which the function is interpolated. One can note that if the interpolating polynomial is defined globally along a given direction, then $M = N \gg 1$; N is the corresponding number of grid points. It should be emphasized that high-order polynomials are prone to oscillations [156], a behavior most often referred to as Runge's phenomenon. This issue can be effectively mitigated using for example a piecewise polynomial interpolation in which the interpolator is defined locally over $M \ll N$ points. However, in this case the order of continuity for the Lagrange interpolation is merely C^0 [154] (each polynomial is defined locally over M points, and thus the continuity of its derivatives between the interpolation segments is not guaranteed). On the other hand, both spline and Hermite interpolation provide polynomials of degree $M-1$, and, contrary to the Lagrange interpolation, ensure high order of continuity, that is equal to $(M-2)/2$. In general, the Hermite interpolation is more expensive due to the fact that in addition to function values, one must also evaluate the first derivatives of the interpolated function at the grid points. In the case of pseudo-spectral codes, it implies $(M/2)^3$ additional

DFTs. Based on the above, it can be concluded that out of the three aforementioned methods, an M-point spline interpolation is preferred (or at least seems sufficient) in terms of determining the fluid velocity at the particle location. On the other hand, in this case a $(M+2) \times (M+2)$ tridiagonal matrix must be inverted for each particle at every time step.

The aim of this Section is to introduce an interpolating spline composed of continuous piecewise polynomial functions of degree m, with continuous derivatives up to order $m-1$ at the knots, i.e., the joining points of the polynomials. This can be achieved using the B-spline interpolation. Recently, this method has been extensively used in the context of particle-laden isotropic turbulence, see, e.g. [16, 18, 59] and the references therein. In should be emphasized that this approach is particularly well suited for pseudo-spectral codes. To get a general overview of this interpolation method as well as some information regarding its accuracy and efficient implementation, one can refer to [154]. Most often, unfortunately, the B-spline interpolation is discussed rather superficially, which essentially leads to insufficient (or even confusing in some places) descriptions of its implementation. This Section aims at providing a comprehensive introduction to the B-spline interpolation, with a particular emphasis on cubic B-splines; however, it should be clarified that all derivations given below are of general form. It is also worth mentioning that the reason for selecting the B-splines of degree $m = 3$ is twofold: (i) while Ireland [16] suggested the use B-splines of degree $m = 7$, in practice, no significant increase in the accuracy is observed for B-splines of degrees higher than $m = 3$ [59] (Maurizio Carbone, personal communication); (ii) limited computational resources available during this work.

Consider a strictly increasing sequence of knot points given as

$$x_0 < x_1 < \cdots < x_{m+1}, \tag{4.10}$$

with a uniform spacing between the knots, that is, $h = x_{i+1} - x_i$ for $i = 0, 1, \ldots, m$, and a normalized B-spline of degree 0 given as

$$B_{i,0}(x) = \begin{cases} 1, & x_i \leq x < x_{i+1}, \\ 0, & \text{otherwise.} \end{cases} \tag{4.11}$$

In addition to that, B-splines of degree $m > 0$ can be defined using the Cox-de Boor[3]

[3]An interesting fact is that Cox [157] and de Boor [158] independently proposed the recursive definition of B-splines

recursive formula, see also Fig. 4.1 (left panel), expressed as

$$B_{i,m}(x) = \frac{x - x_i}{x_{i+m} - x_i} B_{i,m-1}(x) + \frac{x_{i+m+1} - x}{x_{i+m+1} - x_{i+1}} B_{i+1,m-1}(x). \tag{4.12}$$

It is important to note that $B_{i,m}(x)$ are linearly independent, and thus may form a basis for the space of spline functions of degree at most m with knots given as

$$x_0 < x_1 < \cdots < x_{N-1}, \tag{4.13}$$

where $N \geq m + 2$. Adding additional $2m$ knots such that

$$x_{-m} < \cdots < x_{-1} < x_0; \quad x_{N-1} < x_N < \cdots < x_{N-1+m}, \tag{4.14}$$

the spline function $\phi_m(x)$ of degree m can be uniquely expressed as

$$\phi_m(x) = \sum_{i=-m}^{N-2} c_i B_{i,m}(x) \qquad \text{for} \quad x \in [x_0, x_{N-1}], \tag{4.15}$$

where c_i are the spline coefficients [159]. In addition to that, the basis functions $B_{i,m}(x)$ form a partition of unity given as

$$\sum_{i=-m}^{N-2} B_{i,m}(x) = 1, \tag{4.16}$$

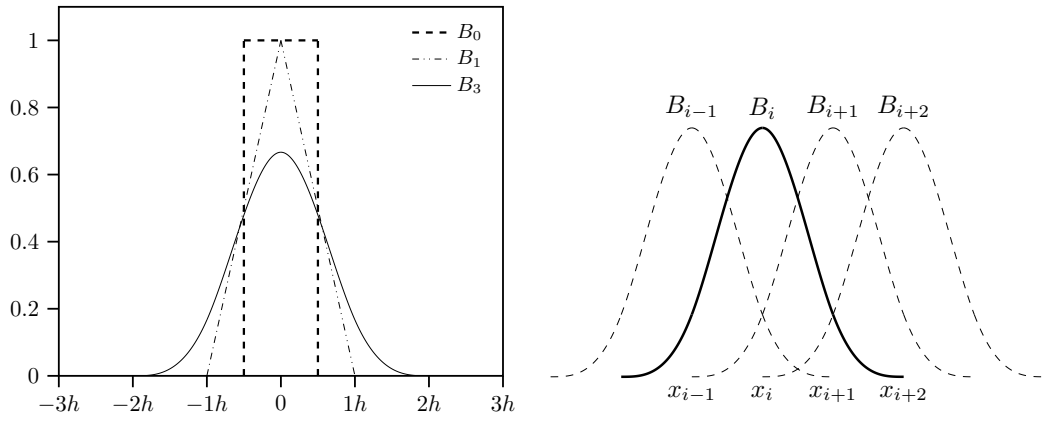

Figure 4.1: B-splines with equally-spaced knot points centered at 0 (left panel); shifting of the i-th B-spline of degree 3 (right panel).

and the i-th B-spline satisfies the following property

$$B_{i,m} = B_{0,m}(x - x_i) = B_m(x - x_i), \tag{4.17}$$

where $B_m(x)$ is the (centered at 0) symmetrical B-spline of degree m defined below, see also Fig. 4.1 (right panel). With the substitution of Eq. (4.17) into Eq. (4.15), one obtains

$$\phi_m(x) = \sum_{i=-m}^{N-2} c_i B_m(x - x_i) \qquad \text{for} \quad x \in [x_0, x_{N-1}], \tag{4.18}$$

where the spline coefficients need to be determined from the interpolation condition which can be expressed as

$$\phi_m(x_j) = u(x_j) \qquad \text{for} \quad x_j = j \ (j = 0, 1, \ldots, N-1), \tag{4.19}$$

where u is the interpolated function, e.g., the fluid velocity. At this point, it is important to note that x was essentially rescaled so that the grid spacing becomes unity[4]. With the substitution of Eq. (4.19) into Eq.(4.18), one obtains

$$\phi_m(x_j) = u(x_j) = \sum_{i=-m}^{N-2} c_i B_m(x_j - x_i) \qquad \text{for} \quad x_j = j \ (j = 0, 1, \ldots, N-1). \tag{4.20}$$

It should be emphasized that due to both the periodicity of the interpolated function and the compact support of B-splines, the foregoing summation may be extended so as to account for all integer coordinates $i \in \mathbb{Z}$ [160]. For this reason, Eq. (4.20) can be rewritten as

$$u(x_j) = (c *_N b_m)(x_j) \qquad \text{for} \quad x_j = j \ (j = 0, 1, \ldots, N-1), \tag{4.21}$$

where $(*_N)$ denotes a circular convolution; b_m is the discrete B-spline, which, following Unser et al. [161], can be obtained by sampling the continuous B-spline according to

$$b_m(x_j) \overset{\text{def}}{=} B_m(x_j) \qquad \text{for} \quad x_j = j \ (j = 0, 1, \ldots, N-1). \tag{4.22}$$

However, as indicated in [154], it is more convenient to define the discrete B-spline of

[4]Note that $x \in [0, L_B]$, thus dividing L_B into N equal segments of length $\Delta x = L_B/N$, one obtains a discrete grid with N points such that $x_j/\Delta x = j$ for $j = 0, 1, \ldots, N-1$; the last grid point is essentially omitted due to periodicity

degree m as

$$b_m(x_j) = \begin{cases} B_m(x_j), & x_j < \frac{N}{2}, \\ B_m(x_j - N), & x_j \geq \frac{N}{2}, \end{cases} \qquad \text{for} \quad x_j = j \ (j = 0, 1, \ldots, N-1), \tag{4.23}$$

where $B_m(x)$ can be determined as in [162]

$$B_m(x) = \sum_{j=0}^{m+1} \frac{(-1)^j}{m!} \binom{m+1}{j} \left(x + \frac{m+1}{2} - j \right)^m \times H\left(x + \frac{m+1}{2} - j \right) \qquad \text{for} \quad x \in R, \tag{4.24}$$

with $H(x)$ being the unit step function given as

$$H(x) = \begin{cases} 0, & x < 0, \\ 1, & x \geq 0. \end{cases} \tag{4.25}$$

Hence, taking advantage of the convolution theorem and using the DFT, the spline coefficients can be obtained from

$$c = \mathcal{F}^{-1}(\hat{u}/\hat{b}_m), \tag{4.26}$$

where the Fourier-transformed discrete B-spline $\hat{b}_m$ can be determined *a priori* using Eqs. (4.23) and (4.26). In addition to the above, it should be emphasized that for any interval $[x_i, x_{i+1})$ at most $m+1$ summands in Eq. (4.18) are not zero. This leads to

$$\phi_m(x) = \sum_{j=i+\frac{1-m}{2}}^{i+\frac{1+m}{2}} c_j B_m(x - x_j) \qquad \text{for} \quad x \in [x_i, x_{i+1}) \ (i = 0, 1, \ldots, N-2), \tag{4.27}$$

where the periodic boundary condition can be taken into account by simply replacing the subscript j with j mod N. Based on the above reasoning, the fluid velocity at the particle location can be expressed as

$$u(x_p) = \sum_{j=i+\frac{1-m}{2}}^{i+\frac{1+m}{2}} c_j B_m(x - x_j)\Big|_{x_p} \qquad \text{for} \quad x_p \in [x_i, x_{i+1}) \ (i = 0, 1, \ldots, N-2). \tag{4.28}$$

Alternatively, the B-spline weights given by $B_{j,m}(x_p)$ can be determined at the neighboring grid nodes once the B-spline is centered at the particle location, see Fig. 4.2. In addition to that, it seems important to note that the discrete sequence of spline

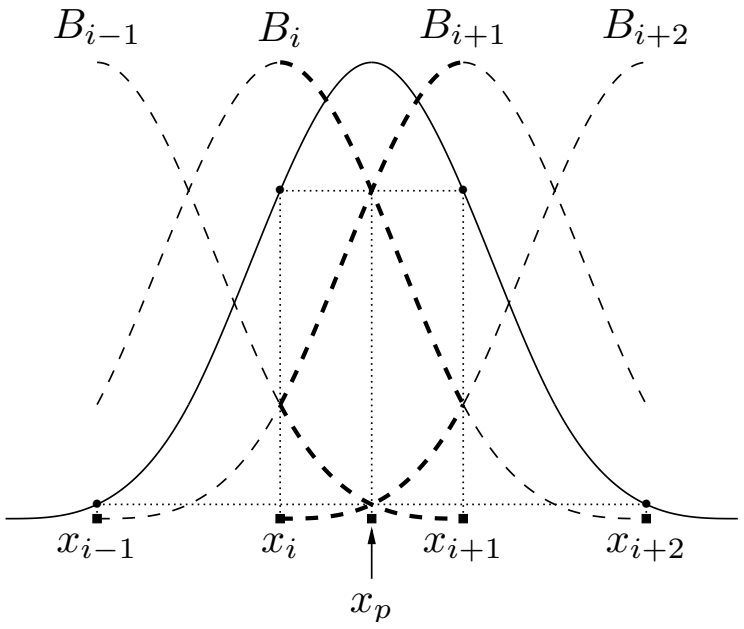

Figure 4.2: Evaluating B-spline weights at adjacent grid points. Thick dashed lines define the interpolating spline on any interval $[x_i, x_{i+1})$; solid line denotes the symmetrical B-spline of degree 3 shifted to the particle location x_p; the location of x_p relative to the adjacent nodes is arbitrary.

coefficients, $\{c_j\}$, can be viewed as a train of weighted delta functions [154], and thus Eq. (4.28) can be rewritten as

$$u(x_p) = \Big[c * B_m\Big](x_p) \qquad \text{for} \quad x_p \in \mathbb{R}, \tag{4.29}$$

which denotes a convolution of spline coefficients with the B-spline of degree m, evaluated at x_p. Due to the compact support of B-splines and with the use of Eq. (4.22), the above convolution reduces to

$$u(x_p) = \sum_{j=i+\frac{1-m}{2}}^{i+\frac{1+m}{2}} c_j b_m(x-x_p)\Big|_{x_{m+2-j}}$$
$$\text{for} \quad x_p \in [x_i, x_{i+1}) \ (i = 0, 1, \ldots, N-2), \text{ and}$$
$$x_j = j \ (j = i + \frac{1-m}{2}, \ldots, i + \frac{1+m}{2}), \tag{4.30}$$

which represents a simple element-wise product of two discrete sequences, $\{c_j\}$ and $\{b_{m+2-j,m}\}$, containing exactly $(m+1)$ elements[5]. The equation above is often mis-

[5]Note that the convolution kernel is flipped

interpreted as the convolution of spline coefficients with the B-spline shifted to the particle location, see, e.g., [59, 88, 163].

In three dimensions, the B-spline coefficients are given as

$$c_\alpha(\boldsymbol{x},t) = \mathcal{F}^{-1}\left[\frac{\hat{u}_\alpha(\boldsymbol{k},t)}{\hat{b}_m(k_1)\hat{b}_m(k_2)\hat{b}_m(k_3)}\right], \tag{4.31}$$

where $\hat{b}_m(k_\alpha)$ $(\alpha = 1,2,3)$ is simply a one-dimensional Fourier transform of the discrete B-spline, and therefore the fluid velocity at the particle location becomes

$$u_\alpha(\boldsymbol{x}_p,t) = \Big[c_\alpha * B_m\Big](\boldsymbol{x}_p,t). \tag{4.32}$$

It should be emphasized that the B-spline weights are evaluated for every particle at each time step, and therefore, instead of using Eq. (4.24), the B-spline should rather be expressed in a nested form by means of Horner's method.

4.4 Time integration

Due to efficiency reasons, the time-stepping scheme used to advance the particle equation of motion in time should be compatible with that of the pseudo-spectral solver. In other words, if multi-stage methods are concerned, then both numerical schemes should have an instantaneous access to the velocity field at every stage of the time integration. In this work, the 5^{th} order implicit Adams-Moulton and the 4^{th} order explicit Adams-Bashforth schemes are combined according to

$$V_\alpha^{n+1} = V_\alpha^n - f_D^n\left(\frac{\Delta t'}{720}\Pi_\alpha^{AM} - \frac{\Delta t'}{24}\Pi_\alpha^{AB}\right) \tag{4.33}$$

where $\Delta t' = \Delta t/\tau_p$, and

$$\Pi_\alpha^{AM} = 251V_\alpha^{n+1} + 646V_\alpha^n - 264V_\alpha^{n-1} + 106V_\alpha^{n-2} - 19V_\alpha^{n-3}. \tag{4.34}$$

The second term on the right-hand side of Eq. (4.33) can be determined from

$$\Pi_\alpha^{AB} = 55u_\alpha^n - 59u_\alpha^{n-1} + 37u_\alpha^{n-2} - 9u_\alpha^{n-3}. \tag{4.35}$$

With the use Eq. (4.33), the particle trajectory is given as

$$x_{p,\alpha}^{n+1} = x_{p,\alpha}^n + \frac{\Delta t'}{720}\Pi_\alpha^{AM}. \tag{4.36}$$

Depending on the Stokes number, $St = \tau_p/\tau_\eta$, the time step Δt becomes additionally restricted by the particle inertia. In general, the following condition applies

$$\Delta t \ll \min(\tau_p, \tau_\eta), \tag{4.37}$$

and thus the computational overhead of the particulate-phase can become prohibitively large for relatively small Stokes numbers ($\tau_p \ll \tau_\eta$) or very large Reynolds numbers. To clarify the latter case, it should emphasized that the size of inertial particles decreases (in code units) with increasing Reynolds number. For this reason, maintaining a constant volume fraction of the dispersed phase implies the need for a larger number of particles. The use of implicit methods arguably contributes to sustaining a reasonable trade-off between accuracy and efficiency.

4.5 Basic particle statistics

This Section introduces basic parameters used throughout this work in order to statistically quantify the motion of small inertial particles suspended in a turbulent flow. Maxey [9], Squires & Eaton [11], and Fessler et al. [164] reported that inertial particles tend to concentrate non-uniformly in regions of low vorticity and high-strain rate, see Fig. 4.3 (right panel). Today, this phenomenon is most commonly referred to as the preferential concentration, which can be roughly quantified using, among a wide range of available methods, the radial distribution function (RDF) given as

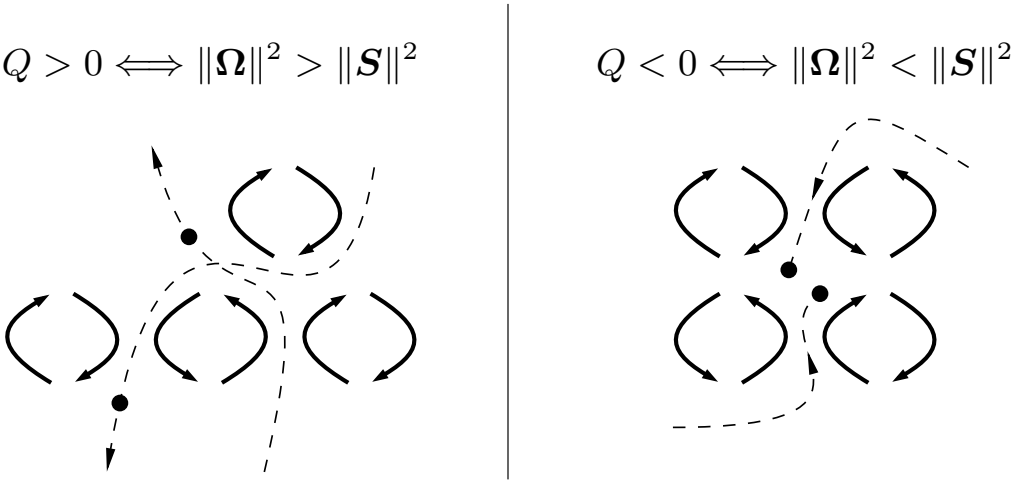

Figure 4.3: Particle preferential concentration; dashed lines denote particle trajectories; particles centrifuged out of the regions of high vorticity (left panel); particles "trapped" in the regions of low vorticity and high strain (right panel).

$$g(r,t) = \frac{N_{\text{pairs}}/V_{\text{shell}}}{N_p(N_p-1)/2V_{\text{box}}}, \tag{4.38}$$

where N_p is the total number of particles in the computational box and N_{pairs} is the total number of particle pairs separated by r. It is readily apparent that the RDF is essentially normalized by the number density of particle pairs, and thus $g(r,t) = 1$ indicates a uniform distribution. At this point, it should also be emphasized that the RDF provides some insight into particle clustering at length scales comparable to the size of the smallest resolved flow scales and, for this reason, is often used to parametrize particle collisions [14].

To account for particle clustering at larger length scales, say on the order of $\mathcal{O}(100\eta)$, one can determine the spectrum function of the particle number density as first proposed by Matsuda et al. [165]. Recently, Matsuda et al. [166] (Supplementary material) have modified the initially proposed method for computing the particle number density spectrum to make use of the FFT, thus rendering the method particularly suitable for pseudo-spectral codes. Following [166], consider a fine-grained particle number density field given as

$$n_\delta(\boldsymbol{x},t) = \frac{1}{n_0}\sum_{l=1}^{N_p}\delta[\boldsymbol{x}-\boldsymbol{x}_{p,l}(t)], \tag{4.39}$$

where $n_0 = N_p/V$ is a normalization coefficient defined so that the average number of particles per unit volume is

$$\langle n_\delta(\boldsymbol{x},t)\rangle = \frac{1}{V}\int n_\delta(\boldsymbol{x},t)\mathrm{d}\boldsymbol{x} = \frac{1}{n_0}\frac{1}{V}\sum_{l=1}^{N_p}\int\delta(\boldsymbol{u})\mathrm{d}\boldsymbol{u} = \frac{1}{n_0}\frac{N_p}{V} = 1, \tag{4.40}$$

where $\boldsymbol{u} = \boldsymbol{x}-\boldsymbol{x}_{p,l}$. Using a piecewise constant function $K_h(\boldsymbol{x})$, the authors introduced the smoothed particle number density field given as

$$n_K(\boldsymbol{x}) \equiv \int K_h(\boldsymbol{x}-\boldsymbol{x}')n_\delta(\boldsymbol{x})\mathrm{d}\boldsymbol{x}', \tag{4.41}$$

and its two-point correlation function expressed as

$$\Phi_K(\boldsymbol{r}) = \langle n_K(\boldsymbol{x})n_K(\boldsymbol{x}+\boldsymbol{x})\rangle. \tag{4.42}$$

In addition to the above, Matsuda et al. [166] put forward the two-point correlation function of the particle number density field $n(\boldsymbol{x})$ given as

$$\Phi(\boldsymbol{r}) = \langle n(\boldsymbol{x}) n(\boldsymbol{x}+\boldsymbol{x}) \rangle, \tag{4.43}$$

where $n(\boldsymbol{x})$ is considered to be $n_\delta(\boldsymbol{x})$ in the limit of $N_p \to \infty$, however, no rigorous mathematical operator taking $n_\delta(\boldsymbol{x})$ to $n(\boldsymbol{x})$ was provided. Thereafter, the Fourier transform of Eq. (4.43) was given as

$$\hat{\Phi}(\boldsymbol{k}) = \frac{1}{\kappa(\boldsymbol{k})^2} \left[\hat{\Phi}_K(\boldsymbol{k}) - \frac{1}{N_p} \right], \tag{4.44}$$

where $\kappa(\boldsymbol{k}) \equiv (2\pi)^3 \hat{K}_h(\boldsymbol{k})$. It should be emphasized that the above equation has been obtained by making some specific assumptions about the form of both $n(\boldsymbol{x})$ and the smoothing kernel $K_h(\boldsymbol{x})$ [166]. To point out the differences, and possibly to clarify the computation of the particle number density spectrum, a rigorous derivation is given below.

In contrast to Matsuda et al. [166], in this work, a fine-grained particle number density field is defined simply as

$$n(\boldsymbol{x}, t) = \frac{1}{n_0} \sum_{l=1}^{N_p} \delta[\boldsymbol{x} - \boldsymbol{x}_{p,l}(t)], \tag{4.45}$$

thus without distinction between discrete and continuous settings, that is $n_\delta(\boldsymbol{x}, t)$ and $n(\boldsymbol{x}, t)$, respectively. Thereafter, assuming the underlying turbulence is isotropic, and taking into account the normalization as given in Eq. (4.39), the two-point correlation function of the particle number density becomes

$$\Phi(\boldsymbol{r}) = \langle n(\boldsymbol{x}) n(\boldsymbol{x}+\boldsymbol{r}) \rangle = \frac{1}{n_0^2} \left\langle \sum_{l=1}^{N_p} \sum_{l'=1}^{N_p} \delta(\boldsymbol{x} - \boldsymbol{x}_{p,l}) \delta(\boldsymbol{x} + \boldsymbol{r} - \boldsymbol{x}_{p,l'}) \right\rangle. \tag{4.46}$$

Depending on whether $l = l'$ or $l \neq l'$, the above equation can be further expanded as

$$\begin{aligned} \Phi(\boldsymbol{r}) = & \frac{1}{n_0^2} \left\langle \sum_{l=1}^{N_p} \delta(\boldsymbol{x} - \boldsymbol{x}_{p,l}) \delta(\boldsymbol{x} + \boldsymbol{r} - \boldsymbol{x}_{p,l}) \right\rangle + \\ & \frac{1}{n_0^2} \left\langle \sum_{l=1}^{N_p} \sum_{\substack{l'=1 \\ l' \neq l}}^{N_p} \delta(\boldsymbol{x} - \boldsymbol{x}_{p,l}) \delta(\boldsymbol{x} + \boldsymbol{r} - \boldsymbol{x}_{p,l'}) \right\rangle \end{aligned} \tag{4.47}$$

The first term on the right-hand side accounts for the so-called one-particle correla-

tions, so to speak, whereas the second one describes two-particle correlations; these terms are temporarily referred to as $\Phi^{(1)}$ and $\Phi^{(2)}$, respectively. One can note that the contribution to $\Phi^{(1)}$ is non-zero if and only if $\boldsymbol{r} = \boldsymbol{0}$, and therefore this term can be rewritten as

$$\Phi^{(1)}(\boldsymbol{r}) = \frac{1}{n_0^2}\frac{N_p}{V}\int \delta(\boldsymbol{r}-\boldsymbol{u})\delta(\boldsymbol{u})\mathrm{d}\boldsymbol{u} = \frac{1}{n_0}\delta(\boldsymbol{r}), \tag{4.48}$$

where $\boldsymbol{u} = \boldsymbol{x}+\boldsymbol{r}-\boldsymbol{x}_{p,l}$. The second term is slightly more complicated since it accounts for the actual particle locations. At this point, one can introduce the pair distribution function given as

$$\begin{aligned} g(\boldsymbol{r}) &= \frac{1}{n_0^2}\left\langle \sum_{l=1}^{N_p}\sum_{\substack{l'=1\\l'\neq l}}^{N_p} \delta(\boldsymbol{x}-\boldsymbol{x}_{p,l})\delta(\boldsymbol{x}+\boldsymbol{r}-\boldsymbol{x}_{p,l'})\right\rangle \\ &= \frac{1}{n_0^2}\sum_{l=1}^{N_p}\sum_{\substack{l'=1\\l'\neq l}}^{N_p}\frac{1}{V}\int \delta(\boldsymbol{x}-\boldsymbol{x}_{p,l})\delta(\boldsymbol{x}+\boldsymbol{r}-\boldsymbol{x}'_{p,l})\mathrm{d}\boldsymbol{x} \\ &= \frac{V}{N_p^2}\sum_{l=1}^{N_p}\sum_{\substack{l'=1\\l'\neq l}}^{N_p}\delta(\boldsymbol{r}-\boldsymbol{r}'), \end{aligned} \tag{4.49}$$

where $\boldsymbol{r}' = \boldsymbol{x}_{p,l'} - \boldsymbol{x}_{p,l}$. It is worth mentioning that in isotropic turbulence the above equation depends only on the magnitude $r = |\boldsymbol{r}|$, and thus $g(\boldsymbol{r})$ reduces to the well-known radial distribution function $g(r)$, see Eq. (4.38). With the substitution of $g(\boldsymbol{r})$, the spatial correlation of the particle number density can be expressed as

$$\Phi(\boldsymbol{r}) = \Phi^{(1)}(\boldsymbol{r}) + \Phi^{(2)}(\boldsymbol{r}) = \frac{1}{n_0}\delta(\boldsymbol{r}) + g(\boldsymbol{r}), \tag{4.50}$$

and therefore its Fourier transform becomes

$$\hat{\Phi}(\boldsymbol{k}) = \frac{1}{n_0}\hat{\delta}(\boldsymbol{k}) + \hat{g}(\boldsymbol{k}) = \frac{1}{N_p} + \hat{g}(\boldsymbol{k}). \tag{4.51}$$

In practice, the delta function requires some regularization. Using the B-spline of degree m, see Section 4.3, a smoothed particle number density field becomes

$$n_B(\boldsymbol{x},t) = \int B_m(\boldsymbol{x}-\boldsymbol{x}')n(\boldsymbol{x}',t)\mathrm{d}\boldsymbol{x}' = \frac{1}{n_0}\sum_{l=1}^{N_p} b_m[\boldsymbol{x}-\boldsymbol{x}_{p,l}(t)], \tag{4.52}$$

where the discrete B-spline b_m is given by Eq. (4.22). One can readily notice that due to Eq. (4.16), $\langle n_B(\boldsymbol{x},t)\rangle = 1$ is also ensured. Consider the spatial correlation of the

smoothed particle number density given as

$$\Phi_B(\boldsymbol{r}) = \langle n_B(\boldsymbol{x}) n_B(\boldsymbol{x}+\boldsymbol{r}) \rangle. \tag{4.53}$$

Adopting the same reasoning as in Eq. (4.47), the smoothed one-particle correlations take the following form

$$\Phi_B^{(1)}(\boldsymbol{r}) = \left\langle \int\int B_m(\boldsymbol{x}-\boldsymbol{x}') B_m(\boldsymbol{x}+\boldsymbol{r}-\boldsymbol{x}'') \times \right. \\ \left. \times \frac{1}{n_0^2} \sum_{l=1}^{N_p} \delta(\boldsymbol{x}'-\boldsymbol{x}_{p,l}) \delta(\boldsymbol{x}''-\boldsymbol{x}_{p,l}) \mathrm{d}\boldsymbol{x}' \mathrm{d}\boldsymbol{x}'' \right\rangle, \tag{4.54}$$

where with the substitution of $\boldsymbol{u} = \boldsymbol{x}'' - \boldsymbol{x}_{p,l}$, $\mathrm{d}\boldsymbol{u} = \mathrm{d}\boldsymbol{x}''$, and $\boldsymbol{r}' = \boldsymbol{x}'' - \boldsymbol{x}'$, one obtains

$$\begin{aligned} \Phi_B^{(1)}(\boldsymbol{r}) &= \left\langle \int B_m(\boldsymbol{x}-\boldsymbol{x}') B_m(\boldsymbol{x}-\boldsymbol{x}'+\boldsymbol{r}-\boldsymbol{r}') \mathrm{d}\boldsymbol{x}' \times \right. \\ &\qquad \left. \times \frac{1}{n_0^2} \sum_{l=1}^{N_p} \int \delta(\boldsymbol{u}) \delta(\boldsymbol{r}'-\boldsymbol{u}) \mathrm{d}\boldsymbol{u} \right\rangle \\ &= \left\langle \frac{1}{n_0} \delta(\boldsymbol{r}') \int B_m(\boldsymbol{x}-\boldsymbol{x}') B_m(\boldsymbol{x}-\boldsymbol{x}'+\boldsymbol{r}-\boldsymbol{r}') \mathrm{d}\boldsymbol{x}' \right\rangle. \end{aligned} \tag{4.55}$$

With the substitution of $\boldsymbol{y} = \boldsymbol{x} - \boldsymbol{x}'$ and taking advantage of the symmetry of B-splines, one obtains

$$\begin{aligned} \Phi_B^{(1)}(\boldsymbol{r}) &= \left\langle \frac{1}{n_0} \delta(\boldsymbol{r}') \int B_m(\boldsymbol{r}-\boldsymbol{r}'-\boldsymbol{y}) B_m(\boldsymbol{y}) \mathrm{d}\boldsymbol{y} \right\rangle \\ &= \left\langle B_m \star B_m(\boldsymbol{r}-\boldsymbol{r}') \frac{1}{n_0} \delta(\boldsymbol{r}') \right\rangle \\ &= \int B_m \star B_m(\boldsymbol{r}-\boldsymbol{r}') \frac{1}{n_0} \delta(\boldsymbol{r}') \mathrm{d}\boldsymbol{r}', \end{aligned} \tag{4.56}$$

from where it can be readily noticed that

$$\Phi_B^{(1)}(\boldsymbol{r}) = B_m \star B_m \star \Phi^{(1)}(\boldsymbol{r}). \tag{4.57}$$

Following the above reasoning, it is straightforward to show that

$$\Phi_B^{(2)}(\boldsymbol{r}) = B_m \star B_m \star \Phi^{(2)}(\boldsymbol{r}). \tag{4.58}$$

Therefore, the spatial correlation function $\Phi(\boldsymbol{r})$ can be rewritten as

$$\Phi(\boldsymbol{r}) = (B_m \star B_m)^{-1} \star \Phi_B(\boldsymbol{r}). \tag{4.59}$$

and its discrete Fourier transform becomes simply

$$\hat{\Phi}(\boldsymbol{k}) = \frac{\hat{\Phi}_B(\boldsymbol{k})}{\hat{b}_m(\boldsymbol{k})\hat{b}_m(\boldsymbol{k})} = \frac{\hat{\Phi}_B(\boldsymbol{k})}{|\hat{b}_m(\boldsymbol{k})|^2}, \tag{4.60}$$

where $\hat{b}_m(\boldsymbol{k})\hat{b}_m(\boldsymbol{k}) = |\hat{b}_m(\boldsymbol{k})|^2$ follows from the fact that $\hat{b}_m$ is purely real. It should be emphasized that if the DFT is normalized, the above result must be multiplied by N^{-6}. One can note that the convolution in physical space, see Eq. (4.52), is followed by a deconvolution in Fourier space, thus, in the limit of disctretization, the impact of the spurious non-locality introduced by the B-spline smoothing on particle clustering should vanish [88].

The Poisson noise resulting from the one-particle correlations can be effectively removed as follows

$$\hat{\tilde{\Phi}}(\boldsymbol{k}) = \hat{\Phi}(\boldsymbol{k}) - \frac{1}{n_0}\hat{\delta}(\boldsymbol{k}) = \frac{\hat{\Phi}_B(\boldsymbol{k})}{|\hat{b}_m(\boldsymbol{k})|^2} - \frac{1}{N_p}. \tag{4.61}$$

Comparing the above equation against Eq. (4.44), two key differences readily appear: (i) in this work, the first term on the right-hand side is consistently computed using the discrete Fourier transform, whereas in [166] both discrete and continuous Fourier transforms are mixed-up; (ii) the second term on the right-hand side in [166] (essentially removing the Poisson noise) is additionally divided by $\kappa(\boldsymbol{k})^2$.

For completeness, one can also note that

$$\begin{aligned}
\widehat{\Phi_B}(\boldsymbol{k}) &= \frac{1}{2\pi^3}\int\left[\frac{1}{V}\int n_B(\boldsymbol{x})n_B(\boldsymbol{x}+\boldsymbol{r})\mathrm{d}\boldsymbol{x}\right]e^{-i\boldsymbol{k}\cdot\boldsymbol{r}}\mathrm{d}\boldsymbol{r} \\
&= \frac{1}{2\pi^3}\int n_B(\boldsymbol{u})e^{-i\boldsymbol{k}\cdot\boldsymbol{u}}\mathrm{d}\boldsymbol{u}\frac{1}{2\pi^3}\int n_B(\boldsymbol{x})e^{i\boldsymbol{k}\cdot\boldsymbol{x}}\mathrm{d}\boldsymbol{x} \\
&= \widehat{n_B}(\boldsymbol{k})\widehat{n_B}(-\boldsymbol{k}) = |\widehat{n_B}(\boldsymbol{k})|^2,
\end{aligned} \tag{4.62}$$

and thus the shell-averaged particle number density spectrum function can be expressed as

$$E_n(k) = \frac{1}{\Delta k}\sum_{\boldsymbol{k}}\hat{\tilde{\Phi}}(\boldsymbol{k}) = \frac{1}{\Delta k}\sum_{\boldsymbol{k}}\left|\widehat{\frac{n_B(\boldsymbol{x})}{b_m(\boldsymbol{x})}}(\boldsymbol{k})\right| - \frac{1}{N_p}. \tag{4.63}$$

It should be emphasized that in this work, the above spectrum function will be extensively used to quantify particle clustering at length scales exceeding η, specifically

in the point-particle LES at high Reynolds numbers.

The impact of turbulent transport on particle motion (specifically in the context of particle collisions) can also be examined by means of the radial relative velocity (RRV) given as

$$w_r(r,t) = \left\langle \left| \left(\boldsymbol{V}_p^{[1]} - \boldsymbol{V}_p^{[2]} \right) \cdot \frac{\boldsymbol{r}}{|\boldsymbol{r}|} \right| \right\rangle, \tag{4.64}$$

where $\langle \cdot \rangle$ denotes the average taken over all particle pairs separated by r. Sundaram & Collins [14] indicated that both the RDF and the RRV are essential for accurately predicting the collision rates of small-inertia particles suspended in a turbulent flow. The authors put forward the so-called cylindrical formulation of the geometrical collision kernel, which, however, was subsequently modified by Wang et al. [13] to give the so-called spherical formulation expressed as

$$\Gamma(r,t) = 2\pi R^2 w_r(R,t) g(R,t). \tag{4.65}$$

The modified formulation was validated against the DNS of isotropic turbulence by Zhou et al. [167]. In the above equation $g(R)$ and $w_r(R)$ denote the values "at contact" of the RDF and the RRV, respectively. It should be underlined that the collision kernel is quoted only to emphasize the importance of both the RDF and the RRV, and will not be further examined in this work. One can refer to, e.g., [13, 67, 85, 86, 168] and the follow-up works concerning the collision-related statistics of inertial particles.

Maxey [9] and Wang & Maxey [12] reported that inertial particles subjected to gravity preferentially sample specific velocity gradients, and thus may experience a significant increase in the average settling velocities when compared to the terminal velocity in still fluid, i.e., $V_T = \tau_p g$. In fact, this phenomenon is most commonly referred to as the preferential sweeping, see Fig. 4.4, and is most pronounced for particles whose normalized settling speed $S_V = V_T/u_\eta$ is on the order of unity. In this work, the impact of the preferential sweeping is approximately quantified by means of a non-dimensional parameter hereinafter referred to as the settling speed enhancement given as

$$\Delta V_s = \frac{\langle \boldsymbol{V}_p \left[\boldsymbol{x}_p(t), t \right] \cdot \boldsymbol{g}/|\boldsymbol{g}| \rangle}{V_T} - 1, \tag{4.66}$$

where $\langle \cdot \rangle$ denotes the average taken over all particles.

As indicated in Section 2.11, the second invariant of the velocity gradient tensor Q can provide some insight into the instantaneous structure of the velocity field, and thus can be useful for the qualitative and quantitative assessment of discrepancies in particle statistics computed from both the DNS and the LES. The second invariant of the velocity gradient tensor sampled at the particle location, here denoted as Q_p,

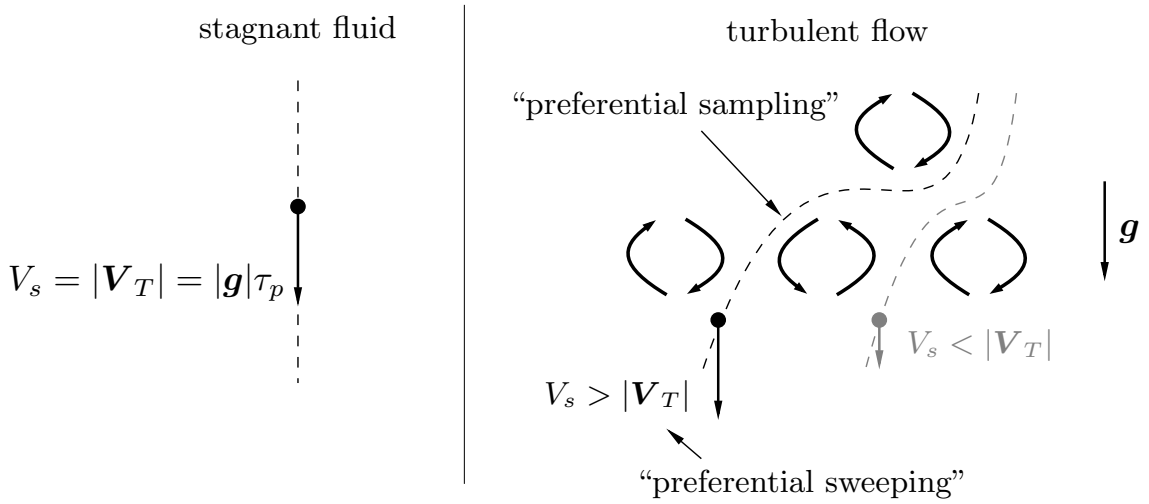

Figure 4.4: Particle settling speed in both still fluid (left panel) and a turbulent flow (right panel); dashed lines denote particle trajectories.

is essentially determined using the same interpolation method as in the case of the fluid velocity, see Section 4.2.

In general, prior to calculating some of the foregoing dispersed phase statistics, particles neighboring with the one of current interest have to be identified. It should be noted that the computational cost of finding all particle pairs is $\mathcal{O}(N_p^2)$, essentially rendering this approach inefficient. However, this can be relatively easily reduced to $\mathcal{O}(N_p)$ using the so-called cell lists (or cell linked-lists) method [169]. In this approach, searching for neighboring particles is restricted to a certain volume around the particle of current interest.

For completeness, it should be emphasized that relevant error bounds were computed using the same approach as in the case of single-phase flows, see Section 2.9.

4.6 Residual fluid velocity at the particle location

In general, if the LES of a particle-laden turbulent flow is considered, then at least three major issues have to be addressed prior to starting the simulation, two of which have already been briefly discussed, that is, (i) the lack of small-scale turbulence caused by spatial filtering and (ii) the accurate determination of the fluid velocity at particle locations. It should be noted that the latter issue is essentially inherent to any numerical simulation of a particle-laden flow in which the Lagrangian particle tracking is employed. In addition to the above, one also has to take a closer look at the particle equation of motion, which in the case of a particle-laden LES can be

expressed as

$$\frac{\mathrm{d}V_\alpha}{\mathrm{d}t} = -f_D \frac{V_\alpha - \Big(\overline{u}_\alpha[\boldsymbol{x}_p(t),t] + u'_\alpha[\boldsymbol{x}_p(t),t]\Big)}{\tau_p} + g_\alpha,$$
$$\frac{\mathrm{d}x_{p,\alpha}}{\mathrm{d}t} = V_\alpha, \tag{4.67}$$

where the local fluid velocity at the particle location is decomposed into the resolved and residual parts as given by Eq. (3.8). As already indicated in Section 3.1, the small-scale (residual) velocity field is lost due to filtering, see Fig. 4.5; however, its impact on the resolved flow scales can be quantified statistically with relative ease, while maintaining satisfactory accuracy. One can recall the fact that usually it is the large flow scales that provide sufficient insight into the physics underlying a single-phase turbulent flow, possibly except for near-wall regions in wall-bounded flows. However, in the case of particulate two-phase flows, depending on the Stokes number $St = \tau_p/\tau_\eta$, which (in some sense) can be considered as a measure of particle inertia, certain dispersed entities may exhibit a tendency to preferentially interact with flow scales that are insufficiently resolved, if at all. Therefore, certain particle statistics obtained using the LES may significantly differ from those computed by means of the DNS. In such a case, due to complex particle-turbulence interactions, predictive value of the point-particle LES strongly depends on the quality of the model for the residual fluid velocity at particle locations [170].

There have been several attempts to quantify the impact of the residual (subgrid-scale) turbulence on particle dynamics, see, e.g., [133, 171, 172, 173], from which a general conclusion is that whether or not the subgrid-scale velocity field can be

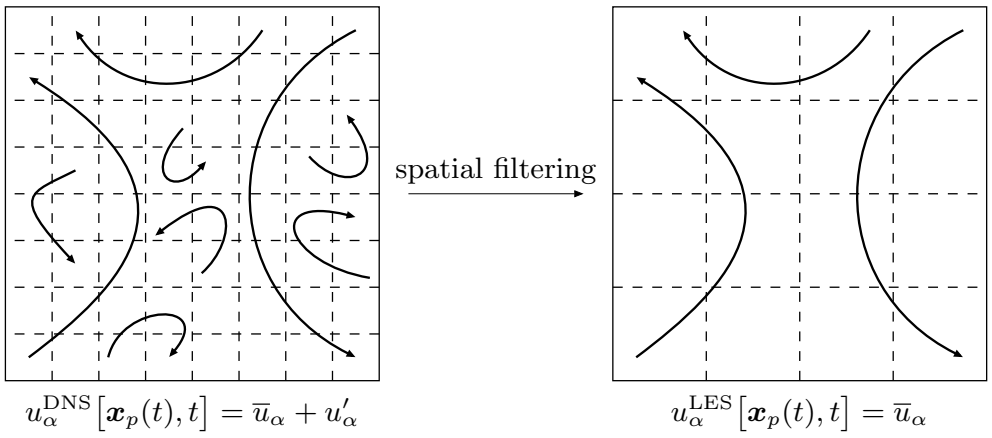

Figure 4.5: The impact of spatial filtering on the fluid velocity at the particle location $\boldsymbol{x}_p$; $\overline{u}_\alpha$ and u'_α are the large-scale and small-scale velocity components, respectively.

neglected depends almost exclusively on particle inertia, which, in some sense, governs the particle-turbulence interaction. On the other hand, some authors argued that as long as the LES is "well-resolved", i.e., accounts for the bulk of kinetic energy, the impact of subgrid-scale turbulence is expected to have a minor influence on particle motion [36, 133]. Although this assumption is not inherently wrong, it has already been indicated in this work that assessing the quality of LES based solely on this criterion is inappropriate.

Following Marchioli [36], one can distinguish between stochastic and structural subgrid-scale models. The first group aims at modeling only some statistical features of the residual velocity field, specifically along particle trajectories. This can be accomplished, e.g., by solving additional stochastic differential equation, see [173, 174, 175, 176]. These models are computationally efficient and usually correctly account for particle turbulent kinetic energy and long-time dispersion; however, by construction, are unable to predict two-particle statistics, e.g., relative dispersion or relative velocities. The latter issue is usually addressed in structural modeling, which aims at generating a synthetic small-scale turbulence. This can be achieved using the so-called kinematic simulations [177] in which a solenoidal turbulent-like velocity field is obtained by means of a truncated Fourier series with coefficients being randomly selected vectors having independent and normally distributed components, each with zero mean and a variance determined so that an imposed energy spectrum function is restored. This model was used to account for turbulent dispersion [178] and particle clustering [179]; however, it seems to reintroduce only the randomizing effect of small-scale turbulence, most pronounced for either small- or large-inertia particles, say $St \ll 1$ and $St \gg 1$, respectively. Kinematic simulations have been referred to as computationally inexpensive [36, 178], however, this is not the case when the LES at high Reynolds number is considered. A well-known drawback of this model is that the evolution of the small-scale turbulence is independent of the resolved one, and thus in principle does not account for either the non-linear interactions between the large and small flow scales or the sweeping effect, i.e., the advection of small eddies by larger ones. Building on [110], Kuerten [180] was the first to model the subgrid-scale contribution in the particle equation of motion based on the convolution of the resolved velocity field with an approximate inverse filter. This work was followed by Shotorban & Mashayek [172] and Marchioli et al. [181]. In general, the approximate deconvolution provides unsatisfactory prediction of the preferential concentration and wall accumulation. The foregoing deficiency is most often partly explained by the fact that in this approach only the flow scales of size comparable to the filter width are enhanced. Recently, Zhou et al. [66] addressed this issue by

combining the approximate deconvolution with the kinematic simulations to study the relative dispersion of fluid particles and reported improved prediction of various Lagrangian statistics when compared to the DNS at moderate Reynolds number. Zhou et al. [40] further extended this work to study collision-related statistics of inertial particles in isotropic turbulence, particularly concerning the RDF and RRV. The authors reported improved predictions when compared to pure LES, however, mostly for large-inertia particles. For this reason, it can be concluded that the model reintroduces only the randomizing effect of small-scale turbulence, and hence is not expected to offer better predictive capabilities than simple stochastic models. Following a similar approach, i.e., based on deconvolution of the resolved velocity field, Park et al. [114] proposed a model depending on differential filters of elliptic type [182], that is dynamically adjusted so as to impose consistency with the subgrid-scale model in the fluid momentum balance equation. Similar to other attempts, the model improves the clustering of both small- and large-inertia particles, i.e., those for which this phenomenon is essentially less pronounced. This model was further extended by Bassenne et al. [115] who combined the approximate deconvolution with the velocity estimation procedure [112] to account for the flow scales of size smaller than the filter width. Although providing significantly better results when compared to either pure LES or the LES enriched with the model of Park et al. [114], the new approach requires a divergence-free projection on a grid comparable to the DNS, thus making it computationally demanding. Recently, Ghate & Lele [116, 117] developed a model to reconstruct the subgrid-scale velocity field using spatially and spectrally localized Gabor modes. Although the enriched turbulence correctly accounts for the energy transfer from the resolved flow scales and has appropriate temporal decorrelation, the velocity field is only approximately solenoidal and long-term simulations require complex re-initialization, as recently stated by Hausmann [183]. Hausmann et al. [118] developed a subgrid-scale model for the fluid velocity at the particle location based on the linearized subfilter-scale Navier-Stokes equations, assuming the velocity field can be expanded in a finite Fourier series within (statistically) homogeneous subdomains. Although the results for particle relative dispersion and particle clustering approximately match the corresponding DNS for a wide range of Stokes numbers, the enriched turbulence is partly discontinuous, and thus the method implies the need for additional interpolation. Hausmann et al. [119] addressed this issue and proposed the use of wavelet enrichment in which the modeled subgrid-scale velocity field is discretized using a divergence-free wavelet vector basis, essentially ensuring a continuous small-scale turbulence over the entire computational domain. As indicated by the authors, when compared to pure LES, the model significantly improves not only the

prediction of particle clustering and particle-pair dispersion, but also the modulation of turbulence due to the momentum exchange between the phases. Nevertheless, the real predictive value of this modeling framework is yet to be determined.

At this point, possibly the most general conclusion is that no model is recognized satisfactory in the context of its efficiency, accuracy or universality [36]. Despite ongoing efforts on developing an accurate and tractable subgrid-scale model for the fluid velocity at the particle location, the issue remains unresolved, and thus is beyond the scope of this dissertation. The reason for this was not to undermine its importance for accurate LES modeling, but rather to focus first on other, equally important aspects.

4.7 Concluding remarks

This Chapter outlined the most important steps for the efficient coupling of the Lagrangian particle tracking with the pseudo-spectral DNS/LES solver for isotropic turbulence. A summary of what appear to be the most important achievements and contributions of this part of the research is provided in the following paragraphs.

First, a detailed introduction to B-spline interpolation as a means for accurate and efficient evaluation of the fluid velocity at the particle location has been provided (Section 4.3, p. 92). The purpose of this was as follows: (i) to keep up with the current state-of-the-art in the point-particle DNS [16, 88, 154], and thus to implement an interpolation tool that fully utilizes the capabilities of the pseudo-spectral solver; (ii) to elaborate on rather insufficient, and thus often misleading descriptions provided in the scientific literature, essentially hindering the use of the B-spline interpolation; (iii) to synthesize the knowledge spread over multiple resources, most often not relevant to the current objective; (iv) to provide a self-contained, detailed, organized and focused (possibly also beginner-friendly) walk-through of the algorithm for combining the B-spline interpolation with a pseudo-spectral solver.

Second, a detailed description of the algorithm for computing the spectrum function of the particle number density has been provided (Section 4.5, p. 99). The reason for this was as follows: (i) to provide a means of quantifying particle clustering also at length scales relevant to the inertial subrange, as recently reported in [165, 166]; (ii) to clarify and extend an incomplete and, to some extent, confusing derivation provided in [166]. In this work, what appears to be a mathematically consistent derivation was provided, which, unlike in [166], renders the method independent of both the selected smoothing kernel and the total number of particles. In addition to the above, it has also been concluded that at length scales relevant to LES, the Poisson noise does not

influence the spectrum function of the particle number density, and thus, somewhat contrary to [166], its removal does not seem to be of critical significance.

Chapter 5

Inertial particle dynamics

5.1 Problem statement

It is well established that depending on the Stokes number, $St = \tau_p/\tau_\eta$, where τ_η is the Kolmogorov time scale, inertial particles suspended in a turbulent flow may exhibit significantly different behavior than fluid particles, i.e., inertia-free entities, also referred to as passive tracers. This non-trivial turbulence-particle interaction can have a significant impact on many environmental phenomena and industrial processes. Among others, this includes sand and dust storms, rain formation, sedimentation processes, cyclone separation, pharmaceutical sprays, fuel atomization and spray combustion. Undoubtedly, an in-depth understanding of turbulent dispersed two-phase flows (also the multi-phase ones) is of profound importance for further advancements in the aforementioned matters. However, it should be emphasized that due to inevitable particle-turbulence and particle-particle interactions, possibly coupled with the heat-transfer, evaporation or even chemical reactions, particle-laden turbulent flows are usually associated with multi-physics (and often multi-scale) complex phenomena, yet to be fully understood, accurately predicted, and, perhaps most importantly, controlled in order to obtain a desired change in the flow behavior. Owing to a wide range of spatial and temporal scales, experimental investigation of dispersed two-phase flows often becomes problematic (if at all possible). Fortunately, continuous development of numerical methods and a rapid growth of computing capabilities provide a unique opportunity to study these complex flows.

As already discussed in Section 4.5, numerical and experimental evidence indicates that inertial particles tend to concentrate non-uniformly in the regions of low vorticity and high strain, eventually leading to increased collision rates or even pronounced modulation of the underlying turbulence. When subjected to gravity, inertial particles tend to sample specific velocity gradients, which leads to increased settling velocities

when compared to the terminal velocity in still fluid. There has been a considerable interest in this matter over the past years, see, e.g., [9, 12, 83, 87, 184, 185]. Although the DNS has already contributed to the understanding of the physics underlying these phenomena, most of the research was conducted at low to moderate Reynolds numbers, say $40 < Re_\lambda < 500$. Therefore, the impact of the Reynolds number on particle dynamics, or, in other words, the extent to which specific flow scales affect the turbulent transport of inertial particles remains undetermined.

To the best of the author's knowledge (despite appreciable developments in high-performance computing), the highest reported to date Taylor-microscale Reynolds number in a well-resolved single-phase isotropic turbulence is on the order of $Re_\lambda \sim 1200$, see, e.g., [127, 128, 130]. Unfortunately, when it comes to particle-laden turbulence, this number is divided roughly in half. As pointed out by Ireland [16], there have been relatively few studies reaching a "well-defined inertial range". On the other hand, it should be emphasized that despite providing the most accurate description, it seems that the DNS of particle-laden turbulent flows at industrially- or environmentally-relevant Reynolds numbers will continue to be unfeasible for many years to come. Presumably, the only way to study particle dynamics at larger Reynolds numbers is by using the LES instead; however, the scope of its application to particle-laden isotropic turbulence has not yet been rigorously examined. To clarify the latter statement, in this work, the scope of application refers to, e.g., the range of reachable Reynolds numbers, spatial resolution requirements, physical correctness of resolved flow scales, etc.

The primary focus of this Chapter is to collect certain statistics quantifying particle motion in a turbulent flow, specifically within the range of conditions relevant to cloud droplets suspended in the turbulent atmosphere, however, specifically concerning the process of "warm" rain formation. "Warm" clouds are typically formed in the lower troposphere and consist mostly of water vapor and droplets formed on aerosol particles[1]. As already indicated in Section 1.2, cloud droplets initially grow by the diffusion of water molecules and their condensation on the so-called cloud condensation nuclei. Once the droplets exceed approximately 20 µm in radius, further growth is governed by collision-coalescence until a typical size of 100 µm is reached, which is essentially considered as the onset of rainfall. Considering a simple gravitational-coalescence mechanism first introduced by Purppacher and Klett [136], the growth of cloud droplets from 5 µm to 100 µm in radius takes approximately one hour. However, it follows from experimental research that precipitation can be initiated in less than

[1]The average temperature throughout the cloud is above the freezing point, or, more generally, the impact of ice-processes on rainfall is considered insignificant

approximately 30 minutes from the development of a cumulus cloud [187]. One can recall that the growth of small droplets, say less than 20 µm, is effectively driven the diffusion of water vapor, whereas the growth of large ones, say greater than 80 µm, follows from the gravity-induced collision-coalescence [33, 188]. Unfortunately, none of the above mechanisms effectively drives the growth of cloud droplets in the intermediate range, often referred to as the "size gap". This issue has received an appreciable interest over the past decades. The outcomes from hundreds of research studies suggest that cloud turbulence enhances the growth of droplets in a number of different ways. This includes for instance (i) the impact of shear flow and air acceleration on the relative motion of settling droplets [13, 14, 32], (ii) enhanced collision rates due to the preferential concentration [14, 32, 167], (iii) enhanced settling due to the preferential sweeping [12, 87, 184]. It has also been argued that particle-particle interactions, e.g., many-body aerodynamic interactions or strong short-range lubrication forces, may affect the collision rates of cloud droplets [189, 190]. In fact, recently such interactions have become the subject of intense research, see, e.g., [67, 84, 191].

Despite appreciable achievements in determining the influence of turbulence on the growth of cloud droplets, the description of such processes is still insufficient. At this point, mostly due to increasing computational capabilities, there is an emphasis on identifying the range of flow scales (or the range of turbulence Reynolds numbers) that influence particle motion the most [16, 18]. As indicated in Section 3.6, in a convective cloud the characteristic length scales can extend from millimeters up to tens of meters resulting in the turbulence Reynolds numbers on the order of $Re_t \sim 10^6 - 10^7$, and thus $Re_\lambda \sim 10000$ [135]. This results in significant intermittency of specific physical quantities, e.g., the kinetic energy dissipation rate [136]. As already mentioned in Section 3.6, in this work, exclusively due to computational limitations, a single set of relevant physical quantities was assumed, that is $\epsilon = 6 \times 10^{-2}$ m^2/s^3 and $\nu = 1.5 \times 10^{-5}$ m^2/s. In addition to that, $g = 9.81$ m/s^2 and $\rho_p/\rho_f = 1000$. This results in $\eta \sim 5 \times 10^{-3}$ m, $Fr \sim 0.2$, and $St \in [0.15, 3.5]$ for $a \in (10, 60)$ µm, where the latter range of droplet radii seems to provide sufficient coverage of the "size gap". To safely neglect the influence of both the two-way momentum coupling and particle-particle interactions, a dilute suspension of droplets is assumed, with the volume fraction of the dispersed phase on the order of $\Phi_V \sim 10^{-5}$.

Before studying the motion of inertial particles suspended in a turbulent flow, one has to convert the input parameters from an arbitrary system of units (SI in this case) to the so-called "code units", which simply take into account that the size of the computational box is $L_B = 2\pi$. For instance, to determine an arbitrary length scale

L in "physical units", so to speak, one can impose the following identity

$$\frac{\eta}{L} = \left(\frac{\eta}{L}\right)^{\mathrm{SI}} \quad \Longrightarrow \quad L^{\mathrm{SI}} = \left(\frac{L}{\eta}\right)\eta^{\mathrm{SI}}. \tag{5.1}$$

Therefore, all quantities in the particle equation of motion, see Eq. (4.7), can be determined exactly in the same way by imposing

$$\frac{a}{\eta} = \left(\frac{a}{\eta}\right)^{\mathrm{SI}} \quad \Longrightarrow \quad a = \eta\left(\frac{a}{\eta}\right)^{\mathrm{SI}}, \tag{5.2}$$

$$Fr = Fr^{\mathrm{SI}} \quad \Longrightarrow \quad g = \frac{u_\eta}{\tau_\eta}\left(g\frac{\tau_\eta}{u_\eta}\right)^{\mathrm{SI}}, \tag{5.3}$$

$$St = St^{\mathrm{SI}} \quad \Longrightarrow \quad \tau_p = \tau_\eta\left(\frac{\tau_p}{\tau_\eta}\right)^{\mathrm{SI}}. \tag{5.4}$$

At this point, it should be emphasized that due to the specific design of the forcing term, see Section 2.5, the Kolmogorov microscales in forced isotropic turbulence are known beforehand, i.e., $\eta = k_{\max}\eta/k_{\max}$, $\tau_\eta = (\eta^2/\epsilon_f)^{1/3}$ and $u_\eta = (\epsilon_f\eta)^{2/3}$. Therefore, the conversion to code units can be accomplished with ease prior to starting the simulation. This is not always the case since other types of forcing usually require the so-called trial and error approach before the final set of parameters can be established.

5.2 Direct Numerical Simulations at low Reynolds number

Taking the above literature survey into account, rather than focusing on extending the understanding of the physics underlying particle-laden flows, the main purposes of this section are (i) to validate the newly developed particulate-phase solver and (ii) to provide the reference data for the point-particle LES, to be enhanced with two different forms (models) of the spectral eddy-viscosity closures, already introduced in Sections 3.6 and 3.7.

For completeness, it should be emphasized that all simulations given in this section followed the same pattern: (i) a monodispersed set of point-particles were randomly and uniformly dispersed over the computational domain once the turbulent flow reached statistical stationarity; in this work, it was no earlier than approximately $15T_e$; (ii) using the B-splines of degree $m = 3$, the particles were given an initial velocity equal to that of the underlying turbulence, and thence were allowed to evolve for approximately $5T_e$ before the data collection began; (iii) following the

recommendation given in [67], the time-step was set according to $\Delta t/\tau_p \approx 10^{-2}$, so that particle statistics can be considered time-step independent; (iv) particle data was gathered every quarter of T_e and all statistics were averaged over at least $25T_e$. While this appears to be more than enough to obtain a reasonable qualitative prediction of certain statistics, significantly longer simulations may be required to accurately quantify the motion of particles subjected to gravity [18].

From Eq. (4.38), it is readily apparent that $g(r)$ depends on the number of particle pairs separated by r. In practice, to determine the RDF at contact, one has to count particle pairs separated by $R - \delta < r < R + \delta$; $R = (a_1 + a_2)/2$; $\delta \approx 0.01R$ [13, 167]; a_1 and a_2 are the particle radii. In dilute suspensions, the number of particle pairs separated by $r \approx R$ may be small (depending on $St = \tau_p/\tau_\eta$ and $S_V = \tau_p g/u_\eta$), essentially leading to large uncertainties in the RDF, and thus making its accurate computation challenging (if at all possible). Based on an extensive body of evidence, see, e.g., [16, 168, 192, 193], it appears that for small separations, i.e., $r/\eta \ll 1$, the RDF exhibits power-like scaling, with the power coefficient being a function of both St and S_V. This observation is confirmed in Fig. 5.1. The results show excellent qualitative agreement with previously reported ones, see, e.g., [168]. Building upon

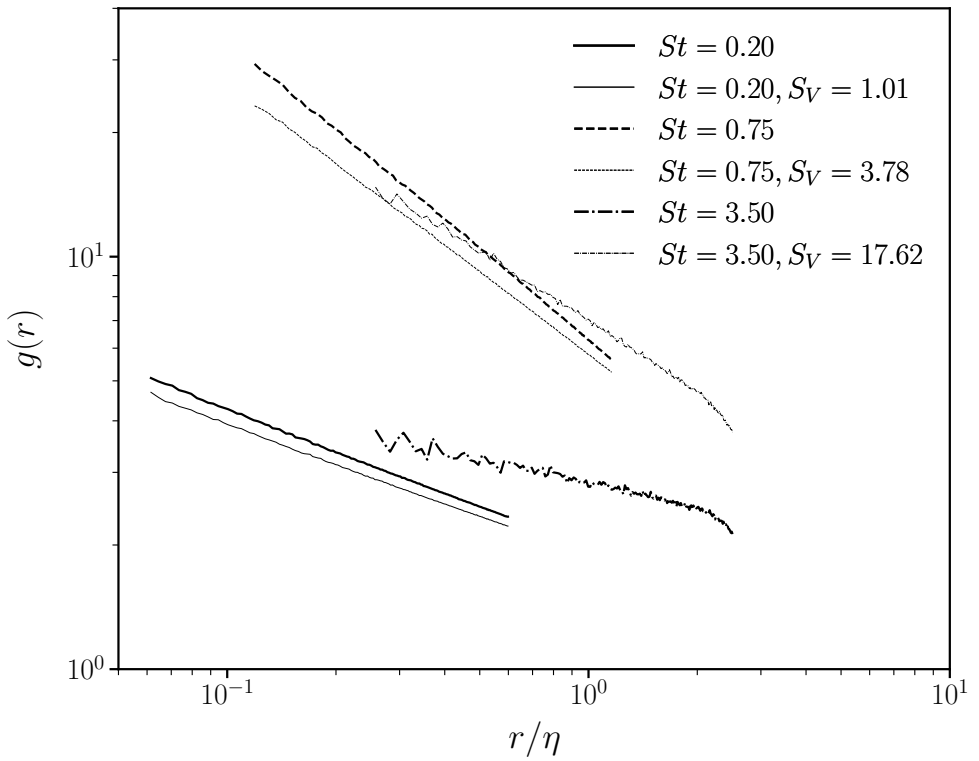

Figure 5.1: RDF for a dilute monodispersed suspension in the DNS at $Re_\lambda \sim 100$; results are plotted as pairs of thick (without gravity) and thin lines (with gravity); $\Phi_V = 10^{-5}$.

this finding, in this work, $g(r)$ is determined for larger separations, say $r/R \in (1,\ 10]$ divided into 180 bins so that $\delta = 9R/180$. Using the least-squares power-law regression, the RDF can be extrapolated for $r = R$, essentially mitigating the above difficulties [168]. This approach is particularly useful (or even essential) when the LES at high Reynolds number is considered.

The RDFs at contact determined from the DNS at $Re_\lambda \sim 100$, with and without gravitational effects, are depicted in Fig. 5.2. It becomes evident that both RDFs resemble a bell-shaped, positively skewed distribution, and reach their maximum value for $St \approx 0.75$. It should be emphasized that these results are in excellent quantitative agreement with the similar ones reported in [67, 168] and confirm previous findings indicating that the clustering of inertial particles is most pronounced for $St = \mathcal{O}(1)$ [14, 192]. Large uncertainties for settling particles whose $St > 1$ (dashed-dotted line) result solely from an insufficient number of particles. At this point, it should be noted that if the volume fraction of particles is kept constant, then increasing St essentially decreases N_p. On the other hand, it is also worth mentioning that if ghost particles[2] are considered, then increasing N_p at the expense of varying Φ_V is

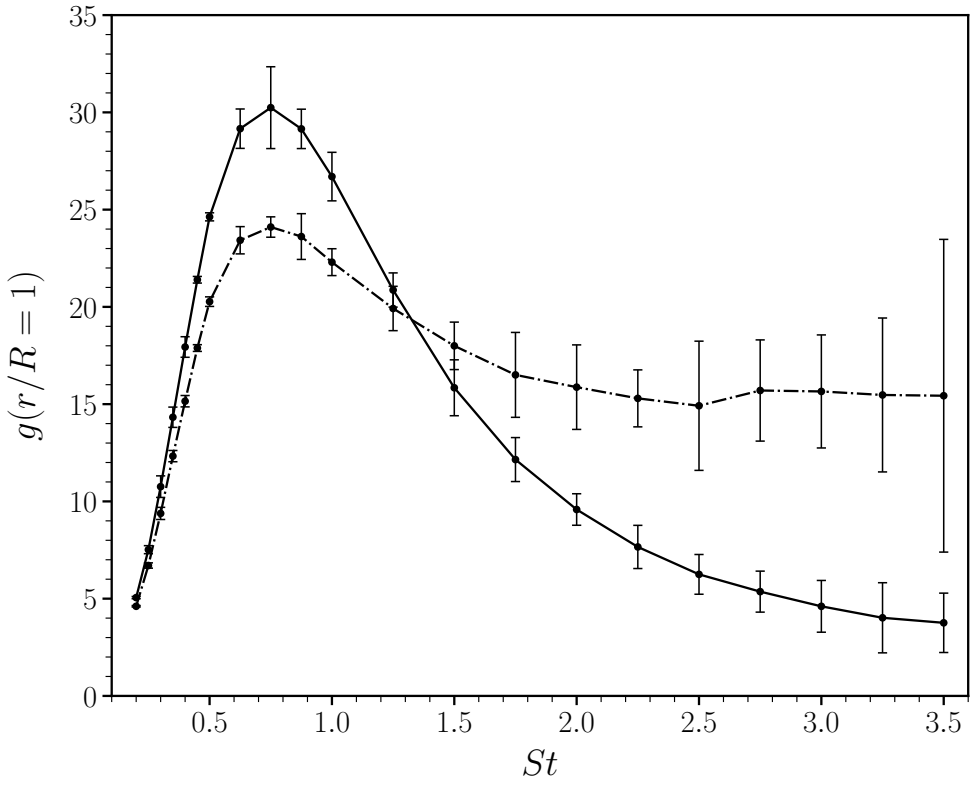

Figure 5.2: RDF at contact for a dilute monodispersed suspension in DNS at $Re_\lambda \sim 100$; $\Phi_V = 10^{-5}$; dashed-dotted line includes gravitational effects.

[2]Particle collisions are excluded, thus all dispersed entities move independently of each other

expected to impact statistical uncertainty only.

From Fig. 5.2, it also becomes evident that gravity modifies the clustering of inertial particles regardless of the Stokes number; however, the net impact depends on both St and S_V, see also Fig. 5.3 for a visual comparison. Although the location of the peak remains unchanged under the influence of gravity, the value of $g(r = R)$ is significantly reduced for $St < 1.5$. On the other hand, for larger particles, say $St > 1.5$, the clustering is somewhat sustained. This behavior can be partly explained by examining the PDF of the second invariant of the velocity gradient tensor sampled at particle locations Q_p, see Fig. 5.4. Thick dashed line denotes fluid (inertia-free) particles, which are expected to sample the flow uniformly at all times. It appears evident that if subjected to gravity, inertial particles (regardless of both St and S_V) tend to sample the regions of high vorticity more frequently than in cases where gravitational effects are excluded. In the case of small-inertia particles, say $St < 1.5$, this can possibly lead to enhanced mixing, which reduces the overall tendency of inertial particles to aggregate in the regions of low vorticity and high strain [173]. However, this conclusion seems to be invalid in the case of large-inertia particles, see

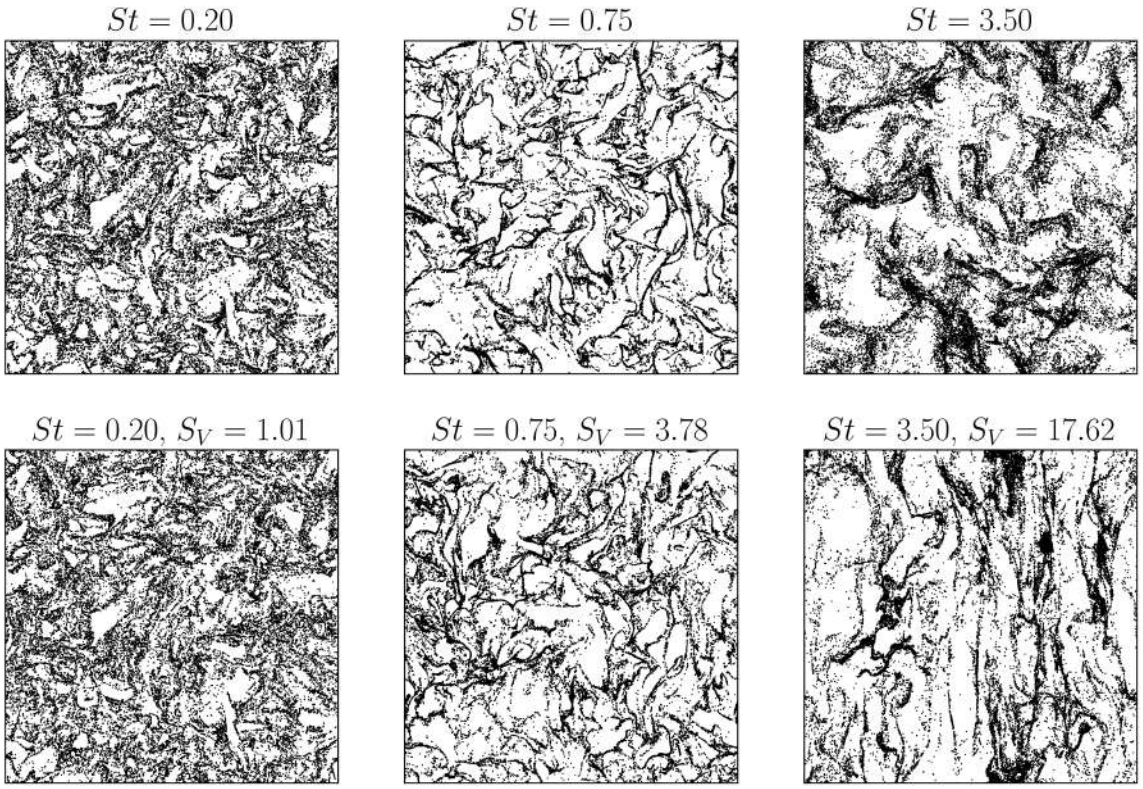

Figure 5.3: Instantaneous particle locations at $Re_\lambda \sim 100$ projected on the cross-section plane $L_B/2 - \Delta z/2 < z < L_B/2 + \Delta z/2$; $\Delta z = L_B/N$; $N = 256$; $Re_\lambda \sim 100$; $N_p = 10^7$; bottom segments account for the gravitational settling.

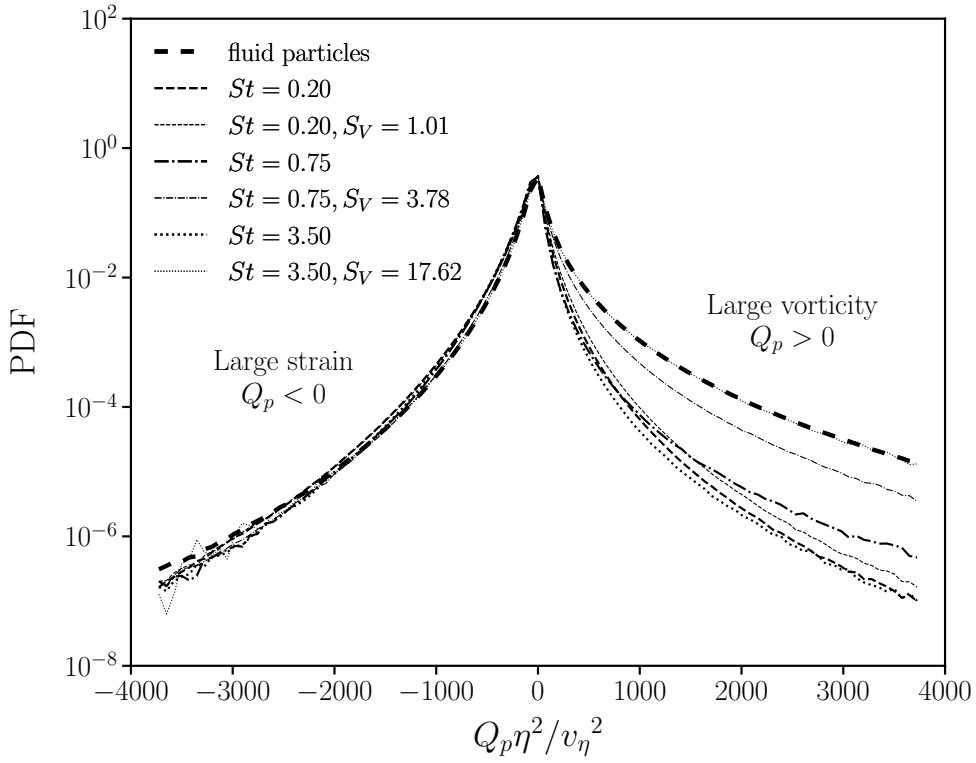

Figure 5.4: PDF of the second invariant of the velocity gradient tensor at $Re_\lambda \sim 100$ sampled at particle locations; the results concerning inertial particles are plotted as pairs of thick (without gravity) and thin lines (with gravity).

$St = 3.5$. Although such entities sample Q_p almost exactly as fluid particles, they still exhibit strong clustering at length scales on the order of $\mathcal{O}(\eta)$. It seems that rapidly settling entities, say $S_V \sim 10$, are less prone to instantaneous changes in the underlying turbulence, and thus tend to form elongated structures, so to speak, see Fig. 5.3 (bottom-right panel). In fact, gravity reduces the time such particles spend interacting with a turbulent flow [16]. Therefore, while falling quickly through the computational domain, such particles can encounter more regions of high vorticity and strain, which is arguably why they sample Q similar to fluid particles. This also indicates that for large-inertia particles subjected to gravity, there may be a slightly different mechanism driving their clustering at length scales comparable to η. In general, it seems that such a phenomenon is the secondary effect of settling particles being "trapped" in elongated clusters.

From Fig. 5.3 (the rightmost panels), it can be inferred that without gravity large-inertia particles tend to form clusters at length scales exceeding η. To quantify this phenomenon, one can consider the spectrum of the particle number density given by Eq. (4.63) and depicted in Fig. 5.5. It can be observed that small-inertia particles tend to cluster at length scales comparable to $\sim 5\eta$ ($k\eta = 0.2$) and are essentially

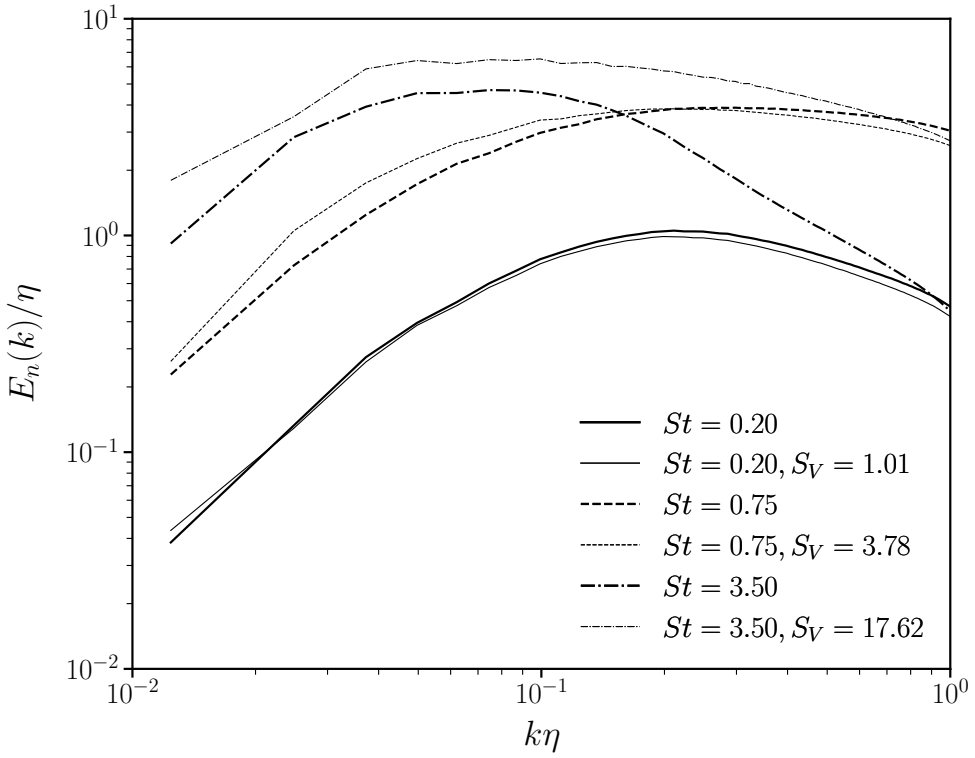

Figure 5.5: Particle number density spectrum at $Re_\lambda \sim 100$; the results are plotted as pairs of thick (without gravity) and thin (with gravity) lines.

immune to gravitational effects. This is consistent with both Figs. 5.2 and 5.3 (the leftmost column). Regardless of whether the gravity is considered or not, the clustering of particles whose $St \sim 1$ is also most pronounced at $\sim 5\eta$, however, unlike for smaller-inertia particles, remains so over a wider range of length scales, say up to $\sim \eta$. It can also be observed that for such particles, the spectrum is slightly reduced at $k\eta = 1$ when gravitational effects are taken into account. This remains in excellent agreement with the RDF depicted in Fig. 5.2. For large-inertia particles, the clustering is most pronounced at length scales on the order of 10–15η, see also Fig. 5.6 to get a better insight. In addition to that, such particles are less susceptible to small-scale turbulence, thus, when compared to $St \sim 1$, the clustering at length scales comparable to η is reduced when the gravity is excluded. On the other hand, the particle number density spectrum reveals that large-inertia particles subjected to gravity exhibit pronounced clustering over a wide range of length scales, including those comparable to the smallest resolved ones. One can note that this observation is essentially consistent with the previous results concerning the RDF at contact.

At length scales comparable to η, the velocity field can change at most linearly with respect to r. Therefore, it seems reasonable to expect that the same relationship holds in the case of the RRV, see Fig. 5.7. For this reason, similar to $g(r)$, the least-squares

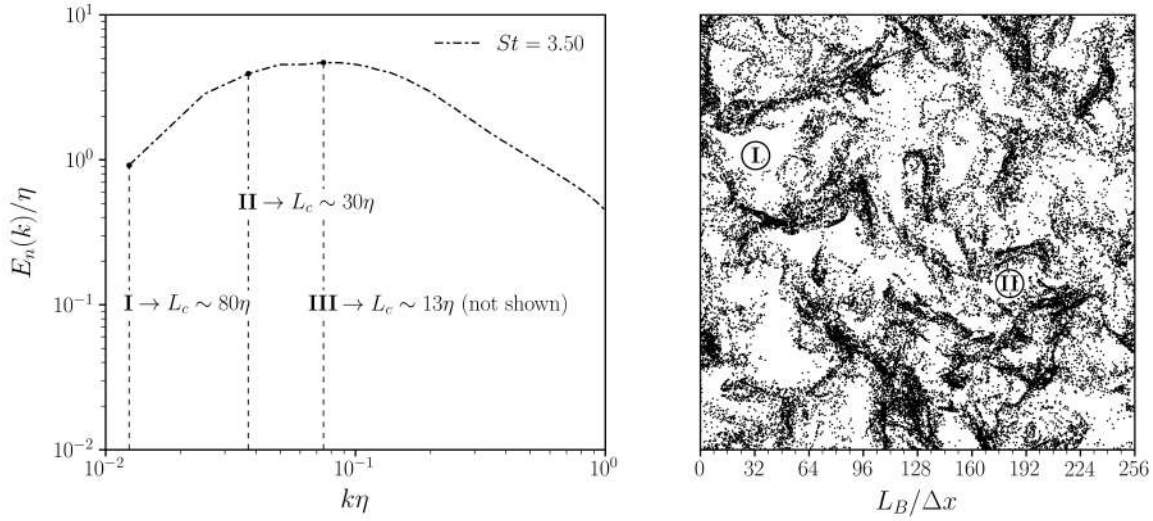

Figure 5.6: Particle number density spectrum at $Re_\lambda \sim 100$ (left panel); instantaneous particle locations (right panel); $\eta \sim k_{\max}\eta\Delta x/\pi$; $k_{\max}\eta = 1.5$; $k_{\max} = 121$.

power-law regression was used to extrapolate the value of the RRV at contact depicted in Fig. 5.8. It should be emphasized that current results remain in excellent qualitative agreement with other studies, see, e.g., [67, 168]. It is readily apparent that without

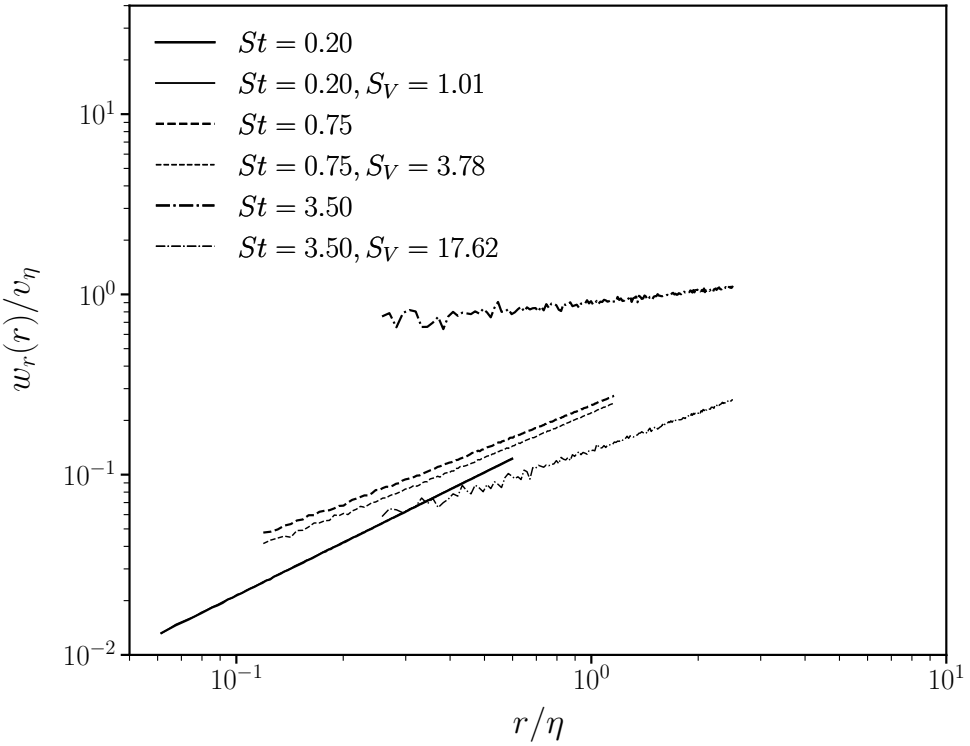

Figure 5.7: RRV for a dilute monodispersed suspension in DNS at $Re_\lambda \sim 100$; results are plotted as pairs of thick (without gravity) and thin lines (with gravity); $\Phi_V = 10^{-5}$; the results for $St = 0.2$ overlap, and thus are statistically indistinguishable.

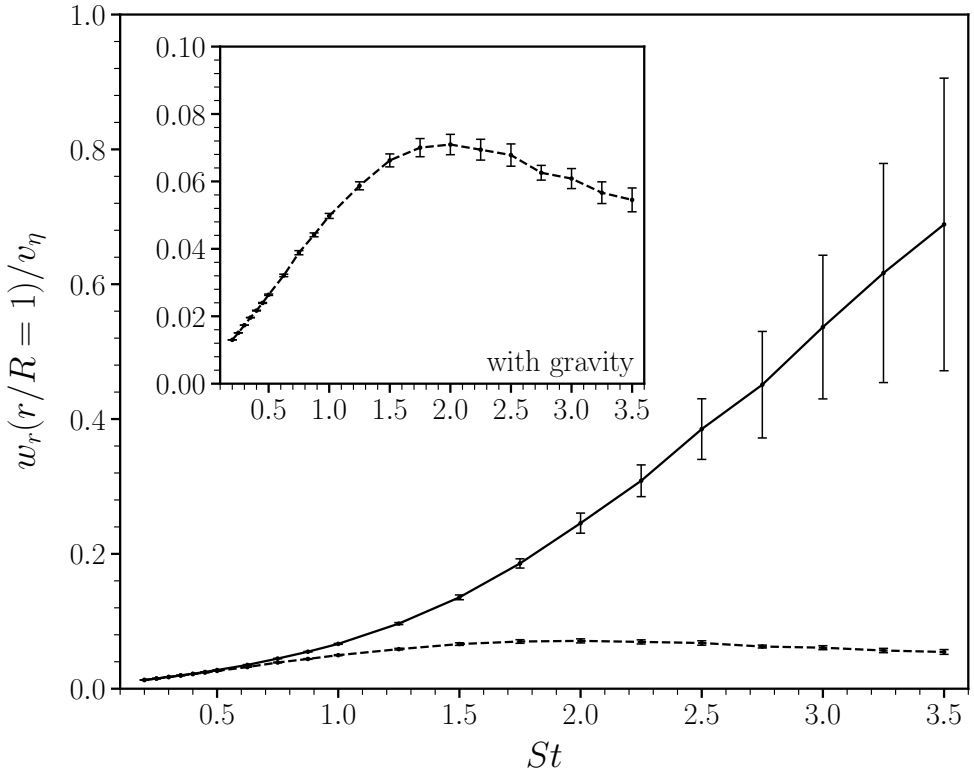

Figure 5.8: Normalized RRV at contact for a dilute monodispersed suspension in DNS at $Re_\lambda \sim 100$; $\Phi_V = 10^{-5}$; dashed line includes gravitational effects.

gravitational effects, the relative velocity increases with increasing St. This can be partly explained by caustics, i.e., the singularities in monodispersed systems, causing large fluctuations in relative velocities [194], eventually leading to the so-called "sling-effect" [195, 196], high-velocity collisions [197] or enhanced collision rates [198, 199]. To get a more profound understanding of this phenomenon, one can refer to [200]. In addition to the above, Ireland et al. [17] indicated that the correlation time scales of the flow along particle trajectories decreases due to gravity, thus reducing the overall impact of the past turbulence-particle interactions on particle relative velocities.

Maxey [9] suggested that turbulence enhances particle settling velocities through the preferential sweeping, which essentially results from the fact that inertial particles preferentially sample specific velocity gradients [18], or, in other words, concentrate in specific regions of the flow where the vertical components of fluid velocity align with gravity. This phenomenon has been observed in DNS [12, 17, 86, 185, 201] and experimental research [202]. Interestingly, it is often argued that the gravitational settling of inertial particles can be reduced by either (i) vortex trapping [203], (ii) non-linear drag [202] or (iii) the so-called "loitering" effect, first observed by Nielsen [204] and later confirmed experimentally by Kawanisi & Shiozaki [205]. Good et al. [202]

suggested that the point-particle DNS cannot capture this phenomenon unless the non-linear drag correction is introduced. Rosa et al. [185] studied this issue and concluded that the aforementioned correction has a negligible impact on particle settling velocities. Recently, the investigation of particle settling under the two-way momentum coupling has attracted considerable attention, see, e.g., [18, 87, 206, 207, 208], from which a general conclusion is that the two-way momentum coupling significantly enhances particle settling velocities when compared to one-way coupling. While the preferential sweeping remains the mechanism causing augmented settling speeds, part of the enhancement results from the increased local fluid velocity due to the particle-turbulence momentum exchange. The impact of the preferential sweeping on the settling velocity of inertial particles is depicted in Fig. 5.9. It is readily apparent that the enhancement is bell-shaped (similar to the RDF at contact), with a peak at $St \sim 0.3$, which essentially corresponds to $S_V \sim 1.5$. This remains in excellent agreement with previous findings, see, e.g., [12, 86, 185]. Low-inertia particles, $St \ll 1$ and $S_v \ll 1$ (not considered in this work) are expected to behave like fluid elements, and thus due to ineffective preferential concentration, such particles are not effectively guided to regions where the vertical components of fluid velocity are aligned with gravity, thus rendering the settling speeds unaffected by the underlying turbulence. It can be readily observed that large-inertia particles show similar behavior; however,

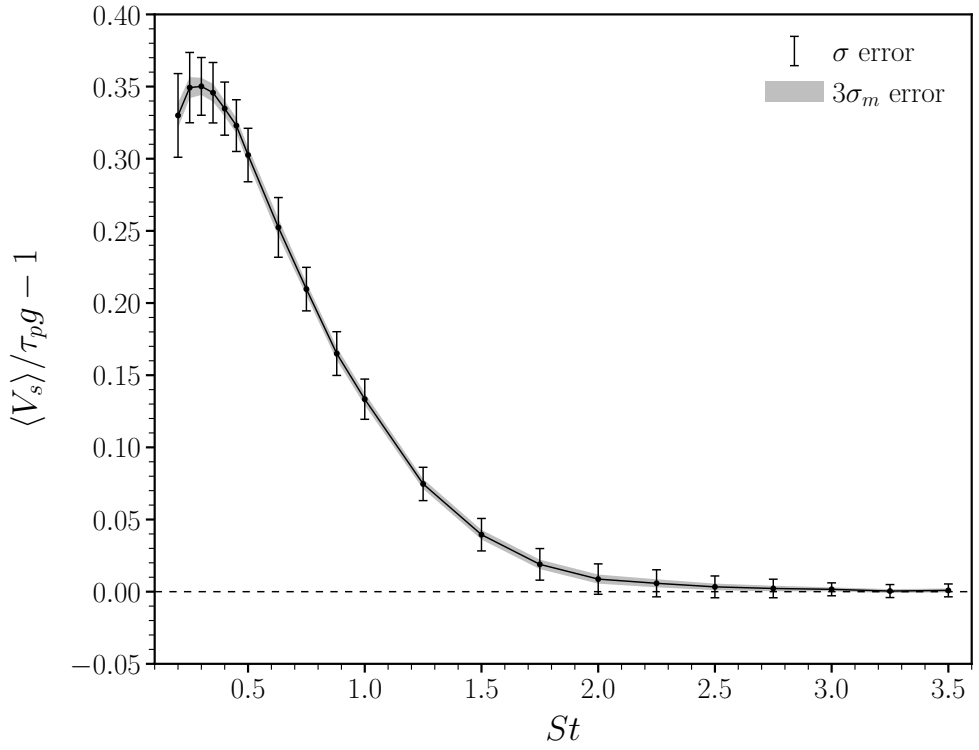

Figure 5.9: Settling speed enhancement at $Re_\lambda \sim 100$.

in this case, gravity dominates over the turbulent dispersion, thus reducing the time inertial particles spend interacting with specific flows scales. For this very reason, the preferential sweeping becomes ineffective in increasing the settling speeds.

For completeness, it should be emphasized that if gravitational effects are included, then periodic boundary conditions can introduce a certain unphysical effect. To be more specific, if the time required to traverse the computational domain is smaller than the characteristic time scale of the underlying turbulence, e.g., the large-eddy turnover time, then a particle can encounter the same large flow scales multiple times [209]. One way to mitigate this issue is to enlarge the computational box in the direction of gravity [17, 201], or simply reduce the range of Stokes numbers being considered. In fact, Ireland [16, 17] extensively studied this issue and introduced a critical Stokes number for which one can expect the results to be immune to periodicity effects

$$St_{\text{crit}} = Fr \left(\frac{L_B}{L} \right) \left(\frac{u'}{u_\eta} \right). \tag{5.5}$$

Considering the DNS at $Re_\lambda \sim 100$, see Table 2.3, St_{crit} is much larger than the largest Stokes number considered in this work, i.e., $St_{\max} = 3.5$.

5.3 Large Eddy Simulations at low Reynolds number

As already indicated, the point-particle LES of isotropic turbulence has been consistently disregarded for studying the physics underlying particle-laden turbulent flows, particularly in the range of Reynolds numbers significantly exceeding those achievable in the DNS of isotropic turbulence. To the best of the author's knowledge, most of the research reported to date was focused on both the subgrid-scale modeling for the fluid velocity at particle locations and its impact on the overall ability of the LES to restore certain particle statistics obtained by means of the DNS. For a more detailed overview, one can refer to Section 4.6 or an extensive review given in [36] and the references therein.

Consider the RDF at contact without gravitational effects depicted in Fig. 5.10. It can be readily noticed that the set of reference DNS data has been extended to account for the FDNS with a hypothetical spectral cutoff at $k_c = 30$. Taking into account the spherical truncation, see Eq. (2.52), the resulting filtered wavenumber space completely covers the one in the LES with the spatial resolution of 64^3 nodes. One can recall that in the point-particle FDNS, the underlying turbulent flow is evolved in time exactly as in the DNS. However, only the filtered (large-scale) fluid velocity field is brought into the particle equation of motion. For this very reason, the

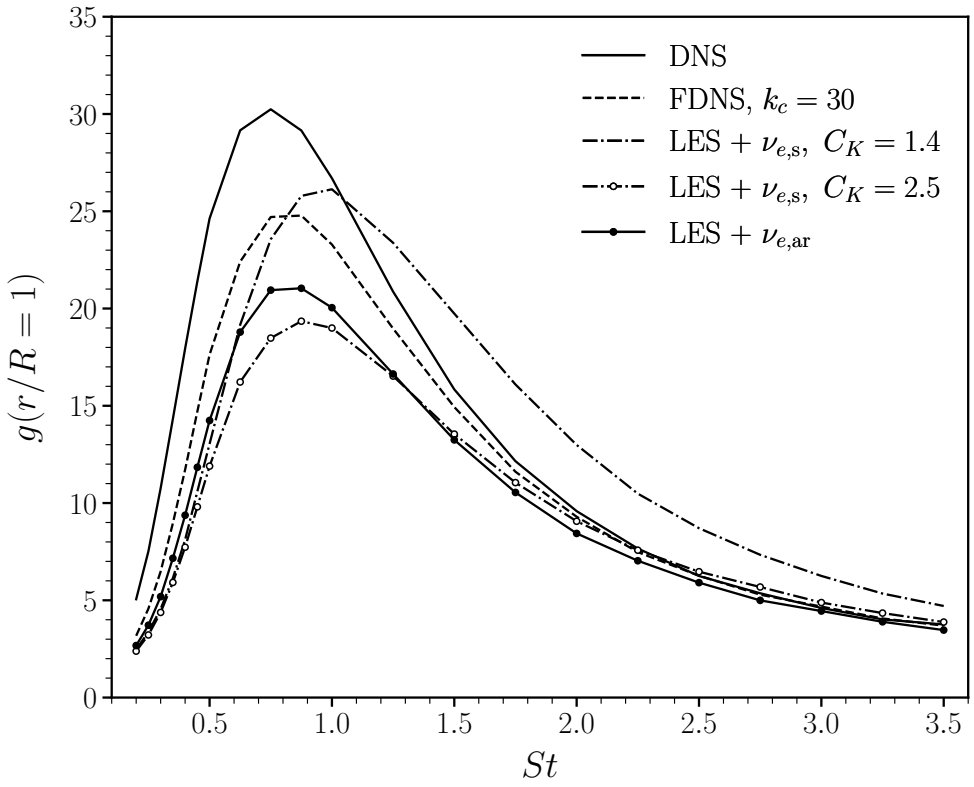

Figure 5.10: The impact of filtering, subgrid-scale modeling, and particle inertia on the RDF at $Re_\lambda \sim 100$ without gravitational effects.

FDNS is often considered as the LES devoid of modeling errors. It can be observed that the impact of spatial filtering (dashed line) is most pronounced for particles whose $St = \mathcal{O}(1)$, as these entities are particularly susceptible to the unresolved small-scale turbulence. For the sake of clarity, it should be once again emphasized that the discrepancies in the RDF between the FDNS and the DNS represent the direct (isolated) impact of filtering on particle motion, and thus follow exclusively from the lack of the subgrid-scale contribution to the fluid velocity at the particle location, see also Eq. (4.67) and Fig. 4.5. What becomes readily apparent is the relatively poor performance of the LES enriched with the standard eddy-viscosity given by Eq. (3.21), where $C_K = 1.4$. To the best of the author's knowledge, this issue has not been reported to date. The RDF is bell-shaped, similar to both the DNS and the FDNS, however, its peak is clearly shifted toward larger St. This behavior presumably follows from inaccurate energy transfer in the vicinity of the spectral cutoff, eventually leading to weakened dynamics of the corresponding flow scales, see Fig. 5.11 (left panel, $R^2 = 0.271$). The aforementioned deficiency possibly disrupts the evolution of these flows scales by modifying their characteristic time scales (when compared to the corresponding DNS). This process can increase the overall time

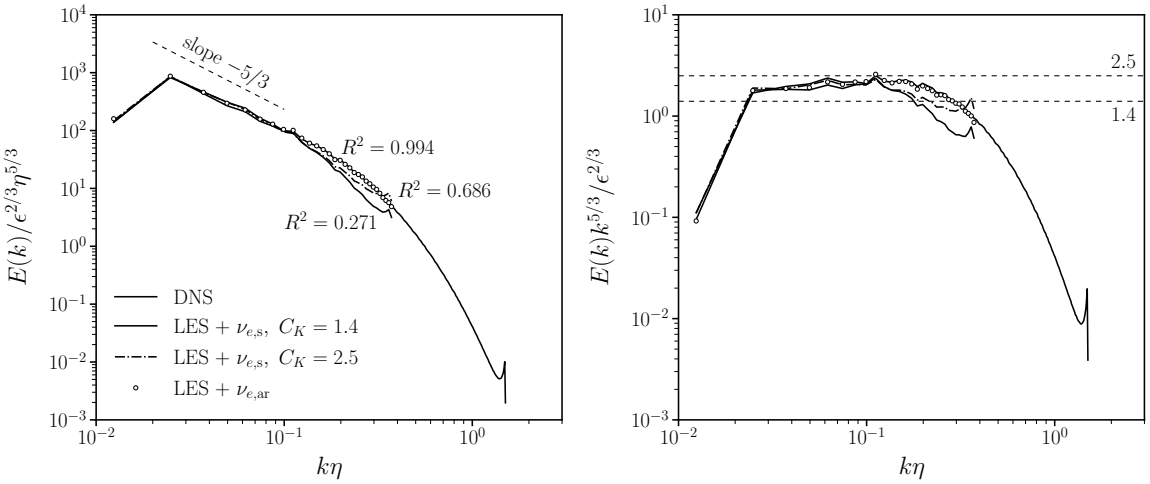

Figure 5.11: The impact of the spectral eddy-viscosity on the energy spectrum function in the LES at $Re_\lambda \sim 100$.

particles spend interacting with specific flow scales, essentially rendering dispersed entities less prone to the underlying turbulence, or, in other words, making particles move as if their inertia is effectively increased. The above reasoning seems to explain the observed shift.

Interestingly, as already indicated in Section 3.4, some authors modify the model constant without reasoning by setting higher values of C_K, see, e.g., [37, 40, 66, 82]. From Fig. 5.11 (left panel), it is readily apparent that such modification indeed leads to a better approximation of the energy spectrum function when compared to the reference DNS. In fact, higher values of C_K can decrease the discrepancies between the energy spectra even more (not shown here). Perhaps the most general conclusion is that there exists a specific value of C_K which provides the highest possible R^2. However, it should be emphasized that if the aforementioned adjustment makes the Kolmogorov constant significantly exceed its typical values[3], then the pursuit of restoring the energy spectrum function becomes devoid of purpose, since the imposed value of the model constant substantially differs from the actual prediction, based on the plateau level in the compensated energy spectrum, see Fig. 5.11 (right panel). Nonetheless, it is difficult to overlook the fact that setting the model constant to $C_K = 2.5$, thus improving the energy spectrum function in the vicinity of the spectral cutoff from $R^2 = 0.271$ to $R^2 = 0.686$, see Fig. 5.11 (left panel), significantly corrects the RDF at contact without gravitational effects as depicted in Fig. 5.10. Therefore, this observation seems to partly explain the motivation for increasing C_K as suggested without reasoning in other research studies.

[3]Recall that based on experiments and numerical simulations, the value of the Kolmogorov constant is expected to fall within $1.4 < C_K < 2.1$

From Fig. 5.2, it also becomes evident that if the LES is enriched with the adaptively-reconstructed spectral eddy-viscosity, then the RDF at contact is significantly improved when compared to the LES enriched with the standard model, however, slightly improved when compared to the one in which the model constant is set to $C_K = 2.5$. For the latter case the improvement is confined mostly to low-inertia particles, say $St < 1.5$, possibly suggesting additional, albeit minor, enrichment of flow scales close to the spectral cutoff. To address the differences between the LES and the FDNS, one has to take into account that although in both methods particles are subjected to the filtered (large-scale) turbulence, the two velocity fields evolve differently. To be more specific, while in the FDNS the instantaneous velocity field results from the non-linear interactions between both the large and small flow scales, the evolution of the LES velocity field is driven exclusively by the large (resolved) ones. For this very reason, the *a priori* LES arguably contains more intermittent regions of high vorticity and strain, thus enriching particle motions more effectively than the LES. This statement is partly supported by the comparison of the PDF of Q_p depicted in Fig. 5.12.

Presumably, the most general conclusion is that while the aforementioned discrepancies in particle statistics are to certain extent caused by the lack of the unresolved small-scale turbulence, they should be attributed to insufficient (or inappropriate) subgrid-scale modeling in the fluid momentum balance equation rather than the absence of the subgrid-scale model for the fluid velocity at particle locations. On the other hand, the two subgrid-scale models are clearly not mutually exclusive, and therefore one can possibly think of a single approach in which the modeled small-scale velocity field is used to enrich both particle dynamics and the resolved turbulence.

From Fig. 5.13, it is readily apparent that gravity modifies the RDF at contact for the entire set of considered Stokes numbers. For small- to moderate-inertia particles, say $St < 1.5$, the lack of small-scale turbulence reduces the preferential sampling, and thus the overall tendency of inertial particles to concentrate in specific regions of the flow (solid line). On the other hand, enhanced clustering observed for large-inertia particles, say $St > 1.5$, is a well-known consequence of weakened turbulent dispersion of such particles [173], essentially increasing the time such entities spend interacting with specific flow scales having characteristic time scales comparable to τ_p. In addition to the above, inertial particles settling in a filtered velocity field seem to become more susceptible to gravitational trapping, so to speak. Initially effective preferential sampling makes particles concentrate in specific regions of the flow where the vertical components are aligned with gravity; however, gravitational effects eventually dominate over the turbulent dispersion, causing more particles to concentrate

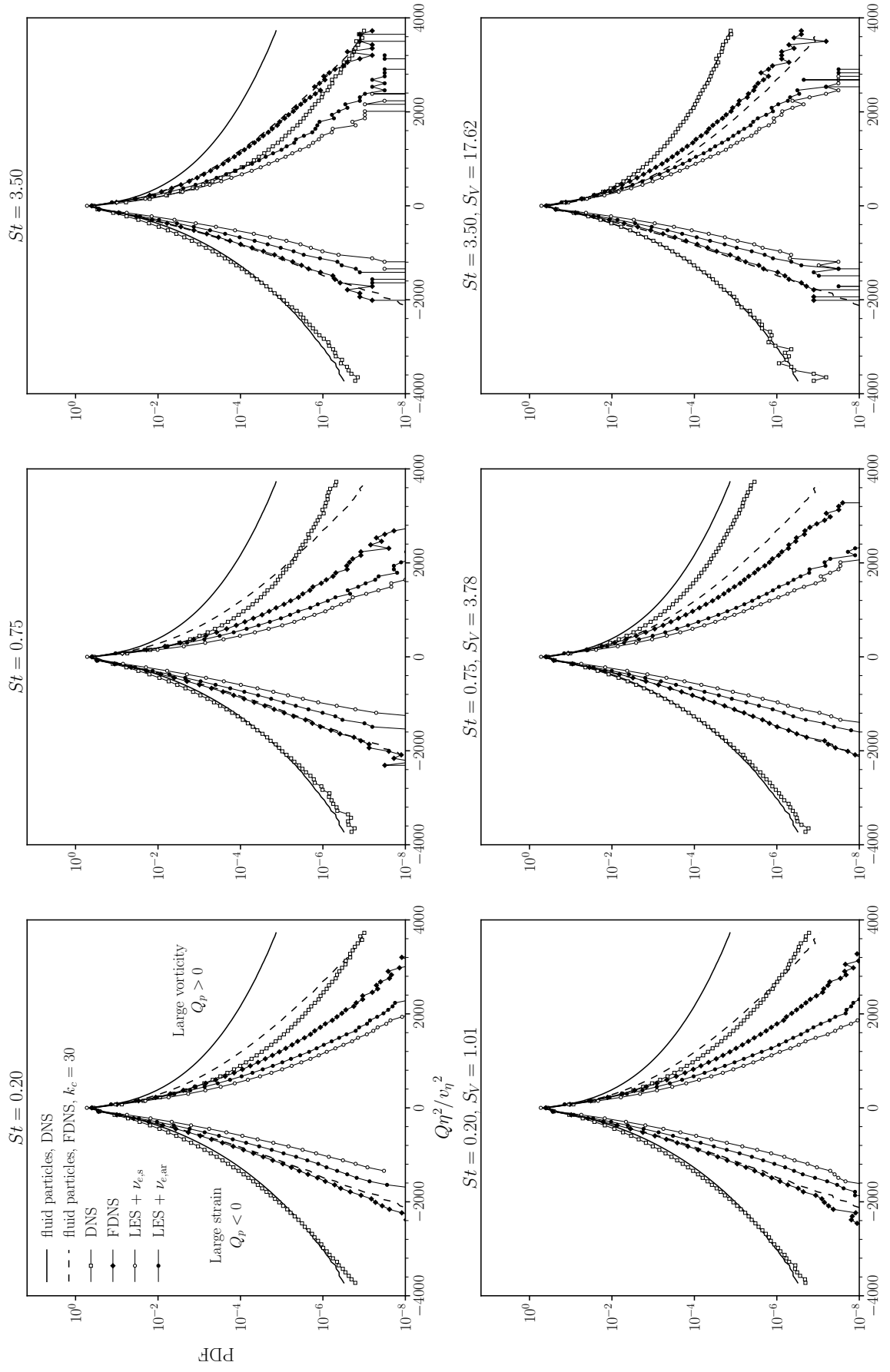

Figure 5.12: The impact of filtering, subgrid-scale modeling, particle inertia, and gravity on the PDF of Q_p at $Re_\lambda \sim 100$.

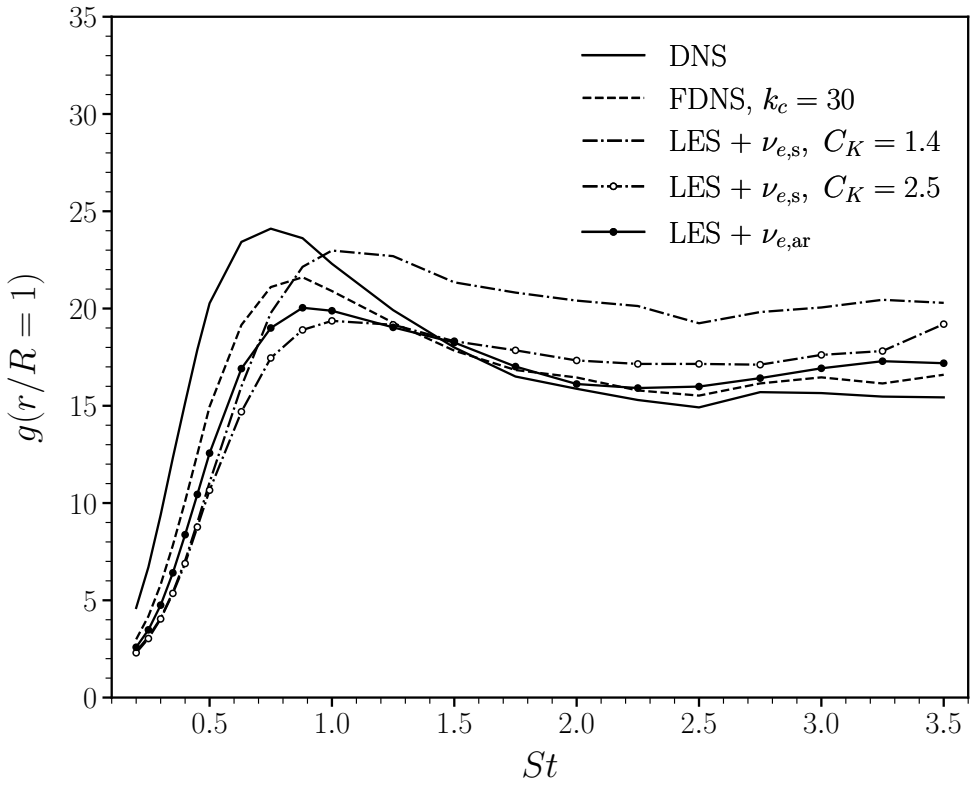

Figure 5.13: The impact of filtering, subgrid-scale modeling, and particle inertia on the RDF at $Re_\lambda \sim 100$ with gravitational effects.

in elongated, filament-like clusters. It can be observed that spatial filtering (dashed line) reduces the clustering of low- to moderate-inertia particles, say $St < 1.5$, however the overall decrease in the RDF is noticeably smaller when compared to the RDF without gravitational effects. This follows from the fact that gravity reduces the time inertial particles spend interacting with specific flow scales, essentially making them less prone to the lack of small-scale turbulence. On the other hand, the clustering is increased for large-inertia particles, say $St > 1.5$. As already mentioned, spatial filtering weakens turbulent dispersion of such particles, thus favoring the clustering. It should be emphasized that assuming the filter width remains constant, the foregoing phenomenon is expected to become progressively enhanced as the Reynolds number increases.

Similar to the previous findings, the LES enriched with the standard spectral eddy-viscosity predicts the RDF at contact exceptionally poor regardless of the particle inertia quantified by the Stokes number. On the other hand, the adaptively-reconstructed eddy-viscosity significantly improves the results, particularly ensuring exceptionally good quantitative agreement with the FDNS. Following the same reasoning addressing the reduced discrepancies between the DNS and the FDNS observed

for low- to moderate-inertia particles (previous paragraph), it can be concluded that in the current LES, inertial particles are less sensitive to both (i) the weakened large-scale turbulence resulting from imperfect (or in appropriate) subgrid-scale modeling in the fluid momentum balance equation and (ii) the actual lack of the subgrid-scale contribution to the fluid velocity at the particle location. It is also worth noting that the adaptively-reconstructed spectral eddy-viscosity further improves the RDF when compared to the standard eddy-viscosity with the adjusted model constant. This presumably follows from the overall better quality of turbulence dynamics, which, on the other hand, results from the improved energy distribution among the resolved flow scales, see Fig. 5.11 (left panel), specifically concerning the improvement from $R^2 = 0.686$ to $R^2 = 0.994$.

Interestingly, although the foregoing particle statistics show pronounced differences between the LES and the DNS, instantaneous particle locations are barely distinguishable as depicted in Figs. 5.14 and 5.15, respectively. This is most likely due to the fact that the spatial resolution of the corresponding LES, $N = 64$ and $k_c = 30$, is sufficient to resolve most of the relevant flows scales at $Re_\lambda \sim 100$. Based

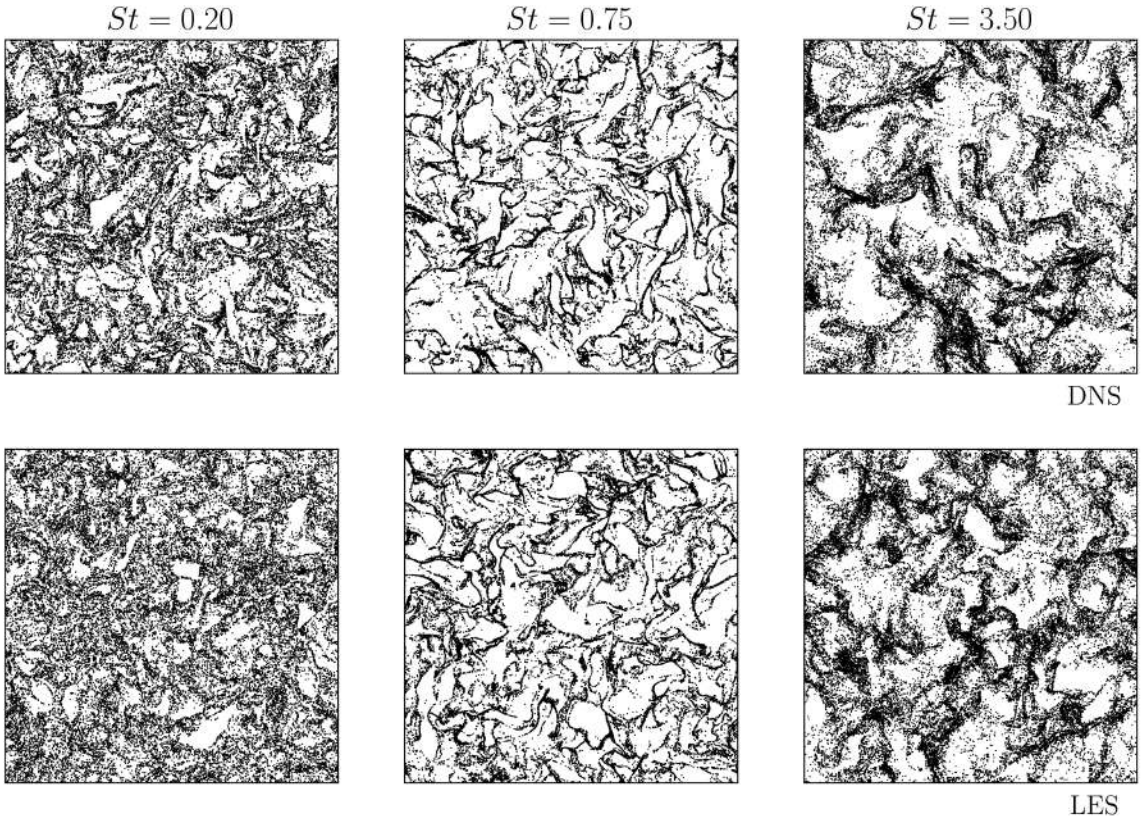

Figure 5.14: Instantaneous particle locations at $Re_\lambda \sim 100$ without gravitational effects; DNS (top panels); LES (bottom panels).

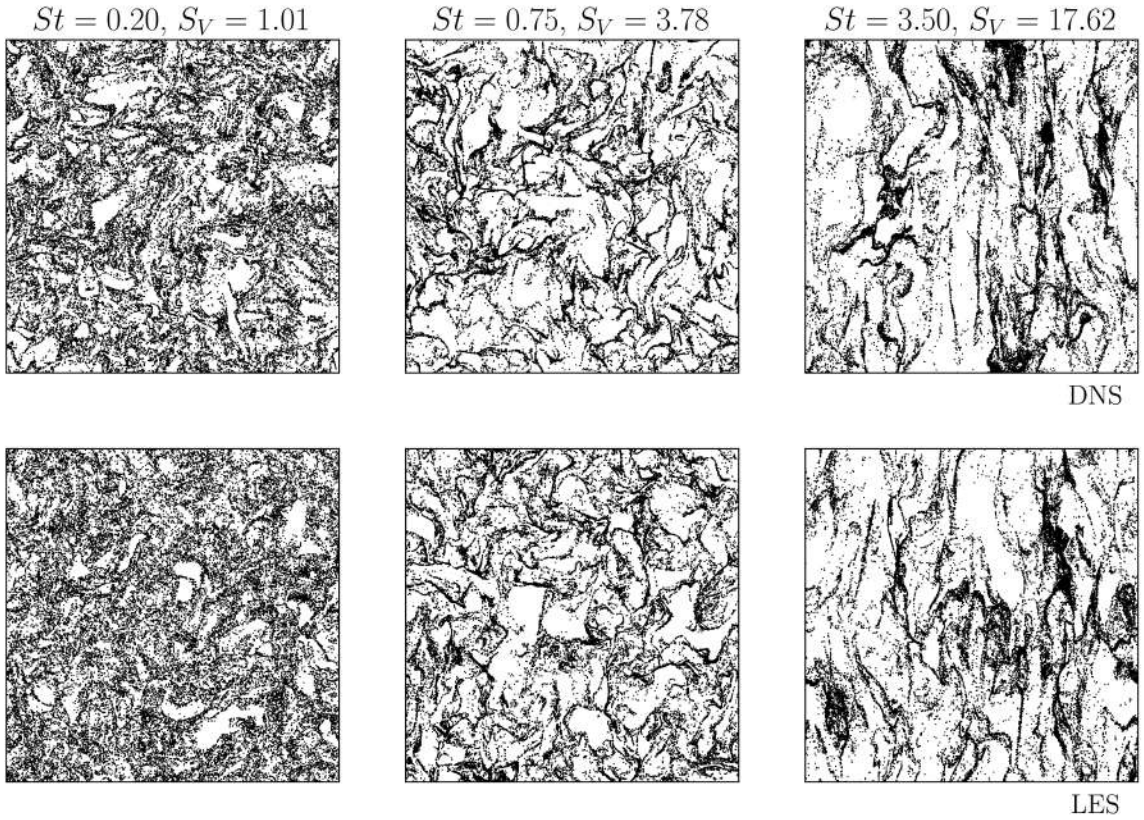

Figure 5.15: Instantaneous particle locations at $Re_\lambda \sim 100$ with gravitational effects; DNS (top panels); LES (bottom panels).

on the foregoing reasoning, in this work, it is argued that assuming appropriate spatial resolution, the LES can predict (at least qualitatively) certain large-scale quantities, e.g., the clustering at length scales much larger than η. On the other hand, it should be emphasized that with increasing Reynolds number, a progressively wider range of flow scales remain unresolved; to clarify, the foregoing statement assumes a fixed spatial resolution. In such a case, significant differences between the instantaneous particle locations are expected for $St = \mathcal{O}(1)$; however, due to weakened turbulent dispersion following from the lack of small-scale turbulence, some discrepancies are also expected for $St \gg 1$ [173].

To assess the above statement, one can consider the spectrum of the particle number density with and without gravitational effects depicted in Figs. 5.16 and 5.17, respectively. In general, it appears that the prediction of particle clustering in LES at length scales larger that η remains in good qualitative agreement with the reference DNS data, regardless of the specific form of the spectral eddy-viscosity; however, it can also be observed that noticeably better quantitative agreement with the corresponding DNS is achieved when the LES is enriched with the adaptively-reconstructed

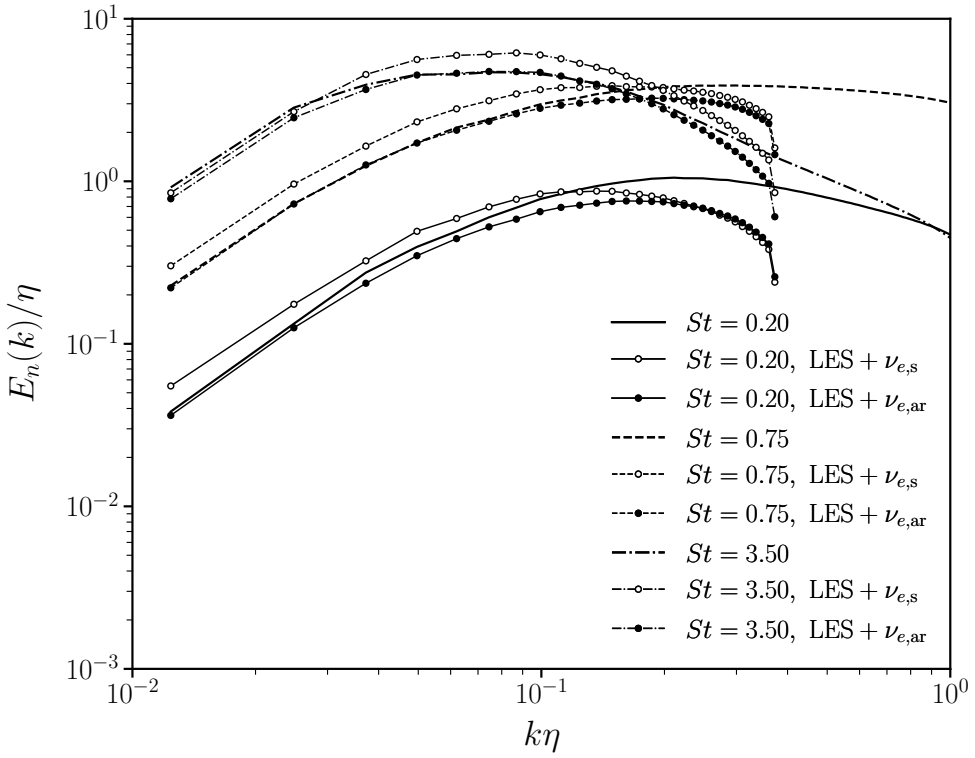

Figure 5.16: The impact of filtering and subgrid-scale modeling on the particle number density spectrum at $Re_\lambda \sim 100$ without gravitational effects.

eddy-viscosity. One can recall that the preferential concentration is most pronounced for $St = \tau_p/\tau_\eta = \mathcal{O}(1)$, see e.g., [14, 173, 192]; however, the above spectra of particle number density reveal a multiscale nature of this phenomenon, possibly suggesting that its intensity can be quantified at different length scales independently. Taking the above reasoning into account, it can be concluded that regardless of particle inertia, the spectra of the particle number density determined using the LES enriched with the adaptively-reconstructed eddy-viscosity remain in excellent quantitative agreement with the corresponding DNS over a wide range of length scales. For this very reason, in this work, it is argued that the current approach can be appropriate for studying particle clustering at length scales comparable to those relevant to the inertial subrange in isotropic turbulence at high Reynolds number, as recently observed in the DNS by Matsuda [165, 166]. This issue will be addressed in the following Section.

Moreover, it can also be observed that the spectra of the particle number density (with and without gravitational effects) tend to underestimate particle clustering at length scales comparable to the smallest resolved ones in the LES. In addition to weakened turbulence dynamics inevitably affecting particle motions, this can be attributed, at least to some extent, to the B-spline smoothing at these very length scales,

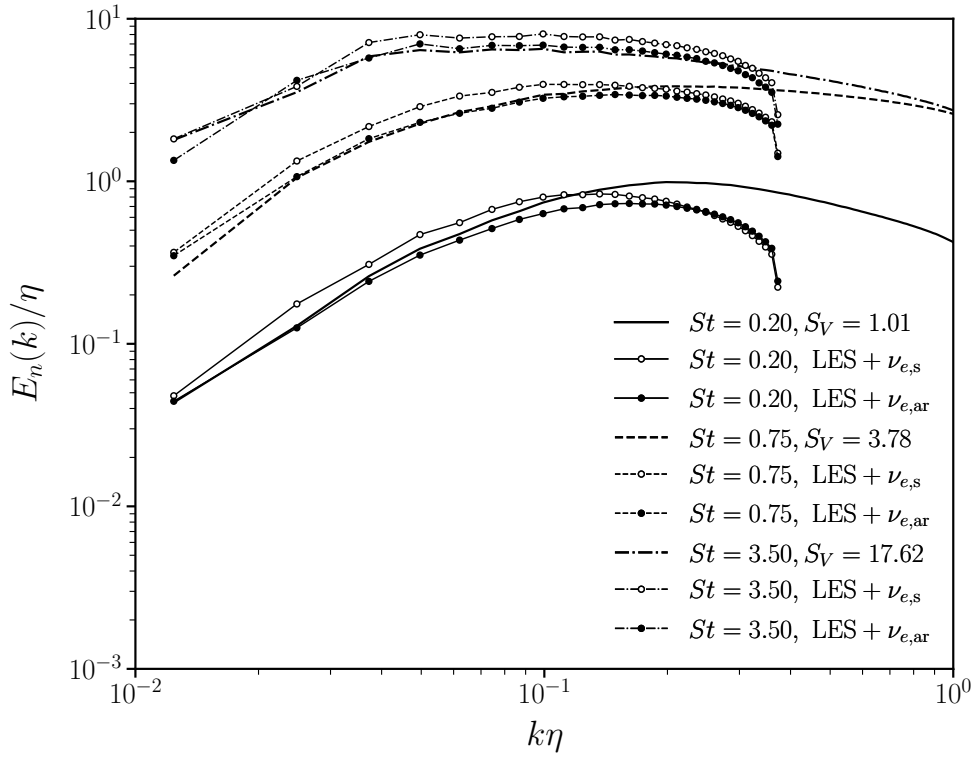

Figure 5.17: The impact of filtering and subgrid-scale modeling on the particle number density spectrum at $Re_\lambda \sim 100$ with gravitational effects.

see Eq. (4.52). Matsuda et al. [166] suggested the use of a piecewise constant function since higher order kernels can introduce artificial smoothing at length scales comparable to the kernel width (Keigo Matsuda, private communication). One can recall that the width of the B-spline kernel is on the order of $\mathcal{O}(\Delta x)$, and thus is comparable to either η in the DNS or Δ in the LES. Regardless of the method, in the vicinity of the spectral cutoff the spectrum of the particle number density may be attenuated by this artificial smoothing. As indicated in Section 4.3 and also in [59, 88, 163], the essence of the B-spline interpolation is based on introducing the convolution in physical space (smoothing) and the subsequent deconvolution in Fourier space. This algorithm should at least mitigate (if not eliminate) the impact of the smoothing kernel on the spectrum function; however, this assumption remains valid only in the limit of the discretization, hence implies $N \to \infty$.

To get a better insight into the B-spline smoothing, one can consider N_p particles randomly and uniformly distributed within the computational box. In this case, the second term in Eq. (4.50) becomes $g(\boldsymbol{r}) = 1$. For this very reason, the total contribution to the spectrum of the particle number density comes from the Poisson noise, and thus $E_n(k) = 4\pi k^2/N_p$. Depending on the order of the B-spline kernel, the actual spectrum function can differ significantly from the exact one as depicted in

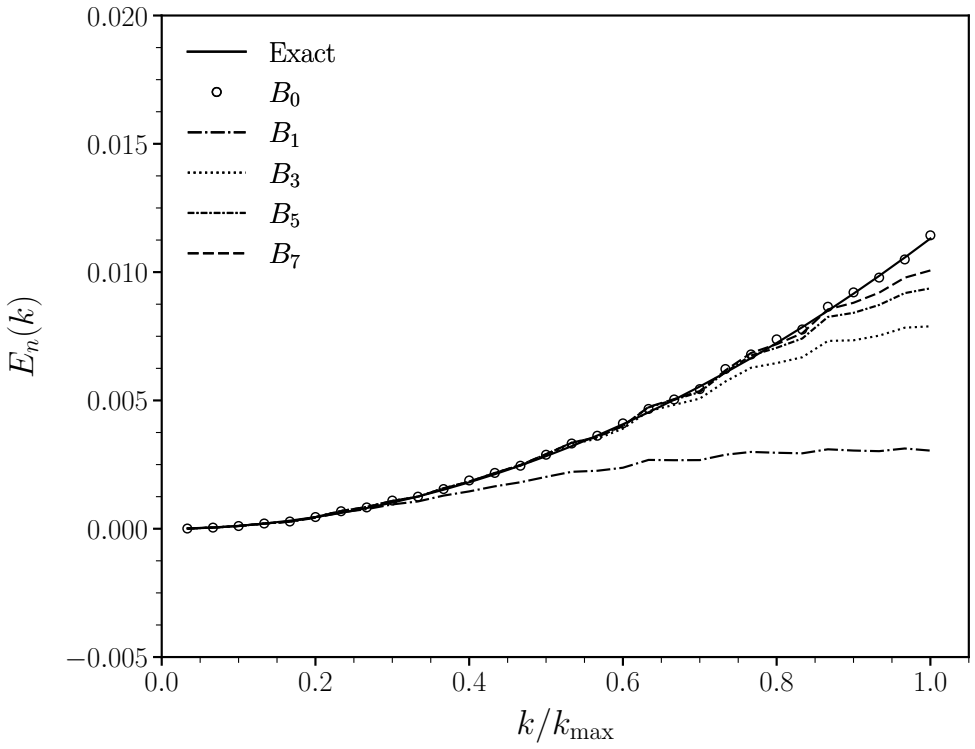

Figure 5.18: Impact of the B-spline smoothing on the particle number density spectrum of randomly distributed particles.

Fig. 5.18. This is consistent with the findings of Matsuda et al. [166] (Keigo Matsuda, private communication). At the time of writing this chapter, the pseudo-spectral code used throughout this work utilized the B-splines of degree 3 precomputed for the purpose of determining the fluid velocity at particle locations. For the sake of both simplicity and efficiency, the spectra of the particle number density were obtained using the very same basis functions. Further work aimed at decoupling these two objectives is therefore needed.

A significant improvement of large-scale dynamics can also be observed in Fig. 5.19. The adaptively-reconstructed spectral eddy-viscosity not only ensures the LES remains in very good quantitative agreement with the FDNS but also outperforms both variants of the standard model. It suggests that the large, energy-containing flow scales contribute most to the particle relative motions. In fact, one can recall that the FDNS with $k_c = 30$, accounts for approximately 98% of the total kinetic energy at $Re_\lambda \sim 100$. The results clearly indicate that assuming appropriate spatial resolution, the LES enriched with the newly developed eddy-viscosity closure can accurately predict relative velocities of inertial particles for a wide range of Stokes numbers.

Similar trends are observed for the settling speed enhancement depicted in Fig. 5.20; however, the improvement when compared to the standard model is rather negligi-

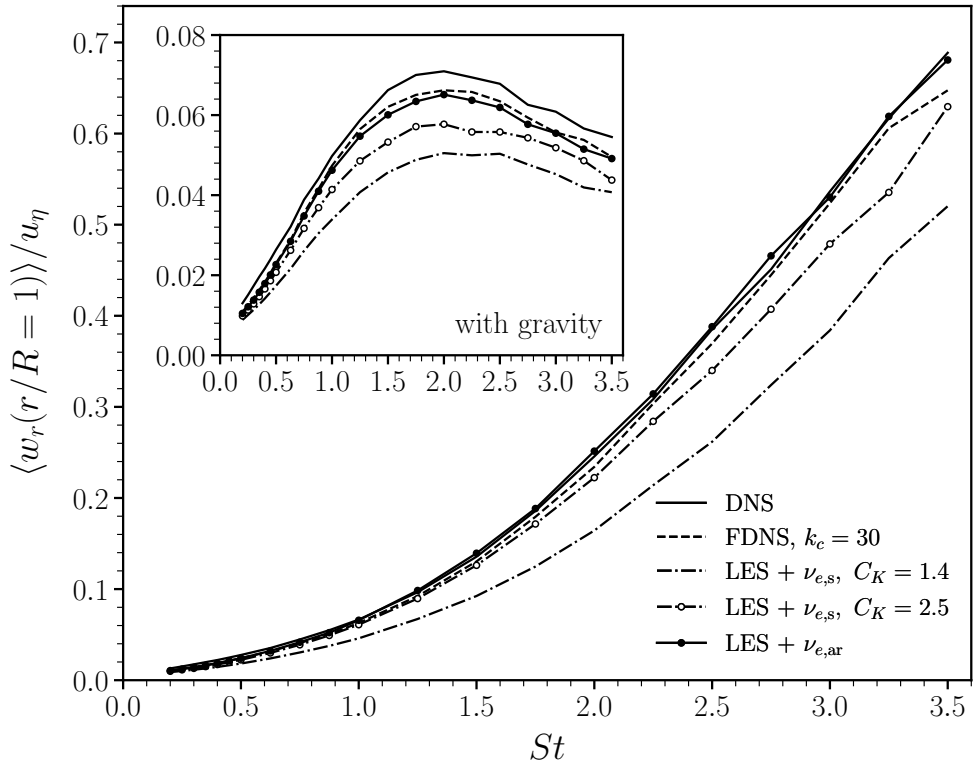

Figure 5.19: The impact of spatial filtering, subgrid-scale modeling, particle inertia, and gravity on the RRV at $Re_\lambda \sim 100$.

ble. It is also worth mentioning that the results were averaged over only at most $25T_e$. It should be emphasized that Rosa et al. [185] pointed out that approximately $100T_e$ is mandatory to achieve statistical convergence of the settling velocity statistics. In general, the spatial filtering removes large velocity gradients associated with the small-scale turbulence, as a result of which low-inertia particles, say $St \leq 0.75$, are less effectively guided into the specific regions of the flow where the fluid velocity is aligned with gravity, essentially making the preferential sweeping less pronounced when compared to either the DNS or the FDNS.

For the given set of simulations, it can be concluded that: (i) the preferential sweeping appears to be mostly driven by the large, energy containing flow scales; (ii) the impact of spatial filtering on the settling speed enhancement, or, interchangeably, the intensity of the preferential sweeping, becomes progressively less pronounced with increasing Stokes number and vanishes completely for moderate- to large-inertia particles, say $St > 0.75$, which essentially corresponds to $S_V > 3.75$.

Although the current LES remains in exceptionally good agreement with either the FDNS or the DNS, it should be emphasized that the preferential sweeping displays a multiscale nature, as recently pointed out by Tom & Bragg [87]. For this very

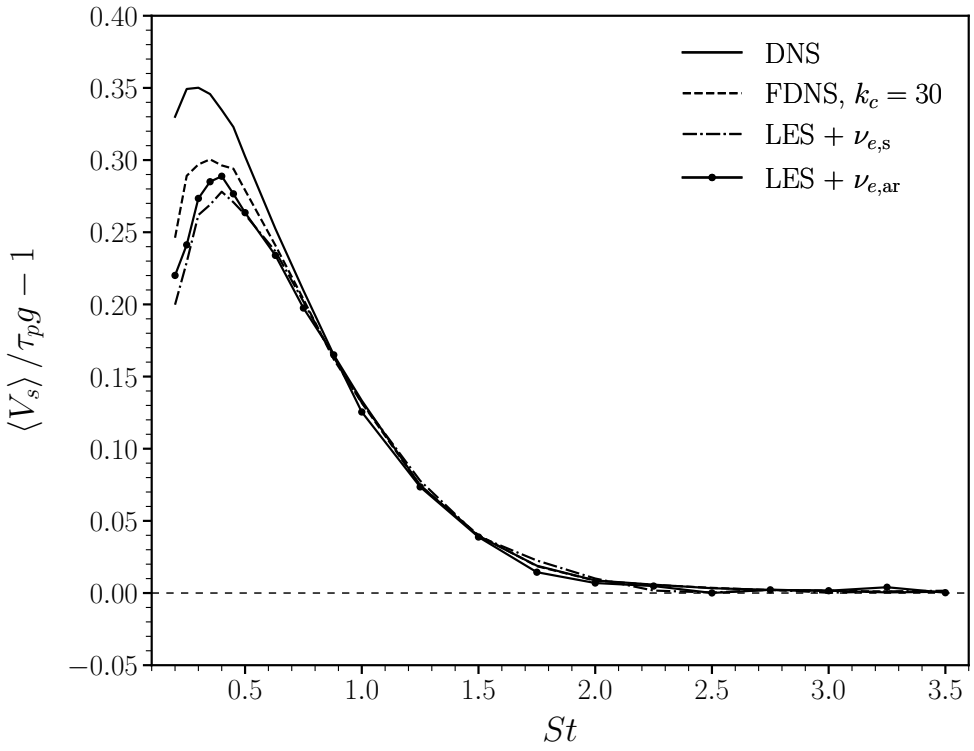

Figure 5.20: The impact of spatial filtering, subgrid-scale modeling, and particle inertia on the settling speed enhancement at $Re_\lambda \sim 100$.

reason, inertial particles can preferentially sample fluid velocity gradients at length scales significantly exceeding those relevant to the dissipation subrange, and thus a combined impact of the spatial filtering and the Reynolds number on the settling velocity statistics of inertial particles is yet to be explored.

5.4 Large Eddy Simulations at high Reynolds number

As already indicated, it is well established that inertial particles preferentially sample specific regions of a turbulent flow. Depending on particle inertia, this behavior can lead to pronounced clustering, i.e., the formation of spatially evolving groups of particles. Recall this phenomenon is often referred to as the preferential concentration or clustering without distinction; however, it should also be emphasized that some authors often distinguish between the two. For instance, Monchaux et al. [15] suggested that the preferential concentration denotes the fact that inertial particles tend to sample specific regions of the flow, whereas the clustering means they also tend to aggregate in those regions. Recently, Bragg et al. [210] pointed out that although

both terms refer to a non-uniform distribution of particles, the preferential concentration additionally implies that the location of dispersed entities is correlated to the local fluid velocity field. As already indicated, this phenomenon was first reported by Maxey [9] and further confirmed numerically by Squires & Eaton [11] as well as experimentally by Fessler et al. [164]. It is also well established that the clustering of inertial particles affects not only the particle-turbulence momentum exchange but also the gravitational settling of such entities, their collisions and also other types of particle-particle interactions. The non-uniform distribution of inertial particles is therefore expected to have a non-negligible impact on various environmental phenomena and industrial processes. The preferential concentration is most pronounced for $St = \mathcal{O}(1)$. Maxey [9] indicated that due to the centrifugal effect, inertial particles tend to concentrate specifically in regions of low vorticity and high strain. On the other hand, Bec et al. [211] reported that at higher Stokes numbers, particles are less effectively centrifuged out of the rotating regions of the flow and suggested that their concentration is most likely driven by the inertial filtering of the fluid velocity field. This suggests that the preferential concentration of inertial particles is not only a multiscale phenomenon but possibly also a multimechanism one.

There have been several studies over the past years that attempted to rigorously explain and accurately predict the clustering of inertial particles; however, as indicated by Bragg & Collins [212], some of them followed a more qualitative research (so to speak), and thus provided somewhat phenomenological, but still to some extent successful, predictions. Whereas others considered far-reaching assumptions regarding the underlying turbulence, see e.g. [212] and the references therein for a more comprehensive review. Chun et al. [193] developed a theory to predict the clustering of small-inertia particles, say $St \ll 1$, at length scales smaller than the smallest resolved ones in a turbulent flow. This range is often formally defined as $r \ll \eta$, and is relevant to the dissipation range of flow scales; to clarify, r represents the distance between two points and η denotes the Kolmogorov length scale. It is also worth mentioning that the recent high-resolution DNS [128] has in fact revealed that the dissipation range can actually extend over approximately 10η [213]. It should also be emphasized that Zaichik & Alipchenkov [214] put forward a more universal theory that attempts to predict the clustering for all St at length scales exceeding the dissipation range. For $St \ll 1$ and $r \ll \eta$ both methods provide similar predictions and agree well with the DNS; however, with increasing St, the foregoing theories begin to diverge in predictions, yet, as indicated by Bragg & Collins [212], that of Zaichik & Alipchenkov is the only one to accurately quantify the clustering of inertial particles with Stokes numbers up to $St = \mathcal{O}(1)$.

It has been long argued that at a sufficiently large Taylor microscale Reynolds number (however, to the best of the author's knowledge, this requirement has not been rigorously quantified by now), inertial particles may also display a tendency to cluster at length scales relevant to the inertial subrange, formally defined as $\eta \ll r \ll L$, where L is the integral length scale of a turbulent flow. This issue has been addressed in several high-resolution DNS of both 2D [215, 216, 217] and 3D [216, 218, 219] particle-laden isotropic turbulence. In [215, 216, 217, 219], it has been argued that particle clustering at length scales relevant to the inertial subrange is driven by the so-called sweep-stick mechanism. In simple words, it has been reported that inertial particles tend to concentrate in regions of low acceleration, which are subjected to sweeping by the local fluid velocity. Bragg et al. [213] studied the exact equation governing the RDF and compared the clustering mechanisms it implies in different regimes. Introducing the so-called scale-dependent particle Stokes number given by $St_r \equiv \tau_p/\langle\epsilon\rangle^{-1/3}r^{2/3}$, the authors indicated that for any separation $r < L$ and $St_r \ll 1$, particle clustering can be attributed to the preferential sampling leading to centrifuging effect, whereas in the opposite regime, i.e., $St_r \gg 1$, the clustering can be attributed to non-local, path-history effects.

To the best of the author's knowledge, although high-resolution DNS has already been applied multiple times to study single-phase isotropic turbulence, see, e.g. [126, 127, 128] for simulations at $Re_\lambda \sim 1200$ having up to $\sim 16384^3$ nodes, and a few recent studies [130, 131, 139] where $Re_\lambda \sim 2500$ was reached using up to $\sim 32768^3$ nodes, particle-laden flows are still limited to $Re_\lambda \sim 600$ and the spatial resolution on the order of $\sim 4096^3$ nodes, see, e.g. [16, 17, 165, 166]. In forced isotropic turbulence, a well-developed inertial subrange can be obtained on condition that sufficient scale separation between the large flow scales and the smallest, dissipative ones is ensured, see, e.g. [220] and the references therein. This implies the need for high Reynolds numbers along with appropriate spatial resolutions. In a properly designed DNS or LES, the span of the inertial subrange can be determined based on a simple dimensional analysis, recall Table 3.1 in Section 3.6 and the reasoning concerning *a priori* prediction of specific LES statistics given there. Assuming this range is formally defined as $\lambda < r < L$ and $L_B/L \sim 8$, the pseudo-spectral DNS (or LES) is expected to capture the inertial subrange which extends over approximately λ^{-1} wavenumbers (including the artificially forced ones). This straightforward prediction gives $k_\lambda \sim 30$ for the DNS at $Re_\lambda \sim 600$ and $N = 4096^3$ as in [166], whereas at $Re_\lambda \sim 2500$ and $N = 32768^3$ [131], this range would be limited by approximately $k_\lambda \sim 100$. At this point, one should also recall that considering the cloud conditions, see Section 5.2, the Taylor microscale Reynolds number and the corresponding inertial

range are on the order of $Re_\lambda \sim 10000$ and $k_\lambda \sim 400$, respectively.

Interestingly, from [166], it seems that at $Re_\lambda = 648$ the Taylor microscale is on the order of $\lambda \approx 0.05$, and thus $k_\lambda \approx 20$. On the other hand, based on the energy spectrum given there, it appears that at most 50 wavenumber shells display the $k^{-5/3}$ scaling, possibly indicating that (i) the inertial subrange extends beyond λ and that (ii) a more stringent spatial resolution than initially proposed in Section 3.7 may be required for the LES to accurately capture the inertial range dynamics. On the other hand, it must be once again emphasized that one should be cautious when determining the extent of the inertial subrange solely from the energy spectrum function (be it raw or compensated). Nevertheless, it appears evident that even for high-resolution DNS, dispersed particles are subjected to a relatively narrow range of length scales displaying the inertial range dynamics.

Matsuda et al. [165, 166] were the first to confirm the multiscale nature of particle clustering using the DNS of isotropic turbulence. By means of the spectrum function of the particle number density, the authors demonstrated that inertial particles whose $St = \mathcal{O}(1)$ exhibit a tendency to cluster at length scales relevant to both the inertial and the dissipation ranges simultaneously. Their results also indicate that regardless of both the Reynolds and the Stokes numbers, inertial particles tend to form clusters at length scales comparable to $\sim 5\eta$. This remains in excellent agreement with the current DNS at $Re_\lambda \sim 100$, see Fig. 5.5. For sufficiently high Reynolds number, that is on the order of $Re_\lambda \sim 600$, the number density spectrum shows a second local maximum, clearly indicating the clustering at length scales on the order of $\sim 200\eta$. Interestingly, experimental study in zero-mean flow air turbulence chamber at $Re_\lambda \sim 500$ revealed that particles with $St > 1$ tend to aggregate at length scales on the order of 300–400η [221]. Some quantitative discrepancies between the DNS and experimental studies are still to be expected. At this point, it should be emphasized that neither the pseudo-spectral DNS nor the LES guarantee physically-correct results, particularly when it comes to capturing the inertial range dynamics. In this work, it has already been demonstrated that in the case of the DNS, an insufficient spatial resolution of both large and small flow scales can lead to artificially correlated velocity fields. In addition to that, an insufficient scale separation in LES can hinder, or even fully suppress the development of the inertial subrange.

The motivation for the remaining part of this research is threefold: (i) to support the ongoing development of theories focused on explaining the clustering of inertial particles; (ii) to provide numerical tools for assessing these theories at Reynolds numbers significantly exceeding the current capabilities of the DNS; (iii) to respond to a brief comment made in [166]—"particle clustering in the inertial subrange could

have an impact on the subgrid-scale modeling for large-eddy simulations".

In this part, the particle-laden LES with the adaptively-reconstructed spectral eddy-viscosity is compared against the DNS data reported in [166]. The referenced code has already been extensively used in other research studies, see, e.g., [165, 222, 223, 224]. The governing Navier-Stokes equations were solved in physical space; the fourth-order central difference scheme was used for the advection and viscous terms [225]; highly simplified marker and cell method [226] was used for the pressure-velocity coupling; the forcing was confined to the first two wavenumber shells, i.e., $|\boldsymbol{k}| < 2.5$, and was applied in either deterministic [227] or stochastic manner [228]. The authors performed a limited forcing independence study in [166] (supplementary material); however, the selection of forced wavenumbers still raises questions about the spatial correlations of the velocity field, which are expected to influence particle motion (recall the results given in Section 2.11). The second-order Runge-Kutta method was used for the time integration of the equations governing the motion of both fluid and inertial particles. To the best of the author's knowledge, the fluid velocity at the particle location was determined using a simple linear interpolation, which, in view of the reasoning provided in Sections 4.2 and 4.3, is to some extent questionable. It should be emphasized that despite some key differences between the two code bases, the results should (theoretically) be statistically indistinguishable.

Consider the compensated energy spectrum function depicted in Fig. 5.21 (left panel). It can be observed that the reference spectrum reaches a plateau for approximately $0.008 < k\eta < 0.03$ with an average Kolmogorov constant $C_K \approx 1.65$ in this range. This remains in excellent agreement with other high-resolution DNS, see,

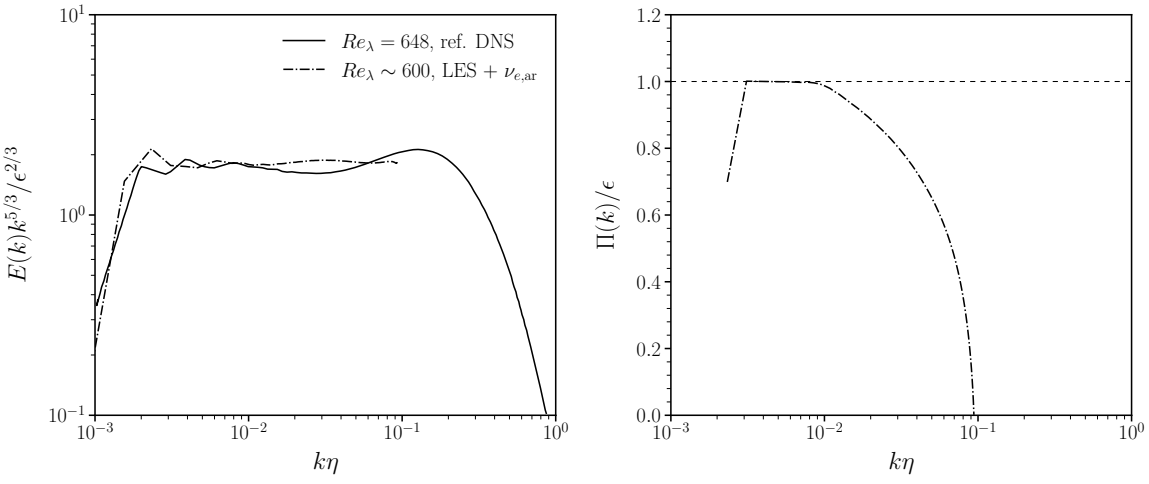

Figure 5.21: Compensated energy spectrum (left panel) and normalized energy flux (right panel) in LES at $Re_\lambda \sim 600$; reference DNS data obtained from [166] and replotted with permission of the authors.

e.g., [128]. It should also be noted that the forcing was confined to $k\eta < 2.5 \times 10^{-3}$. The local maximum at approximately $k\eta = 0.15$ results from the viscous effects on the spectral transfer and is often referred to as the "bottleneck" effect, see e.g., [220] and the references therein to get more insight into this issue. The corresponding spectral LES at $Re_\lambda \sim 600$ was obtained using the spatial resolution of 256^3 nodes. The spectral eddy-viscosity was determined according to Eqs. (3.42) and (3.43) with the transition point and the expected Kolmogorov constant set equal to $k_t = 0.1k_c$ and $C_K = 1.85$, respectively. The forcing was confined to $k\eta < 2.5 \times 10^{-3}$. When compared to the reference DNS, this seemingly gives an impression that the two forcing terms cover the same range of wavenumbers. This is not true because in fact $\eta^{\mathrm{REF}}/\eta^{\mathrm{LES}} \sim 10$. In this work, η^{LES} is essentially the predicted smallest resolved length scale at the particular Reynolds number. It should be emphasized that the spatial resolution of LES given by $k_c\lambda \approx 4.6$ is insufficient, however, exclusively constrained by the computational limitations. One can recall the resolution requirement given by Eq. (3.45) and the reasoning beneath it. Nevertheless, it is readily visible that the two spectra agree well for approximately $0.003 < k\eta < 0.015$, arguably suggesting that the current LES accurately predicts the onset of the inertial subrange. This statement can be partly supported by the spectrum function of the normalized energy flux depicted in Fig. 5.21 (right panel), from which it can be observed that for the relevant range of wavenumbers, the energy is transferred at approximately correct rate.

As already indicated, the second invariant of the velocity gradient tensor Q can provide valuable insight into the clustering of inertial particles. Therefore, its compensated spectra are compared in Fig. 5.22 (left panel). Matsuda et al. [166] pointed out that in a turbulent flow at high Reynolds number, the spectrum of Q displays the $k^{5/3}$ scaling. This appears to be case for their DNS at $Re_\lambda = 648$ and $0.008 < k\eta < 0.015$, arguably suggesting a well-developed inertial subrange, however, with a possibly smaller width than initially estimated. In the current LES, the spectrum of Q remains in good agreement with the DNS, particularly for the largest resolved flows scales. Surprisingly enough, within the anticipated inertial subrange, i.e., $0.003 < k\eta < 0.015$, the $k^{5/3}$ is not captured despite ensuring $\Pi(k) \approx \epsilon$. This is in contradiction with the previous findings and may suggest that the characteristics of the inertial subrange are in fact not accurately resolved, if at all captured. Fortunately (so to speak), the spectrum of Q displays a strong dependence on the spatial resolution, see Fig. 5.22 (right panel), arguably suggesting that the discrepancies between the two spectra will be significantly reduced once a proper spatial resolution of LES is ensured (this statement cannot be supported with the current computational limita-

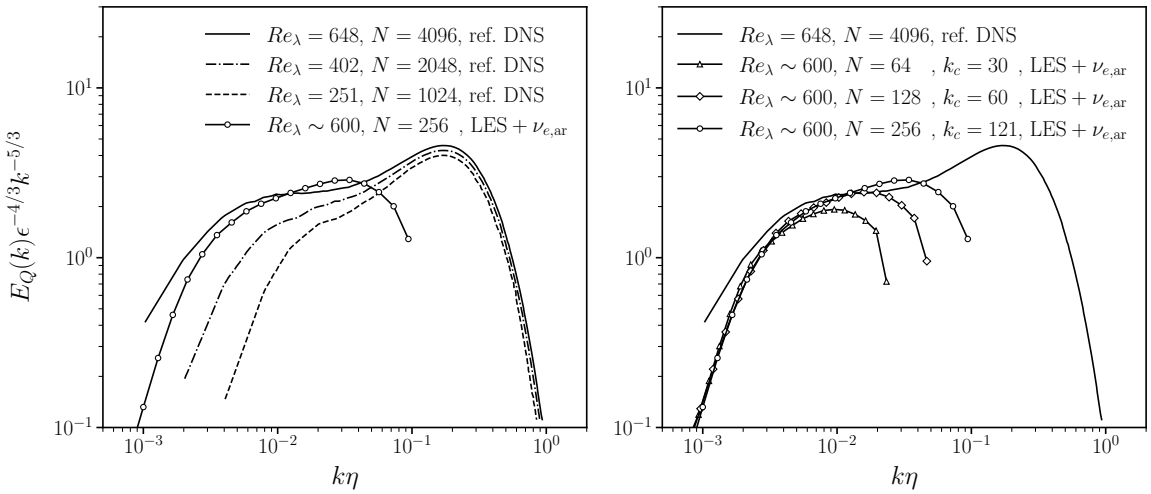

Figure 5.22: Compensated spectrum of Q (left panel) and the impact of spatial resolution (right panel) in LES at $Re_\lambda \sim 600$; reference DNS data obtained from [166] and replotted with permission of the authors.

tions). A somewhat satisfactory quantitative agreement between the two spectra for $0.003 < k\eta < 0.04$ may suggest that the instantaneous structure of the large-scale velocity field depends weakly on the unresolved small-scale turbulence. This can greatly simplify the subgrid-scale modeling or justify a simple statistical description as in the current work.

The normalized spectra of the particle number density are depicted in Fig. 5.23. For the sake of clarity, it should be emphasized the DNS and LES results are plotted in pairs composed of thick and thin lines, respectively. Following [166], these are compared for three Reynolds numbers $Re_\lambda = 251$, 402 and 648 and five Stokes numbers $St = 0.2, 0.5, 1.0, 2.0, 5.0$, except for $Re_\lambda = 648$ where $St = 0.2$ was omitted due to the computational cost of the simulation. Assessing the impact of gravitational effects is intended for further research. Recall the spectra were computed using the B-spline kernel which decreases the spectrum function in the vicinity of the spectral cutoff. However, this is not of concern in the current study since its sole purpose is to assess whether the LES can capture the inertial particle clustering at length scales much larger than $\sim k_c^{-1}$.

Consider the LES at $Re_\lambda \sim 250$ (top panel) for which $N_{\mathrm{DNS}}/N_{\mathrm{LES}} = 4$ and $k_c\lambda \approx 11.6$. Based on the reasoning concerning the required spatial resolution of LES given in Section 3.7, the selected number of nodes appears to be sufficient to ensure accurate resolution of the relevant range of flow scales. It is readily apparent that regardless of St, all spectra are in exceptionally good agreement with the DNS for $k\eta < 0.1$. Small discrepancies can probably be attributed to the fact that, for such a low Reynolds number, the $k^{-5/3}$ scaling enforced in the model energy spectrum during the adaptive

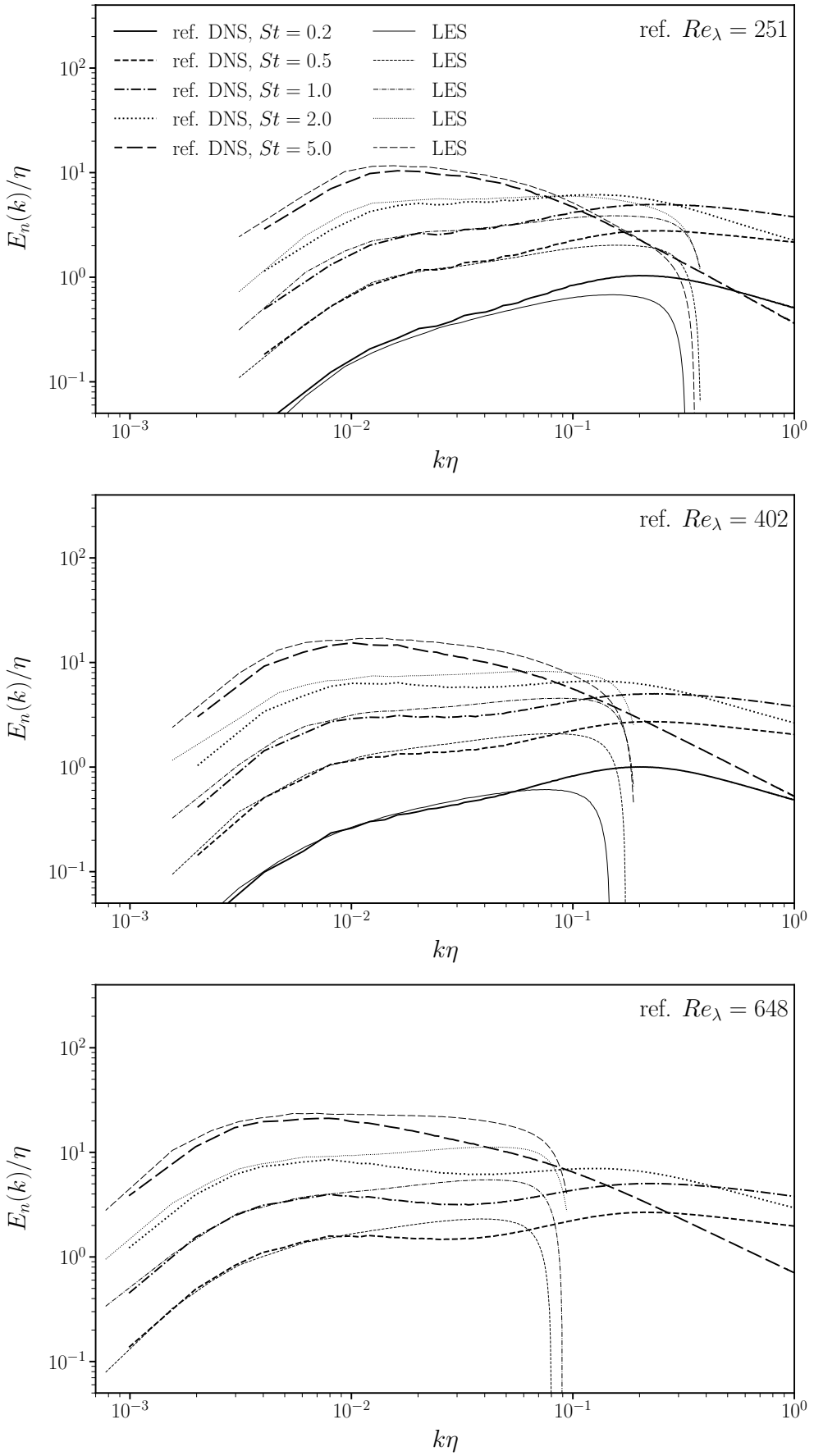

Figure 5.23: Spectrum of the particle number density at different Reynolds numbers; results are plotted as pairs of thick (DNS) and thin (LES) lines; reference DNS data obtained from [166] and replotted with permission of the authors.

reconstruction can actually lead to less accurate approximation of the actual DNS energy spectrum. Therefore, this case should be considered more as a proof of concept. It is expected that these discrepancies will be reduced once the DNS energy spectrum is brought into the model. Nevertheless, these results seem to support the previous statements regarding the subgrid-scale modeling and essentially suggest that the large-scale clustering of inertial particles is weakly dependent on the small-scale turbulence.

In the LES at $Re_\lambda \sim 400$ (middle panel), the spatial resolution is given by $N_{\mathrm{DNS}}/N_{\mathrm{LES}} = 8$ and $k_c\lambda \approx 7.3$. Nevertheless, the two spectra are in very good agreement for $k\eta < 0.03$. It should be emphasized that in a properly designed spectral simulation, both the large-scale, $L_B/L \approx 8$, and small-scale, $k_{\max}\eta > 1$, resolutions are ensured regardless of the Reynolds number. Therefore, the largest flow scales are accurately resolved for all Reynolds numbers considered in this work, which appears to support the foregoing observation. A more pronounced clustering for $k\eta > 0.03$, when compared to the DNS, can suggest a weakened turbulent dispersion of inertial particles, which, in turn, can increase the time particles spend interacting with specific flow scales. On the one hand, this can be attributed to the lack of small-scale turbulence, but on the other one, taking into account the previous findings, it seems that an insufficient spatial resolution is more likely to be the root cause of this phenomenon.

In the LES at $Re_\lambda \sim 600$ (bottom panel) the spatial resolution is limited to $N_{\mathrm{DNS}}/N_{\mathrm{LES}} = 16$ and $k_c\lambda \approx 4.6$. It can be observed that regardless of the Stokes number, the LES remains in excellent quantitative agreement with the reference DNS data for $k\eta \leq 0.01$. The results arguably suggest that: (i) the large-scale clustering of inertial particles depends weakly on the unresolved small-scale turbulence; (ii) the multiscale nature of the preferential concentration can be explored at different length scales somewhat independently; (iii) the filtered Navier-Stokes equations can accurately capture the dynamics of large flow scales on condition that sufficient spatial resolution is ensured. Pronounced discrepancies between the DNS and the LES observed for $k\eta > 0.01$ can be to some extent attributed to insufficient spatial resolution; however, these differences are expected to decrease with increasing $k_c\lambda$. Perhaps the most general conclusion is that the LES enriched with the adaptively-reconstructed spectral eddy-viscosity can accurately capture the clustering of particles at length scales relevant to the inertial subrange.

5.5 Concluding remarks

This Chapter was focused on modeling specific physical phenomena associated with the motion of inertial particles suspended in a turbulent flow. Particular emphasis has been put on using the point-particle LES as a means of extending the range of Reynolds numbers currently achievable in the DNS of particle-laden isotropic turbulence. Despite its evident potential, the pseudo-spectral LES coupled with the Lagrangian particle tracking has been consistently disregarded for studying the physics underlying particulate two-phase flows. As previously mentioned, this state of affairs appears to result solely from the fact that the modeling of the residual small-scale turbulence remains an open issue, not only in the case of single-phase flows but also dispersed two-phase ones. In addition to that, detailed (if any) guidelines on how it should be addressed are yet to be established. In fact, to the best of the author's knowledge, most of the research concerning the point-particle LES reported to date was limited to relatively low Reynolds numbers, and was primarily focused on either (i) assessing the impact of the unresolved turbulence on particle motion or (ii) developing the models for the fluid velocity along particle trajectories, that specifically attempt to improve the agreement of certain particle statistics between the LES and the DNS. To the best of the author's knowledge, the point-particle LES of isotropic turbulence has not been applied, surprisingly enough, to study the physics underlying particulate two-phase flows at high Reynolds numbers; to clarify the latter statement, the Reynolds numbers exceeding those currently achievable in the DNS of either single-phase flows or particle-laden ones.

For these very reasons, the purpose of this Chapter was as follows: (i) to validate the newly developed pseudo-spectral LES solver coupled with the Lagrangian particle tracking; (i) to obtain reference DNS/FDNS data for the research concerning the point-particle LES; (iii) to assess the impact of the standard spectral eddy-viscosity on the ability of the LES to capture specific physical phenomena associated with the motion of inertial particles suspended in a turbulent flow; (iv) to assess how the newly developed subgrid-scale closure influences inertial particle dynamics in isotropic turbulence at low Reynolds numbers, and (v) to determine its usefulness for studying the physics underlying particulate two-phase flows, specifically at high Reynolds numbers; (vi) to provide a self-contained guideline but also (vi), to put forward a set of good practices concerning the LES of particle-laden isotropic turbulence.

In general, this Chapter contains a brief introduction to particle-laden turbulent flows, particularly concerning their major practical importance, complexity and some issues (or bottlenecks) that one usually encounters when studying the underlying

physics. The flow "within a box" was given a more physical context by selecting the relevant parameters so that the dispersed phase was, to some extent, related to cloud droplets suspended in the turbulent atmosphere. Although this is certainly a multiscale phenomenon in which specific physical parameters can change by orders of magnitude, all simulations were carried out under fixed conditions. This was motivated exclusively by the computational limitations. A summary of what appear to be the most important achievements and contributions of this part of the research is provided in the following paragraphs.

First, the point-particle DNS has provided some insight into the physics underlying particulate two-phase flows, with an emphasis on the preferential concentration and the preferential sweeping, as these two phenomena are of significant importance to many environmental and industrial processes (Section 5.2). In general, it has been concluded that: (i) the newly developed pseudo-spectral solver coupled with the Lagrangian particle tracking constitutes a robust and accurate tool for studying particle-laden turbulent flows, and (ii) all results display physical correctness and, most importantly, remain in excellent qualitative agreement with other research studies reported in the scientific literature.

Second, the impact of the well-established standard spectral eddy-viscosity on particle motion has been thoroughly examined (Section 5.3). In general, when compared to the FDNS, such LES: (i) is unable to accurately predict both the RDF and the RRV at contact, and therefore appears to be inappropriate for gathering collision-related statistics; however, it provides a qualitatively accurate prediction of both (ii) the preferential sweeping, quantified by means of the average settling speed enhancement, and (iii) the preferential concentration at length scales larger than the smallest resolved ones, quantified using the spectrum of the particle number density. It has also been indicated that the prediction of the aforementioned statistics can be significantly improved when the model constant is increased from $C_K = 1.4$ to $C_K = 2.5$, where the latter value is often reported in the scientific literature without reasoning. It has also been pointed out that higher values of C_K provide increasingly better agreement in the energy spectra between the DNS and the LES; however, this artificial modification eventually makes C_K inconsistent with the value of the Kolmogorov constant determined from the compensated energy spectrum. Therefore, perhaps the most general conclusion is that the standard spectral-eddy-viscosity contains an adjustable parameter, which largely depends on the specific case, and whose impact on the final outcome cannot be predicted prior to starting the simulation. For these very reasons, the LES enriched with the standard model has no real predictive value at Reynolds numbers exceeding those achievable in the DNS, and thus does not appear

appropriate for studying the physics underlying particulate two-phase flows.

Third, the impact of the adaptively-reconstructed spectral eddy-viscosity on particle motion has been thoroughly examined (Section 5.4). It has been concluded, solely based on the PDF of the second invariant of the velocity gradient tensor sampled at particle locations, that at low Reynolds number: (i) particle dynamics is only slightly enhanced when compared to the LES enriched with the standard eddy viscosity; (ii) the turbulence experienced by the particles remains significantly weakened when compared to either the FDNS or the DNS. Nevertheless, when compared to the standard model, the adaptively-reconstructed eddy-viscosity provides a significant improvement in the prediction of both the RDF and the RRV at contact, particularly ensuring exceptionally good qualitative agreement with the FDNS. Some discrepancies between the *a priori* and the *a posteriori* LES have been attributed to imperfect subgrid-scale modeling in the fluid momentum balance equation, rather than the actual lack of the residual fluid velocity in the particle equation of motion. The proposed LES provides a qualitatively accurate prediction of the preferential sweeping and a very good quantitative prediction of clustering at length scales larger than the smallest resolved ones.

Fourth, the performance of the LES enriched with the adaptively-reconstructed eddy-viscosity has been assessed in isotropic turbulence at high Reynolds number, with a particular emphasis on its capability to capture the clustering of inertial particles at length scales relevant to the inertial subrange. Based on the comparison with the current state-of-the-art in the point-particle DNS, it has been concluded that the proposed LES can accurately predict the clustering at length scales orders of magnitude larger than the smallest resolved ones, essentially quantified using the spectrum of the particle number density. In addition to the above, it has been pointed out that: (i) the clustering of inertial particles is a multiscale phenomenon that can be quantified at different length scales to some extent independently; (ii) assuming sufficient spatial resolution, the LES enriched with the proposed spectral eddy-viscosity becomes an exceptionally accurate tool for studying the influence of large, energy-containing flow scales on the motion of inertial particles, and thus can support the on-going efforts in developing theories explaining the turbulent transport of inertial particles.

Chapter 6

Summary and future research

This dissertation was devoted to numerical modeling of turbulent single-phase and dispersed two-phase flows. Homogeneous and isotropic turbulence was selected as the simplest yet non-trivial mathematical model of a real turbulent flow. The pseudo-spectral approximation was used to solve the Navier-Stokes equations governing the motion of an incompressible carrier phase, while the point-particle approach along with the Lagrangian particle tracking was used to study the motion of dispersed particles. All simulations performed in this work are of general purpose, and hence their outcomes can be used to quantify various physical processes on condition that relevant dimensionless numbers remain unchanged. However, to provide a more physical context, all simulations were performed within the range of parameters relevant to cloud turbulence, potentially supporting the ongoing efforts to elucidate the process of warm rain formation.

6.1 Summary of achievements

Taking into account that a detailed overview of this dissertation has already been provided, and that the outcomes of each chapter have been extensively concluded, this Section only contains a summary of what appears to be the most important achievements and contributions of this dissertation.

Chapter 2: Direct Numerical Simulations

(1) I have designed and implemented almost entirely from the ground up an accurate and efficient pseudo-spectral code to solve the incompressible Navier-Stokes equations; I have provided a self-contained, detailed, organized and focused walk-through of the most important steps relevant to the DNS.

(2) I investigated the issues that can arise (due to an inherently deficient floating-point arithmetic) during the time integration of the Fourier-transformed Navier-Stokes equations, particularly when using the FFT libraries that take advantage of the Hermitian symmetry; I have identified the root cause of these issues and suggested a straightforward approach to eliminate them.

(3) I investigated the impact of forcing on the quality of simulated turbulence and have indicated that the well-established guidelines concerning the selection of forced wavenumbers can lead to artificially correlated velocity fields; I elaborated on the well-known deterministic forcing term and have provided a universal and almost self-contained parametrization of its adjustable parameters, which ensures the appropriate spatial resolution of relevant flow scales on condition that a reasonable value of the control parameter $k_{\max}\eta$ is imposed.

Chapter 3: Large Eddy Simulations

(4) I determined the spectral eddy-viscosity using the FDNS and have for the first time assessed its usefulness in the *a posteriori* LES; I have indicated that the *a priori* spectral eddy-viscosity can significantly improve the energy distribution near the spectral cutoff when compared to the standard model of Chollet & Lesieur [120], and thus effectively align the results with the *a priori* LES.

(5) I thoroughly examined the capability of the LES enriched with the standard spectral eddy-viscosity to capture the inertial range dynamics and have concluded that the overall quality of the simulated turbulence is satisfactory, however, due to suboptimal functional form, the standard model suppresses the development of the inertial subrange.

(6) I have proposed a new modeling approach that allows to adaptively determine the scale-dependent eddy-viscosity based on the instantaneous difference between the resolved and the imposed energy spectra.

(7) I have proposed an alternative functional form of the scale-dependent eddy-viscosity along with an algorithm that allows to determine its unknown coefficients with ease; I have established the requirements and good practices allowing to capture the inertial range dynamics in the pseudo-spectral LES of isotropic turbulence at high Reynolds numbers; I have indicated that using modern high-performance computing resources, the LES can significantly extend the range of Reynolds numbers currently achievable in the corresponding DNS of single-phase

isotropic turbulence, and therefore can provide new insights into the physics of large flow scales.

Chapter 4: Lagrangian particle tracking

(8) I elaborated on the B-spline interpolation introduced in [16, 88, 154] by providing a self-contained, detailed, organized and focused description (along with relevant derivations) of the algorithm coupling this interpolation method with a pseudo-spectral solver.

(9) I elaborated on the methodology of determining the spectrum function of the particle number density recently proposed by Matsuda [166] and have provided a mathematically consistent and universal algorithm for its computation (along with relevant derivations).

Chapter 5: Inertial particle dynamics

(10) I investigated the impact of the standard spectral eddy-viscosity on particle motion in LES of isotropic turbulence at high Reynolds numbers and have indicated that the LES enriched with such a subgrid-scale closure cannot accurately quantify certain collision-related statistics.

(11) I investigated the impact of the newly developed scale-dependent eddy-viscosity closure on particle motion in LES of isotropic turbulence at low and high Reynolds numbers and have indicated that: (i) the capability of the LES to capture the inertial range dynamics seems to depend solely on both the imposed spatial resolution and the functional form the spectral eddy-viscosity; (ii) the LES provides a relatively accurate prediction of various particle statistics when compared to the corresponding DNS on condition that an appropriate spatial resolution is ensured; (iii) the LES can accurately predict particle clustering at length scales relevant to the inertial subrange, clearly indicating that this phenomenon has a minor impact on the subgrid-scale modeling in the particle equation of motion. It should be emphasized that the latter conclusion essentially contradicts the hypothesis recently proposed in [166].

(12) I have indicated that using modern high-performance computing resources, the point-particle LES can significantly extend the range of Reynolds numbers currently achievable in the corresponding DNS of particle-laden isotropic turbulence, and therefore can provide new insights into the multiscale nature of various physical processes associated with the motion of inertial particles suspended in a turbulent flow.

6.2 Future research

Although the point-particle DNS has contributed greatly to the current understanding of the physics underlying particle-laden turbulent flows, quantitative agreement with experiments is still below expectations, as pointed out by respectable authorities in this matter; one can refer to, e.g., [7, 8, 23, 229] for extensive, up-to-date reviews. Changing this state of affairs requires time, substantial computational resources and further efforts not only to provide new physical insights or research hypotheses but also to develop numerical and experimental methods that can contribute to supporting these.

As already pointed out, in the case of single-phase flows, the DNS results are in excellent agreement with experimental data, and thus, for this very reason, the method itself has attained the status of a numerical experiment over the past decades. Taking into account the invaluable practical significance of the point-particle DNS, all the efforts to grant this approach the very same status appear to be well justified. At this point in time, neither the point-particle simulations nor the particle-resolved ones are feasible at Reynolds numbers and/or particulate phase volume fractions relevant to the majority of environmental phenomena or industrial processes. It seems that the LES is the most natural way to mitigate these issues. Therefore, its further development is desirable in order to provide new insights into the physics underlying particle-laden turbulent flows, particularly at high Reynolds numbers.

Possible directions of further research, or rather a relatively subjective extension of this work, can take into account the following:

(1) the development of a unified, massively parallel, open-source solver for the point-particle DNS and LES of isotropic turbulence;

(2) the development of a massively parallel post-processing tools for data analysis, manipulation and visualization, specifically in the context of particle-laden turbulent flows;

(3) further development of the forcing term to: (i) ensure a smooth distribution of the kinetic energy over the forced wavenumber band; (ii) provide a more physical value of the Kolmogorov constant at high Reynolds numbers; (iii) provide a better control over the large-scale resolution; (iv) account for the two-way momentum coupling;

(4) further development of the so-called super-particle (also referred to as particle parcels) approximation seems rather mandatory in order to improve both

the accuracy and the tractability of the point-particle LES at high Reynolds numbers;

(5) an attempt to develop a tractable subgrid-scale model in the particle equation of motion, possibly consistent with the one in the fluid momentum balance equation.

It should be emphasized that among the reasons outlined above, (1) and (2) appear to be of critical importance for ensuring not only accurate and efficient exascale simulations but also (perhaps even most importantly) redress the balance in performing them. Concerning the scientific issues addressed in this work, there are currently only a few groups recognized as leading contributors, most of which have gathered tremendous experience over the past decades of intense research. Those efforts have often resulted in developing in-house methodologies, best practices, tools and codes. This makes it almost impossible (or at least highly challenging) for the newcomers to catch up with the scientific forefront.

Further development of the forcing term as proposed in (3) results solely from the fact that various currently available approaches come with different drawbacks and can introduce their own sources of uncertainty, thus affecting the reliability of simulations. It appears that the number of adjustable parameters in a deterministic forcing scheme can be reduced to one, i.e., the small-scale resolution $k_{\max}\eta$, with all remaining parameters being gracefully parametrized.

Within $1\,\mathrm{m}^3$, a typical cumulus cloud contains approximately 10^8 droplets. For this reason, the resolution requirements of the point-particle DNS limit current research efforts to simulating flow scales whose size extends from approximately 1 mm up to at most several meters [35], however, taking into account the number of droplets set to match the relevant liquid water content. Although the LES can significantly increase the size of the largest resolved flow scales, explicit tracking of the appropriate number of dispersed entities is currently unfeasible. Therefore, further developments of the super-particle parametrization, as proposed in (4), appear to be indispensable; however, since parcels usually represent a large group of real particles, certain two-point statistics cannot be accurately predicted, and thus the foregoing approximation introduces a new set of modeling issues similar in their nature to the subgrid-scale modeling for the residual velocity field.

Based on a significant amount of research, extensively quoted throughout this dissertation, it seems that: (i) the trade-off between the computational cost of the currently most advanced subgrid-scale models and their accuracy is unsatisfactory; on the other hand, (ii) the development of an accurate and universal model is most

likely beyond hope; (iii) recently popular, deep learning-based models are developed using the DNS data gathered at relatively low Reynolds numbers, and thus their real predictive value remains unknown. For these very reasons, all the research focused on the subgrid-scale modeling (particularly in the particle equation of motion), as given in (5), should rather be case-oriented, so to speak, and based on a solid scientific rationale.

Somewhat contrary to the statement concerning the on-going research efforts aimed at developing accurate subgrid-scale models made in [16]—"the field is not yet mature enough to justify using LES to predict the dynamics of small, dispersed particles"—the outcomes of this dissertation suggest that the LES can, in fact, quickly become the method of choice when studying the multiscale nature of various physical processes associated with particle-laden turbulent flows. Perhaps the single most important remark is that, apart from immense practical significance, the purpose of numerical simulations is to stimulate discussions, support theoretical explorations, and partly to open new directions for experimental research. To achieve these goals, there is arguably no need for a rigorous or an ultimate method. There is no doubt that the LES has all of these features.

References

[1] Lesieur, M. (1990) *Turbulence in Fluids* (Rev. ed.), Kluwer Academic Publishers, Dordrecht.

[2] Pope, S. B. (2000) *Turbulent Flows*, Cambridge University Press, Cambridge.

[3] Reynolds, O. (1883) An experimental investigation of the circumstances which determine whether the motion of water shall be direct or sinuous, and the law of resistance in parallel channels, *Philos. Trans. Royal Soc. A*, **174**:935–82.

[4] Reynolds, O. (1894) On the dynamical theory of incompressible viscous fluids and the determination of the criterion, *Philos. Trans. Royal Soc. A*, **186**:123–64.

[5] Leslie, D. C. (1973) *Developments in the Theory of Turbulence*, Clarendon Press, Oxford.

[6] McComb, W. D. (1990) *The Physics of Fluid Turbulence*, Oxford University Press, Oxford.

[7] Kuerten, J. G. M. (2016) Point-Particle DNS and LES of particle-laden turbulent flow–a state-of-the-art review, *Flow Turbul. Combust.*, **97**:689–713.

[8] Elghobashi, S. (2019) Direct numerical simulation of turbulent flows laden with droplets or bubbles, *Annu. Rev. Fluid Mech.*, **51**:217–44.

[9] Maxey, M. R. (1987) The gravitational settling of aerosol particles in homogeneous and random flow fields, *J. Fluid Mech.*, **174**:441-65.

[10] Squires, K. D. and Eaton, J. K. (1990) Particle response and turbulence modification in isotropic turbulence, *Phys. Fluids A*, **2**:1191–203.

[11] Squires, K. D. and Eaton, J. K. (1991) Preferential concentration of particles by turbulence, *Phys. Fluids A*, **3**:1169–78.

[12] Wang, L.-P. and Maxey, M. R. (1993) Settling velocity and concentration distribution of heavy particles in homogeneous isotropic turbulence, *J. Fluid Mech.*, **256**:27–68.

[13] Wang, L.-P., Wexler, A. S. and Zhou, Y. (2000) Statistical mechanical description and modeling of turbulent collision of inertial particles, *J. Fluid Mech.*, **415**:117-53.

[14] Sundaram, S. and Collins, L. R. (1997) Collision statistics in an isotropic particle-laden turbulent suspension. Part 1. Direct numerical simulations, *J. Fluid Mech.*, **335**:75–109.

[15] Monchaux, R., Bourgoin, M. and Cartellier, A. (2012) Analyzing preferential concentration and clustering of inertial particles in turbulence, *Int. J. Multiph. Flow*, **40**:1–18.

[16] Ireland, P. J. (2015) *Computational Investigation of the Effects of Turbulence, Inertia, and Gravity on Particle Dynamics*, PhD thesis, Cornell University.

[17] Ireland, P. J., Bragg, A. D. and Collins, L. R. (2016) The effects of Reynolds number on inertial particle dynamics in isotropic turbulence. Part 2. Simulations with gravitational effects, *J. Fluid Mech.*, **796**:659–711.

[18] Tom, J. (2022) *An Investigation into the Multiscale Nature of Turbulence and its Effect on Particle Transport*, PhD thesis, Duke University.

[19] Boivin, M., Simonin, O. and Squires, K. D. (1998) Direct numerical simulation of turbulence modulation by particles in isotropic turbulence, *J. Fluid Mech.*, **375**:235–63.

[20] Sundaram, S. and Collins, L. R. (1999) A numerical study on the modulation of isotropic turbulence by suspended particles, *J. Fluid Mech.*, **379**:105–43.

[21] Hwang, W. and Eaton, J. K. (2006) Homogeneous and isotropic turbulence modulation by small heavy ($St \sim 50$) particles, *J. Fluid Mech.*, **564**:361–93.

[22] Eaton, J. K. (2009) Two-way coupled turbulence simulations of gas-particle flows using point-particle tracking, *Int. J. Multiph. Flow*, **35**:792–800.

[23] Balachandar, S. and Eaton, J. K. (2010) Turbulent dispersed multiphase flows, *Annu. Rev. Fluid Mech.*, **42**:111–33.

[24] Brandt, L. and Coletti, F. (2022) Particle-laden turbulence: progress and perspectives, *Annu. Rev. Fluid Mech.*, **54**:158–89.

[25] Burton, T. M. and Eaton, J. K. (2005) Fully resolved simulations of particle-turbulence interaction, *J. Fluid Mech.*, **545**:67–111.

[26] Vreman, A. W. (2016) Particle-resolved direct numerical simulation of homogeneous isotropic turbulence modified by small fixed spheres, *J. Fluid Mech.*, **796**:40–85.

[27] Uhlmann, M. (2008) Particle-resolved direct numerical simulation of homogeneous isotropic turbulence modified by small fixed spheres, *Phys. Fluids*, **20**:053305.

[28] Ten Cate, A., Derksen, J. J., Portela, L. M. and Van Den Akker, H. E. A. (2004) Fully resolved simulations of colliding monodisperse spheres in forced isotropic turbulence, *J. Fluid Mech.*, **519**:233–71.

[29] Wang, L.-P., Ayala, O., Gao, H., Andersen, C. and Mathews, K. L. (2014) Study of forced turbulence and its modulation by finite-size solid particles using the lattice Boltzmann approach, *Comput. Math. Appl.*, **67**:363–80.

[30] Wang, L.-P., Peng, C., Guo, Z. and Yu, Z. (2016) Lattice Boltzmann simulation of particle-laden turbulent channel flow, *Comput. Fluids*, **124**:226–36.

[31] Wang, L.-P., Peng, C., Guo, Z. and Yu, Z. (2016) Flow modulation by finite-size neutrally buoyant particles in a turbulent channel flow, *J. Fluids Eng.*, **138**:041306.

[32] Pinsky, M. B. and Khain, A. P. (1997) Turbulence effects on droplet growth and size distribution in clouds–A review, *J. Aerosol Sci.*, **28**:1177–214.

[33] Wang, L.-P. and Grabowski, W. W. (2009) The role of air turbulence in warm rain initiation, *Atmos. Sci. Lett.*, **10**:1–8.

[34] Grabowski, W. W. and Wang, L.-P. (2013) Growth of cloud droplets in a turbulent environment, *Annu. Rev. Fluid Mech.*, **45**:293–324.

[35] Morrison, H., van Lier-Walqui, M., Fridlind, A. M., Grabowski, W. W., Harrington, J. Y., Hoose, C., et al. (2020) Confronting the challenge of modeling cloud and precipitation microphysics, *J. Adv. Model. Earth Syst.*, **12**:e2019MS001689.

[36] Marchioli, C. (2017) Large-eddy simulation of turbulent dispersed flows: a review of modelling approaches, *Acta Mech.*, **228**:741–71.

[37] Jin, G., He, G.-W. and Wang L.-P. (2010) Large-eddy simulation of turbulent collision of heavy particles in isotropic turbulence, *Phys. Fluids*, **22**:055106.

[38] Jin, G. and He, G.-W. (2013) A nonlinear model for the subgrid timescale experienced by heavy particles in large eddy simulation of isotropic turbulence with a stochastic differential equation, *New J. Phys.*, **15**:034011.

[39] Chen, J. and Jin, G. (2017) Large-eddy simulation of turbulent preferential concentration and collision of bidisperse heavy particles in isotropic turbulence, *Powder Technol.*, **314**:281–90.

[40] Zhou, Z., Wang, S., Yang, X. and Jin, G. (2018) A structural subgrid-scale model for relative dispersion in large-eddy simulation of isotropic turbulent flows by coupling kinematic simulation with approximate deconvolution method, *Phys. Fluids*, **32**:095103.

[41] Wu, Q., Zhao, Y., Shi, Y. and Chen, S. (2022) Large-eddy simulation of particle-laden isotropic turbulence using machine-learned subgrid-scale model, *Phys. Fluids*, **34**:065129.

[42] Batchelor, G. K. (1967) *An Introduction to Fluid Dynamics*, Cambridge University Press, Cambridge.

[43] Canuto, C., Hussaini, M. Y., Quarteroni, A. and Zang, T. A. (1987) *Spectral Methods in Fluid Dynamics*, Springer-Verlag, New York.

[44] Orszag, S. A. (1969) Numerical methods for the simulation of turbulence, *Phys. Fluids*, **12**:II-250.

[45] Orszag, S. A. (1971) Numerical simulation of incompressible flows within simple geometries. I. Galerkin (Spectral) representations, *Stud. Appl. Math.*, **50**:293-327.

[46] Cooley, J. W. and Tukey, J. W. (1965) An algorithm for the machine calculation of complex Fourier series, *Math. Comp.*, **19**:297–301.

[47] Orszag, S. A. (1971) Numerical simulation of incompressible flows within simple boundaries: accuracy, *J. Fluid Mech.*, **49**:75-112.

[48] Patterson, G. S., Jr. and Orszag, S. A. (1971) Spectral calculations of isotropic turbulence: Efficient removal of aliasing interactions, *Phys. Fluids*, **14**:2538–41.

[49] Yoffe, S. R. (2012) *Investigation of the Transfer and Dissipation of Energy in Isotropic Turbulence*, PhD thesis, University of Edinburgh.

[50] Rogallo, R. S. (1981) Numerical experiments in homogeneous turbulence, NASA TM-81315.

[51] Young, A. J. (2002) *Investigation of Renormalization Group Methods for the Numerical Simulation of Isotropic Turbulence*, PhD thesis, University of Edinburgh.

[52] Vincent, A. and Meneguzzi, M. (1991) The spatial structure and statistical properties of homogeneous turbulence, *J. Fluid. Mech*, **225**:1–20.

[53] Kerr, R. M. (1985) Higher-order derivative correlations and the alignment of small-scale structures in isotropic numerical turbulence, *J. Fluid Mech.*, **153**:31–58.

[54] Eswaran, V. and Pope, S. B. (1988) An examination of forcing in direct numerical simulations of turbulence, *Comput. Fluids*, **16**:257–78.

[55] Grossmann, S. and Lohse, D. (1994) Scale resolved intermittency in turbulence, *Phys. Fluids*, **6**:611–17.

[56] Ghosal, S., Lund, T. S., Moin, P. and Akselvoll, K. (1995) A dynamic localization model for large-eddy simulation of turbulent flows, *J. Fluid Mech.*, **286**:229–55.

[57] Lamorgese, A. G., Caughey, D. A. and Pope, S. B. (2005) Direct numerical simulation of homogeneous turbulence with hyperviscosity, *Phys. Fluids*, **17**:015106.

[58] Machiels, L. (1997) Predictability of small-scale motion in isotropic fluid turbulence, *Phys. Rev. Lett.*, **79**:3411.

[59] Carbone, M. (2020) *Particle Motion and Gradient Dynamics in Turbulent Flows: Theory and Numerical Simulations*, PhD thesis, Politecnico di Torino.

[60] Witkowska, A., Juvé, D. and Brasseur, J. G. (1997) Numerical study of noise from isotropic turbulence, *J. Comput. Acoust.*, **5**:317–36.

[61] Seror, C., Sagaut, P., Bailly, C. and Juvé, D. (2001) On the radiated noise computed by large-eddy simulation, *Phys. Fluids*, **13**:476–82.

[62] Siggia, E. D. and Patterson, G. S. (1978) Intermittency effects in a numerical simulation of stationary three-dimensional turbulence, *J. Fluid Mech.*, **86**:567–92.

[63] Sullivan, N. P., Mahalingam, S. and Kerr, R. M. (1994) Deterministic forcing of homogeneous, isotropic turbulence. *Phys. Fluids*, **6**:1612-14.

[64] Wang, L.-P., Chen, S., Brasseur, J. G. and Wyngaard, J. C. (1996) Examination of hypotheses in the Kolmogorov refined turbulence theory through high-resolution simulations. Part 1. Velocity field, *J. Fluid. Mech*, **309**:113–56.

[65] Chen, S. and Shan, X. (1992) High-resolution turbulent simulations using the Connection Machine-2, *Comput. Phys.*, **6**:643–6.

[66] Zhou, Z., Wang, S. and Jin, G. (2020) A structural subgrid-scale model for the collision-related statistics of inertial particles in large-eddy simulations of isotropic turbulent flows, *Phys. Fluids*, **32**:095103.

[67] Ababaei, A., Rosa, B., Pozorski, J. and Wang, L.-P. (2021) On the effect of lubrication forces on the collision statistics of cloud droplets in homogeneous isotropic turbulence, *J. Fluid. Mech.*, **918**:A22.

[68] Rosa, B., Pozorski, J. and Wang, L.-P. (2020) Effects of turbulence modulation and gravity on particle collision statistics, *Int. J. Multiph. Flow*, **129**:103334.

[69] Yeung, P.-K. and Pope, S. B. (1989) Lagrangian statistics from direct numerical simulations of isotropic turbulence, *J. Fluid Mech.*, **207**:531–86.

[70] Rosales, C. and Meneveau, C. (2005) Linear forcing in numerical simulations of isotropic turbulence: Physical space implementations and convergence properties, *Phys. Fluids*, **17**:095106.

[71] Yeung, P.-K. and Pope, S. B. (1988) An algorithm for tracking fluid particles in numerical simulations of homogeneous turbulence, *J. Comput. Phys.*, **79**:373-416.

[72] Eswaran, V. and Pope, S. B. (1988) Direct numerical simulations of the turbulent mixing of a passive scalar, *Phys. Fluids*, **31**:506-20.

[73] Wang, L.-P. and Rosa, B. (2009) A spurious evolution of turbulence originated from round-off error in pseudo-spectral simulation, *Comput. Fluids*, **38**:1943–49.

[74] Curry, J. H., Herring, J. R., Loncaric, J. and Orszag, S. A. (1984) Order and disorder in two- and three-dimensional Bénard convection, *J. Fluid Mech.*, **147**:1–38.

[75] Fullerton, G. H. (2001) *Investigation of Non-Newtonian Fluid Turbulence via Direct Numerical Simulation*, PhD thesis, University of Edinburgh.

[76] Box, G. E., Jenkins, G. M., Reinsel, G. C. and Ljung, G. M. (2015) *Time Series Analysis: Forecasting and Control*, John Wiley & Sons, Hoboken, New Jersey.

[77] Chebyshev, P. L. (1867) Des valeurs moyennes, *J. Math. Pures Appl.*, **12**:177–84.

[78] Taylor, G. I. and Green, A. E. (1937) Mechanism of the production of small eddies from large ones, *Proc. Roy. Soc. A*, **158**:499–521.

[79] Brachet, M. E., Meiron, D. I., Orszag, S. A., Nickel, B. G., Morf, R. H. and Frisch, U. (1983) Small-scale structure of the Taylor-Green vortex, *J. Fluid. Mech.*, **130**:411–52.

[80] Dairay, T., Lamballais, E., Laizet, S. and Vassilicos, J. C. (2017) Numerical dissipation vs. subgrid-scale modelling for large eddy simulation, *J. Comput. Phys.*, **337**, 252–74.

[81] Orszag, S. A. (1973) Numerical simulation of the Taylor-Green vortex, in *Computing Methods in Applied Sciences and Engineering* (Part 2) International Symposium, Versailles, December 17–21, Springer-Verlag, Berlin-Heidelberg, 50–64.

[82] Rosa, B. and Pozorski J. (2017) Impact of subgrid fluid turbulence on inertial particles subject to gravity, *J. Turbul.*, **18**:634–52.

[83] Rosa, B., Kopeć, S., Ababaei, A. and Pozorski, J. (2022) Collision statistics and settling velocity of intertial particles in homogeneous turbulence from high-resolution DNS under two-way momentum coupling, *Int. J. Multiph. Flow*, **148**:103906.

[84] Ababaei, A., Michel, A. and Rosa, B. (2024) Collision statistics of droplets in turbulence considering lubrication interactions, mobility of interfaces, and non-continuum molecular effects, *Flow Turbul. Combust.*, **112**:33–59.

[85] Ayala, O., Grabowski, W. W. and Wang, L.-P. (2007) A hybrid approach for simulating turbulent collisions of hydrodynamically-interacting particles, *J. Comput. Phys.*, **225**:51–73.

[86] Ayala, O., Rosa, B. and Wang, L.-P. (2008) Effects of turbulence on the geometric collision rate of sedimenting droplets. Part 1. Results from direct numerical simulation, *New J. Phys.*, **10**:075105.

[87] Tom, J. and Bragg, A. D. (2019) Settling of small particles near vortices and in turbulence, *J. Fluid Mech.*, **871**:244–70.

[88] Carbone, M. and Iovieno, M. (2018) Application of the nonuniform fast Fourier transform to the direct numerical simulation of two-way coupled particle laden flows, *WIT Trans. Eng. Sci.*, **120**:237–53.

[89] Hunt, J. C. R., Wray, A. A. and Moin, P. (1988) Eddies, streams and convergence zones in turbulent flows, In *Proc. Summer Program 1988*, Center for Turbulence Research, Stanford.

[90] Overholt, M. R. and S. B. Pope (1998) A deterministic forcing scheme for direct numerical simulations of turbulence, *Comput. Fluids*, **27**:11–28.

[91] Kraichnan, R. H. (1976) Eddy viscosity in two and three dimensions, *J. Atmos. Sci.*, **33**:1521–36.

[92] Landau, L. D. and Lifshitz, E. M. (1959) *Fluid Mechanics*, Addison-Wesley.

[93] Frisch, U. (1994) *Turbulence*, Cambridge University Press, Cambridge.

[94] Leonard, A. (1974) Energy cascade in large eddy simulations of turbulent fluid flows, *Adv. Geophys.*, **18A**:237–48.

[95] Speziale, C. G. (1985) Galilean invariance of subgrid-scale stress models in large-eddy simulation of turbulence, *J. Fluid Mech.*, **156**:55–62.

[96] Germano, M. (1986) A proposal for a redefinition of the turbulent stresses in the filtered Navier-Stokes equations, *Phys. Fluids*, **29**:2323–24.

[97] Smagorinsky, J. (1963) General circulation experiments with the primitive equations: I. The basic equations, *Mon. Weather Rev.*, **91**:99–164.

[98] Lilly, D. (1967) The representation of small-scale turbulence in numerical simulation experiments, in *Proc. IBM Scientific Computing Symp. on Environmental Sciences*, Goldstein, H. H. Ed., IBM, Yorktown Heights, NY, 195–210.

[99] Domaradzki, J. A. (2021) Large eddy simulations of high Reynolds number turbulence based on interscale energy transfer among resolved scales, *Phys. Rev. Fluids*, **6**:044609.

[100] Rogallo, R. S. and Moin, P. (1984) Numerical simulation of turbulent flows, *Annu. Rev. Fluid Mech.*, **16**:99–137.

[101] Sagaut, P. (2006) *Large Eddy Simulation for Incompressible Flows: An Introduction* (3rd ed.), Springer, Berlin.

[102] Deardorff, J. W. (1970) A numerical study of three-dimensional turbulent channel flow at large Reynolds numbers, *J. Fluid Mech.*, **41**:453–80.

[103] Kwak, D., Reynolds, W. C. and Ferziger, J. H. (1975) Three-dimensional time-dependent computation of turbulent flow, *Rep. TF-5*, Stanford University.

[104] McMillan, O. J., Ferziger, J. H. (1979) Direct testing of subgrid-scale models, *AIAA J.*, **17**:1340–46.

[105] Germano, M., Piomelli, U., Moin, P. and Cabot, W. H. (1991) A dynamic subgrid-scale eddy viscosity model, *Phys. Fluids*, **3**:1760–65.

[106] Fröhlich, J. and Rodi, W. (2002) Introduction to large eddy simulation of turbulent flows, in *Closure Strategies for Turbulent and Transitional Flows*, Launder, B. E. and Sandham, N. D. Eds., Cambridge University Press, Cambridge.

[107] Moin, P., Squires K., Cabot, W. and Lee, S. (1991) A dynamic subgrid-scale model for compressible turbulence and scalar transport, *Phys. Fluids*, **3**:2746–57.

[108] Lilly, D. K. (1992) A proposed modification of the Germano subgrid-scale closure method, *Phys. Fluids*, **4**:633-35.

[109] Bardina, J., Ferziger, J. and Reynolds, W. C. (1980) Improved subgrid-scale models for large-eddy simulation, presented in 13th Fluid and Plasma Dynamics Conference, 14–16 July, Snowmass, Colorado.

[110] Stolz, S. and Adams, N. A. (1999) An approximate decovolution procedure for large-eddy simulation, *Phys. Fluids*, **11**:1699-701.

[111] Domaradzki, J. A. (1997) A subgrid-scale model based on the estimation of unresolved scales of turbulence, *Phys. Fluids*, **9**:2148–64.

[112] Domaradzki, J. A. and Loh, K.-C. (1999) The subgrid-scale estimation model in the physical space representation, *Phys. Fluids*, **11**:2330–42.

[113] Scotti, A. and Meneveau, C. (1999) A fractal model for large eddy simulation of turbulent flow, *Phys. D: Nonlinear Phenom.*, **127**:198–232.

[114] Park, G. I., Bassenne, M., Urzay, J. and Moin, P. (2017) simple dynamic subgrid-scale model for LES of particle-laden turbulence, *Phys. Rev. Fluids*, **2**:044301.

[115] Bassenne, M., Esmaily, M., Livescu, D., Moin, P. and Urzay, J. (2019) A dynamic spectrally enriched subgrid-scale model for preferential concentration in particle-laden turbulence, *Int. J. Multiph. Flow*, **116**:270–80.

[116] Ghate, A. S. and Lele, S. K. (2017) Subfilter-scale enrichment of planetary boundary layer large eddy simulation using discrete Fourier-Gabor modes, *J. Fluid Mech.*, **819**:494–539.

[117] Ghate, A. S. and Lele, S. K. (2019) Gabor mode enrichment in large eddy simulations of turbulent flow, *J. Fluid Mech.*, **903**:A13.

[118] Hausmann, M., Evrard, F. and van Wachem, B. (2022) An efficient model for subgrid-scale velocity enrichment for large-eddy simulations of turbulent flows, *Phys. Fluids*, **34**:115135.

[119] Hausmann, M., Evrard, F. and van Wachem, B. (2023) Wavelet-based modeling of subgrid scales in large-eddy simulation of particle-laden turbulent flows, *Phys. Rev. Fluids*, **8**:104604.

[120] Chollet, J.-P. and Lesieur, M. (1981) Parameterization of small scales of three-dimensional isotropic turbulence utilizing spectral closures, *J. Atmos. Sci.*, **38**:2747–57.

[121] Orszag, S. A. (1970) Analytical theories of turbulence, *J. Fluid. Mech.*:**41**:363–86.

[122] Lesieur, M. and Métais, O. (1996) New trends in large-eddy simulations of turbulence, *Annu. Rev. Fluid. Mech.*, **28**:45–82.

[123] Domaradzki, J. A. (2024) Autonomous large-eddy simulations of turbulence using eddy viscosity derived from the subgrid-scale similarity stress tensor, *J. Fluid Mech.*, **985**:A48.

[124] Métais, O. and Lesieur, M. (1992) Spectral large-eddy simulation of isotropic and stably stratified turbulence, *J. Fluid. Mech*, **239**:157–94.

[125] Chollet, J.-P. (1985) Two-point closure used for a sub-grid scale model in large eddy simulations, in *Turbulent Shear Flows IV*, Bradbury et al. Eds., Springer.

[126] Kaneda, Y., Ishihara, T., Yokokawa, M., Itakura, K. and Uno, A. (2003) Energy dissipation rate and energy spectrum in high resolution direct numerical simulations of turbulence in a periodic box, *Phys. Fluids*, **15**:L21–L23.

[127] Ishihara, T., Kaneda, Y., Yokokawa, M., Itakura, K. and Uno, A. (2007) Small-scale statistics in high-resolution direct numerical simulation of turbulence: Reynolds number dependence of one-point velocity gradient statistics, *J. Fluid Mech.*, **592**:335–66.

[128] Ishihara, T., Gotoh, T. and Kaneda, Y. (2009) Study of high-Reynolds-number isotropic turbulence by direct numerical simulation, *Annu. Rev. Fluid Mech.*, **31**:165–80.

[129] Yeung, P.-K., Donzis, D. A. and Sreenivasan, K. R. (2012) Dissipation, enstrophy, and pressure statistics in turbulence simulations at high Reynolds numbers, *J. Fluid Mech.*, **700**:5–15.

[130] Ishihara, T., Morishita, K., Yokokawa, M., Uno, A. and Kaneda, Y. (2016) Energy spectrum in high-resolution direct numerical simulation of turbulence, *Phys. Rev. Fluids*, **1**:082403.

[131] Yeung, P.-K., Ravikumar, K., Nichols, S. and Uma-Vaideswaran, R. (2025) GPU-enabled extreme-scale turbulence simulations: Fourier pseudo-spectral algorithms at the exascale using OpenMP offloading, *Comput. Phys. Commun.*, **306**:109364.

[132] Domaradzki, J. A., Metcalfe, R. W., Rogallo, R. S. and Riley, J. J. (1987) Analysis of subgrid-scale eddy viscosity with use of results from direct numerical simulations, *Phys. Rev. Lett.*, **58**:547.

[133] Armenio, V., Piomelli, U. and Fiorotto, V. (1999) Effect of the subgrid scales on particle motion, *Phys. Fluids*, **11**:3030–42.

[134] Pope, S. B. (2004) Ten questions concerning the large-eddy simulation of turbulent flows, *New J. Phys.*, **6**:35.

[135] Shaw, R. A. (2003) Particle-turbulence interactions in atmospheric clouds, *Annu. Rev. Fluid Mech.*, **35**:183–227.

[136] Pruppacher, H. R. and Klett, J. D. (1997) *Microphysics of Clouds and Precipitation*, Reidel, Dordrecht.

[137] Domaradzki, J. A. (2022) Near-autonomous large eddy simulations of turbulence based on interscale energy transfer among resolved scale, *Phys. Rev. Fluids*, **7**:114601.

[138] Sreenivasan, K. R. (1995) On the universality of the Kolmogorov constant, *Phys. Fluids*, **7**:2778–84.

[139] Yeung, P.-K. and Ravikumar, K. (2020) Advancing understanding of turbulence through extreme-scale computation: intermittency and simulations at large problem sizes, *Phys. Rev. Fluids*, **5**:110517.

[140] Tadmor, E. (1989) Convergence of spectral methods for nonlinear conservation laws, *SIAM J. Numer. Anal.*, **26**:30–44.

[141] Karamanos, G. S. and Karniadakis, G. E. (2000) A spectral vanishing viscosity method for large-eddy simulations, *J. Comput. Phys.*, **163**:22–55.

[142] Lamballais, E., Fortuné, V. and Laizet, S. (2011) Straightforward high-order numerical dissipation via the viscous term for direct and large eddy simulation, *J. Comput. Phys.*, **230**:3270–75.

[143] Tchen, C. M. (1947) *Mean Value and Correlation Problems with the Motion of Small Particles Suspended in a Turbulent Flow*, PhD thesis, Delft University of Technology.

[144] Corrsin, S. and Lumley, J. (1956) On the equation of motion for a particle in turbulent fluid, *App. Sci. Res.*, **6**:114-16.

[145] Riley, J. J. (1971) *Computer Simulations of Turbulent Dispersion*, PhD thesis, The Johns Hopkins University, Baltimore, Maryland.

[146] Maxey, M. R. and Riley, J. J. (1983) Equation of motion for a small rigid sphere in a nonuniform flow, *Phys. Fluids*, **26**:883–89.

[147] Faxen, H. (1922) The resistance against the movement of a rigour sphere in viscous fluids, which is embedded between two parallel layered barriers, *Ann. Phys.*, **68**:89–119.

[148] Auton, T. R., Hunt, J. C. R. and Prud'Homme, M. (1988) The force exerted on a body in inviscid unsteady non-uniform rotational flow, *J. Fluid Mech.*, **197**:241–57.

[149] Loth, E. (2010), *Particles, Drops and Bubbles: Fluid Dynamics and Numerical Methods*, Cambridge University Press, Cambridge.

[150] Schiller, L. and Naumann, A. Z. (1933) Über die grundlegende Berechnungen bei der Schwerkraft-aufbereitung, *Zeit. Ver. Deut. Ing.*, **77**:318–20.

[151] Riley, J. J. and Patterson, G. S., Jr. (1974) Diffusion experiments with numerically integrated isotropic turbulence, *Phys. Fluids*, **17**:292–97.

[152] Balachandar, S. and Maxey, M. R. (1989) Methods for evaluating fluid velocities in spectral simulations of turbulence, *J. Comput. Phys.*, **83**:96–125.

[153] Lekien, F. and Marsden, J. (2005) Tricubic interpolation in three dimensions, *Int. J. Numer. Methods Eng.*, **63**:455–71.

[154] van Hinsberg, M. A. T., Ten Thije Boonkkamp, J. H. M., Toschi, F. and Clercx, H. J. H. (2012) On the efficiency and accuracy of interpolation methods for spectral codes, *SIAM J. Sci. Comput.*, **34**:B479–B498.

[155] Sundaram, S. and Collins, L. R. (1996) Numerical considerations in simulating a turbulent suspension of finite-volume particles, *J. Comput. Phys.*, **124**:337–50.

[156] Runge, C. (1901) Über empirische Funktionen und die Interpolation zwischen äquidistanten Ordinaten, *Zeit. Math. Phys.*, **46**:224–43.

[157] Cox, M. G. (1972) The numerical evaluation of B-splines, *J. Inst. Math. Appl.*, **10**:134–49.

[158] de Boor, C. (1972) On calculating with B-splines, *J. Approx. Theory*, **6**:50–62.

[159] Schoenberg, I. J. (1946) Contributions to the problem of approximation of equidistant data by analytic functions. Part B. On the problem of osculatory interpolation. A second class of analytic approximation formulae, *Quart. Applied Math.*, **4**:112–41.

[160] Thévenaz, P., Blu, T. and Unser, M. (2000) Image interpolation and resampling, in *Handbook of Medical Imaging. Processing and Analysis*, Bankman, I. N. Ed., 394–420, Academic Press.

[161] Unser, M., Aldroubi, A. and Eden, M. (1991) Fast B-spline transforms for continuous image representation and interpolation, *IEEE Trans. Pattern Anal. Mach. Intell.*, **13**:227–85.

[162] Unser, M., Akram, A. and Murray, M. (1991) B-spline signal processing. I. Theory, *IEEE Trans. Signal Process.*, **41**:821–33.

[163] Carbone, M. and Iovieno, M. (2020) Accurate direct numerical simulation of two-way coupled particle-laden flows through the nonuniform fast Fourier transform, *Int. J. Safety and Sec. Eng*, **10**:191–200.

[164] Fessler, J. R., Kulick, K. D. and Eaton, J. K. (1994) Preferential concentration of heavy particles in a turbulent channel flow, *Phys. Fluids*, **6**:3742–49.

[165] Matsuda, K., Onishi, R., Hirahara, M., Kurose, R., Takahashi, K. and Komori, S. (2014) Influence of microscale turbulent droplet clustering on radar cloud observations, *J. Atmos. Sci.*, **71**:3569–82.

[166] Matsuda, K., Yoshimatsu, K. and Schneider, K. (2024) Heavy particle clustering in inertial subrange of high-Reynolds number turbulence, *Phys. Rev. Lett.*, **132**:234001.

[167] Zhou, Y., Wexler, A. S. and Wang, L.-P. (2001) Modeling of turbulent collision of bidisperse inertial particles, *J. Fluid Mech.*, **433**:77–104.

[168] Rosa, B., Parishani, H., Ayala, O., Grabowski, W. W. and Wang, L.-P. (2013) Kinematic and dynamic collision statistics of cloud droplets from high-resolution simulations, *New J. Phys.*, **15**:045032.

[169] Allen, M. P. and Tildesley, D. J. (1990) *Computer Simulation of Liquids*, Oxford University Press, New York.

[170] Moser, R. D., Haering, S. W. and Yalla, G. R. (2021) Statistical properties of subgrid-scale turbulence models, *Annu. Rev. Fluid Mech.*, **53**:255–86.

[171] Fede, P. and Simonin, O. (2006) Numerical study of the subgrid fluid turbulence effects on the statistics of heavy colliding particles, *Phys. Fluids*, **18**:045103.

[172] Shotorban, B. and Mashayek, F. (2005) Modeling subgrid-scale effects on particles by approximate deconvolution, *Phys. Fluids*, **17**:081701.

[173] Pozorski, J. and Apte, S. V. (2009) Filtered particle tracking in isotropic turbulence and stochastic modeling of subgrid-scale dispersion, *Int. J. Multiph. Flow*, **35**:118–28.

[174] Fede, P., Simonin, O., Villedieu, P. and Squires, K. D. (2006) Stochastic modelling of the turbulent subgrid fluid velocity along inertial particle trajectories, Proceedings of the Summer Program, Center for Turbulence Research, Stanford University, 247–58.

[175] Shotorban, B. and Mashayek, F. (2006) A stochastic model for particle motion in large-eddy simulation, *J. Turbul.*, **7**:N18.

[176] Knorps, M. and Pozorski, J. (2021) Stochastic modeling for subgrid-scale particle dispersion in large-eddy simulation of inhomogeneous turbulence, *Phys. Fluids*, **33**:043323.

[177] Fung, J. C. H., Hunt, J. C. R., Malik, N. A. and Perkins, R. J. (1992) Kinematic simulation of homogeneous turbulence by unsteady random Fourier modes, *J. Fluid Mech.*, **236**:281–318.

[178] Malik, N. A. and Vassilicos, J. C. (1999) A Lagrangian model for turbulent dispersion with turbulent-like flow structure: Comparison with direct numerical simulation for two-particle statistics, *Phys. Fluids*, **11**:1572–80.

[179] Ray, B. and Collins, L. R. (2014) A subgrid model for clustering of high-inertia particles in large-eddy simulations of turbulence, *J. Turbul.*, **15**:366–85.

[180] Kuerten, J. G. M. (2006) Subgrid modeling in particle-laden channel flow, *Phys. Fluids*, **18**:025108.

[181] Marchioli, C., Salvetti, M. V. and Soldati, A. (2008) Appraisal of energy recovering sub-grid scale models for large-eddy simulation of turbulent dispersed flows, *Acta Mech.*, **201**:277–96.

[182] Germano, M. (1986) Differential filters of elliptic type, *Phys. Fluids*, **29**:1757–58.

[183] Hausmann, M. (2024) *Advanced modeling using large eddy simulations applied to particle-laden turbulent flows*, PhD thesis, Otto von Guericke University of Magdeburg.

[184] Davila, J. and Hunt, J. C. R. (2001) Settling of small particles near vortices and in turbulence, *J. Fluid Mech.*, **440**:117–45.

[185] Rosa, B., Parishani, H., Ayala, O. and Wang, L.-P. (2016) Settling velocity of small inertial particles in homogeneous isotropic turbulence from high-resolution DNS, *Int. J. Multiph. Flow*, **83**:217–31.

[186] Lamb, D. and Verlinde, J. (2011) *Physics and Chemistry of Clouds*, Cambridge University Press.

[187] Szumowski, M. J., Rauber, R. M., Ochs III, H. T. and Beard, K. V. (1998) The microphysical structure and evolution of Hawaiian rainband clouds. Part II: Aircraft measurements within rainbands containing high reflectivity cores, *J. Atmos. Sci.*, **55**:208–26.

[188] Beard, K. V. and Ochs III, H. T. (1993) Warm-rain initiation: An overview of microphysical mechanisms, *J. Appl. Meteorol.*, **32**:608–25.

[189] Koziol, A. S. and Leighton, H. G. (1996) The effect of turbulence on the collision rates of small cloud drops, *J. Atmos. Sci.*,**53**:1910–20.

[190] Pinsky, M. B., Khain, A. and Shapiro, M. (1999) Collisions of small drops in a turbulent flow. Part I: Collision efficiency. Problem formulation and preliminary results, *J. Atmos. Sci.*,**56**:2585–600.

[191] Michel, A., Ababaei, A. and Rosa, B. (2023) The influence of gravity and mass loading on the coalescence of aerodynamically interacting droplets in homogeneous isotropic turbulence, *J. Atmos. Sci.*, **80**:2207–20.

[192] Reade, W. C. and Collins, L. R. (2000) Effect of preferential concentration on turbulent collision rates, *Phys. Fluids*, **12**:2530–40.

[193] Chun, J., Koch, D. L., Rani, S., Ahluwalia, A. and Collins, L. R. (2005) Clustering of aerosol particles in isotropic turbulence, *J. Fluid Mech*, **536**:219–51.

[194] Meibohm, J., Pandey, V., Bhatnagar, A., Gustavsson, K., Mitra, D., Perlekar, P. and Mehlig, B. (2021) Paths to caustic formation in turbulent aerosols, *Phys. Rev. Fluids*, **6**:L062302.

[195] Falkovich, G., Fouxon A. and Stepanov, M. G. (2002) Acceleration of rain initiation by cloud turbulence, *Nature*, **419**:151–54.

[196] Falkovich, G. and Pumir, A. (2007) Sling effect in collisions of water droplets in turbulent clouds, *J. Atmos. Sci.*, **64**:4497–505.

[197] Perrin, V. E. and Jonker, H. J. J. (2014) Preferred location of droplet collisions in turbulent flows, *Phys. Rev. E*, **89**:033005.

[198] Perrin, V. E. and Jonker, H. J. J. (2015) Relative velocity distribution of inertial particles in turbulence–A numerical study, *Phys. Rev. E*, **92**:043022.

[199] Voßkuhle, M., Pumir, A., Lévêque, E. and Wilkinson, M. (2014) Prevalence of the sling effect for enhancing collision rates in turbulent suspensions, *J. Fluid Mech.*, **149**:841–52.

[200] Bragg, A. D. and Collins, L. R. (2014) New insights from comparing statistical theories for inertial particles in turbulence: II. Relative velocities, *New J. Phys.*, **16**:055014.

[201] Bec, J., Homann, H. and Ray, S. S. (2014) Gravity-driven enhancement of heavy particle clustering in turbulent flow, *Phys. Rev. Lett.*, **112**:184501.

[202] Good, G. H., Ireland, P. J., Bodenschatz, E., Collins, L. R. and Warhaft, Z. (2014) Settling regimes of inertial particles in isotropic turbulence, *J. Fluid Mech.*, **759**:R3.

[203] Tooby, P. F., Gerald, L. W. and John, D. I. (1977) The motion of a small sphere in a rotating velocity field: A possible mechanism for suspending particles in turbulence, *J. Geophys. Res.*, **85**:2096–100.

[204] Nielsen, P. (1993) Turbulence effects on the settling of suspended particles, *J. Sediment. Res.*, **63**:835–38.

[205] Kawanisi, K. and Shiozaki, R. (2008) Turbulent effects on the settling velocity of suspended sediment, *J. Hydraul. Eng.*, **134**:261–66.

[206] Monchaux, R. and Dejoan, A. (2017) Settling velocity and preferential concentration of heavy particles under two-way coupling effects in homogeneous turbulence, *Phys. Rev. Fluids*, **2**:104302.

[207] Hassaini, R., Petersen, A. J. and Coletti, F. (2023) Effect of two-way coupling on clustering and settling of heavy particles in homogeneous turbulence, *J. Fluid Mech.*, **976**:A12.

[208] Bhattacharjee, S., Tom, J., Carbone, M. and Bragg, A. D. (2024) Investigating the parametric dependence of the impact of two-way coupling on inertial particle settling in turbulence, *J. Fluid Mech.*, **987**:A17.

[209] Woittiez, E. J. P., Jonker, H. J. J. and Portela, L. M. (2009) On the combined effects of turbulence and gravity on droplet collisions in clouds: A numerical study, *J. Atmos. Sci.*, **66**:1926–43.

[210] Bragg, A. D., Ireland, P. J. and Collins, L. R. (2015) On the relationship between the non-local clustering mechanism and preferential concentration, *J. Fluid Mech.*, **780**:327–43.

[211] Bec, J., Biferale, L., Boffetta, G., Celani, A., Cencini, M., Lanotte, A., Musacchio, S. and Toschi, F. (2006) Acceleration statistics of heavy particles in turbulence, *J. Fluid Mech.* **550**:349–58.

[212] Bragg, A. D. and Collins, L. R. (2014) New insights from comparing statistical theories for inertial particles in turbulence: I. Spatial distribution of particles, *New J. Phys.*, **16**:055013.

[213] Bragg, A. D., Ireland, P. J. and Collins, L. R. (2015) Mechanisms for the clustering of inertial particles in the inertial range of isotropic turbulence, *Phys. Rev. E*, **92**:023029.

[214] Zaichik, L. I. and Alipchenkov, V. M. (2007) Refinement of the probability density function model for preferential concentration of aerosol particles in isotropic turbulence, *Phys. Fluids*, **19**:113308.

[215] Chen, L., Goto, S. and Vassilicos, J. C. (2006) Turbulent clustering of stagnation points and inertial particles, *J. Fluid Mech.*, **553**:143–55.

[216] Coleman, S. W. and Vassilicos, J. C. (2009) A unified sweep-stick mechanism to explain particle clustering in two- and three-dimensional homogeneous, isotropic turbulence, *Phys. Fluids*, **21**:113301.

[217] Goto, S. and Vassilicos, J. C. (2006) Self-similar clustering of inertial particles and zero-acceleration points in fully developed two-dimensional turbulence, *Phys. Fluids*, **18**:115103.

[218] Bec, J., Biferale, L., Cencini, M., Lanotte, A., Musacchio, S. and Toschi, F. (2007) Heavy particle concentration in turbulence at dissipative and inertial scales, *Phys. Rev. Lett.*, **98**:084502.

[219] Goto, S. and Vassilicos, J. C. (2008) Sweep-stick mechanism of heavy particle clustering in fluid turbulence, *Phys. Rev. Lett.*, **100**:035504.

[220] Yeung, P.-K. and Zhou, Y. (1997) Universality of the Kolmogorov constant in numerical simulations of turbulence, *Phys. Rev. E*, **56**:1746.

[221] Petersen, A. J., Baker, L. and Coletti, F. (2019) Experimental study of inertial particles clustering and settling in homogeneous turbulence, *J. Fluid Mech.*, **864**:925–70.

[222] Onishi, R., Takahashi, K. and Vassilicos, J. C. (2013) An efficient parallel simulation of interacting inertial particles in homogeneous isotropic turbulence, *J. Comput. Phys.*, **242**:809–27.

[223] Matsuda, K. and Onishi, R. (2019) Turbulent enhancement of radar reflectivity factor for polydisperse cloud droplets, *Atmos. Chem. Phys.*, **19**:1785–99.

[224] Matsuda, K., Schneider, K. and Yoshimatsu, K. (2021) Scale-dependent statistics of inertial particle distribution in high Reynolds number turbulence, *Phys. Rev. Fluids*, **6**:064304.

[225] Morinishi, Y., Lund, T. S., Vasilyev, O. V. and Moin, P. (1998) Fully conservative higher order finite difference schemes for incompressible flow, *J. Comput. Phys.*, **143**:90–124.

[226] Hirt, C. and Cook, J. (1972) Calculating three-dimensional flow around structure, *J. Comput. Phys.*, **10**:324–40.

[227] Onishi, R., Baba, Y. and Takahashi, K. (2011) Large-scale forcing with Less communication in finite-difference simulations of steady isotropic turbulence, *J. Comput. Phys.*, **230**:4088-99.

[228] Yoshida, K. and Arimitsu, T. (2007) Inertial-subrange structures of isotropic incompressible magnetohydrodynamic turbulence in the Lagrangian renormalized approximation, *Phys. Fluids*, **19**:045106.

[229] Voth, G. A. and Soldati, A. (2017) Anisotropic particles in turbulence, *Annu. Rev. Fluid Mech.*, **49**:249–76.